



Universiteit
Leiden

The Netherlands

Focal-plane wavefront sensors for direct exoplanet imaging: theory, simulations and on-sky demonstrations

Bos, S.P.

Citation

Bos, S. P. (2021, September 30). *Focal-plane wavefront sensors for direct exoplanet imaging: theory, simulations and on-sky demonstrations*. Retrieved from <https://hdl.handle.net/1887/3214244>

Version: Publisher's Version

License: [Licence agreement concerning inclusion of doctoral thesis in the Institutional Repository of the University of Leiden](#)

Downloaded from: <https://hdl.handle.net/1887/3214244>

Note: To cite this publication please use the final published version (if applicable).

Focal-plane wavefront sensors for direct exoplanet imaging

Theory, simulations and on-sky demonstrations

Proefschrift

ter verkrijging van
de graad van doctor aan de Universiteit Leiden,
op gezag van rector magnificus prof. dr. ir. Hester Bijl,
volgens besluit van het college voor promoties
te verdedigen op donderdag 30 september 2021
klokke 16:15 uur

door

Steven Peter Bos

geboren te Delft, Nederland
in 1993

Promotor: Prof. dr. Christoph Keller
Co-promotor: Dr. ir. Frans Snik

Promotiecommissie:	Prof. dr. Huub Röttgering (voorzitter)	Universiteit Leiden
	Prof. dr. ir. Niek Doelman (secretaris)	Universiteit Leiden
Overige commissieleden:	Prof. dr. Sjoerd Stallinga	Technische Universiteit Delft
	Dr. Rebecca Oppenheimer	American Museum of Natural History
	Dr. Sandrine Thomas	Vera C. Rubin Observatory

*Voor mijn ouders
&
Voor Charlotte*

Don't quit

*“When things go wrong as they sometimes will,
when the road you're trudging seems all up hill,
when the funds are low and the debts are high
and you want to smile, but you have to sigh,
when care is pressing you down a bit,
rest if you must, but don't you quit.
Life is strange with its twists and turns
as every one of us sometimes learns
and many a failure comes about
when he might have won had he stuck it out;
don't give up though the pace seems slow—
you may succeed with another blow.
Success is failure turned inside out—
the silver tint of the clouds of doubt,
and you never can tell just how close you are,
it may be near when it seems so far;
so stick to the fight when you're hardest hit—
it's when things seem worst that you must not quit.”*

—John Greenleaf Whittier

Cover design: Artistic representations of the metaphorical mountains that I have climbed during my academic career and would have climbed if I had chosen to stay. On top of these mountains are the telescopes that I (would) have observed with during the different phases in my career. Also shown are two of the (in my opinion) most impressive objects and phenomena in astronomy: the Andromeda galaxy and a solar eclipse.

Back cover: The mountain on the left represents my Bachelor's and has the Isaac Newton Telescope (La Palma) on top. Also placed on this mountain is my personal Meade ETX-125 telescope pointed at the Andromeda galaxy. The mountain on the right represents my Master's with the William Herschel Telescope (La Palma). Shown in the upper left is a solar eclipse with the Minnaert and Van de Hulst neutral points denoted as white points. In the lower right I placed the Leiden Eclipse Imaging Polarimeter, which is the instrument we used to observe these neutral points in polarized light. In the upper right is the Andromeda galaxy, which is the most distant object that can be observed with the naked eye.

Front cover: The mountain on the left represents my PhD. The telescopes placed on top are the Subaru telescope (Hawaii) and the Keck telescopes (Hawaii). Also shown on the top of this mountain is a group of people observing the Andromeda galaxy. The mountain on the right represents the career in astronomy that I would have had if I decided to stay in astronomy. The Extremely Large Telescope (Chile), currently under construction, is placed on top.

Printed by: Gildeprint

ISBN: 978-94-6419-250-6

An electronic copy of this thesis can be found at <https://openaccess.leidenuniv.nl>

© Steven P. Bos, 2021

Contents

1	Introduction	1
1.1	Detecting exoplanets	1
1.2	Direct imaging of exoplanets	4
1.2.1	Wavefront aberrations	6
1.2.2	Adaptive optics	8
1.2.3	Coronagraphy	10
1.2.4	Observing strategies and post processing	12
1.2.5	Detecting exoplanet variability	13
1.3	Focal-plane wavefront sensing	14
1.3.1	Theory	14
1.3.2	Family of focal-plane wavefront sensors	19
1.4	This thesis	24
2	Focal-plane wavefront sensing with the vector-Apodizing Phase Plate	33
2.1	Introduction	34
2.2	Theory	37
2.2.1	Phase retrieval	37
2.2.2	vAPP design for phase retrieval	41
2.3	Aberration estimation algorithm	44
2.3.1	Maximum a posteriori estimation	44
2.3.2	Coronagraph model	45
2.4	Simulations	47
2.4.1	Photon and read noise sensitivity	49
2.4.2	Mode photon noise sensitivity	50
2.4.3	Dynamic range algorithm	52
2.5	Demonstration at SCExAO	53
2.5.1	SCExAO	53
2.5.2	Algorithm implementation in SCExAO	53
2.5.3	Internal source demonstration	55
2.5.4	On-sky demonstration	58
2.6	Discussion and conclusion	58
2.7	Appendix	66
2.7.1	Phase retrieval examples	66
2.7.2	Implications for spatial LDFC	67
2.7.3	Derivatives objective function	68
3	Linear Dark Field Control at Subaru/SCExAO	73
3.1	Introduction	75
3.2	Combining spatial LDFC with an APvAPP	78
3.2.1	Spatial LDFC	78
3.2.2	FPWFS with the APvAPP	81
3.3	Deploying LDFC on SCExAO	81
3.3.1	Instrument parameters	82
3.3.2	Deriving the reference PSF	82

3.3.3	Bright pixel selection	83
3.3.4	Modal basis set and control matrix	84
3.3.5	LDFC closed-loop operation	88
3.3.6	Noise analysis for LDFC with the SCEExAO APvAPP	90
3.4	Results	91
3.5	Discussion and Conclusions	96
4	On-sky demonstration of Linear Dark Field Control	101
4.1	Introduction	102
4.2	LDFC at SCEExAO	104
4.2.1	Principle	104
4.2.2	SCEExAO	105
4.2.3	Static wavefront error calibration	106
4.2.4	Reference image and bright pixel selection	106
4.2.5	Response and control matrix	111
4.3	On-sky demonstration	115
4.3.1	Static eigenmode aberration	115
4.3.2	On-sky atmospheric residuals	118
4.4	Discussion and conclusion	122
5	The polarization-encoded self-coherent camera	129
5.1	Introduction	130
5.2	Theory	133
5.2.1	Polarization-encoded self-coherent camera	135
5.2.2	Reference hole diameter	137
5.2.3	Reference hole distance	137
5.2.4	Focal-plane sampling constraints	138
5.2.5	Spectral bandwidth limitations	139
5.2.6	Instrumental polarization	141
5.2.7	Polarization leakage	143
5.2.8	Coherent differential imaging	144
5.3	Simulations	145
5.3.1	Wavefront sensing	146
5.3.2	Wavefront sensing & control	154
5.3.3	Coherence differential imaging	164
5.4	Discussion and conclusions	164
6	On-sky verification of Fast and Furious focal-plane wavefront sensing	175
6.1	Introduction	177
6.2	Fast and Furious algorithm	180
6.3	Demonstration at Subaru/SCEExAO	182
6.3.1	SCEExAO and algorithm implementation	182
6.3.2	Quantifying PSF quality	185
6.3.3	Internal source demonstration	186
6.3.4	On-sky demonstration	192

6.4	Discussion and conclusion	198
7	The Vector Speckle Grid	205
7.1	Introduction	206
7.2	Theory	207
7.2.1	Vector phase speckle grid	207
7.2.2	Vector amplitude speckle grid	210
7.3	Simulations	211
7.3.1	Performance quantification	211
7.3.2	Degree of polarization effects	218
7.4	Implementation of vector speckle grid	220
7.5	Discussion and conclusion	220
8	Outlook	225
	Nederlandstalige samenvatting	229
	Publication list	239
	Curriculum Vitae	245
	Acknowledgements	247

1 | Introduction

1.1 Detecting exoplanets

Major discoveries in astronomy have regularly led to paradigm shifts. Such a shift occurred when Galileo Galilei pointed his home-made telescope towards the skies and observed that Venus goes through a full set of phases that are similar to that of the Moon. This was evidence that Venus orbits the Sun, and therefore strengthened the case of the heliocentric model. When future astronomers discover life on an exoplanet, a planet orbiting another star, this will undoubtedly also change the view of humanity on its place in the universe. For centuries people have philosophized about the possibility of alien life on other worlds in the universe. This intriguing subject inspired people to actually prove the existence of these worlds. William Stephen Jacob, the director of Madras observatory, already claimed in 1855 to have discovered an exoplanet in orbit around the binary system 70 Ophiuchi (Jacob, 1855). This claim, and many others that followed throughout the 19th and 20th centuries, were subsequently refuted, usually because there was some systematic error that was not included in the initial analysis.

At the end of the 20th century, various technological developments enabled instruments to finally reach the required precision to actually detect an exoplanet. In 1992, two exoplanets were found to orbit the pulsar PSR B1257+12 (Wolszczan & Frail, 1992), a stellar remnant from a supernova. Three years later, in 1995, Michel Mayor and Didier Queloz announced the discovery of 51 Pegasi b, the first detected exoplanet orbiting a sun-like star (Mayor & Queloz, 1995). These discoveries were completely unexpected, as these two exoplanetary systems are so different than the solar system. Many astronomers did not expect to find exoplanets around pulsars, because they thought that exoplanets could not survive the supernova that precedes to the formation of the pulsar, and thus were surprised by the exoplanets orbiting PSR B1257+12. Astronomers also did not expect to find exoplanets close to their host stars, and yet 51 Pegasi b has an orbital period of just over four days, placing it closer to its host star than Mercury is to the Sun. Since then, over a quarter of a century later, exoplanet science has become a flourishing research field. At the time of writing this thesis, more than 4300 exoplanets have been discovered¹, and tens of thousands are waiting to be seen by the Gaia satellite (Lindegren et al., 2007; Perryman et al., 2014), and over a thousand by the Transiting Exoplanet Survey Satellite (TESS; Barclay et al. 2018; Ricker et al. 2014). The already accumulated wealth of information has taught us much about the exoplanet population. For example, we have inferred from extended surveys that ~22% of the sun-like stars harbors an Earth-like exoplanet in an orbit such that liquid water can exist on its surface (Petigura et al., 2013; Winn & Fabrycky, 2015). However, much remains to be discovered before we can confirm that these Earth-like exoplanets are actually habitable. We have to detect water, study the atmospheric pressure to determine if an ocean can be sustained, and measure the atmospheric composition to inform us about (bio)chemical processes occurring on the exoplanet. By studying the surface properties we will be able to distinguish between exoplanets domi-

¹To be precise, at the moment of writing, January 26, 2021, there are 4331 confirmed exoplanet discoveries. Source: <https://exoplanets.nasa.gov>

nated by oceans or land mass.

The existence of most of the current, and the to be discovered exoplanets is inferred by indirect methods. That means that the exoplanet itself is not directly seen, but its effect on the host star. There are three main indirect methods of discovering exoplanets:

1

- **Radial velocity method:** Mayor and Queloz made their discovery with the ELODIE spectrograph (Baranne et al., 1996) by carefully measuring the radial velocity of 51 Pegasi over the course of hours, days and weeks. The radial velocity is found by measuring Doppler shifts in the star's spectrum. Any periodicity in the radial velocity indicates that there is an unknown body that pulls on the star while making its orbit (Struve, 1952). Analyzing the radial velocity as a function of time yields many of the exoplanet's orbital parameters. The amplitude of the signal gives a lower limit of the exoplanet's mass, and when the inclination of the orbit is known, its true mass can be calculated. The radial velocity method is responsible for exoplanet candidate detections around the closest neighbor of the Sun, Proxima Centauri (Anglada-Escudé et al., 2016; Damasso et al., 2020).
- **Transit photometry method:** A small fraction of exoplanets pass right in front of their star. This reduces the brightness of the star by a small fraction. If regular brightness dips are observed over long periods of time, then this is a strong indication of an exoplanet (Henry et al., 1999). The duration between dips and the shape of the brightness curve during transit contain information on the orbital parameters. Furthermore, the fraction of starlight that is blocked by the exoplanet is directly related to its radius. Using transit spectroscopy, the composition of the exoplanet's atmosphere can be measured. Transit photometry is responsible for the greatest number of exoplanet discoveries, the Kepler space-observatory alone has discovered over 3000 new exoplanets (Borucki et al., 2010).
- **Astrometry method:** When an exoplanet moves through its orbit, it causes a reflex motion of the star. The radial component of this motion is measured by the radial velocity method, and the lateral components are measured by the astrometry method. The astrometry method carefully measures the position of the star in the sky over a long period of time. A careful analysis of the time series of the star's position can, again, reveal orbital parameters of the exoplanet and its mass. The method's greatest achievement thus far is the measurement of the mass of Beta Pictoris b (Snellen & Brown, 2018), however, when the Gaia satellite's full dataset becomes available (Brown et al., 2018, 2016), over ten thousand exoplanet discoveries are expected.

When these methods are combined, they give a detailed view of the exoplanet's orbit, mass and radius. However, they are rather limited in characterizing the exoplanet's atmosphere and surface, of which the properties are far more interesting in the context of habitability and signs of life.

The direct imaging method is far more promising for exoplanet characterization as it aims to spatially separate the exoplanet's light from that of the star. This allows for a

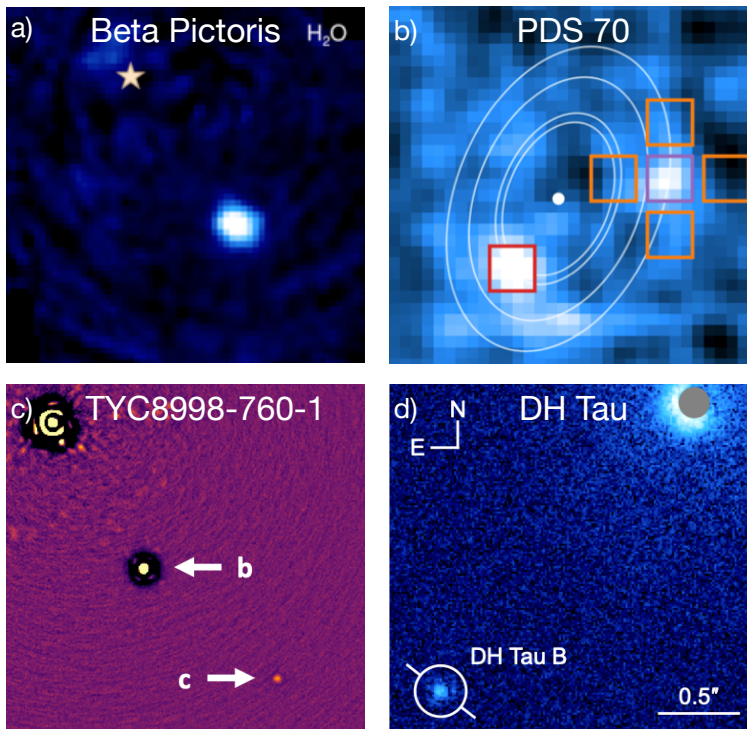


Figure 1.1: Images of exoplanets. a) Detection of H₂O in the atmosphere of Beta Pictoris b. Adopted from Hoeijmakers et al. (2018). b) Two accreting exoplanets in the disk around PDS 70. Adopted from Haffert et al. (2019). c) Two planets orbiting the solar-type star TYC8998-760-1. Adopted from Bohn et al. (2020). d) Polarized intensity image of the DH Tau system, revealing a disk around DH Tau b. Adopted from van Holstein et al. (2021).

far more detailed view of the exoplanet, because the temporal, spectral and polarization properties of the planet light itself can be analyzed. For example, the medium-resolution integral-field spectrograph SINFONI (Eisenhauer et al., 2003) yielded strong detections of CO and H₂O in the atmosphere of Beta Pictoris b (Hoeijmakers et al., 2018), and a survey with the polarimetric imaging mode of SPHERE/IRDIS (De Boer et al., 2020; Langlois et al., 2014) detected signs of disks around young exoplanets (van Holstein et al., 2021). Furthermore, as direct imaging observations explore the entire close-in circumstellar environment, they provide a unique opportunity to study the interaction between circumstellar disks and exoplanets during planet formation. The most famous example is PDS 70 (Hafert et al., 2019; Keppler et al., 2018; Wagner et al., 2018). Modern ground-based direct imaging instruments are capable of imaging young jovian planets on outer solar system-like scales around nearby stars (Bohn et al., 2020; Chauvin et al., 2017; Macintosh et al., 2015; Marois et al., 2008). However, the exoplanet yield from surveys with the current suite of instruments (VLT/SPHERE Beuzit et al. 2019; Subaru/SCEXAO Jovanovic et al. 2015b; Gemini/GPI Macintosh et al. 2014) have been lower than predicted by models that extrapolated findings of indirect methods (Nielsen et al., 2019; Vigan et al., 2020). This led to motion multiple upgrade programs to improve the performance of these instruments, which will enable them to detect greater numbers of exoplanets (Boccaletti et al., 2020; Chilcote et al., 2018). Furthermore, new survey strategies have been developed that use input from the radial velocity and astrometry method to target stars that already show signs of the presence of a companion (Brandt et al., 2019; Currie et al., 2020a).

1.2 Direct imaging of exoplanets

The direct imaging technique is the most promising method to detect and characterize exoplanets and look for signs of life. Direct imaging has to overcome two fundamental challenges: **angular separation** and **contrast**. These challenges are the result of the wave-like nature of light. A star emits light as a spherical wave. When it arrives at Earth, it has effectively become a flat wavefront because of the large distances involved. When a space-based telescope captures the light, it cuts out part of the wavefront in the shape of its primary mirror. Due to diffraction and the finite extent and sharp edges of the telescope mirror, the image of the star is not infinitely sharp. The star looks like a central core of light surrounded by rings that become fainter with distance, but are still much brighter than exoplanets. This structure is referred to as the point spread function (PSF; Goodman 2005), and limits the angular resolution of the telescope ($\Delta\theta$) to:

$$\Delta\theta = 1.22 \frac{\lambda}{D}, \quad (1.1)$$

with λ the wavelength and D the telescope diameter. An 8-meter class telescope operating at $1 \mu\text{m}$ has a resolution limit of ~ 0.03 arcsec. Suppose that we want to observe the Earth orbiting the Sun from a distance of 10 pc in the visible ($\sim 0.3\text{-}1 \mu\text{m}$). At maximum separation, the angular separation between the two objects would be ~ 0.1 arcsec. The brightness ratio between the Earth and the Sun, referred to as contrast, is $\sim 10^{-10}$ (Traub & Oppenheimer, 2010). Due to this extreme contrast, direct imaging is regularly referred

The high-contrast imaging instrument

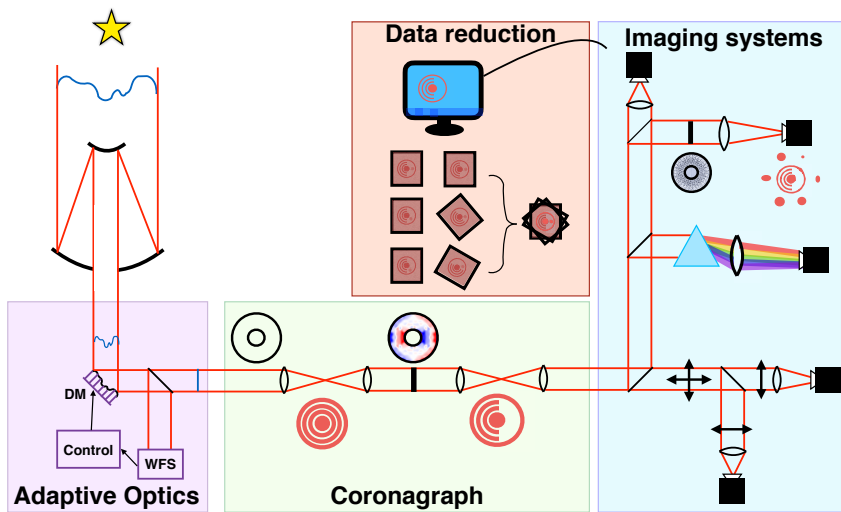


Figure 1.2: Schematic overview of a high-contrast imaging instrument. Acronyms in the figure are: DM = deformable mirror, WFS = wavefront sensor. Image courtesy of David Doelman.

to as **high-contrast imaging (HCI)**.

Ground-based telescopes face an additional challenge posed by the Earth's atmosphere. Turbulence within the atmosphere causes wavefront aberrations in the light propagating through it, distorting the PSF and degrading the resolution achieved by the telescope significantly. To enable direct imaging of exoplanets with ground-based telescopes, these wavefront aberrations need to be measured and corrected.

To overcome these challenges, HCI instruments are complex optical systems. They consist of multiple subsystems designed to correct wavefront aberrations, suppress starlight and analyze exoplanet light. Figure 8.2 shows a schematic of a ground-based HCI instrument. Light from the star is distorted by the Earth's, turbulent atmosphere before being captured by the telescope. The first subsystem is the adaptive optics (AO) system that measures and optically corrects wavefront aberrations. The coronagraph subsequently suppresses the starlight such that exoplanets can be observed and feeds the residual starlight and exoplanet light to various imaging systems. These imaging systems use various observing strategies to separate the residual starlight from the planet during data reduction. The exoplanet is then characterized by analyzing the spectrum and polarization state of light. The subsystems and other challenges in high-contrast imaging will be discussed in the following subsections.

1.2.1 Wavefront aberrations

HCI instruments are always limited by uncorrected wavefront aberrations. These wavefront aberrations create **speckles**, which are stellar PSF structures that closely mimic the exoplanet's signal. This noise source is referred to as **speckle noise** (Racine et al., 1999). Wavefront aberrations are deviations from the ideal wavefront that would otherwise generate a perfect PSF. Usually, wavefront aberrations are described in the pupil plane of the optical system and are divided into phase and amplitude aberrations. Phase aberrations result in a rugged wavefront, and when there are no phase aberrations, the wavefront is perfectly flat. Amplitude aberrations are intensity variations over the wavefront, and when not present, the wavefront has uniform intensity. Phase aberrations usually have a much stronger impact on the image than amplitude aberrations.

For ground-based observations, we can distinguish three important sources of wavefront aberrations.

Atmospheric turbulence

Before the light is captured by the telescope, it propagates through the Earth's atmosphere, which distorts the wavefront. When left uncorrected, starlight is spread over a larger area, degrading the resolution of the telescope to $\sim \lambda/r_0$, with r_0 the Fried parameter describing the spatial scale over which the root-mean-square wavefront error is less than 1 radian (Fried, 1966). For $\lambda = 500$ nm, r_0 is usually about 10 - 15 cm (Hardy, 1998) for a good site at night, and results in a deterioration of the angular resolution of an 8-meter class telescope by a factor $\sim 50 - 80$. The Fried parameter increases with wavelength, $r_0 \propto \lambda^{6/5}$ (Hardy, 1998), and therefore HCI observations in the visible light are more challenging than in the mid infrared. The atmosphere evolves over a timescale $\tau_0 \sim r_0/v$ (Greenwood, 1977), with v the wind speed. Therefore, speckles generated by atmospheric turbulence have a typical lifetime of milliseconds (Macintosh et al., 2005). Atmospheric phase aberrations are dominant over atmospheric amplitude aberrations (also referred to as scintillation) for large telescopes (Guyon et al., 2018). However, amplitude aberrations can become relevant during HCI observations when they correlate with phase aberrations, leading to the asymmetric wind-driven halo (Cantalloube et al., 2018, 2020).

Telescope effects

The telescope is also a cause of wavefront aberrations. It is mainly related to temperature differences between the telescope and the surrounding air. Mirror seeing occurs when the temperature of the telescope's primary mirror is different to that of the surrounding air (Tallis et al., 2020). The warm mirror leads to natural convection, which is turbulent, directly in the path of the incoming light and thus degrading the wavefront. Another effect is the low-wind effect (LWE; Sauvage et al. 2015; Sauvage et al. 2016; Milli et al. 2018). The LWE occurs when the ground wind speed is very low (under a few m/s), which otherwise would be considered to be amongst the best observing conditions. It has now been well understood to be caused by radiative heat exchange between the telescope structure and night sky (Holzlöhner et al., 2020). When the dome opens for observations, it exposes the telescope structure to the night sky, resulting in rapid radiative cooling of the structure

The low-wind effect

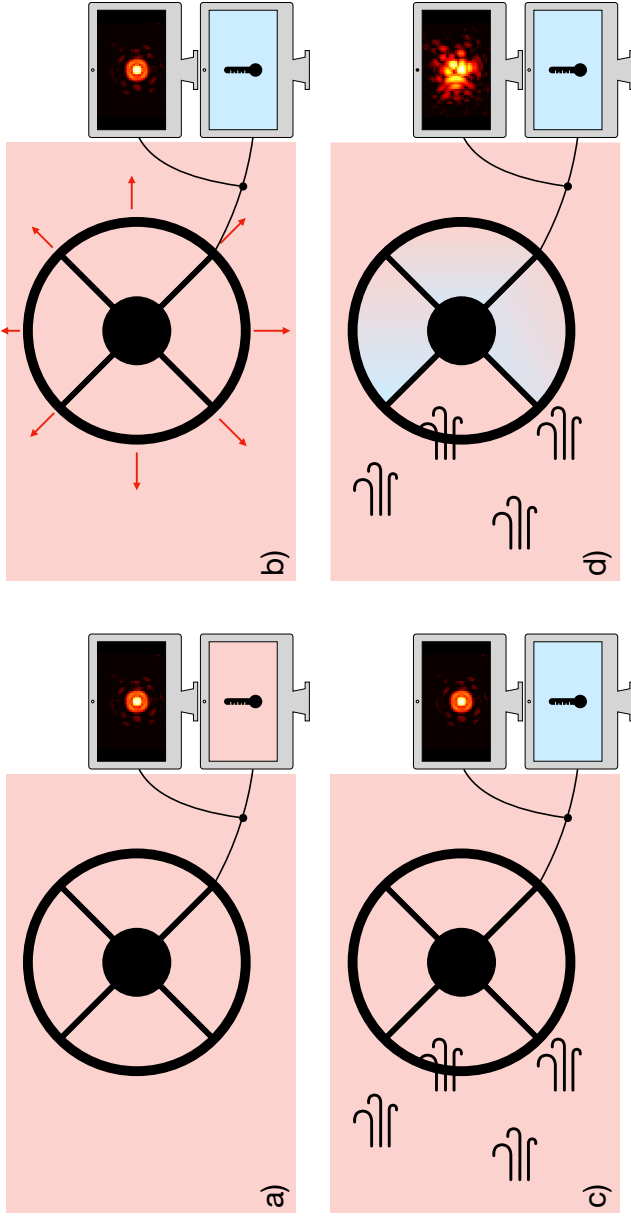


Figure 1.3: Explanation of the low-wind effect (LWE). a) Before observations, the telescope and surrounding air have the same temperature. b) When the dome opens, the telescope is exposed to the night sky. Depending on the mass, the heat capacity and the emissivity of the particular part of the telescope, it can rapidly cool down by radiative transfer. c) Air is flowing over the structure with a low wind speed. d) The air in contact with the spider rapidly cools down and changes its refractive index. Resulting in a sharp OPD step over the spider that is not easily seen by the wavefront sensor, but strongly distorts the PSF.

to a temperature below that of the ambient air. An example of this happening with the secondary mirror support structure (or spiders) is illustrated in Figure 1.3. Air flows over the cold spiders with a low wind speed. The air in contact with the spider rapidly cools down and changes its refractive index. This introduces a sharp optical path length difference (OPD) between light passing on opposite sides of a spider, which strongly distorts the PSF. The aberrations generated by the LWE were measured to have a peak-to-valley wavefront error of up to hundreds of nanometers (Sauvage et al., 2015) and evolve on timescales of seconds (Milli et al., 2018). Typical AO systems have difficulties measuring and correcting the LWE, and therefore the LWE is one of the limitations to the direct imaging of exoplanets at small angular separations.

Instrumental aberrations

Usually, the first sub-system within the HCI instrument is the AO system (Figure 8.2), which measures and corrects upstream wavefront aberrations. However, optics downstream of the wavefront sensor also introduce wavefront aberrations due to optical misalignments, manufacturing errors and internal seeing. These aberrations are not sensed by the main wavefront sensor, but do affect the optical quality of the imaging system, and are referred to as **non-common path aberrations** (NCPA). Due to temperature, humidity and gravitational vector changes, NCPA slowly evolve over timescales of minutes and hours (Goebel et al., 2018; Martinez et al., 2013, 2012; Milli et al., 2016). NCPA generate quasi-static speckles that are especially challenging to remove in post-processing and are one of the current limitations in HCI (Hinkley et al., 2007).

1.2.2 Adaptive optics

The subsystem that deals with wavefront aberrations is the AO system. It consists of a wavefront sensor (WFS) positioned behind a deformable mirror (DM) as shown in Figure 8.2. A real-time control system converts WFS measurements into DM actuator displacements in a closed-loop configuration. For the purpose of detecting exoplanets, the AO system needs to deliver extremely high wavefront quality, and is therefore regularly referred to as extreme AO (XAO; Guyon 2018). The XAO system needs to operate fast enough to keep up with the atmosphere and runs typically at kHz (Greenwood, 1977).

The DM is a reflective optic that can change its shape very precisely at a high frequency (Madec, 2012). The WFS estimates the wavefront from intensity measurements by means of optical manipulations. Currently, the most common WFSs are the Shack-Hartmann WFS (SH-WFS; Hartmann 1900; Shack 1971) and the Pyramid WFS (PyWFS; Ragazzoni 1996). The latter being more sensitive, but requires that the magnitude of the wavefront aberrations is smaller. The sensitivity of the WFS plays an important role in the on-sky contrast (Guyon, 2005), and therefore the current generation of HCI instruments is transitioning towards the PyWFS.

A limitation of these WFSs is the island effect (IE; Le Louarn et al. 2013). The IE occurs when the telescope pupil is strongly fragmented by the spiders supporting the secondary mirror, as shown in Figure 1.4. When the spiders become too wide, the SH-WFS and

The island effect

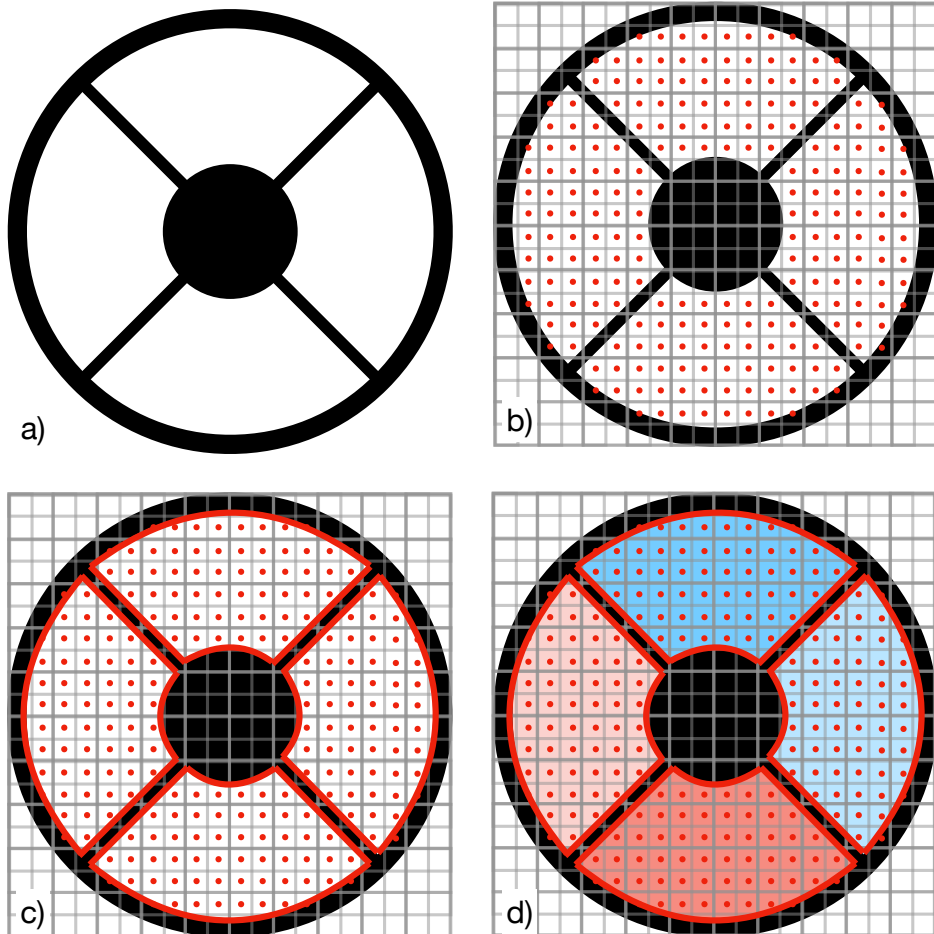


Figure 1.4: Explanation of the island effect using a SH-WFS. a) The telescope pupil with shadows of the secondary mirror and its support structure. The beams of the support structure are referred to as the spiders. b) An array of microlenses is placed over the pupil and generates spots on the detector used for wavefront sensing (the red dots). The position of the spots indicates the local gradient of the wavefront. c) The wavefront is reconstructed by integrating over the wavefront gradient measurements of adjacent spots. However, because the spiders cover some microlenses, the wavefront can only be reconstructed within four “islands”. d) When an aberration with sharp phase discontinuities over the spiders occurs, for example the LWE (Figure 1.3), the WFS can not accurately measure the discontinuity. This leads to unmeasured and thus uncorrected wavefront errors.

PyWFS poorly sense sharp discontinuities in the wavefront across these gaps. This is because these WFSs measure the gradient of the wavefront in two orthogonal directions. The wavefront is reconstructed by stitching together these gradient measurements. When there is a discontinuity in the gradient measurements due to a spider, it can be difficult to accurately reconstruct the wavefront. The IE is the reason that the WFSs such as the SH-WFS and PyWFS have difficulties with measuring the LWFE. Another limitation is that the WFS only measures aberrations upstream of its position in the optical train, and (significant) NCPA are left unmeasured and uncorrected. To this end, additional WFSs downstream of the AO system have been developed. These WFSs use either the starlight rejected light by the coronagraph (Singh et al., 2017, 2014, 2015), very sensitive WFS designs complementary to the SH- and PYWFS (Doelman et al., 2019; N’Diaye et al., 2013, 2016; Vigan et al., 2019), or the science focal plane (Jovanovic et al., 2018). Focal-plane wavefront sensing is the most promising solution as it completely eliminates NCPA, and is amongst the most sensitive wavefront sensing solutions (Guyon, 2005). It is also the main subject of this thesis, and a more extensive introduction on focal-plane wavefront sensing is presented in section 1.3.

1.2.3 Coronagraphy

The AO system feeds the light to the coronagraph. The goal of the coronagraph is to suppress the starlight while transmitting the exoplanet light. Furthermore, it also reduces speckle noise, because bright diffraction structures, to which some speckles are otherwise ‘pinned’, are removed (Bloemhof et al., 2001; Soummer et al., 2007).

Over the years many different coronagraph concepts have been proposed (Mawet et al., 2012; Ruane et al., 2018). These concepts can be roughly divided into two categories:

- **Focal-plane coronagraphs:** A focal-plane optic is placed on the on-axis star and either absorbs the starlight or diffracts it outside of the downstream pupil by either amplitude (Lyot, 1939) or phase manipulation (Roddiier & Roddiier, 1997). An additional optic in the downstream pupil-plane, referred to as the Lyot stop, blocks the starlight. Because the exoplanet is spatially separated from the star, its light is only slightly attenuated and not diffracted outside the pupil and therefore is transmitted towards the detector. Additional pre-apodizers in the pupil-plane upstream of the focal-plane improve the rejection of the star (Aime et al., 2002; Por, 2020; Soummer et al., 2003). These coronagraphs offer very high contrasts with good exoplanet throughput, but are sensitive to vibrations and the finite diameter of the star.
- **Pupil-plane coronagraphs:** A pupil-plane optic shapes the PSF such that starlight is cancelled on one or two sides of the PSF by either amplitude (Kasdin et al., 2003) or phase manipulation (Codona & Angel, 2004). The region where the starlight is cancelled is referred to as the dark hole. As both the star and planet propagate through the coronagraph, the exoplanet will also acquire the coronagraphic PSF, spreading the exoplanet light over a larger area on the detector. However, these

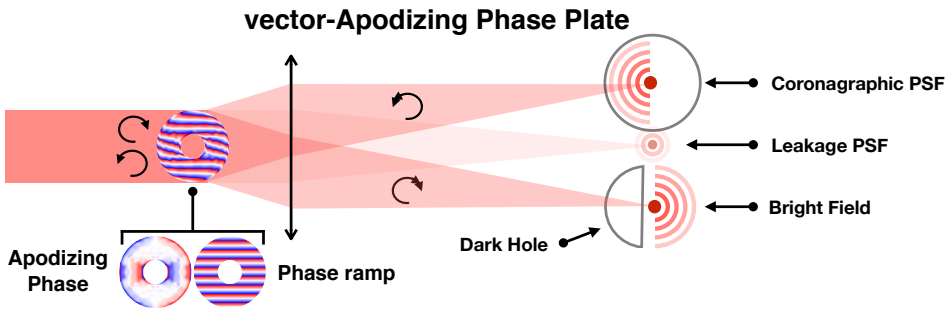


Figure 1.5: Schematic of the vAPP coronagraph. The coronagraphic PSFs are separated by a phase ramp that is included into the phase design.

coronagraphs are completely insensitive to the finite diameter of the star, and are easily implemented into instruments.

Particularly relevant to this thesis is the vector-Apodizing Phase Plate (vAPP; Snik et al. 2012). The vAPP induces the required pupil-plane phase by means of the geometric phase (Berry, 1987; Pancharatnam, 1956) on opposite circular polarization states. The vAPPs geometric phase is introduced when the fast-axis angle of a half-wave retarder is spatially varying. The phase that is induced is twice the fast-axis angle, and is opposite for the opposite circular polarization states, which results in two coronagraphic PSFs with opposite dark holes. This is shown in Figure 1.5. Due to its geometric origin, the induced geometric phase is completely independent of wavelength, but the efficiency with which the phase is transferred to the light depends on the retardance offset from half wave. Light that does not acquire the desired phase is generally referred to as leakage, and in the case of the vAPP will form a non-coronagraphic PSF. High leakage will affect coronagraphic performance as light from the leaked PSF can contaminate the dark hole. Half-wave retarders with spatially varying fast-axis angle can be implemented with liquid-crystal technology (Escuti et al., 2016). Using a direct-write system, the desired fast-axis angle can be printed into a liquid-crystal photo-alignment layer that has been deposited on a substrate (Miskiewicz & Escuti, 2014). To achromatise the half-wave retarder, several layers of carefully designed, self-aligning birefringent liquid crystals can be deposited on top of the initial layer (Komanduri et al., 2013). This technology has shown to achieve minimal leakage over a broad wavelength range (Doelman et al., 2020, 2017). In the simplest and most common implementation the two coronagraphic PSFs are spatially separated with a polarization-sensitive grating (Oh & Escuti, 2008) that is integrated into the phase design (Otten et al., 2014). These coronagraphs are mainly used for operation with narrowband filters or integral-field spectrographs. This is because diffraction effects scale with wavelength, and therefore, when observing in a broadband filter with a vAPP, the grating will smear the coronagraphic PSFs.

1.2.4 Observing strategies and post processing

Due to uncorrected atmospheric wavefront errors, ground-based HCI observations are limited to raw contrasts of $\sim 10^{-5}$ at a few λ/D (Guyon et al., 2012). Within the control radius the dominant noise sources are the finite time delay between measuring and correcting the wavefront, and photon noise in the wavefront sensor measurements. It is possible to detect and characterize exoplanets below this contrast level by separating the star and planet light with advanced post-processing methods. These methods use a known diversity in the dataset to either build up an estimate of the stellar PSF, which can then be subtracted from the individual images to reveal the exoplanet (Cantalloube et al., 2021), or use fundamental differences between the properties of star and planet light (e.g. spectrum, polarization or coherence). The observing strategy is designed to provide this diversity, and the following methods are either in use or being developed (presented in alphabetic order):

- **Angular differential imaging** (ADI; Marois et al. 2006a): During an observation, the sky, and therefore the exoplanet, is allowed to rotate over the detector while taking images. The orientation of the stellar PSF remains fixed over time. The PSF of the target star is then estimated from this time series.
- **Coherence differential imaging** (CDI; Guyon 2004): Stellar speckles are coherent with starlight, while the exoplanet light is incoherent. This is because exoplanet light originates from a spatially separated source. By measuring the coherence of the light on the detector, the light from the star and exoplanet are separated.
- **Orbit differential imaging** (ODI; Males et al. 2015): The target is observed multiple times with long periods of time in between them. The diversity is then provided by the movement of the exoplanet in its orbit.
- **Polarization differential imaging** (PDI; Kuhn et al. 2001): Starlight is unpolarized to a very high degree, while light reflected from the surface of the exoplanet is polarized. By adding a polarizing beam splitter to the HCI instrument, the polarization state of the incident light can be measured and the star and planet light separated.
- **Reference star differential imaging** (RDI; Smith & Terile 1984): Another star, with the same spectral properties as the target star and without companions, is observed with the same instrument and telescope settings. The PSF of the target star is estimated with these images.
- **Spectral differential imaging** (SDI; Sparks & Ford 2002): Due to temperature and atmospheric composition differences, the spectrum of the star and exoplanet light are different. By measuring the spectrum of the light, the star and exoplanet are separated.

It is also possible and advantageous to combine several of these observation strategies (Christiaens et al., 2019; van Holstein et al., 2017).

PDI and SDI have the additional advantage that they simultaneously act as characterization diagnostic. Observations by medium- and high-resolution integral-field spectrographs can be used to detect atomic and molecular lines from an exoplanet's atmosphere (Bowler et al., 2019; Snellen et al., 2015). Using polarimetry, it is possible to study cloud structures in the exoplanet's atmosphere (De Kok et al., 2011; Stam et al., 2004), and circumplanetary disks (Stolker et al., 2017). Combining both techniques in spectropolarimetric observations enables constraints on water clouds and oceans (Karalidi et al., 2012), and even (maybe) measure biological activity (Patty et al., 2019).

1.2.5 Detecting exoplanet variability

Like the majority of the planets in the solar system, exoplanets are expected to have clouds in their atmospheres (Helling, 2019). Detecting and studying clouds on exoplanets will improve our understanding of the atmospheric composition and weather systems on these other worlds. Brown dwarfs have cloud structures (Cooper et al., 2003), that express themselves in brightness variations while the object rotates (Apai et al., 2013; Eriksson et al., 2019; Metchev et al., 2015). Exoplanets are expected to exhibit similar variability (Apai et al., 2019; Biller, 2017; Kostov & Apai, 2012). Thus far, variability has only been observed with the extremely stable Hubble Space Telescope (HST) for the exoplanet 2M1207b, which has photometric variations at the 0.78-1.36% level (Zhou et al., 2016). Ground-based observations of HR 8799 with VLT/SPHERE have not yet led to conclusive detections of variability (Apai et al., 2016; Biller et al., 2021).

Observing exoplanet variability is not trivial because most coronagraphs occult the host star, which is usually the direct photometric reference. This makes it challenging to disentangle exoplanet variability from seeing and transmission changes in the Earth's atmosphere. To overcome this problem, Marois et al. (2006b) and Sivaramakrishnan & Oppenheimer (2006) introduced diffractive methods to generate artificial speckles that serve as photometric references. These methods apply static phase or amplitude modulations in the pupil plane before the coronagraph's focal-plane optic. The artificial speckles are designed to not be occulted by the coronagraph. An additional advantage is that the reference speckles can be closer to the exoplanet in intensity, which prevents possible issues with saturation and detector non-linearities. Current HCI instruments implement these artificial speckles either with a square grid that acts as an amplitude grating (Gemini/GPI; Wang et al. 2014), or with a static DM modulation (VLT/SPHERE; Langlois et al. 2013). However, the limiting factor of these solutions is their coherency with the time-varying speckle background, which results in interference that dynamically distorts the shape and brightness of the artificial speckles. This in turn ultimately limits their photometric precision (Jovanovic et al., 2015a). The origin of these background speckles has been extensively discussed in subsection 1.2.1. Subaru/SCEXAO circumvents this problem by high-speed, temporal DM modulation that switches (< 1 ms) the phase of the artificial speckles between 0 and π (Jovanovic et al., 2015a). Due to the modulation, the interference averages out, and the artificial speckles effectively become incoherent, increasing their precision by a factor of between two and three. Recently, a more advanced method was presented that also alternates the position of the speckles, allowing for accu-

rate background estimation, improving the photometric precision to $< 1\%$ for 80 second exposures (Sahoo et al., 2020).

1.3 Focal-plane wavefront sensing

As discussed in the above sections, one of the current limitations in high-contrast imaging are non-common path aberrations (NCPA). NCPA originate from misalignments, fabrication errors, and temperature changes in the optics and internal turbulence downstream of the system's main WFS. In subsection 1.2.1 we have seen that they slowly evolve with time, which makes their removal in post-processing very challenging. The best solution is to measure NCPA using the science detector located in the focal plane, and optically correct them with a DM. We define focal-plane wavefront sensing (FPWFS) as follows.

Focal-plane wavefront sensing

is estimating the pupil-plane or focal-plane electric field by means of measurements with the science camera (or equivalent) placed in the focal plane.

In this section we introduce the theory behind focal-plane wavefront sensing, discuss the challenges and cluster the different focal-plane wavefront sensors into different families.

1.3.1 Theory

The fundamental problem in FPWFS is, with the current detector technology, that we do not have direct access to the focal-plane electric field, but instead measure the focal-plane intensity. The result is that only the focal-plane amplitude can be recovered and not the focal-plane phase. This is shown by the following equations:

$$E_{\text{foc}} = A_{\text{foc}} e^{i\theta_{\text{foc}}}, \quad (1.2)$$

$$I_{\text{foc}} = |E_{\text{foc}}|^2 \quad (1.3)$$

$$= A_{\text{foc}}^2, \quad (1.4)$$

with A_{foc} the amplitude and θ_{foc} the phase of the focal-plane electric field (E_{foc}), and I_{foc} the focal-plane intensity. To retrieve the amplitude **and** the phase, we have to manipulate E_{foc} such that these parameters are encoded in the intensity signal. In this subsection we will identify the requirements on pupil-plane manipulations that enable measuring pupil-plane phase with focal-plane images.

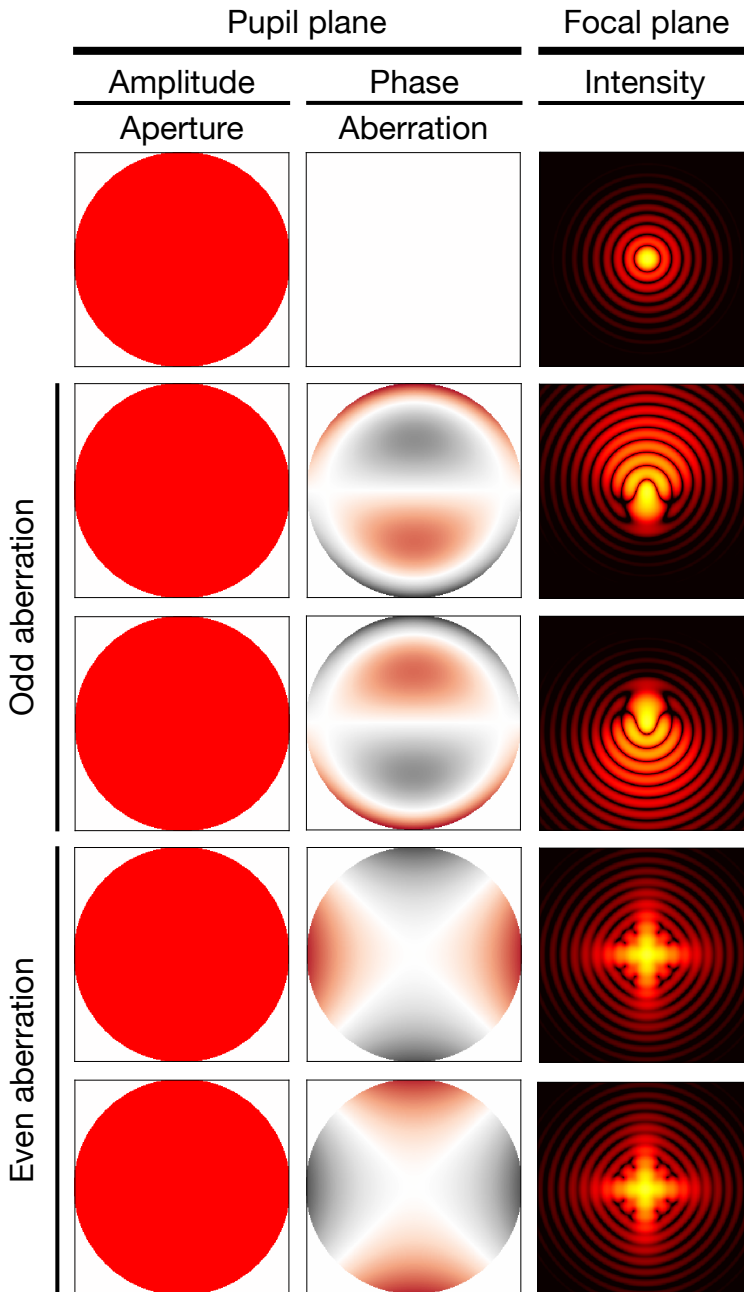


Figure 1.6: Effect of sign changes of even and odd pupil-plane phase aberrations on the PSF. The PSF is formed by an even aperture, and the phase aberrations have a 1 radian root-mean-square wavefront error. The scales of the colormaps are the same for every column of images. The focal-plane intensity is shown in log scale.

To understand the challenge of estimating pupil-plane phase with focal-plane images, we simulate PSFs for a circular aperture with various wavefront aberrations (even and odd, and changing aberration sign). The results are presented in Figure 1.6. It shows that the sign of odd pupil-plane phase aberrations can be distinguished by observing the shape of the PSF. However, for even pupil-plane phase aberrations it is not possible to determine the sign, because the PSFs look identical for opposite signs. The only information that can be retrieved is the magnitude of the even phase aberration.

To understand the origin of this sign ambiguity, we start by writing the the pupil-plane electric field (E_{pup}) as follows:

$$E_{\text{pup}} = A_{\text{pup}} e^{i\theta_{\text{pup}}} \quad (1.5)$$

$$= A_{\text{pup}} \cos(\theta_{\text{pup}}) + iA_{\text{pup}} \sin(\theta_{\text{pup}}), \quad (1.6)$$

with A_{pup} the pupil-plane amplitude and θ_{pup} the pupil-plane phase. The focal-plane electric field (E_{foc}) is formed by propagating E_{pup} using the Fraunhofer propagation operator $\mathcal{P}\{\cdot\} \propto \frac{1}{i} \mathcal{F}\{\cdot\}$ (Goodman, 2005), with $\mathcal{F}\{\cdot\}$ the Fourier transform.

$$E_{\text{foc}} = \mathcal{P}\{E_{\text{pup}}\} \quad (1.7)$$

$$= \mathcal{P}\{A_{\text{pup}} \cos(\theta_{\text{pup}})\} + \mathcal{P}\{iA_{\text{pup}} \sin(\theta_{\text{pup}})\} \quad (1.8)$$

$$= a + ib, \quad (1.9)$$

with a and b the real and imaginary parts of E_{foc} , respectively. The terms a and b generally consists of a mixture of $\mathcal{P}\{A_{\text{pup}} \cos(\theta_{\text{pup}})\}$ and $\mathcal{P}\{A_{\text{pup}} \sin(\theta_{\text{pup}})\}$, and as we will see, this depends on the symmetries of A_{pup} and θ_{pup} . The focal-plane intensity, or PSF, is given by:

$$I_{\text{foc}} = |E_{\text{foc}}|^2 \quad (1.10)$$

$$= a^2 + b^2. \quad (1.11)$$

Before we continue, we recall the following mathematical properties:

1. A function $f(r)$ can be decomposed into even (f_{even}) and odd (f_{odd}) functions:

$$f(r) = f_{\text{even}}(r) + f_{\text{odd}}(r), \quad (1.12)$$

$$f_{\text{even}}(r) = \frac{f(r) + f(-r)}{2}, \quad (1.13)$$

$$f_{\text{odd}}(r) = \frac{f(r) - f(-r)}{2}. \quad (1.14)$$

This is useful, because even and odd function behave differently under the Fraunhofer propagation operator, which is shown in Table 2.1.

2. The composition and multiplication properties of even and odd functions:

$$f_{\text{even}}(r) \cdot g_{\text{odd}}(r) = h_{\text{odd}}, \quad (1.15)$$

$$f_{\text{odd}}(r) \cdot g_{\text{odd}}(r) = h_{\text{even}}, \quad (1.16)$$

$$f_{\text{even}}(r) \cdot g_{\text{even}}(r) = h_{\text{even}}, \quad (1.17)$$

$$f_{\text{even}}[g_{\text{odd}}(r)] = h_{\text{even}}, \quad (1.18)$$

$$f_{\text{odd}}[g_{\text{odd}}(r)] = h_{\text{odd}}, \quad (1.19)$$

$$f_{\text{odd}}[g_{\text{even}}(r)] = h_{\text{even}}, \quad (1.20)$$

$$f_{\text{even}}[g_{\text{even}}(r)] = h_{\text{even}}. \quad (1.21)$$

These determine the symmetries of the real and imaginary terms of E_{pup} (Equation 7.1).

3. The symmetry properties of the Fraunhofer propagation are shown in Table 2.1. These determine how pupil-plane aberrations map to the real and/or imaginary terms of the focal-plane electric field.
4. Finally, the hermitian property of the Fraunhofer propagation. This states that a conjugated pupil-plane electric field $E'_{\text{pup}} = E_{\text{pup}}^*$ (i.e. a phase sign flip; * denotes the conjugation) results in a flipped and conjugated focal-plane electric field $E'_{\text{foc}} = \mathcal{P}\{E'_{\text{pup}}\}$:

$$E'_{\text{foc}} = -E_{\text{foc}}(-r)^*. \quad (1.22)$$

The reason that the symmetry decomposition, combined with the decomposition of E_{pup} into its real and imaginary components (Equation 7.1), is important is that the Fraunhofer propagation operator maps combinations of these decompositions into either real or imaginary components of E_{foc} , as shown in Table 2.1. Combined with the symmetries of the aperture, it determines whether a sign ambiguity will be present or not.

Now, suppose that the aperture is even ($A_{\text{pup}} = A_e$), which is true for most telescope apertures, and that we have an even phase aberration ($\theta_{\text{pup}} = \theta_e$). We then find the following pupil-plane electric field:

$$E_{\text{pup}} = A_e e^{i\theta_e} \quad (1.23)$$

$$= \underbrace{A_e \cos(\theta_e)}_{\text{even}} + i \underbrace{A_e \sin(\theta_e)}_{\text{even}}. \quad (1.24)$$

We note that only the imaginary term contains information on the sign of θ_e . Propagating E_{pup} to the focal plane yields (Table 2.1):

$$E_{\text{foc}} = \underbrace{a}_{\mathcal{P}\{iA_e \sin(\theta_e)\}} + \underbrace{ib}_{\mathcal{P}\{A_e \cos(\theta_e)\}} \quad (1.25)$$

$$I_{\text{foc}} = \underbrace{a^2}_{\text{even}} + \underbrace{b^2}_{\text{even}} \quad (1.26)$$

Table 1.1: Fraunhofer propagation symmetry properties (Goodman, 2005), these are the Fourier properties multiplied with a factor $-i$ ($E_{\text{foc}} = \mathcal{F}\{E_{\text{pup}}\} \propto \frac{1}{i} \mathcal{F}\{E_{\text{pup}}\}$).

Pupil-plane electric field		Focal-plane electric field	
$E_{\text{pup}} = A \cos(\theta) + iA \sin(\theta)$		$E_{\text{foc}} = a + ib$	
Term	Term symmetry	A, θ symmetry	Term symmetry
$A \cos(\theta)$	Even	$(A_{\text{even}}, \theta_{\text{even}}), (A_{\text{even}}, \theta_{\text{odd}})$	Even
$A \cos(\theta)$	Odd	$(A_{\text{odd}}, \theta_{\text{even}}), (A_{\text{odd}}, \theta_{\text{odd}})$	Odd
$iA \sin(\theta)$	Even	$(A_{\text{even}}, \theta_{\text{even}}), (A_{\text{odd}}, \theta_{\text{odd}})$	Even
$iA \sin(\theta)$	Odd	$(A_{\text{even}}, \theta_{\text{odd}}), (A_{\text{odd}}, \theta_{\text{even}})$	Odd

When the sign of the even aberration changes ($\theta_e \rightarrow -\theta_e$), we will not observe a change in I_{foc} . This is because a , which contains the sign information, is an even function, and therefore does not show a response under sign change.

We can do a similar calculation for an odd phase aberration ($\theta_{\text{pup}} = \theta_o$). Here we also assume that the aperture is even ($A_{\text{pup}} = A_e$). The pupil-plane electric field is then:

$$E_{\text{pup}} = \underbrace{A_e \cos(\theta_o)}_{\text{even}} + i \underbrace{A_e \sin(\theta_o)}_{\text{odd}}. \quad (1.27)$$

Again, the sign information carrying term is the imaginary part of the electric field. Calculating the focal-plane electric field and intensity we find:

$$E_{\text{foc}} = \underbrace{ib}_{\mathcal{P}\{A_e \cos(\theta_o) + iA_e \sin(\theta_o)\}}, \quad (1.28)$$

$$I_{\text{foc}} = b^2 \quad (1.29)$$

$$= \underbrace{\mathcal{P}\{A_e \cos(\theta_o)\}^2}_{\text{even}} + \underbrace{\mathcal{P}\{A_e \sin(\theta_o)\}^2}_{\text{even}} + \underbrace{2\mathcal{P}\{A_e \cos(\theta_o)\}\mathcal{P}\{A_e \sin(\theta_o)\}}_{\text{odd}}. \quad (1.30)$$

This calculation shows that in the case of odd phase aberrations, the real and imaginary parts of the pupil-plane electric field both map to the imaginary part of the focal-plane electric field. The result is that in the focal-plane intensity there is an interference term with odd symmetry that changes its shape under sign change. This interference term enables that sign changes of odd pupil-plane phase aberrations are observable in the PSF.

The previous calculations show that whether or not a sign ambiguity exists is determined by the presence of additional term that interferes with the sign carrying term. In Equation 1.25 we found that the sign information of even pupil-plane phase aberrations is located in the real part of the focal-plane electric field. Inspecting Table 2.1 shows that additional terms in the real part of the focal-plane electric field can be created by applying either a known odd pupil-plane amplitude, a known even pupil-plane phase, or a combination of both. These solutions correspond with well-known focal-plane wavefront sensing techniques. Phase diversity techniques apply even pupil-plane phase modes (Gonsalves, 1982; Paxman et al., 1992), and techniques such as the Asymmetric Pupil Fourier Wavefront Sensor (APFWFS; Martinache 2013) and the differential Optical Transfer Functions wavefront sensor (dOTF; Codona 2013) use odd pupil-plane amplitude.

1.3.2 Family of focal-plane wavefront sensors

Many different FPWFSs have been developed over the years, each with their own unique implementation. A review is presented in Jovanovic et al. (2018). Here we aim to extend this review and categorize the different FPWFSs according to their method of breaking the sign degeneracy.

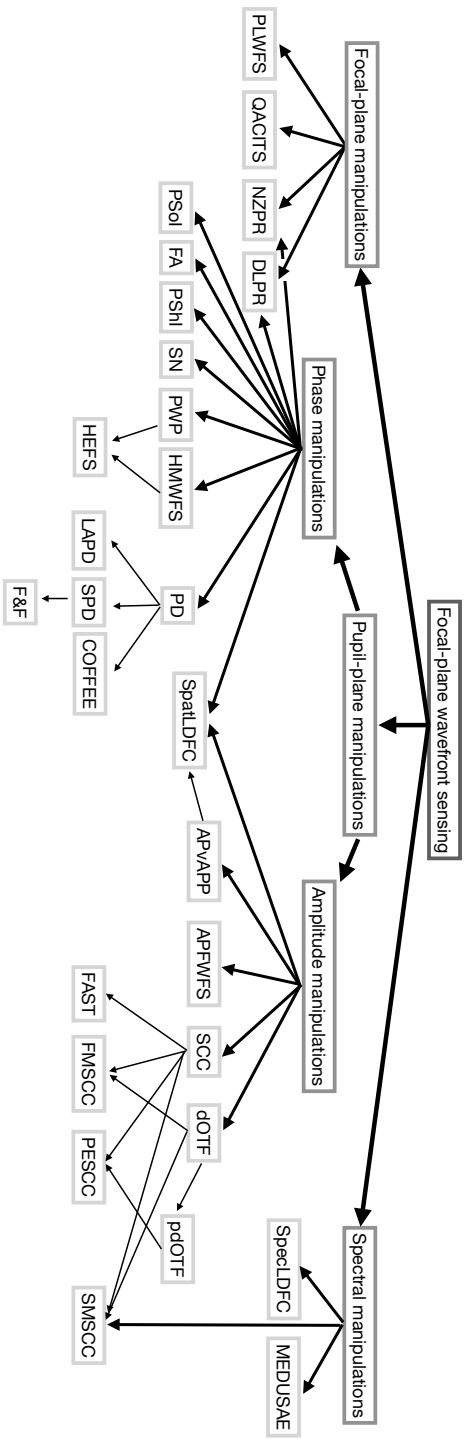


Figure 1.7: Acronyms in the figure are: **Focal-plane manipulations:** NZPR = Nijboer-Zernike Phase Retrieval, QACITS = Quadrant Analysis of Coronagraphic Images for Tip-tilt Sensing, PLWFS = Photonic Lantern WaveFront Sensor, DLPR = Deep Learning Phase Retrieval, **Pupil-plane phase manipulations:** PD = Phase Diversity, COFFEE = Coronagraphic Focal-plane waveFront Estimation for Exoplanet detection, SPD = Sequential-phase diversity, F&F = Fast and Furious, LAPD = Linearized Analytical Phase Diversity, FA = Fraun Algorithm, PSol = Phase Sorting Interferometry, PShI = Phase Shifting Interferometry, LAPPD = Linearized Analytical Phase Diversity, SN = Speckle Nulling, HMMWFS = Holographic Modal WaveFront Sensor, HEFS = Holographic Electric Field Sensor, **Pupil-plane amplitude manipulations:** spatLDFC = Spatial Linear Dark Field Control, APFWFS = Asymmetric Pupil Fourier WaveFront Sensor, APVAPP = Asymmetric Pupil vector-Apodizing Phase Plate, SCC = Self-Coherent Camera, FAST = Fast Atmospheric SCC Technique, FMSSCC = Fast-Modulated Self-Coherent Camera, PESCC = Polarization-Encoded Self-Coherent Camera, SSMSSCC = Spectral-Modulated Self-Coherent Camera, DOTF = differential Optical Transfer Function, pdOTF = polarization differential Optical Transfer Function **Spectral manipulations:** SpecLDFC = Spectral Linear Dark Field Control, MEDUSAE = Multispectral Exoplanet Detection Using Simultaneous Aberration Estimation,

Figure 1.7 shows the family tree with, to our best knowledge, the FPWFSs currently used or being developed in HCI. Three distinct branches can be distinguished that each use a different kind of manipulation to break the sign ambiguity:

- **Focal-plane manipulation:** A device located in a focal-plane (e.g. a focal-plane coronagraph or photonic lantern) breaks the sign ambiguity by means of optical manipulations.
- **Pupil-plane manipulation:** The pupil-plane amplitude and/or phase are manipulated such that the sign ambiguity is broken for focal-plane intensity measurements.
- **Spectral manipulation:** The chromatic nature of aberrations is used to measure the wavefront.

We more extensively discuss the members of the families below.

Focal-plane manipulation

As mentioned above, the focal-plane manipulation branch uses optical devices in the focal plane to lift the phase ambiguity. The Quadrant Analysis of Coronagraphic Images for Tip-tilt Sensing (QACITS; Huby et al. 2015) is based on the analysis of the Vector Vortex Coronagraph (VVC; Mawet et al. 2005) images to infer the direction and magnitude of pointing errors. QACITS is regularly used for HCI observations with the Keck/NIRC2 (Huby et al., 2017). The VVC is a focal-plane coronagraph that induces an opposite vortex phase to opposite circular polarization states. The vortex phase is what breaks the sign ambiguity for even pupil-plane phase aberrations. Other techniques also use the diversity provided by the VVC, but are aimed to provide higher-order wavefront measurements. The Nijboer-Zernike Phase Retrieval method (NZPR; Riaud et al. 2012a) splits the opposite circular polarization images to derive the wavefront by an analytical approach. The NZPR only operates in the small aberration regime. Deep Learning Phase Retrieval methods (DLPR; Quesnel et al. 2020) also use the vortex phase to break the sign ambiguity, but extend the use beyond the small phase regime by using machine learning techniques. Then, there are also techniques that put a photonic lantern in the focal plane. A photonic lantern is a device that splits a multimode fiber into multiple single-mode fibers. In the photonic lantern, the focal-plane electric field is mixed in the multimode fiber and then filtered by the single-mode fibers such that from its output the different electric field components can be reconstructed. One of these single-mode fibers can feed a high-resolution spectrograph, while the output of the other single-mode fibers can be used for wavefront sensing. The first implementation only focussed on detecting pointing errors (Corrigan et al., 2018), but it was recently demonstrated that higher-order wavefront aberrations can also be measured (Norris et al., 2020).

Pupil-plane manipulation

The pupil-plane manipulation is the largest branch of the family tree shown in Figure 1.7. In subsection 1.3.1 we discussed how the pupil-plane phase and amplitude should be manipulated to overcome the sign ambiguity. This branch can be divided into two smaller branches based on whether the FPWFS uses phase or amplitude manipulation. Starting

with the pupil-plane phase branch, the most well-known and used method is phase diversity (PD; Gonsalves 1982; Paxman et al. 1992). This method fits a non-linear image formation model to in- and out-of-focus PSFs to retrieve pupil-plane phase aberrations. PD has led to many other FPWFSs. For example, the COronagraphic Focal-plane waveFront Estimation for Exoplanet detection (COFEE; Paul et al. 2013) FPWFS includes a coronagraph to the image formation model for HCI observations. COFEE was subsequently extended to also measure pupil-plane amplitude aberrations (Herscovici-Schiller et al., 2018), and include atmospheric turbulence in the model (Herscovici-Schiller et al., 2019). Linearized Analytical Phase Diversity or LAPD (Vievard et al., 2020) uses a linear approximation to measure the wavefront, and was mainly developed to co-phase segmented telescopes. LAPD is now also being tested to measure the LWE at Subaru/SCEXAO (Vievard et al., 2019). Sequential-Phase Diversity (SPD; Gonsalves 2002) was developed to be able to run continuously in closed-loop, without defocussing the camera, by using the previous DM command as diversity and assuming that the algorithm operates in the small aberration regime. Fast and Furious (F&F; Keller et al. 2012; Korkiakoski et al. 2014) extends the regime in which SPD can operate by introducing a higher-order approximation of the PSF. F&F has been successfully tested on-sky in the context of measuring and correcting the LWE at Subaru/SCEXAO (Chapter 6; Bos et al. 2020b). The NZPR and DLPR techniques described in the focal-plane manipulation branch are also used with phase diversity (Quesnel et al., 2020; Riaud et al., 2012b; van Haver et al., 2006). Then, the next focal-plane wavefront sensor in this branch is the Holographic Modal Wavefront Sensor (HMWFS; Wilby et al. 2017). Using a static optic, the HMWFS generates a number of PSF copy pairs, and each pair is biased with a pupil-plane phase mode with opposite sign. By monitoring the relative brightness of the PSF pairs, the magnitudes and signs of a set of pupil-plane modes can be measured. It was successfully tested during an observing run with WHT/LEXI (Haffert et al., 2018).

The following FPWFSs also belong to the pupil-plane manipulation branch, but focus on measuring the focal-plane electric field. Speckle Nulling (SN; Bordé & Traub 2006) singles out bright speckles in the coronagraphic image, and commands the DM to add artificial speckles on top of them. By alternating the phase of the artificial speckle and observing the combined brightness, SN finds the appropriate DM command to cancel the speckle. It has been successfully tested on-sky with Subaru/SCEXAO (Martinache et al., 2014) and Keck/NIRC2 (Bottom et al., 2016), and is also used for space-based HCI experiments (Trauger & Traub, 2007). Pair-wise probing (PWP; Give'on et al. 2011) extends SN by simultaneously probing large parts of the focal-plane with DM commands. It is mainly considered for space-based observatories (Groff et al., 2015), but was recently also installed on VLT/SPHERE for on-sky tests (Potier et al., 2020b). PWP and the HMWFS are combined in the Holographic Electric Field Sensor (HEFS; Por & Keller 2016) as a static solution of PWP. Phase-shifting interferometry (PShI; Bottom et al. 2017; Guyon 2004) modulates the focal-plane intensity by moving a small part of the Lyot stop. Phase-sorting interferometry (PSoI; Codona et al. 2008) and the Frazin algorithm (FA; Frazin 2013) both use naturally occurring speckles due to the atmospheric turbulence to measure the focal-plane electric field. This requires them to combine milli-second exposure images with synchronized wavefront telemetry from the main WFS. The phase and am-

plitude of the atmospheric speckles are derived from the WFS measurements. The interference between the atmospheric speckles and more slowly evolving speckles originating from NCPA allows for measuring the phase and amplitude of the NCPA speckles.

There is also an entire class of FPWFSs that use pupil-plane amplitude manipulations. The Asymmetric Pupil Fourier WaveFront Sensor (APFWFS; Martinache 2013) uses an interferometric approach based on kernel phase analysis (Martinache, 2010) to retrieve the pupil-plane phase aberrations based on a non-coronagraphic PSF formed by an asymmetric pupil. It has seen multiple successful on-sky tests with Subaru/SCEXAO (Martinache et al., 2016; N'Diaye et al., 2018). The Asymmetric Pupil vector-Apodizing Phase Plate or APvAPP (Chapter 2; Bos et al. 2019) is a pupil-plane coronagraph integrated with a pupil-plane amplitude asymmetry. The pupil-plane phase is retrieved with a non-linear coronagraphic model fitted to the coronagraphic image. This technique has also seen successful on-sky tests, and can be extended to measure pupil-plane amplitude aberrations as well (Bos et al., 2020a). Spatial Linear Dark Field Control (SpatLDFC; Miller et al. 2017) monitors the bright field opposite to the dark hole for intensity fluctuations generated by wavefront aberrations. This is because LDFC assumes that intensity fluctuations in the bright field have a linear response to wavefront aberrations, while those in the dark hole have a quadratic response. Using an empirical calibration, these intensity fluctuations are converted to appropriate DM commands to cancel aberrations. SpatLDFC is designed to be a wavefront stabilization technique, and cannot create a dark hole on its own. It is implemented both with pupil- and focal-plane coronagraphs. The coronagraph dictates the method that SpatLDFC relies on to break the sign ambiguity. For pupil-plane coronagraphs, such as the APvAPP, there is a bright coronagraphic PSF that requires an amplitude asymmetry to provide the diversity. SpatLDFC combined with an APvAPP has been successfully tested on the Subaru/SCEXAO system with the internal source (Chapter 3; Miller et al. 2021) and on-sky (Chapter 4; Bos et al. submitted). For a focal-plane coronagraph, the bright field predominately consists of uncorrected wavefront aberrations that break the sign degeneracy. Laboratory experiments for space-based observatories have been successfully performed in this context as well (Currie et al., 2020b).

The differential Optical Transfer Functions (dOTF; Codona 2013) uses a Fourier analysis on two images (one with and one without amplitude asymmetry) to retrieve the pupil-plane phase and amplitude aberrations. The asymmetry can also be introduced by a linear polarizer, which then requires a polarizing beam splitter to do the dOTF analysis. This is referred to as the polarization dOTF (pdOTF; Brooks et al. 2016).

The self-coherent camera (SCC; Baudoz et al. 2005) places a reference hole in an off-axis position of the coronagraph's Lyot stop. The reference hole transmits light that is diffracted by the coronagraph outside of the geometric pupil that would have otherwise been blocked by the Lyot stop. This light propagates to the focal plane, interferes with the on-axis beam, and generates high spatial-frequency fringes. The focal-plane electric field is spatially modulated and directly available through a Fourier analysis of the image. It has been tested at high contrasts for space-based systems (Potier et al., 2020a) and on-sky for ground-based systems (Galicher et al., 2019). The Fast Atmospheric SCC

Technique (FAST; Gerard & Marois 2020; Gerard et al. 2018, 2019) modifies the coronagraph’s focal-plane optic such that the core of the PSF is diffracted onto the reference hole, drastically increasing the light available for wavefront sensing. Other variants of the SCC exist that combine the SCC with other FPWFS concepts. The fast-modulated SCC (FMSCC; Martinez 2019) effectively combines the dOTF concept with the SCC by temporally modulating the reference light. The polarization-encoded SCC (PESCC; Chapter 5; Bos 2021) has a similar combination with the pdOTF. Lastly, the spectral-modulated SCC (SMSCC; Haffert in prep.) encodes the reference hole in different spectral channels.

Spectral manipulation

Finally, there is a family of techniques that use spectral manipulations to estimate aberrations. For example, the Multispectral Exoplanet Detection Using Simultaneous Aberration Estimation (MEDUSAE; Ygouf et al. 2013) technique jointly estimates the wavefront aberrations and astronomical object given a multispectral dataset. MEDUSAE has currently only been tested as post-processing method, but also has the capability to be run in realtime for wavefront sensing. Spectral Linear Dark Field control (SpecLDFC; Guyon et al. 2017) is very similar to SpatLDFC, but instead of measuring the wavefront at a different location, it measures the wavefront using other wavelengths. SpecLDFC uses the linear relationship between the intensity of bright speckles outside of the science bandwidth and residual wavefront aberrations. By monitoring brightness changes of these speckles, it derives DM commands that correct for wavefront drifts.

1.4 This thesis

This thesis presents and validates new focal-plane wavefront sensors in theory, simulation, and on-sky tests, and introduces a new optic to enable the detection of exoplanet variability. The ultimate goal is to enable the direct imaging and characterization of rocky exoplanets with the future extremely large telescopes. The main focus of this thesis lies on developing integrated coronagraph and focal-plane wavefront-sensing solutions to measure and correct non-common path aberrations in high-contrast imaging instruments (Chapters 2 – 5). The last two chapters investigate on-sky tests of a focal-plane wavefront sensing solution to address the low-wind effect (Chapter 6), and a new concept to dramatically increase the signal-to-noise ratio of exoplanet variability measurements (Chapter 7).

Chapter 2: Focal-plane wavefront sensing with the vector-Apodizing Phase Plate coronagraph

This chapter introduces a novel focal-plane wavefront sensor by combining the vector-Apodizing Phase Plate (vAPP) coronagraph with an asymmetric pupil wavefront sensor. A non-linear, model-based wavefront sensing algorithm is presented as well. We study the performance of the vAPP and the wavefront-sensing algorithm in idealized simulations. Furthermore, the wavefront sensing capabilities are demonstrated on the Subaru/SCE_xAO system with the internal source and on-sky. For the on-sky tests, we report a raw contrast improvement of a factor ~ 2 between 2 and 4 λ/D when measuring and controlling the thirty lowest Zernike modes.

Chapter 3 and 4: Spatial Linear Dark Field Control with the vector-Apodizing Phase Plate

These two chapters present the successful deployment of spatial Linear Dark Field Control (LDFC) to Subaru/SCEExAO. LDFC assumes a linear relationship between intensity changes in some parts of the bright field of the vAPP coronagraphic PSF and changing wavefront aberrations. We show that, to successfully operate LDFC with the vAPP without defocus, an amplitude asymmetry needs to be integrated into the vAPP design.

Chapter 3 describes the implementation of LDFC at Subaru/SCEExAO, including a noise analysis of LDFC's performance with the SCEExAO vAPP. Furthermore, the results of lab tests are presented that simulate temporally-correlated, evolving phase aberrations with the deformable mirror (DM). We find that, when LDFC is operating in closed-loop, there is a factor of ~ 3 improvement in raw contrast across the dark hole during the full duration of the test.

Chapter 4 describes the results of the first successful LDFC on-sky tests. Two types of tests are presented: (1) correction of artificially introduced aberrations, and (2), correction of wavefront errors that originate from the telescope, instrument, and atmosphere. When introducing aberrations with the DM, we find that LDFC improves the raw contrast by a factor 3–7 over the dark hole by decreasing the residual wavefront error from ~ 90 nm to ~ 40 nm root mean square. For the second type of tests, we show that the current implementation of LDFC is able to suppress evolving aberrations with timescales $< 0.1 - 0.4$ Hz, and is limited by the current Python implementation. We find that the power at 10 mHz is reduced by factor $\sim 20, 7,$ and 4 for spatial frequency bins at $2.5, 5.5,$ and $8.5 \lambda/D$, respectively.

Chapter 5: The polarization-encoded self-coherent camera

This chapter presents the polarization-encoded self-coherent camera (PESCC), an integrated focal-plane wavefront sensor and coronagraph, which is a new and powerful variant of the self-coherent camera (SCC). The PESCC implements a Lyot stop with a reference hole featuring a polarizer, and a downstream polarizing beamsplitter. We show that the PESCC relaxes the requirements on the optics size, focal-plane sampling, and spectral resolution with respect to the SCC. Furthermore, we find via numerical simulations that the PESCC has effectively access to ~ 16 times more photons, improving the wavefront sensing sensitivity by a factor ~ 4 . We also show that, without additional measurements, coherent differential imaging (CDI) is enabled as a contrast-enhancing post-processing technique for every observation. In idealized simulations representative of space-based systems with a charge two vortex coronagraph, we show that wavefront sensing and control, combined with CDI, can achieve a 1σ raw contrast of $\sim 3 \cdot 10^{-11} - 8 \cdot 10^{-11}$ between 1 and $18 \lambda/D$.

Chapter 6: Controlling the Low Wind Effect with Fast and Furious focal-plane wavefront sensing

This chapter presents the deployment of the Fast and Furious (F&F) focal-plane wavefront sensing algorithm to Subaru/SCEExAO to measure and correct the low-wind effect (LWE). F&F is a sequential phase-diversity algorithm and a software-only solution to focal-plane

1

wavefront sensing. Tests with the internal source results show that F&F can correct a wide range of LWE-like aberrations and bring the PSF back to a high Strehl ratio ($> 90\%$) and high symmetry. Furthermore, we present on-sky results that show that F&F is able to improve the PSF quality during very challenging atmospheric conditions ($1.3 - 1.4''$ seeing at 500 nm). Simultaneous observations of the PSF in the optical ($\lambda = 750$ nm, $\Delta\lambda = 50$ nm) show that we were correcting aberrations common to the optical and NIR paths within SCE_xAO.

Chapter 7: High-precision astrometry and photometry of directly imaged exoplanets with the Vector Speckle Grid

This chapter presents the theory and simulations of the vector speckle grid (VSG). The VSG is a new optical element to generate artificial speckles that serve as photometric and astrometric references when studying directly imaged exoplanets. We show, by imposing opposite amplitude or phase modulation on the opposite polarization states in the pupil plane, that artificial speckles are generated that are incoherent with the underlying speckle halo. This greatly increases the astrometric and photometric precision. In simulation we find that, for short-exposure images, the VSG reaches a $\sim 0.3 - 0.8\%$ photometric error and $\sim 3 - 10 \cdot 10^{-3} \lambda/D$ astrometric error, which is a performance improvement of a factor ~ 20 and ~ 5 compared to scalar variants, respectively. Furthermore, we outline how VSGs could be implemented using liquid-crystal technology to impose the geometric phase on the circular polarization states.

Bibliography

- Aime, C., Soummer, R., & Ferrari, A. 2002, *Astronomy & Astrophysics*, 389, 334
- Anglada-Escudé, G., Amado, P. J., Barnes, J., et al. 2016, *Nature*, 536, 437
- Apai, D., Radigan, J., Buenzli, E., et al. 2013, *The Astrophysical Journal*, 768, 121
- Apai, D., Kasper, M., Skemer, A., et al. 2016, *The Astrophysical Journal*, 820, 40
- Apai, D., Biller, B., Burgasser, A., et al. 2019, *Bulletin of the American Astronomical Society*, 51, 204
- Baranne, A., Queloz, D., Mayor, M., et al. 1996, *Astronomy and Astrophysics Supplement Series*, 119, 373
- Barclay, T., Pepper, J., & Quintana, E. V. 2018, *The Astrophysical Journal Supplement Series*, 239, 2
- Baudoz, P., Boccaletti, A., Baudrand, J., & Rouan, D. 2005, *Proceedings of the International Astronomical Union*, 1, 553
- Berry, M. V. 1987, *Journal of Modern Optics*, 34, 1401
- Beuzit, J.-L., Vigan, A., Mouillet, D., et al. 2019, *Astronomy & Astrophysics*, 631, A155
- Biller, B. 2017, *Astronomical Review*, 13, 1
- Biller, B., Apai, D., Bonnefoy, M., et al. 2021, arXiv preprint arXiv:2101.08514
- Bloemhof, E., Dekany, R., Troy, M., & Oppenheimer, B. 2001, *The Astrophysical Journal Letters*, 558, L71
- Boccaletti, A., Chauvin, G., Mouillet, D., et al. 2020, arXiv preprint arXiv:2003.05714
- Bohn, A. J., Kenworthy, M. A., Ginski, C., et al. 2020, *The Astrophysical Journal Letters*, 898, L16
- Bordé, P. J., & Traub, W. A. 2006, *The Astrophysical Journal*, 638, 488
- Borucki, W. J., Koch, D., et al. 2010, in *AAS/Division for Planetary Sciences Meeting Abstracts# 42*, 47–03
- Bos, S., Miller, K., Lozi, J., et al. submitted, *Astronomy & Astrophysics*
- Bos, S. P. 2021, *Astronomy & Astrophysics*, 646, A177
- Bos, S. P., Doelman, D. S., Miller, K. L., & Snik, F. 2020a, in *Adaptive Optics Systems VII*, Vol. 11448, *International Society for Optics and Photonics*, 114483W
- Bos, S. P., Doelman, D. S., Lozi, J., et al. 2019, *Astronomy & Astrophysics*, 632, A48
- Bos, S. P., Viedard, S., Wilby, M. J., et al. 2020b, arXiv preprint arXiv:2005.12097
- Bottom, M., Femenia, B., Huby, E., et al. 2016, in *Adaptive Optics Systems V*, Vol. 9909, *International Society for Optics and Photonics*, 990955
- Bottom, M., Wallace, J. K., Bartos, R. D., Shelton, J. C., & Serabyn, E. 2017, *Monthly Notices of the Royal Astronomical Society*, 464, 2937
- Bowler, B., Sallum, S., Boss, A., et al. 2019, arXiv preprint arXiv:1903.06299
- Brandt, T., Briesemeister, Z., Savransky, D., et al. 2019, *Bulletin of the American Astronomical Society*, 51, 269
- Brooks, K. J., Catala, L., Kenworthy, M. A., Crawford, S. M., & Codona, J. L. 2016, in *Advances in Optical and Mechanical Technologies for Telescopes and Instrumentation II*, Vol. 9912, *International Society for Optics and Photonics*, 991203
- Brown, A., Vallenari, A., Prusti, T., et al. 2018, *Astronomy & Astrophysics*, 616, A1
- Brown, A. G., Vallenari, A., Prusti, T., et al. 2016, *Astronomy & Astrophysics*, 595, A2
- Cantalloube, F., Por, E., Dohlen, K., et al. 2018, *Astronomy & Astrophysics*, 620, L10
- Cantalloube, F., Farley, O., Milli, J., et al. 2020, *Astronomy and Astrophysics-A&A*
- Cantalloube, F., Gomez-Gonzalez, C., Absil, O., et al. 2021, arXiv preprint arXiv:2101.05080
- Chauvin, G., Desidera, S., Lagrange, A.-M., et al. 2017, *Astronomy & Astrophysics*, 605, L9
- Chilcote, J. K., Bailey, V. P., De Rosa, R., et al. 2018, in *Ground-based and Airborne Instrumenta-*

- tion for Astronomy VII, Vol. 10702, International Society for Optics and Photonics, 1070244
- Christiaens, V., Casassus, S., Absil, O., et al. 2019, *Monthly Notices of the Royal Astronomical Society*, 486, 5819
- Codona, J. L. 2013, *Optical Engineering*, 52, 097105
- Codona, J. L., & Angel, R. 2004, *The Astrophysical Journal Letters*, 604, L117
- Codona, J. L., Kenworthy, M. A., & Lloyd-Hart, M. 2008, in *Adaptive Optics Systems*, Vol. 7015, International Society for Optics and Photonics, 70155D
- Cooper, C. S., Sudarsky, D., Milsom, J. A., Lunine, J. I., & Burrows, A. 2003, *The Astrophysical Journal*, 586, 1320
- Corrigan, M. K., Morris, T. J., Harris, R. J., & Anagnos, T. 2018, in *Adaptive Optics Systems VI*, Vol. 10703, International Society for Optics and Photonics, 107035H
- Currie, T., Brandt, T. D., Kuzuhara, M., et al. 2020a, *The Astrophysical Journal Letters*, 904, L25
- Currie, T., Pluzhnik, E., Guyon, O., et al. 2020b, *Publications of the Astronomical Society of the Pacific*, 132, 104502
- Damasso, M., Del Sordo, F., Anglada-Escudé, G., et al. 2020, *Science advances*, 6, eaax7467
- De Boer, J., Langlois, M., Van Holstein, R. G., et al. 2020, *Astronomy & Astrophysics*, 633, A63
- De Kok, R., Stam, D., & Karalidi, T. 2011, *The Astrophysical Journal*, 741, 59
- Doelman, D. S., Auer, F. F., Escuti, M. J., & Snik, F. 2019, *Optics letters*, 44, 17
- Doelman, D. S., Por, E. H., Ruane, G., Escuti, M. J., & Snik, F. 2020, *Publications of the Astronomical Society of the Pacific*, 132, 045002
- Doelman, D. S., Snik, F., Warriner, N. Z., & Escuti, M. J. 2017, in *Techniques and Instrumentation for Detection of Exoplanets VIII*, Vol. 10400, International Society for Optics and Photonics, 104000U
- Eisenhauer, F., Abuter, R., Bickert, K., et al. 2003, in *Instrument Design and Performance for Optical/Infrared Ground-based Telescopes*, Vol. 4841, International Society for Optics and Photonics, 1548–1561
- Eriksson, S. C., Janson, M., & Calissendorff, P. 2019, *Astronomy & Astrophysics*, 629, A145
- Escuti, M. J., Kim, J., & Kudenov, M. W. 2016, *Optics and Photonics News*, 27, 22
- Frazin, R. A. 2013, *The Astrophysical Journal*, 767, 21
- Fried, D. L. 1966, *JOSA*, 56, 1372
- Galicher, R., Baudoz, P., Delorme, J.-R., et al. 2019, *Astronomy & Astrophysics*, 631, A143
- Gerard, B. L., & Marois, C. 2020, *Publications of the Astronomical Society of the Pacific*, 132, 064401
- Gerard, B. L., Marois, C., & Galicher, R. 2018, *The Astronomical Journal*, 156, 106
- Gerard, B. L., Marois, C., Galicher, R., et al. 2019, arXiv preprint arXiv:1910.04554
- Give'on, A., Kern, B. D., & Shaklan, S. 2011, in *Techniques and Instrumentation for Detection of Exoplanets V*, Vol. 8151, International Society for Optics and Photonics, 815110
- Goebel, S. B., Guyon, O., Hall, D. N., et al. 2018, *Publications of the Astronomical Society of the Pacific*, 130, 104502
- Gonsalves, R. A. 1982, *Optical Engineering*, 21, 215829
- Gonsalves, R. A. 2002, in *European Southern Observatory Conference and Workshop Proceedings*, Vol. 58, 121
- Goodman, J. W. 2005, *Introduction to Fourier optics* (Roberts and Company Publishers)
- Greenwood, D. P. 1977, *JOSA*, 67, 390
- Groff, T. D., Riggs, A. E., Kern, B., & Kasdin, N. J. 2015, *Journal of Astronomical Telescopes, Instruments, and Systems*, 2, 011009
- Guyon, O. 2004, *The Astrophysical Journal*, 615, 562
- . 2005, *The Astrophysical Journal*, 629, 592
- . 2018, *Annual Review of Astronomy and Astrophysics*, 56, 315

- Guyon, O., Martinache, F., Cady, E. J., et al. 2012, in *Adaptive Optics Systems III*, Vol. 8447, International Society for Optics and Photonics, 84471X
- Guyon, O., Mazin, B., Fitzgerald, M., et al. 2018, in *Adaptive Optics Systems VI*, Vol. 10703, International Society for Optics and Photonics, 107030Z
- Guyon, O., Miller, K., Males, J., Belikov, R., & Kern, B. 2017, arXiv preprint arXiv:1706.07377
- Haffert, S., Bohn, A., de Boer, J., et al. 2019, *Nature Astronomy*, 3, 749
- Haffert, S., Wilby, M., Keller, C., et al. 2018, in *Society of Photo-Optical Instrumentation Engineers (SPIE) Conference Series*, Vol. 10703, SPIE
- Haffert, S. Y. in prep.
- Hardy, J. W. 1998, *Adaptive optics for astronomical telescopes*, Vol. 16 (Oxford University Press on Demand)
- Hartmann, J. 1900, *Zeitschrift für Instrumentenkunde*, 20, 47
- Helling, C. 2019, *Annual Review of Earth and Planetary Sciences*, 47, 583
- Henry, G. W., Marcy, G. W., Butler, R. P., & Vogt, S. S. 1999, *The Astrophysical Journal Letters*, 529, L41
- Herscovici-Schiller, O., Mugnier, L. M., Baudoz, P., et al. 2018, *Astronomy & Astrophysics*, 614, A142
- Herscovici-Schiller, O., Sauvage, J.-F., Mugnier, L. M., Dohlen, K., & Vigan, A. 2019, *Monthly Notices of the Royal Astronomical Society*, 488, 4307
- Hinkley, S., Oppenheimer, B. R., Soummer, R., et al. 2007, *The Astrophysical Journal*, 654, 633
- Hoeijmakers, H., Schwarz, H., Snellen, I., et al. 2018, *Astronomy & Astrophysics*, 617, A144
- Holzlöhner, R., Kimeswenger, S., Kausch, W., & Noll, S. 2020, arXiv preprint arXiv:2010.01978
- Huby, E., Baudoz, P., Mawet, D., & Absil, O. 2015, *Astronomy & Astrophysics*, 584, A74
- Huby, E., Bottom, M., Femenia, B., et al. 2017, *Astronomy & Astrophysics*, 600, A46
- Jacob, W. 1855
- Jovanovic, N., Guyon, O., Martinache, F., et al. 2015a, *The Astrophysical Journal Letters*, 813, L24
- Jovanovic, N., Martinache, F., Guyon, O., et al. 2015b, *Publications of the Astronomical Society of the Pacific*, 127, 890
- Jovanovic, N., Absil, O., Baudoz, P., et al. 2018, arXiv preprint arXiv:1807.07043
- Karalidi, T., Stam, D., & Hovenier, J. 2012, *Astronomy & Astrophysics*, 548, A90
- Kasdin, N. J., Vanderbei, R. J., Spergel, D. N., & Littman, M. G. 2003, *The Astrophysical Journal*, 582, 1147
- Keller, C. U., Korkiakoski, V., Doelman, N., et al. 2012, in *Adaptive Optics Systems III*, Vol. 8447, International Society for Optics and Photonics, 844721
- Keppler, M., Benisty, M., Müller, A., et al. 2018, *Astronomy & Astrophysics*, 617, A44
- Komanduri, R. K., Lawler, K. F., & Escuti, M. J. 2013, *Optics Express*, 21, 404
- Korkiakoski, V., Keller, C. U., Doelman, N., et al. 2014, *Applied optics*, 53, 4565
- Kostov, V., & Apai, D. 2012, *The Astrophysical Journal*, 762, 47
- Kuhn, J., Potter, D., & Parise, B. 2001, *The Astrophysical Journal Letters*, 553, L189
- Langlois, M., Vigan, A., Moutou, C., et al. 2013, in *Proceedings of the Third AO4ELT Conference*, 63
- Langlois, M., Dohlen, K., Vigan, A., et al. 2014, in *Ground-based and Airborne Instrumentation for Astronomy V*, Vol. 9147, International Society for Optics and Photonics, 91471R
- Le Louarn, M., Béchet, C., & Tallon, M. 2013, in *Proc. of the Third AO4ELT Conference*
- Lindgren, L., Babusiaux, C., Bailer-Jones, C., et al. 2007, *Proceedings of the International Astronomical Union*, 3, 217
- Lyot, B. 1939, *Monthly Notices of the Royal Astronomical Society*, 99, 580
- Macintosh, B., Poyneer, L., Sivaramkrishnan, A., & Marois, C. 2005, in *Astronomical Adaptive Optics Systems and Applications II*, Vol. 5903, International Society for Optics and Photonics,

- 59030J
- Macintosh, B., Graham, J. R., Ingraham, P., et al. 2014, *Proceedings of the National Academy of Sciences*, 111, 12661
- Macintosh, B., Graham, J., Barman, T., et al. 2015, *Science*, 350, 64
- Madec, P.-Y. 2012, in *Adaptive Optics Systems III*, Vol. 8447, International Society for Optics and Photonics, 844705
- Males, J. R., Belikov, R., & Bendek, E. 2015, in *Techniques and Instrumentation for Detection of Exoplanets VII*, Vol. 9605, International Society for Optics and Photonics, 960518
- Marois, C., Lafreniere, D., Doyon, R., Macintosh, B., & Nadeau, D. 2006a, *The Astrophysical Journal*, 641, 556
- Marois, C., Lafreniere, D., Macintosh, B., & Doyon, R. 2006b, *The Astrophysical Journal*, 647, 612
- Marois, C., Macintosh, B., Barman, T., et al. 2008, *science*, 322, 1348
- Martinache, F. 2010, *The Astrophysical Journal*, 724, 464
- . 2013, *Publications of the Astronomical Society of the Pacific*, 125, 422
- Martinache, F., Jovanovic, N., & Guyon, O. 2016, *Astronomy & Astrophysics*, 593, A33
- Martinache, F., Guyon, O., Jovanovic, N., et al. 2014, *Publications of the Astronomical Society of the Pacific*, 126, 565
- Martinez, P. 2019, *Astronomy & Astrophysics*, 629, L10
- Martinez, P., Kasper, M., Costille, A., et al. 2013, *Astronomy & Astrophysics*, 554, A41
- Martinez, P., Loose, C., Carpentier, E. A., & Kasper, M. 2012, *Astronomy & Astrophysics*, 541, A136
- Mawet, D., Riaud, P., Absil, O., & Surdej, J. 2005, *The Astrophysical Journal*, 633, 1191
- Mawet, D., Pueyo, L., Lawson, P., et al. 2012, in *Space Telescopes and Instrumentation 2012: Optical, Infrared, and Millimeter Wave*, Vol. 8442, International Society for Optics and Photonics, 844204
- Mayor, M., & Queloz, D. 1995, *Nature*, 378, 355
- Metchev, S. A., Heinze, A., Apai, D., et al. 2015, *The Astrophysical Journal*, 799, 154
- Miller, K., Guyon, O., & Males, J. 2017, *Journal of Astronomical Telescopes, Instruments, and Systems*, 3, 049002
- Miller, K., Bos, S., Lozi, J., et al. 2021, *Astronomy & Astrophysics*, 646, A145
- Milli, J., Banas, T., Mouillet, D., et al. 2016, in *Adaptive Optics Systems V*, Vol. 9909, International Society for Optics and Photonics, 99094Z
- Milli, J., Kasper, M., Bourget, P., et al. 2018, in *Adaptive Optics Systems VI*, Vol. 10703, International Society for Optics and Photonics, 107032A
- Miskiewicz, M. N., & Escuti, M. J. 2014, *Optics Express*, 22, 12691
- N'Diaye, M., Dohlen, K., Fusco, T., & Paul, B. 2013, *Astronomy & Astrophysics*, 555, A94
- N'Diaye, M., Martinache, F., Jovanovic, N., et al. 2018, *Astronomy & Astrophysics*, 610, A18
- N'Diaye, M., Vigan, A., Dohlen, K., et al. 2016, *Astronomy & Astrophysics*, 592, A79
- Nielsen, E. L., De Rosa, R. J., Macintosh, B., et al. 2019, *The Astronomical Journal*, 158, 13
- Norris, B. R., Wei, J., Betters, C. H., Wong, A., & Leon-Saval, S. G. 2020, *arXiv preprint arXiv:2003.05158*
- Oh, C., & Escuti, M. J. 2008, *Optics letters*, 33, 2287
- Otten, G. P., Snik, F., Kenworthy, M. A., et al. 2014, in *Advances in Optical and Mechanical Technologies for Telescopes and Instrumentation*, Vol. 9151, International Society for Optics and Photonics, 91511R
- Pancharatnam, S. 1956, in *Proceedings of the Indian Academy of Sciences-Section A*, Vol. 44, Springer, 398–417
- Patty, C. L., Ten Kate, I. L., Buma, W. J., et al. 2019, *Astrobiology*, 19, 1221

- Paul, B., Mugnier, L., Sauvage, J.-F., Dohlen, K., & Ferrari, M. 2013, *Optics Express*, 21, 31751
- Paxman, R. G., Schulz, T. J., & Fienup, J. R. 1992, *JOSA A*, 9, 1072
- Perryman, M., Hartman, J., Bakos, G. Á., & Lindgren, L. 2014, *The Astrophysical Journal*, 797, 14
- Petigura, E. A., Howard, A. W., & Marcy, G. W. 2013, *Proceedings of the National Academy of Sciences*, 110, 19273
- Por, E. H. 2020, *The Astrophysical Journal*, 888, 127
- Por, E. H., & Keller, C. U. 2016, in *Adaptive Optics Systems V*, Vol. 9909, International Society for Optics and Photonics, 990959
- Potier, A., Baudoz, P., Galicher, R., Singh, G., & Boccaletti, A. 2020a, *Astronomy & Astrophysics*, 635, A192
- Potier, A., Galicher, R., Baudoz, P., et al. 2020b, arXiv preprint arXiv:2005.02179
- Quesnel, M., de Xivry, G. O., Louppe, G., & Absil, O. 2020, in *Adaptive Optics Systems VII*, Vol. 11448, International Society for Optics and Photonics, 114481G
- Racine, R., Walker, G. A., Nadeau, D., Doyon, R., & Marois, C. 1999, *Publications of the Astronomical Society of the Pacific*, 111, 587
- Ragazzoni, R. 1996, *Journal of modern optics*, 43, 289
- Riaud, P., Mawet, D., & Magette, A. 2012a, *Astronomy & Astrophysics*, 545, A151
- . 2012b, *Astronomy & Astrophysics*, 545, A150
- Ricker, G. R., Winn, J. N., Vanderspek, R., et al. 2014, *Journal of Astronomical Telescopes, Instruments, and Systems*, 1, 014003
- Roddier, F., & Roddier, C. 1997, *Publications of the Astronomical Society of the Pacific*, 109, 815
- Ruane, G., Riggs, A., Mazoyer, J., et al. 2018, in *Space Telescopes and Instrumentation 2018: Optical, Infrared, and Millimeter Wave*, Vol. 10698, International Society for Optics and Photonics, 106982S
- Sahoo, A., Guyon, O., Lozi, J., et al. 2020, *The Astronomical Journal*, 159, 250
- Sauvage, J.-F., Fusco, T., Guesalaga, A., et al. 2015, in *Adaptive Optics for Extremely Large Telescopes 4—Conference Proceedings*, Vol. 1
- Sauvage, J.-F., Fusco, T., Lamb, M., et al. 2016, in *Adaptive Optics Systems V*, Vol. 9909, International Society for Optics and Photonics, 990916
- Shack, R. V. 1971, *J. Opt. Soc. Am.*, 61, 656
- Singh, G., Lozi, J., Jovanovic, N., et al. 2017, *Publications of the Astronomical Society of the Pacific*, 129, 095002
- Singh, G., Martinache, F., Baudoz, P., et al. 2014, *Publications of the Astronomical Society of the Pacific*, 126, 586
- Singh, G., Lozi, J., Guyon, O., et al. 2015, *Publications of the Astronomical Society of the Pacific*, 127, 857
- Sivaramakrishnan, A., & Oppenheimer, B. R. 2006, *The Astrophysical Journal*, 647, 620
- Smith, B. A., & Terrile, R. J. 1984, *Science*, 226, 1421
- Snellen, I., & Brown, A. 2018, *Nature Astronomy*, 2, 883
- Snellen, I., de Kok, R., Birkby, J., et al. 2015, *Astronomy & Astrophysics*, 576, A59
- Snik, F., Otten, G., Kenworthy, M., et al. 2012, in *Modern Technologies in Space-and Ground-based Telescopes and Instrumentation II*, Vol. 8450, International Society for Optics and Photonics, 84500M
- Soummer, R., Aimé, C., & Falloon, P. 2003, *Astronomy & Astrophysics*, 397, 1161
- Soummer, R., Ferrari, A., Aime, C., & Jolissaint, L. 2007, *The Astrophysical Journal*, 669, 642
- Sparks, W. B., & Ford, H. C. 2002, *The Astrophysical Journal*, 578, 543
- Stam, D., Hovenier, J., & Waters, L. 2004, *Astronomy & Astrophysics*, 428, 663
- Stolker, T., Min, M., Stam, D. M., et al. 2017, *Astronomy & Astrophysics*, 607, A42

- 1
- Struve, O. 1952, *The Observatory*, 72, 199
- Tallis, M., Bailey, V. P., Macintosh, B., et al. 2020, *Journal of Astronomical Telescopes, Instruments, and Systems*, 6, 015002
- Traub, W. A., & Oppenheimer, B. R. 2010, *Exoplanets*, 111
- Trauger, J. T., & Traub, W. A. 2007, *Nature*, 446, 771
- van Haver, S., Braat, J. J., Dirksen, P., & Janssen, A. J. 2006, *Journal of the European Optical Society-Rapid publications*, 1
- van Holstein, R., Stolker, T., Jensen-Clem, R., et al. 2021, *Astronomy & Astrophysics*
- van Holstein, R. G., Snik, F., Girard, J. H., et al. 2017, in *Techniques and Instrumentation for Detection of Exoplanets VIII*, Vol. 10400, International Society for Optics and Photonics, 1040015
- Vievard, S., Bonnefois, A., Cassaing, F., Montri, J., & Mugnier, L. 2020, arXiv preprint arXiv:2011.10696
- Vievard, S., Bos, S., Cassaing, F., et al. 2019, arXiv preprint arXiv:1912.10179
- Vigan, A., N'Diaye, M., Dohlen, K., et al. 2019, *Astronomy & Astrophysics*, 629, A11
- Vigan, A., Fontanive, C., Meyer, M., et al. 2020, arXiv preprint arXiv:2007.06573
- Wagner, K., Follete, K. B., Close, L. M., et al. 2018, *The Astrophysical Journal Letters*, 863, L8
- Wang, J. J., Rajan, A., Graham, J. R., et al. 2014, in *Ground-based and Airborne Instrumentation for Astronomy V*, Vol. 9147, International Society for Optics and Photonics, 914755
- Wilby, M. J., Keller, C. U., Snik, F., Korkiakoski, V., & Pietrow, A. G. 2017, *Astronomy & Astrophysics*, 597, A112
- Winn, J. N., & Fabrycky, D. C. 2015, *Annual Review of Astronomy and Astrophysics*, 53
- Wolszczan, A., & Frail, D. A. 1992, *Nature*, 355, 145
- Ygouf, M., Mugnier, L. M., Mouillet, D., Fusco, T., & Beuzit, J.-L. 2013, *Astronomy & Astrophysics*, 551, A138
- Zhou, Y., Apai, D., Schneider, G. H., Marley, M. S., & Showman, A. P. 2016, *The Astrophysical Journal*, 818, 176

2 | Focal-plane wavefront sensing with the vector-Apodizing Phase Plate

Adapted from

S.P. Bos, D.S. Doelman, J. Lozi, O. Guyon, C.U. Keller, K.L. Miller,
N. Jovanovic, F. Martinache, F. Snik
Astronomy & Astrophysics, 632, A48 (2019)

One of the key limitations of the direct imaging of exoplanets at small angular separations are quasi-static speckles that originate from evolving non-common path aberrations (NCPA) in the optical train downstream of the instrument's main wavefront sensor split-off. In this article we show that the vector-Apodizing Phase Plate (vAPP) coronagraph can be designed such that the coronagraphic point spread functions (PSFs) can act as wavefront sensors to measure and correct the (quasi-)static aberrations without dedicated wavefront sensing holograms or modulation by the deformable mirror. The absolute wavefront retrieval is performed with a nonlinear algorithm. The focal-plane wavefront sensing (FPWFS) performance of the vAPP and the algorithm are evaluated via numerical simulations to test various photon and read noise levels, the sensitivity to the 100 lowest Zernike modes, and the maximum wavefront error (WFE) that can be accurately estimated in one iteration. We apply these methods to the vAPP within SCExAO, first with the internal source and subsequently on-sky. In idealized simulations we show that for 10^7 photons the root mean square (RMS) WFE can be reduced to $\sim \lambda/1000$, which is 1 nm RMS in the context of the SCExAO system. We find that the maximum WFE that can be corrected in one iteration is $\sim \lambda/8$ RMS or ~ 200 nm RMS (SCExAO). Furthermore, we demonstrate the SCExAO vAPP capabilities by measuring and controlling the 30 lowest Zernike modes with the internal source and on-sky. On-sky, we report a raw contrast improvement of a factor ~ 2 between 2 and 4 λ/D after five iterations of closed-loop correction. When artificially introducing 150 nm RMS WFE, the algorithm corrects it within five iterations of closed-loop operation. FPWFS with the vAPP coronagraphic PSFs is a powerful technique since it integrates coronagraphy and wavefront sensing, eliminating the need for additional probes and thus resulting in a 100% science duty cycle and maximum throughput for the target.

2.1 Introduction

The exploration of circumstellar environments at small angular separations by means of direct imaging is crucial for the detection and characterization of exoplanets. The challenges that need to be overcome are that of high contrast and small angular separation. E.g. the angular separation and contrast between the Earth and the Sun at 10 pc in the visible ($\sim 0.3\text{-}1\ \mu\text{m}$) is respectively ~ 100 milliarcseconds (mas) and $\sim 10^{-10}$ (Traub & Oppenheimer, 2010).

The current generation of ground-based high-contrast imaging instruments SPHERE (Beuzit et al., 2019), GPI (Macintosh et al., 2014), the upcoming MagAO-X (Males et al. 2018; Close et al. 2018), and Subaru Coronagraphic Extreme Adaptive Optics (SCEXAO; Jovanovic et al. 2015) are pushing towards contrasts of $\sim 10^{-6}$ at angular separations of 200 mas after post-processing in the near-infrared ($0.95\text{-}2.3\ \mu\text{m}$; Vigan et al. 2015). These instruments are equipped with extreme adaptive optics systems to flatten the wavefront after the turbulent atmosphere, coronagraphs to suppress the star light and contrast-enhancing post-processing techniques that employ some form of diversity such as angular differential imaging (Marois et al., 2006), reference star differential imaging (Ruane et al., 2019), spectral differential imaging (Sparks & Ford, 2002), and polarimetric differential imaging (Snik & Keller, 2013). The latter two techniques can also be used as a characterization diagnostic. Medium- and high-resolution integral-field spectroscopy can be used to detect atomic and molecular lines from a planet's atmosphere (e.g., Haffert et al. 2019 and Hoeijmakers et al. 2018), while polarimetry can be used to detect cloud structures (Stam et al. 2004; De Kok et al. 2011; van Holstein et al. 2017).

The coronagraph relevant for the present work is the vector-Apodizing Phase Plate (vAPP; Snik et al. 2012; Otten et al. 2017), which manipulates the phase in the pupil-plane such that in selected regions in the focal plane the starlight is cancelled; these areas are referred to as dark holes. The phase is induced through the achromatic geometric phase (Pancharatnam 1956; Berry 1987) on the circular polarization states by a half-wave liquid-crystal layer with a varying fast-axis orientation. The two circular polarization states both receive equal but opposite phases, resulting in two coronagraphic point spread functions (PSFs) with opposite dark holes, as shown in Figure 2.1. The geometric phase is inherently achromatic as it depends on geometric effects, but the efficiency with which the light acquires the phase is determined by the retardance of the liquid-crystal layer. Retardance offsets from half-wave result in leakage; light that has not acquired the desired phase will form a non-coronagraphic PSF based on the aperture geometry. Generally, vAPP coronagraphs are designed to have minimal leakage over a broad wavelength range. High leakage will affect coronagraphic performance as light from the leaked PSF will contaminate the dark hole. In the simplest and most common implementation the two coronagraphic PSFs are spatially separated with a polarization-sensitive grating (Oh & Escuti, 2008) that is integrated in the phase design. These coronagraphs are known as grating-vAPPs (Otten et al., 2014) and are mainly used for operation with narrowband filters or integral-field spectrographs to prevent smearing by the grating. In this article the grating-vAPP is referred to as a vAPP. The vAPP has been put on-sky with several instruments: CHARIS/SCEXAO (Doelman et al., 2017), MagAO/Clio2 (Otten et al., 2017),

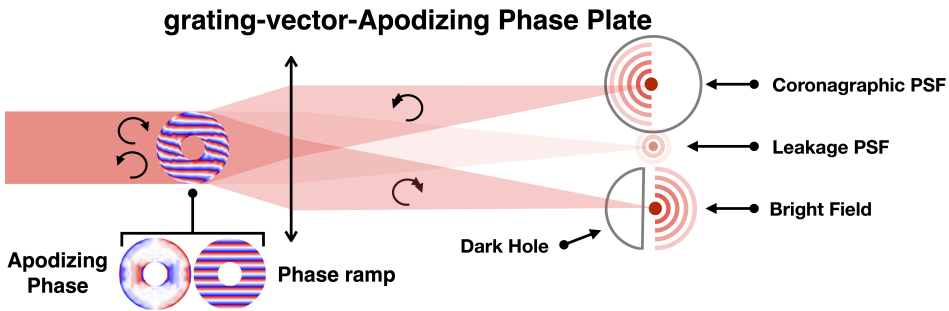


Figure 2.1: Working principle of the grating-vector-Apodizing Phase Plate. The grating-vAPP is a half-wave retarder pupil-plane optic with a spatially varying fast-axis orientation. The varying fast-axis orientation induces the phase through the geometric phase on the circular polarization states. These polarization states receive the opposite phase and therefore have flipped coronagraphic point spread functions (PSFs). The PSFs are spatially separated by adding a phase ramp to the design. Any offsets from half-wave retardance within the optic reduces the efficiency with which the light will be transferred to the coronagraphic PSFs and results in a leakage PSF.

LMIRCAM/LBT (Doelman et al., 2017), and LEXI (Haffert et al., 2018). Furthermore, vAPPs have been designed for the following instruments: HiCIBaS (Côté et al., 2018), MagAO-X (Miller et al., 2018), ERIS (Boehle et al., 2018), METIS (Kenworthy et al., 2018), and MICADO (Davies et al., 2018).

One of the key limitations of the current high-contrast imaging instruments that limit them to contrasts above $\sim 10^{-6}$ within 300 mas are quasi-static speckles that originate from slowly evolving instrumental aberrations caused by changing temperature, humidity, and gravity vector during observations (Martinez et al. 2012; Martinez et al. 2013; N'Diaye et al. 2016; Vigan et al. 2018). When these aberrations occur in the optical train downstream of the main wavefront sensor split-off, they are not sensed and therefore cannot be corrected. Additional focal-plane wavefront sensing (FPWFS) with the science detector is a highly desirable solution to these non-common path aberrations (NCPA). In addition to eliminating the NCPAs, a FPWS can also address chromatic errors between the main sensing and science channels. Another advantage of FPWFS is that it has been shown by Guyon (2005) that it is able to reach high sensitivities for all spatial frequencies, only being surpassed in sensitivity by the Zernike wavefront sensor (N'Diaye et al. 2013; Doelman et al. 2019). A notable FPWFS is the Self-Coherent Camera (SCC; Baudoz et al. 2005; Galicher et al. 2008; Mazoyer et al. 2013). This is a WFS that is combined with a coronagraph, which uses focal-plane optics to block starlight. It operates by placing a small hole in the pupil-plane Lyot stop outside of the geometric pupil where the scattered starlight is located. This hole creates a reference beam that generates high spatial frequency fringes in the focal-plane image, which can be used to determine the full electric field. The SCC has a 100% science duty cycle, but requires a high focal-plane sampling to resolve the fringes, and optics of a sufficient size to accommodate the refer-

ence beam. FPWS has also been conducted by using vAPPs. Previous work focused on adding additional holograms in the focal plane that either encode wavefront information (Wilby et al., 2017) or directly probe the electric field (Por & Keller, 2016); these will not be considered here.

An overview of FPWFS techniques can be found in Jovanovic et al. (2018). There are three FPWFS and control methods that are particularly relevant: The COFFEE; Sauvage et al. 2012; Paul et al. 2013a) wavefront sensor is an extension of classical phase diversity (Gonsalves 1982; Paxman et al. 1992) to coronagraphic imaging. Aberrations in a physical model of the coronagraphic system are fitted to two focal-plane images, one of which has a known phase diversity (e.g., defocus). The method has been demonstrated in the lab (Paul et al., 2013b) and on the SPHERE system using the internal calibration source (Paul et al., 2014). Recent extensions enable COFFEE to measure phase in long-exposure images affected by residual turbulence (Herscovici-Schiller et al., 2017), and measure both phase and amplitude (Herscovici-Schiller et al., 2018).

An interferometric approach to FPWFS is the Asymmetric Pupil Fourier Wavefront Sensor (APF-WFS; Martinache 2013). The APF-WFS assumes the small aberration regime enabling a Fourier analysis of focal-plane images to determine pupil-plane phase aberrations. The image is formed by an asymmetric pupil, which enables the full phase determination. The theory behind this technique is more extensively discussed in section 7.2. The wavefront sensor has been demonstrated on-sky in closed-loop operation controlling the lowest-order Zernike modes (Martinache et al., 2016), also in the context of controlling the “island effect” (N’Diaye et al., 2018).

Linear dark-field control (LDFC; Guyon et al. 2017) and more specifically the spatial LDFC variant (Miller et al., 2017). The idea behind spatial LDFC is to measure and control small aberrations that pollute the dark hole (created by the vAPP or other techniques) by measuring the response of the bright field (see Figure 2.1) relative to a reference state. This response is approximately linear for small aberrations. In Miller et al. (2017) it was shown to work for one-sided dark holes and modes that have a response in the bright field and the dark hole, but in this case there is also a spatial null-space consisting of the modes that do not have a response in the bright field but do pollute the dark hole. The authors overcame this problem by using the vAPP (Miller et al., 2018), where the bright field of one coronagraphic PSF covers the dark hole of the other. This has been shown to work in the laboratory (Miller, 2018), but there is still a significant null space for most vAPP designs; it is insensitive to the even pupil phase modes (see section 7.2).

COFFEE and the APF-WFS both suffer from low duty cycles as the science observations have to be stopped for the phase diversity probes or moving the asymmetric mask in and out the beam. LDFC, on the other hand, has a 100% duty cycle, but has currently only been considered for vAPPs with a significant null space (the even pupil phase modes), it only works in the small aberration regime, and does not perform an absolute phase measurement. In section 7.2 we combine the APF-WFS and LDFC with vAPPs, eliminating the null space and improving the duty cycle to 100%. In section 2.3 we present a non-linear algorithm similar to COFFEE that can perform absolute phase retrieval. In sec-

tion 7.3 we explore the theoretical FPWFS performance of the vAPP and the non-linear algorithm with simulations for the vAPP installed at SCEXAO. In section 6.3 we demonstrate the method first with the internal source and subsequently on-sky. In section 7.5 we discuss the results and present the conclusions.

2.2 Theory

2.2.1 Phase retrieval

Phase retrieval techniques in astronomy deal with sensing pupil-plane phase aberrations by analyzing focal-plane images. These techniques require a unique response in the focal-plane intensity for every phase mode and sign of its modal coefficient (the amount of wavefront error in the specific phase mode). For symmetric pupils such a unique response does not exist for the sign of the modal coefficients of even phase modes. For example, it is easy to determine how an optic needs to be moved to correct for tip and/or tilt (odd Zernike mode). But when the PSF is defocused (even Zernike mode), it is not immediately clear in which direction the optic needs to be moved to bring the PSF back into focus. In this section we demonstrate the origin of this well-known sign ambiguity (Gonsalves 1982; Paxman et al. 1992).

The electric field in the pupil-plane consists of an amplitude component $A(r)$ and a phase component $\theta(r)$:

$$E_{\text{pup}}(r) = A(r)e^{i\theta(r)} \quad (2.1)$$

$$= A(r) \cos[\theta(r)] + iA \sin[\theta(r)]. \quad (2.2)$$

Here the electric field E_{pup} and its constituents, A and θ , are 2D entities where the position vector r , defined from the center of the pupil, is omitted from here on. The focal-plane electric field $E_{\text{foc}}(x)$ is formed by propagating E_{pup} using the Fraunhofer propagation operator $C\{\cdot\} \propto \frac{1}{i} \mathcal{F}\{\cdot\}$ (Goodman, 2005). We use the Fraunhofer propagator, instead of just the Fourier transform because it is the physically correct propagator:

$$E_{\text{foc}}(x) = C\{E_{\text{pup}}\} \quad (2.3)$$

$$= C\{A \cos(\theta)\} + C\{iA \sin(\theta)\} \quad (2.4)$$

$$= a(x) + ib(x). \quad (2.5)$$

Here $a(x)$ and $b(x)$ are the real and imaginary components of $E_{\text{foc}}(x)$, respectively, and generally contain a mixture of $C\{A \cos(\theta)\}$ and $C\{iA \sin(\theta)\}$. The focal-plane coordinates are denoted by x and are omitted from here on as well. The focal-plane intensity I_{foc} or PSF is subsequently given by

$$I_{\text{foc}} = |E_{\text{foc}}|^2 \quad (2.6)$$

$$= |a|^2 + |b|^2 \quad (2.7)$$

Before we continue with an example of even phase aberrations, we recall the following:

Table 2.1: Fraunhofer propagation symmetry properties (Goodman, 2005), these are the Fourier properties multiplied with a factor $-i$ ($E_{\text{foc}} = C\{E_{\text{pup}}\} \propto \frac{1}{i}\mathcal{F}\{E_{\text{pup}}\}$).

Pupil-plane electric field		Focal-plane electric field	
$E_{\text{pup}} = A \cos(\theta) + iA \sin(\theta)$		$E_{\text{foc}} = a + ib$	
Term	Term symmetry	A, θ symmetry	Term symmetry
$A \cos(\theta)$	Even	$(A_{\text{even}}, \theta_{\text{even}}), (A_{\text{even}}, \theta_{\text{odd}})$	Even
$A \cos(\theta)$	Odd	$(A_{\text{odd}}, \theta_{\text{even}}), (A_{\text{odd}}, \theta_{\text{odd}})$	Odd
$iA \sin(\theta)$	Even	$(A_{\text{even}}, \theta_{\text{even}}), (A_{\text{odd}}, \theta_{\text{odd}})$	Even
$iA \sin(\theta)$	Odd	$(A_{\text{even}}, \theta_{\text{odd}}), (A_{\text{odd}}, \theta_{\text{even}})$	Odd

1. The decomposition of a function $f(r)$ into even and odd functions:

$$f(r) = f_{\text{even}}(r) + f_{\text{odd}}(r), \quad (2.8)$$

$$f_{\text{even}}(r) = \frac{f(r) + f(-r)}{2}, \quad (2.9)$$

$$f_{\text{odd}}(r) = \frac{f(r) - f(-r)}{2}. \quad (2.10)$$

An example of a symmetry decomposition of phase and amplitude in the context of the APP coronagraph is shown in Figure 2.4.

2. The multiplication and composition properties of even and odd functions:

$$f_{\text{even}}(r) \cdot g_{\text{odd}}(r) = h_{\text{odd}}(r), \quad (2.11)$$

$$f_{\text{odd}}(r) \cdot g_{\text{odd}}(r) = h_{\text{even}}(r), \quad (2.12)$$

$$f_{\text{even}}(r) \cdot g_{\text{even}}(r) = h_{\text{even}}(r), \quad (2.13)$$

$$f_{\text{even}}[g_{\text{odd}}(r)] = h_{\text{even}}(r), \quad (2.14)$$

$$f_{\text{odd}}[g_{\text{odd}}(r)] = h_{\text{odd}}(r), \quad (2.15)$$

$$f_{\text{odd}}[g_{\text{even}}(r)] = h_{\text{even}}(r), \quad (2.16)$$

$$f_{\text{even}}[g_{\text{even}}(r)] = h_{\text{even}}(r). \quad (2.17)$$

3. The symmetry properties of Fraunhofer propagation (see Table 2.1).
4. The Hermitian properties of the Fraunhofer propagation, which say that a conjugated pupil-plane electric field $E'_{\text{pup}} = E_{\text{pup}}^*$ (i.e., a phase sign flip; * denotes the conjugation) will result in a flipped and conjugated focal-plane electric field $E'_{\text{foc}} = C\{E'_{\text{pup}}\}$:

$$E'_{\text{foc}}(r) = -E_{\text{foc}}(-r)^*. \quad (2.18)$$

The reason that the symmetry decomposition, combined with the decomposition of E_{pup} in its real and imaginary components (Equation 2.2), is important, is that the Fraunhofer propagation maps combinations of these decompositions into either real or imaginary components of E_{foc} , as shown in Table 2.1. We show below that these properties of the Fraunhofer propagation determine what kind of symmetry has to be introduced in the pupil-plane to determine the sign of even phase aberrations.

Let us assume that A is even, which is true for most instrument pupils. If an even phase aberration (e.g., astigmatism) is added, the terms $A \cos(\theta)$ and $iA \sin(\theta)$ will both be even. We note that only the imaginary term contains sign information on the aberration. In this example, when they are propagated to the focal plane, $A \cos(\theta)$ will go to ib and $iA \sin(\theta)$ to a (respectively shown in the first and third row of Table 2.1). These terms are still even and the sign information on the aberration is encoded in the real part of the focal-plane electric field. The resulting PSF recorded by the detector is even. These steps are shown in the top row of Figure 2.2 a. If the sign of the aberration flips (i.e., a conjugation of the pupil-plane electric field), the PSF flips, but as the PSF is even, there is no morphology change recorded and thus the sign information cannot be retrieved (see

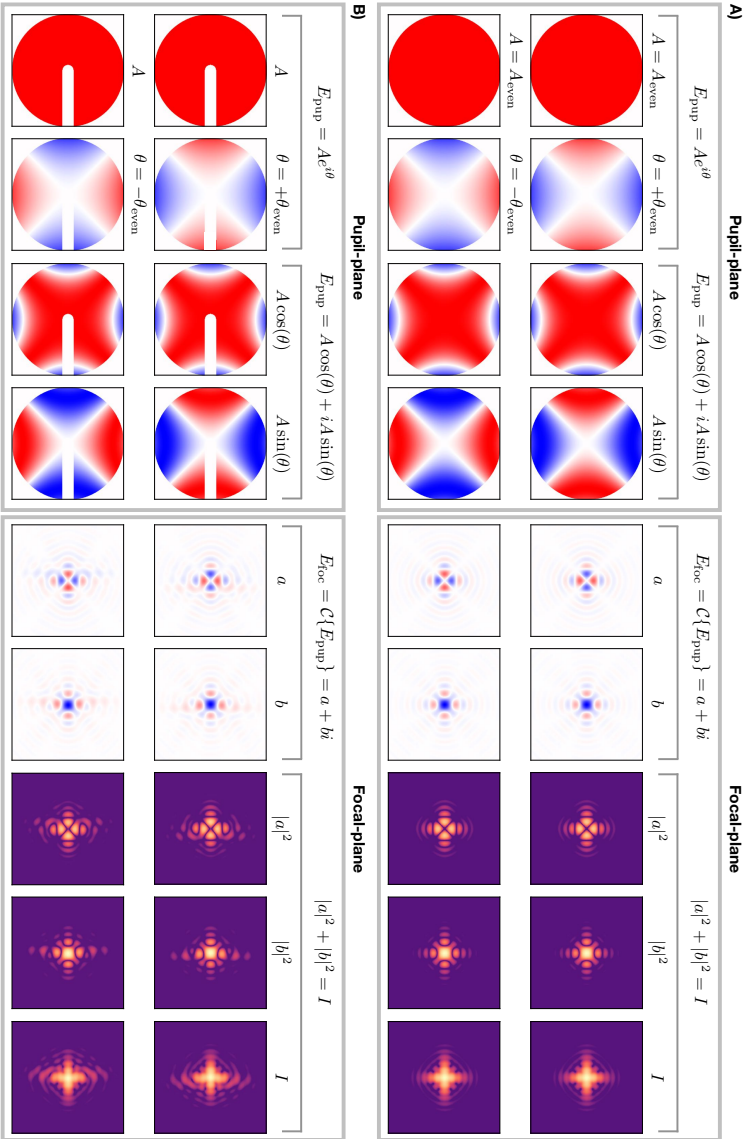


Figure 2.2: Focal- and pupil-plane quantities of an even phase aberration (astigmatism) through a symmetric pupil (a) and an asymmetric pupil (b). The two rows show opposite signs for the phase aberration. The columns in the pupil-plane box (from left to right) show the amplitude, phase, and real and imaginary electric fields. In the focal-plane box the columns show the real and imaginary electric fields, the power in the real and imaginary electric fields, and the total power.

Figure 2.2 a, bottom row). We can only hope to determine the sign by measuring the real electric field as that is where the sign information is encoded. For odd phase aberrations the sign flip will result in a morphology change and can therefore be measured.

If the same exercise is performed with a pupil amplitude asymmetry, there will be a morphology change. This is shown in the top and bottom rows of Figure 2.2 b. The reason is that an even pupil amplitude, as shown in the top row of Figure 2.3 a, will only generate an imaginary electric field and therefore will not interfere with sign information containing a real electric field caused by even aberrations. This is not the case for an asymmetric pupil amplitude as it also generates a real electric field due to odd pupil amplitude (second row of Table 2.1). This real electric field interferes with the aberration's real electric field and thus enables the sign determination. The electric field of an asymmetric pupil is shown in the bottom row of Figure 2.3 a. More examples of pupil-plane phase retrieval with focal-plane images can be found in subsection 2.7.1.

This is the working principle of the Asymmetric Pupil Fourier Wavefront Sensor (Martinache, 2013). Interestingly, other focal-plane wavefront sensing methods such as the differential Optical Transfer Function (Codona & Doble, 2012) and Self-Coherent Camera (Baudoz et al. 2005) also rely on pupil asymmetries, even though they use other reconstruction algorithms. Classical phase diversity techniques (Gonsalves 1982; Paxman et al. 1992) come to a similar result by introducing a known even phase aberration (e.g., defocus; odd phase modes can never be used; see top row of Figure 2.3 b). This is the only other way of probing the real part of the focal-plane electric field (Table 2.1). Therefore, all these methods can now be understood as one family that probes the real focal-plane electric field by manipulating either pupil-plane phase or the pupil-plane amplitude. In the context of FPWFS with the vAPP, it is undesirable to use an even pupil-plane phase to break the sign ambiguity because it fills up the dark-hole of the coronagraph and therefore prevents simultaneous science observations and wavefront measurements. On the other hand, vAPPs can be designed for pupils with an amplitude asymmetry, this will be shown in the next subsection, and therefore can combine science observations and wavefront sensing. This result also applies to other FPWFS techniques; for example, it affects spatial LDFC (see subsection 2.7.2).

2.2.2 vAPP design for phase retrieval

Our framework of describing how pupil-plane phase and amplitude symmetries map to the focal-plane electric field also helps us understand some of the aspects of APP design and the requirements for turning an APP into an FPWFS. The optimization method that guarantees optimal APP designs, which are phase-only solutions, is detailed in Por (2017) and is not discussed here. The APPs considered in this section are all designed to have a one-sided D-shaped dark hole from $1.8 \lambda/D$ to $10 \lambda/D$ with a raw contrast of $< 10^{-5}$. The dark hole is defined as the area in the focal plane where the raw contrast meets the requirement.

Let us suppose that we want to design an APP with a one-sided dark hole (= PSF with odd symmetry) for a symmetric aperture (A_{even}). Such an aperture will yield a completely imaginary focal-plane electric field with even symmetry (top row of Figure 2.3). As the APP manipulates phase, this imaginary electric field needs to be cancelled on one side us-

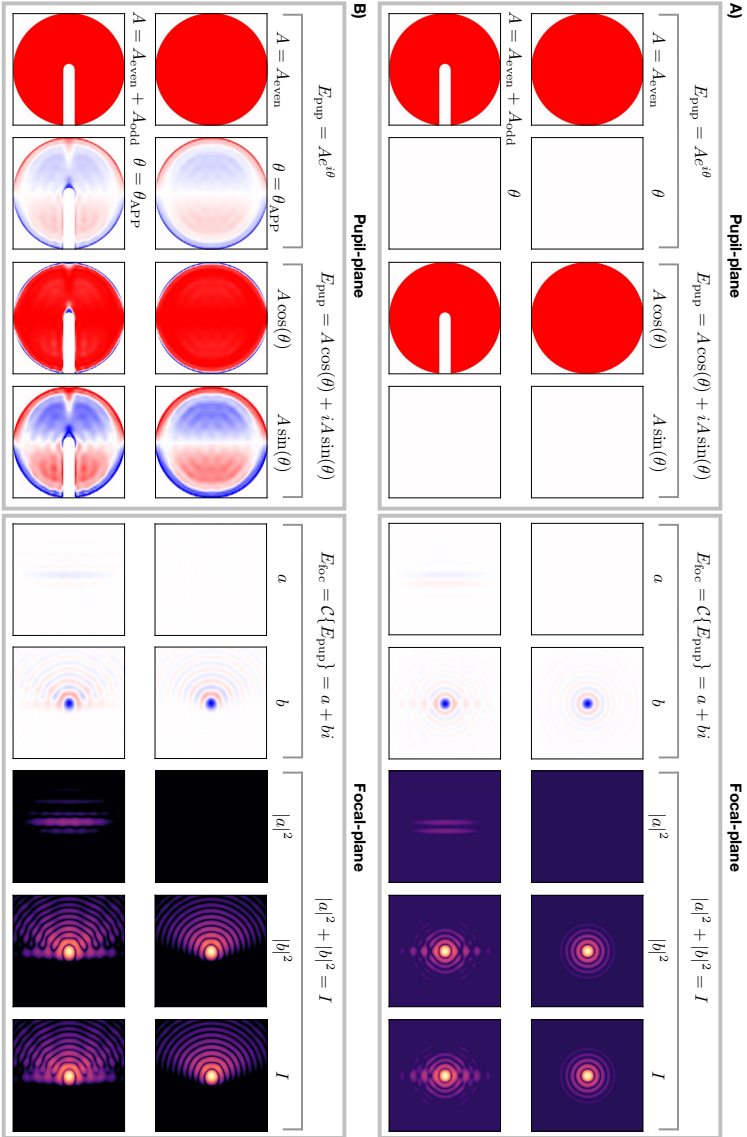


Figure 2.3: Focal- and pupil-plane quantities for (a) a symmetric and asymmetric pupil, and (b) vAPPs designed for these pupils. The columns in the pupil-plane box show (from left to right) the amplitude, phase, and real and imaginary electric fields. In the focal-plane box the columns show the real and imaginary electric fields, the power in the real and imaginary electric fields, and the total power.

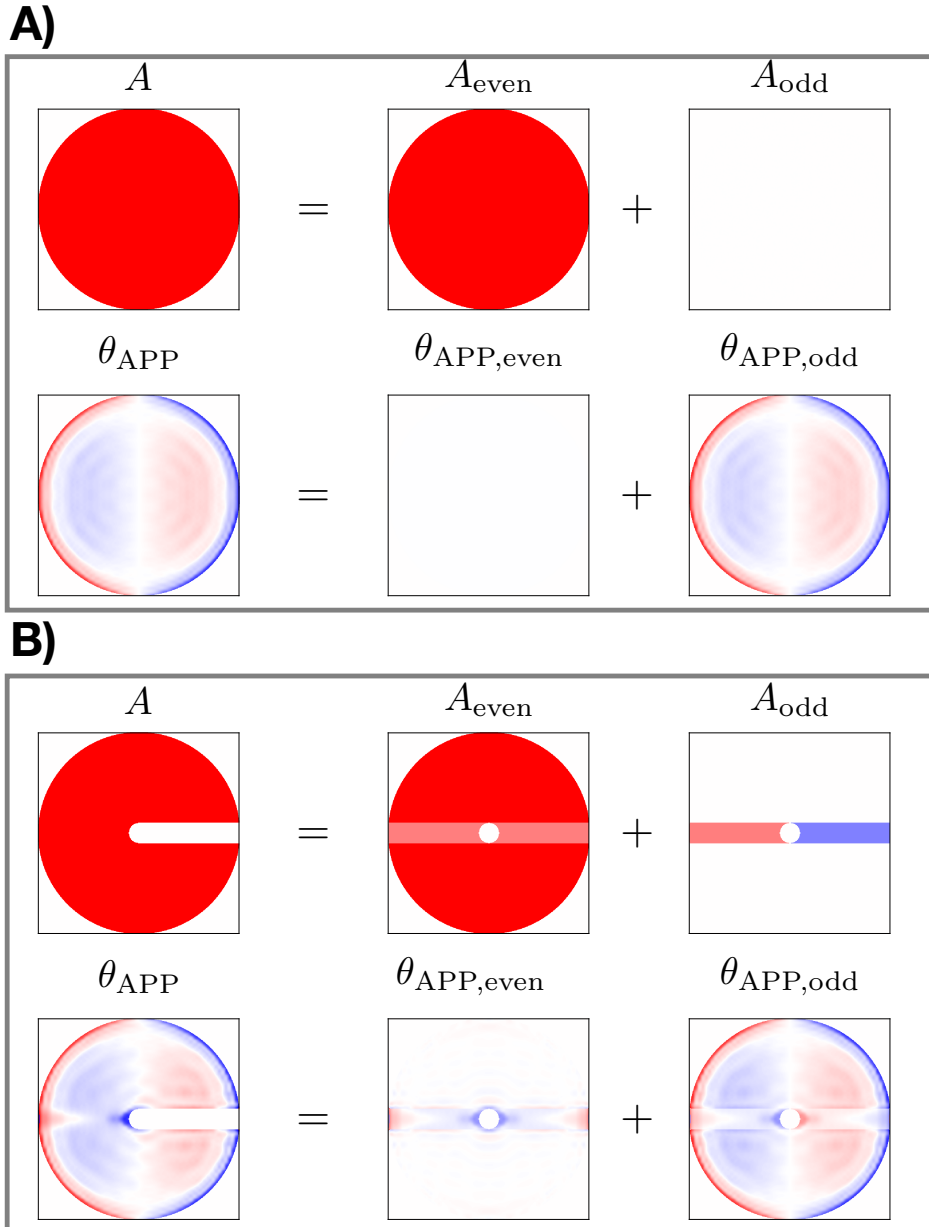


Figure 2.4: Decomposition of the pupil-plane phase and amplitude into their even and odd constituents for the two APP designs in Figure 2.3 b. (a) An APP designed for a symmetric aperture. (b) An APP designed for an asymmetric aperture.

ing pupil-plane phase. The last row of Table 2.1 indicates that the only way of removing an odd part of the imaginary focal-plane electric field (ib) for an even aperture (A_{even}) is by introducing a purely odd pupil-plane phase. This indeed results from the optimization method (top row of Figure 2.3 b, and Figure 2.4 a).

An asymmetric aperture (bottom row of Figure 2.3 a) yields a focal-plane electric field with real and imaginary components. The asymmetric aperture consists of a central obscuration that is 10% of the aperture diameter and a bar with the same width that connects the central obscuration with the edge of the aperture. Cancelling the focal-plane electric field on one side to create the dark hole requires an odd pupil phase to cancel the imaginary focal-plane electric field (last row of Table 2.1), and an even pupil-plane phase for the real part (third row of Table 2.1). Again, this is the solution the optimization method comes up with (see bottom rows of Figure 2.3 b and Figure 2.4 b). Crucially for FPWFS with the APP, the real focal-plane electric field originating from the odd pupil amplitude component cannot be completely removed by the even pupil-plane phase, but is enhanced on the bright side of the APP coronagraphic PSF, as shown in the bottom row of Figure 2.3 b.

To summarize, FPWFS capabilities of the vAPP are fundamentally enabled by the pupil amplitude asymmetry. This asymmetry introduces a real focal-plane electric field that interferes with the even pupil-plane phase aberrations and enables their sign determination. The vAPP allows for simultaneous science observations by removing the real electric field from the dark hole and moving it to the bright field (see subsection 2.7.1 for figures that demonstrate this).

2.3 Aberration estimation algorithm

2.3.1 Maximum a posteriori estimation

We developed an algorithm that gives a maximum a posteriori estimation of the phase aberrations by maximizing the posterior likelihood $p(\alpha, N_p, N_b, \nu, L|D)$. It takes into account a physical, non-linear model of the vAPP (shown in the next subsection), noise statistics, and prior knowledge of the estimated parameters. Given an image D the algorithm estimates α , a vector containing the amplitudes of the phase aberration modes of interest. There is the option to additionally estimate the following parameters: the number of source photons in the image N_p , the background level N_b , the fractional degree of circular polarization ν , and the fractional strength of the leakage PSF integrated over the spectral band L . These parameters are summarized in Table 2.2. The estimation of the phase aberrations is more conveniently performed by minimizing $\mathcal{L}(\alpha, N_p, N_b, \nu, L|D)$, which is the negative logarithm of the likelihood function ($\mathcal{L}(\alpha, N_p, N_b, \nu, L|D) = -\ln[p(\alpha, N_p, N_b, \nu, L|D)]$):

$$\hat{\alpha}, \hat{N}_p, \hat{N}_b, \hat{\nu}, \hat{L} = \arg \min_{\alpha, N_p, N_b, \nu, L} \mathcal{L}(\alpha, N_p, N_b, \nu, L|D). \quad (2.19)$$

Parameters of \mathcal{L} that have been estimated are denoted with a hat. The objective function \mathcal{L} is given by

$$\mathcal{L}(\alpha, N_p, N_b, \nu, L|D) = \sum_x \frac{1}{2\sigma_n^2} (D - M(\alpha, N_p, N_b, \nu, L))^2 + \mathcal{R}(\alpha), \quad (2.20)$$

with $D(x)$ the 2D image containing the data and $M(\alpha, N_p, N_b, \nu, L)$ the 2D model of the vAPP PSF, which is discussed in the next subsection. The algorithm fits the model to the entire image and thus does not exclude any regions in $D(x)$. The sum over x is over all spatial pixels. The algorithm is applied to long-exposure images that have high photon numbers, which can be approximated to contribute spatially changing Gaussian noise (σ_p^2), and detector noise (σ_d^2), assumed to be white Gaussian noise. Therefore, the total noise is Gaussian and the variance is the sum of variances of the two independent processes ($\sigma_n^2 = \sigma_p^2 + \sigma_d^2$). Prior information on the phase aberrations is taken into account explicitly by adding a term $\mathcal{R}(\alpha)$ to the objective function, which is given by

$$\mathcal{R}(\alpha) = \frac{1}{2} \sum_{k=1}^N \frac{\alpha_k^2}{k^\gamma}, \quad (2.21)$$

with α_k the modal coefficients and γ the assumed power spectrum. This term penalizes high spatial frequency modes according to assumptions on or measurements of the spatial power spectrum. Implicitly, we also regularize by using a truncated mode basis.

We minimize \mathcal{L} using the bounded limited-memory Broyden-Fletcher-Goldfarb-Shanno algorithm (L-BFGS-B; Byrd et al. 1995), which is a quasi-Newton optimization algorithm that assumes a differentiable scalar objective function. The algorithm accepts analytically calculated gradients to increase the speed and accuracy. The analytical expressions of the gradients of Equation 2.20 are given in subsection 2.7.3. The algorithm also requires a start position for the estimated parameters. Generally, N_p, N_b, ν , and L can be easily estimated from the data, as is shown in section 6.3. From experience, setting $\alpha = 0$ (i.e., no aberration) works best when there is no initial guess available for the aberrated wavefront.

2.3.2 Coronagraph model

The vAPP is a half-wave retarder with a spatially varying fast-axis; these spatial variations induce geometric phase on the circular polarization states. Opposite circular polarizations receive the opposite phase, creating two similar but mirror-imaged coronagraphic PSFs (see Figure 2.1). Additionally, as the optic is not perfectly half-wave, part of the light does not receive the desired phase and creates an extra non-coronagraphic PSF; we refer to this PSF as the leakage. The relative intensity of the coronagraphic PSFs depends on the fractional degree of circular polarization ν (normalized to the total intensity) and the amount of leakage. In the model we assume a single point source and therefore the image plane is given by

$$M(\alpha, N_p, N_b, \nu, L) = N_p \left(\sum_{j=1}^3 a_j(\nu, L) I_{\text{foc},j}(\alpha) \right) + N_b, \quad (2.22)$$

Table 2.2: Parameters presented in section 2.3.

Variable	Description
α	Vector containing the modal coefficients α_i .
$\hat{\alpha}$	Estimation of α by algorithm.
γ	Assumed power spectrum in the regularization term.
θ_j	Pupil-plane phase of PSF j (aberration + vAPP).
θ_{APP}	Pupil-plane phase of the vAPP.
σ_d^2	Variance of detector noise.
σ_n^2	Total noise variance ($\sigma_n^2 = \sigma_p^2 + \sigma_d^2$).
σ_p^2	Variance of photon noise.
ϕ_i	Pupil-plane phase of aberration mode i .
a_j	Relative intensity PSF j , see Equations (2.23) to (2.25).
A	Pupil-plane amplitude.
$C\{\cdot\}$	Fraunhofer propagator (Goodman, 2005).
E_{pup}	Pupil-plane electric field.
D	Image used for wavefront sensing.
$I_{\text{foc},j}$	PSF j , see Equation 7.11.
L	Fractional strength of leakage PSF.
\hat{L}	Estimation of L by algorithm.
\mathcal{L}	Objective function, see Equation 2.20.
M	PSF model of vAPP, see Equation 2.22.
N_p	Total number of photons in image.
\hat{N}_p	Estimation of N_p by algorithm.
N_b	Background level in image.
\hat{N}_b	Estimation of N_b by algorithm.
\mathcal{R}	Regularization term, see Equation 2.21.
ν	Fractional degree of circular polarization.
$\hat{\nu}$	Estimation of ν by algorithm.

with N_p the total number of photons in the image, N_b the background level (sky background, dark current, or bias), $I_{\text{foc},j}$ the image from either left- ($j=1$) or right-handed ($j=2$) circular polarization or from leakage ($j=3$). The $a_j(v, L)$ terms describe the relative intensities of these PSFs and are given by

$$a_1(v, L) = \frac{1+v}{2}(1-L), \quad (2.23)$$

$$a_2(v, L) = \frac{1-v}{2}(1-L), \quad (2.24)$$

$$a_3(v, L) = L. \quad (2.25)$$

The PSFs are normalized such that the sum over all pixels in the image is one: $\sum_r I_{\text{foc},j} = 1$. We note that we can incoherently add the leakage term and the coronagraphic PSFs because orthogonal polarization states emitted by blackbody sources are incoherent, even when they are transformed to the same polarization state (Fresnel-Arago laws; Kanseri et al. 2008; Mujat et al. 2004). The $I_{\text{foc},j}$ is given by

$$I_{\text{foc},j}(\alpha) = |C\{E_{\text{pup}}(\alpha)\}|^2 \quad (2.26)$$

$$= |C\{Ae^{i(\theta_j + \sum_i \alpha_i \phi_i)}\}|^2, \quad (2.27)$$

with A the amplitude of the aperture, $\theta_j = \pm\theta_{\text{app}}$ for $j = 1, 2$ and $\theta_j = 0$ for $j = 3$. The phase aberration is expanded in the mode basis $\{\phi_i\}$, with α_i being the estimated coefficients. This last equation shows the non-linearity of the model: 1) we estimate phase, which is contained in the complex exponent, and 2) the estimation is performed on intensity images, which are the square of the electric field.

2.4 Simulations

In this section we explore the performance of the algorithm in idealized circumstances by numerical simulations. Performance will be reported in absolute units (nm) in the context of the SCEXAO vAPP and in relative units (fractional λ) to allow comparison with other methods.

The design of the SCEXAO vAPP is detailed in Doelman et al. (2017); here we only discuss the most relevant details. The D-shaped dark holes have a raw contrast of 10^{-5} with respect to the peak flux of the coronagraphic PSF and extend from 2 to 11 λ/D . In addition to the two coronagraphic PSFs and the central leakage PSF, two more phase diversity PSFs were added. These PSFs have opposite defocus aberration and can be used for classical phase diversity, but are not considered in this work. The top row of Figure 2.5 shows the pupil-plane amplitude for which the vAPP was designed, the subsequent phase design, and the focal-plane intensity. As detailed in the bottom row of the figure, there is a clear amplitude asymmetry due to the blocking of dead deformable mirror (DM) actuators. This odd amplitude component A_{odd} , combined with the even phase θ_{even} that cancels the effect of the asymmetry in the dark holes, results in the real focal-plane electric field that is used to probe even pupil-plane phase aberrations. Approximately 3.5 % of the focal-plane power is in the real electric field, and is therefore available to sense

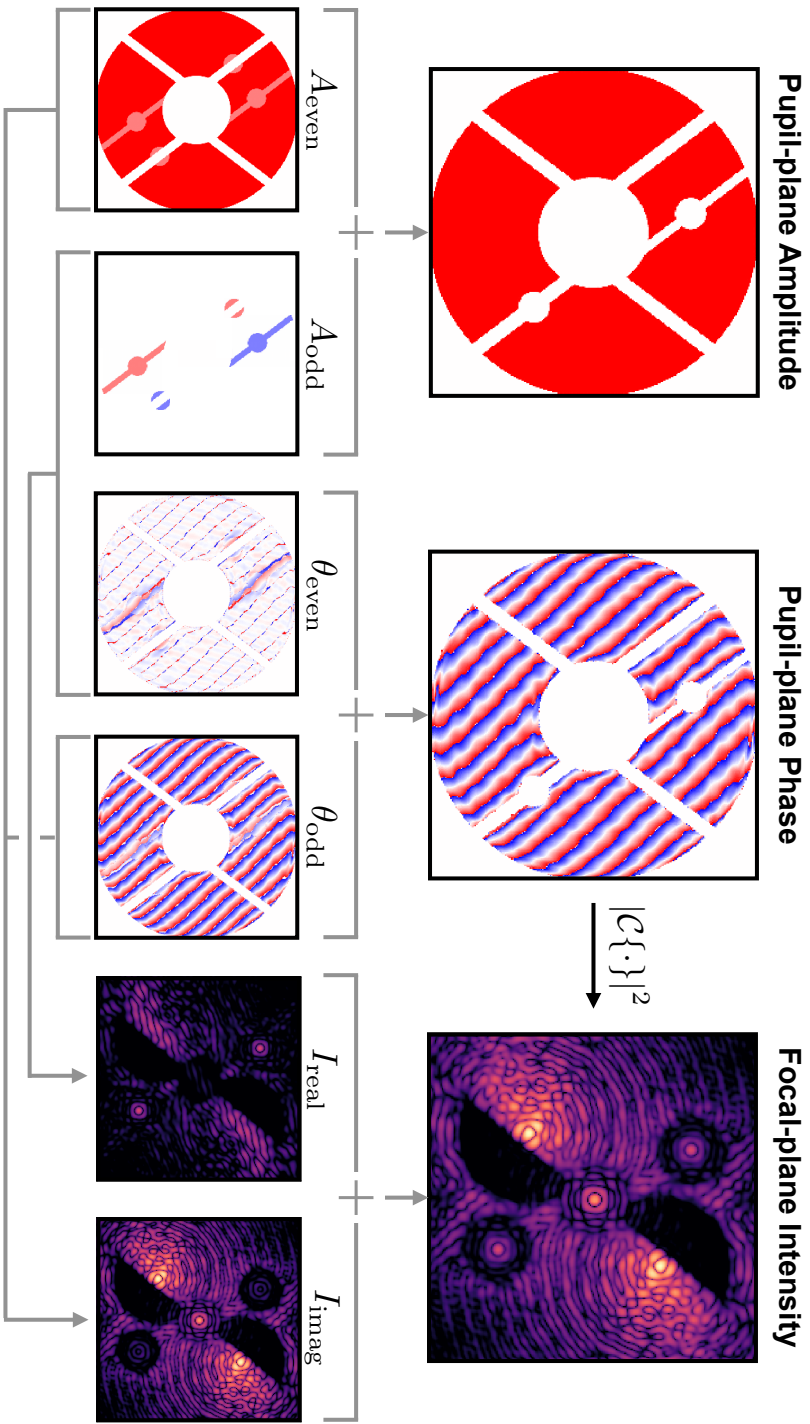


Figure 2.5: Amplitude and phase design of the SCEXAO vAPP (Doelman et al., 2017) and its resulting PSF. The pupil-plane quantities are decomposed into their even and odd constituents, while the focal-plane PSF is decomposed into the power in the real and imaginary parts of the electric field.

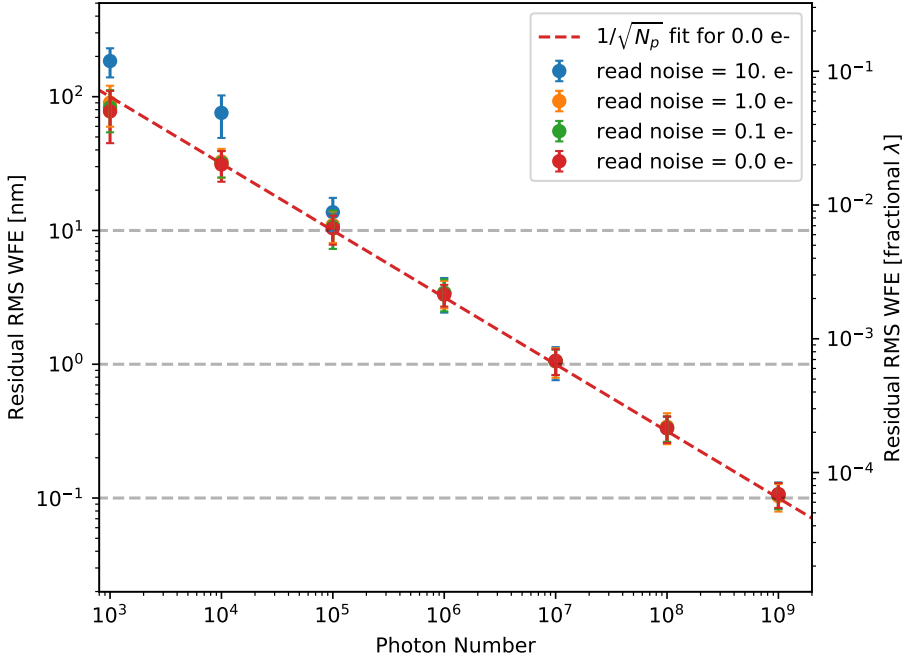


Figure 2.6: Residual RMS WFE as a function of photon number N_p for the SCExAO vAPP. Different colors denote various read noise levels. The dotted line shows a $1/\sqrt{N_p}$ fit to the pure photon noise case. The RMS WFE in nm assumes $\lambda = 1550$ nm.

even phase aberrations.

Simulations are performed with the HCIPy package (Por et al., 2018), an open-source software for high-contrast imaging simulations that is available on GitHub¹. The simulations are monochromatic ($\lambda=1550$ nm). They sample the pupil-plane with 256×256 pixels and use the Fraunhofer approximation to propagate the electric field to the focal plane, which is sampled with 150×150 pixels for 3 pixels per λ/D . The aberration estimation algorithm is Python-based, uses the HCIPy package for the coronagraph model and the Scipy library (Jones et al., 2014) to minimize the objective function.

2.4.1 Photon and read noise sensitivity

Figure 2.6 presents the sensitivity of the algorithm and the SCExAO vAPP when considering varying levels of photon and read noise. The modal basis set used for these tests consists of the first 30 Zernike modes, starting at defocus. All induced aberrations were a linear sum of these modes. The aberrated phase screen is created by first calculating a phase screen following a spatial power spectrum with a slope of -2.5. This slope is steeper

¹<https://github.com/ehpor/hcipy>

than a slope of -2, usually considered for the power spectrum of NCPA, but was chosen to put more power in the low-order modes as we focus on measuring them. Subsequently, this phase screen is projected onto the 30 Zernike modes, which were added together and scaled to a $\sim \lambda/16$ (100 nm) root mean square (RMS) wavefront error (WFE). The algorithm estimated the same Zernike modes as were used to generate the phase screen. For every photon number N_p ($10^3 - 10^9$ photons) we generated ten different phase screens and, for each phase screen, ten photon noise realizations. Furthermore, four levels of read noise were tested: $0 e^-$, $0.1 e^-$, $1 e^-$, and $10 e^-$. The results of the simulations are plotted in Figure 2.6, where the dots denote the mean RMS WFE per photon number and read noise level, and the error bars denote the 1σ deviation. The dotted line is a fit of a $\propto 1/\sqrt{N_p}$ function to the pure photon noise simulations, confirming that the performance scales with the photon noise. The algorithm therefore is photon noise limited (i.e., no algorithmic effects limit the performance). For the photon-limited case, a $< \lambda/1000$ residual RMS WFE is reached with 10^7 photons. In the context of the SCEXAO system (section 6.3) this would be a 1 nm residual WFE for a ~ 5 second integration on a $m_H = 8$ star. The simulations also show that increasing the read noise to $0.1 e^-$ or $1 e^-$ does not significantly impact the performance of the algorithm (i.e., the error is still dominated by photon noise). For a read noise level of $10 e^-$ and photon numbers $< 10^6$, the read noise starts to dominate the error and decreases the performance by a factor of $\sim 2 - 3$.

2

2.4.2 Mode photon noise sensitivity

In Guyon (2005) the photon noise sensitivity β_p of a WFS to a single mode m is defined as

$$\beta_p = \sigma_m \sqrt{N_p}, \quad (2.28)$$

with σ_m the reconstruction error for mode m and N_p the number of photons in the image. According to Guyon (2005), the ideal WFS will have $\beta_p = 1$ for all reconstructed modes. Here we explore the sensitivity of the SCEXAO vAPP to the first 100 Zernike modes (starting with defocus as the vAPP is tip/tilt insensitive), expecting that the vAPP has a lower sensitivity (resulting in a higher β_p) for the even modes than for the odd modes (see discussion in section 7.2). The reconstruction error σ_m was determined by calculating the standard deviation of the $\hat{\alpha}_m$ distribution, obtained after simulating 100 different photon noise realizations per photon number (10^7 , 10^8 , and 10^9) and estimating only $\hat{\alpha}_m$ (no other modes were estimated simultaneously). This resulted in three β_p values (one for each tested photon number), which were subsequently averaged to obtain the final result. The results are shown in Figure 2.7, with the ideal WFS ($\beta_p = 1$) shown as the horizontal gray dotted line. The gray boxes denote the even modes, and the white boxes the odd modes. The first thing to note is that the even modes perform a factor $\sim 4 - 10$ worse than the odd modes. This occurs because, as discussed in section 7.2, the real part of the focal-plane electric field probes the even modes, and in the case of the SCEXAO vAPP is relatively weak: $\sim 3.5\%$ of the total power is in the real electric field. Therefore, it is expected that β_p is $\sqrt{1/0.035} = 5.3$ times higher for even modes compared to the odd modes, which is approximately observed. Furthermore, it should be noted that the spatial frequency content of the Zernike modes increases with the Noll index. Therefore, due to lower S/N at higher frequencies, sensitivity to both even and odd modes decreases with

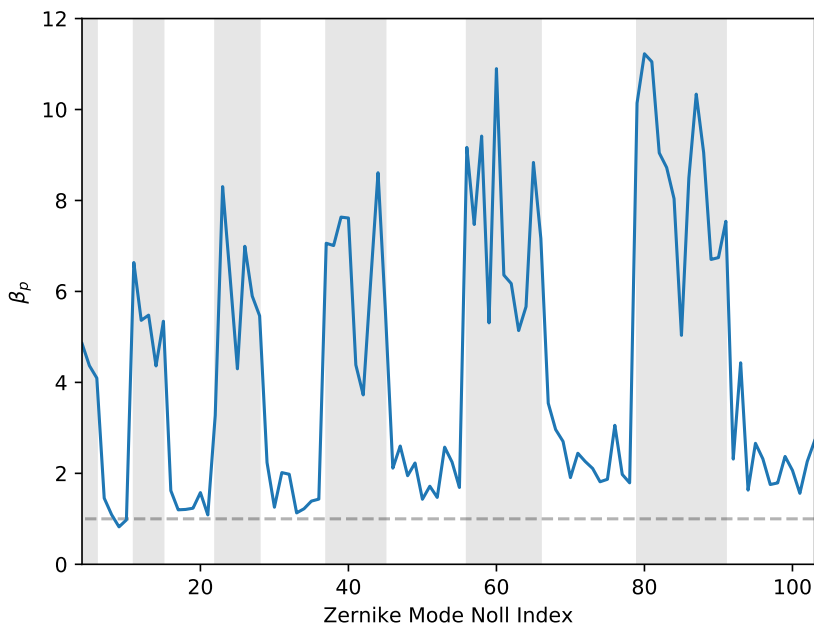


Figure 2.7: Photon noise sensitivity of the SCEXAO vAPP to the first 100 Zernike modes, starting at defocus. The gray boxes denote the even Zernike modes, and the white boxes the odd Zernike modes.

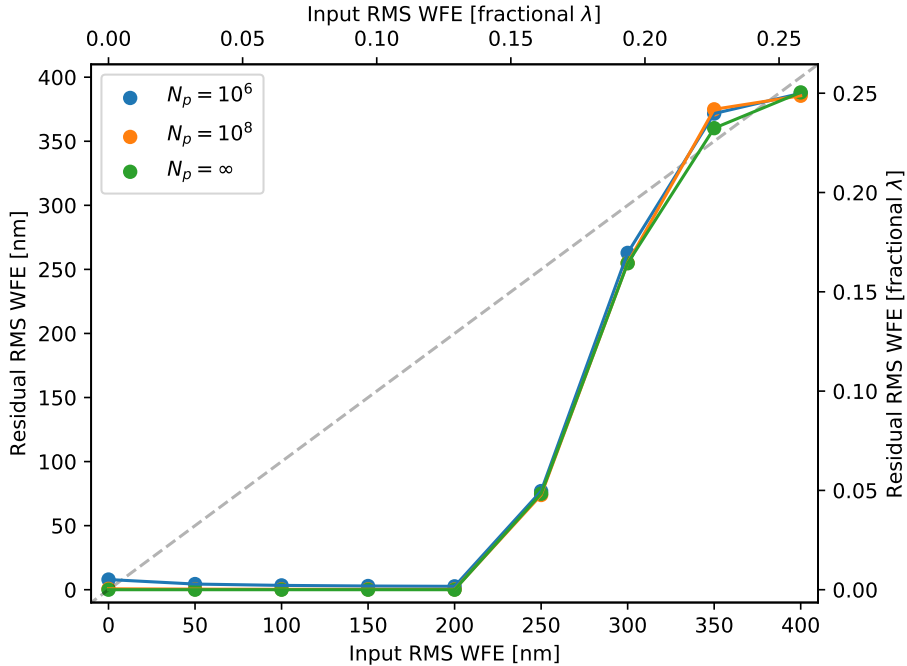


Figure 2.8: Residual RMS WFE as function of introduced RMS WFE for the SCExAO vAPP. The colors denote various photon numbers. The dashed, gray line separates the regions where the wavefront improves or deteriorates. The wavelength is 1550 nm.

increasing mode number. The sensitivity to even modes decreases faster than the odd mode sensitivity because the real part of the focal-plane electric field is limited in extent compared to the imaginary part (shown in Figure 2.5). We note that this analysis does not include any cross-talk effects, which are taken into account in the next section.

2.4.3 Dynamic range algorithm

Here we explore the maximum RMS WFE for which the algorithm can accurately recover estimates for each modal coefficient in a single step. This limitation is mainly driven by modal cross-talk and determines the WFE for which the algorithm can converge to a low ($\sim \lambda/1000 - \lambda/100$ or 1-10 nm) residual RMS WFE in one iteration, assuming that the estimation is perfectly applied by the DM. We simulated phase screens consisting of 30 Zernike modes (starting with defocus), following a spatial power spectrum with a -2.5 slope, with increasing WFE. For RMS WFE values between 0 and $\sim \lambda/4$ (400 nm) we simulated ten wavefronts, with either no photon noise ($N_p = \infty$) or high photon numbers ($N_p = 10^6, 10^8$). For the simulations with photon noise, we simulated ten photon-noise realizations per phase screen. The algorithm estimated the same Zernike modes. The

residual RMS WFE was determined by subtracting the estimation from the initial, aberrated wavefront. The mean residual RMS WFEs are shown in Figure 2.8. The performance of the algorithm does not significantly vary between the different photon number realizations. The algorithm converges in one iteration with an input aberration RMS of up to $\sim \lambda/8$ or 200 nm. For WFE between $\lambda/8$ - $\lambda/5$ (200-300 nm), the algorithm still improves the wavefront, but there is significant residual WFE after one iteration. In this regime the algorithm converges to $< \lambda/1000$ or 1 nm RMS WFE within two or three iterations in closed-loop operation. A WFE larger than $\lambda/5$ (300 nm) RMS does not significantly improve after one iteration. We note that this performance is very similar to the non-coronagraphic results reported by Martinache et al. (2016) for the Asymmetric Pupil Fourier Wavefront Sensor.

2.5 Demonstration at SCExAO

2.5.1 SCExAO

The Subaru Coronagraphic Extreme Adaptive Optics (SCExAO) instrument (Jovanovic et al., 2015) is a high-contrast imaging instrument at the Subaru Telescope. It operates downstream of the AO188 system (Minowa et al., 2010), which gives an initial low-order correction. SCExAO drives a 2000-actuator DM based on wavefront measurements from a pyramid wavefront sensor (PYWFS) from the optical to near-IR (NIR) (in the range 600-900 nm) that can run at 3.5 kHz, but most often runs at 2 kHz. There are 45 actuators across the pupil, giving the system the ability to correct out to $22.5\lambda/D$. The real-time control of SCExAO is handled by the compute and control for adaptive optics (cacao) package (Guyon et al., 2018). Cacao allows NCPA corrections to be handled by a separate DM channel, where the software automatically sends offsets to the PYWFS. These offsets ensure that the PYWFS does not sense and attempt to control the NCPA corrections. The instrument routinely achieves Strehl ratios $> 80\%$ in the H band on-sky. SCExAO feeds the post-AO JHK bands to the integral field spectrograph CHARIS (Peters-Limbach et al. 2013; Groff et al. 2014). The ultimate goal is to operate the vAPP FPWFS with the CHARIS data; however, the tests were performed with the internal NIR camera for ease of operation. The NIR camera has recently (Lozi et al., 2018) been upgraded to a C-RED 2 detector (Feautrier et al., 2017), which has a 640×512 pixel InGaAs sensor that is cooled to -40°C .

2.5.2 Algorithm implementation in SCExAO

The algorithm has to be adapted to the SCExAO parameters and the vAPP design. To calibrate the model of the vAPP we had to take into account the following:

1. **Pupil undersizing:** To account for pupil misalignments the design of the vAPP was undersized by 1.5% (Doelman et al., 2017) with respect to the nominal SCExAO pupil.
2. **Pupil rotation:** To optimally block dead actuators in the DM, the SCExAO pupil was rotated by -6.25° , affecting the orientation of the PSF on the detector.

3. **Detector pixel scale:** For accurate propagation to the focal plane of the NIR camera, the pixel scale was determined manually (which was deemed sufficient for low-order Zernike mode measurement and correction) to be 15.6 mas per pixel at 1550 nm.

The coronagraph model described in section 2.3 assumes a monochromatic light source, and the closest available option, in terms of bandwidth, for the NIR camera in SCEXAO is the $\Delta\lambda = 25$ nm filter centered around $\lambda = 1550$ nm. For this filter, a 128×128 pixel sub-window in the NIR internal camera is sufficient to contain the vAPP PSFs. The image fed to the algorithm consists of the sum of 1000 unsaturated images (either of the internal source or the star; individual exposure times are on the order of 1-10 milliseconds) that are dark-subtracted, aligned with a reference PSF generated with the coronagraph model and subsequently stacked and calibrated for the camera system gain ($2.33 \text{ e}^-/\text{ADU}$; Feautrier et al. 2017). The large number of stacked images should generally bring the algorithm into the 1 nm residual RMS WFE regime (Figure 2.6) in ideal circumstances and is the best performance we can expect. After image acquisition and before running the algorithm, the parameters N_p , N_b , v , and L have to be estimated. N_b is estimated first by selecting the corners in the image where there is no light from the vAPP. N_p is estimated by subtracting N_b from the image and summing the values in all pixels. The grating in the vAPP acts as a circularly polarized beam-splitter, thus v is determined by aperture photometry on the two coronagraphic PSFs. From these intensity measurements, I_1 and I_2 , the fractional degree of circular polarization can be determined by

$$v = \frac{I_1 - I_2}{I_1 + I_2}. \quad (2.29)$$

The amount of leakage L is similarly calculated by aperture photometry on the two coronagraphic (I_1 and I_2) and the leakage PSFs (I_3):

$$L = \frac{I_3}{I_1 + I_2 + I_3}. \quad (2.30)$$

After this initial estimation, the estimation of these parameters can also be improved by the algorithm. This is generally not done for N_b , v , and L as it has not been found to improve the wavefront estimation. On the other hand, we find that estimating N_p using the algorithm does improve the estimation. Another concern is that estimating some of these parameters could induce cross-talk with the aberration coefficients. An example of such cross-talk would be between the wavefront aberration coma and v , as both parameters result in relative brightness changes between the two coronagraphic PSFs. Therefore, the algorithm could tune either parameter to fit a relative brightness change and arrive at the wrong result. We did not extensively study the effects of this cross-talk.

The closed-loop correction is performed by phase conjugation, where the DM command $\theta_{\text{DM},i}$ at iteration i is calculated as

$$\theta_{\text{DM},i} = \theta_{\text{DM},i-1} - \frac{g}{2} \sum_j \alpha_j \phi_j, \quad (2.31)$$

with g the closed-loop gain that can be freely chosen, the factor $\frac{1}{2}$ to account for the reflective nature of the DM, α_j the estimated modal coefficients, and $\{\phi_j\}$ the mode basis.

When estimating 30 Zernike modes with the SCExAO implementation of the algorithm, the computation time per iteration is $\sim 30 - 50$ seconds. Generally, the convergence time increases when sensing more modes and larger wavefront errors. The convergence time is mainly limited by the Python library versions installed at SCExAO, and more fundamentally by the implementation in Python.

2.5.3 Internal source demonstration

We performed FPWFS tests with the SCExAO vAPP using the internal source in November and December 2018. The goal was to demonstrate the principle of FPWFS with the vAPP coronagraphic PSFs, and we therefore focused on measuring and correcting low-order modes (30-50 Zernike modes, starting with defocus). Figure 2.9 shows these results, where the 1σ raw contrast was determined by calculating the standard deviation of $1 \lambda/D$ wide annuli covering both PSFs that were normalized by the maximum number of counts in the image. The top row in the figure presents the pre- and post-correction PSFs and the radial averaged contrast improvements (panels a, b, and c, respectively) for the nominal SCExAO system using 30 Zernike modes, after one iteration with the algorithm ($g = 1$). The estimated wavefront is shown in Figure 2.10 a, and the measured WFE in the 30 Zernike modes is ~ 100 nm RMS. The dominant mode is astigmatism at ~ 86 nm RMS. The next three largest aberrations were coma, quadrafoil, and secondary astigmatism at respectively ~ 28 nm, ~ 24 nm, and ~ 23 nm RMS. Qualitatively, the wavefront improvement can be observed in the more symmetric leakage and phase diversity PSFs, and the dark hole better defined as an aberrated structure at a few λ/D was removed. Quantitatively, the peak flux of the leakage increased by $\sim 10\%$, and the raw contrast at $2.5 \lambda/D$ improved from $\sim 2 \cdot 10^{-3}$ to $\sim 6 \cdot 10^{-4}$ (solid lines in Figure 2.9 c). Only the lowest Zernike modes (both even and odd) were corrected, which is clearly visible as the contrast improvement decreases with λ/D . The dash-dotted lines in Figure 2.9 c show the results of a similar correction performed at another moment in time, but here the images used for the raw contrast determination were saturated such that the raw contrast was speckle-noise limited, instead of read noise limited as with the solid lines. The bottom row shows the result of a closed-loop correction where we introduced and estimated a 300 nm RMS WFE with 50 Zernike modes, which should be correctable according to Figure 2.8. Panels b and c show the pre- and post-correction after five iterations of closed-loop correction. The total duration of these corrections was around 4 minutes. These figures show that the algorithm can correct large WFE, recovering a PSF that is qualitatively very similar to what is shown in Figure 2.9 b. As shown in Figure 2.9 f, we recover similar or deeper raw contrasts compared to the nominal system after correction, Figure 2.9 c. In Figure 2.10 b and c, the introduced and estimated wavefronts are shown. The WFE for these figures are respectively ~ 293 nm and ~ 311 nm. We note that the estimated wavefront also includes WFE already present in the system before adding the known aberration, as this was not corrected before the test. Tests conducted on another day suggest that the remaining WFE after correction is on the order of ~ 59 nm RMS. These tests consist of sequential measurements of the nominal wavefront and a 150 nm RMS introduced wavefront error. These measurements were then compared to find a residual WFE. This error consists of evolved NCPA between measurements, DM calibration errors, and algorithm errors. We

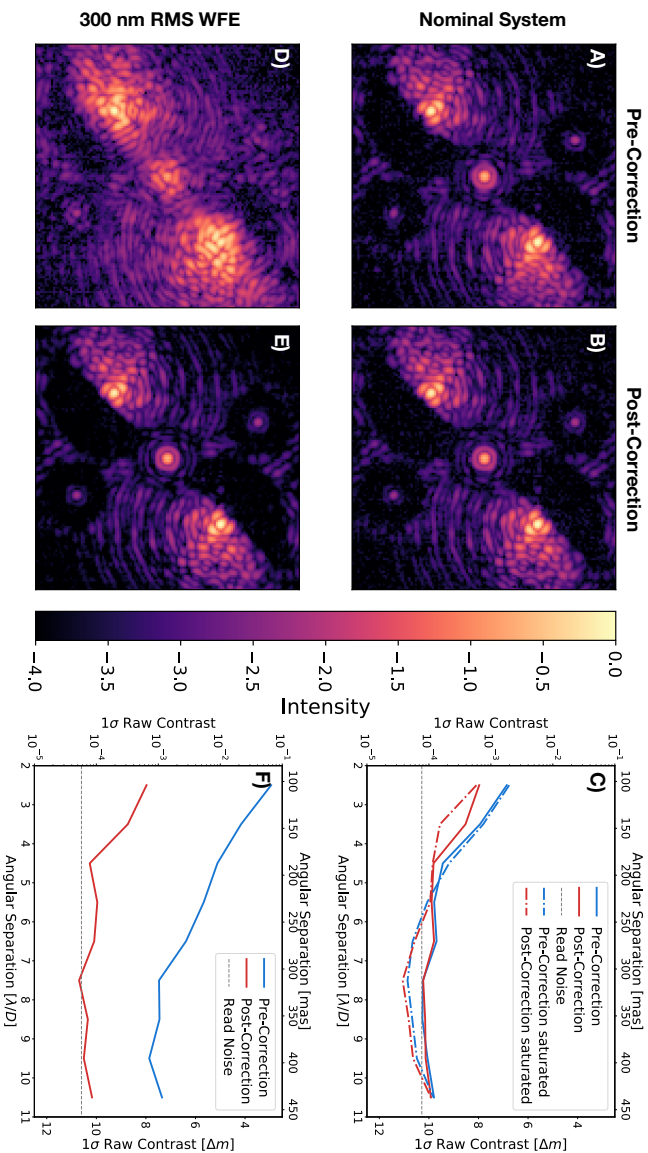


Figure 2.9: Focal-plane images and 1σ raw contrast curves pre- and post-correction with the internal source within SCExAO. (a) Pre- and (b) post-correction images for the nominal SCExAO system. (c) The 1σ raw contrast curves for the correction of the nominal system. The solid lines relate to panels (a) and (b) and are read noise limited beyond $7.5 \lambda/D$, which is shown by the horizontal dashed line. The dot-dashed lines show a similar correction performed at a different time. For these lines the images for raw contrast determination were saturated such that they were speckle noise limited (instead of read noise limited), reaching deeper contrasts in the dark holes. (d) Pre- and (e) post-correction images for an introduced waveform of 300 nm RMS. (f) The 1σ raw contrast curves for the correction of the system with the introduced 300 nm RMS waveform, with again the horizontal dashed line denoting the read noise.

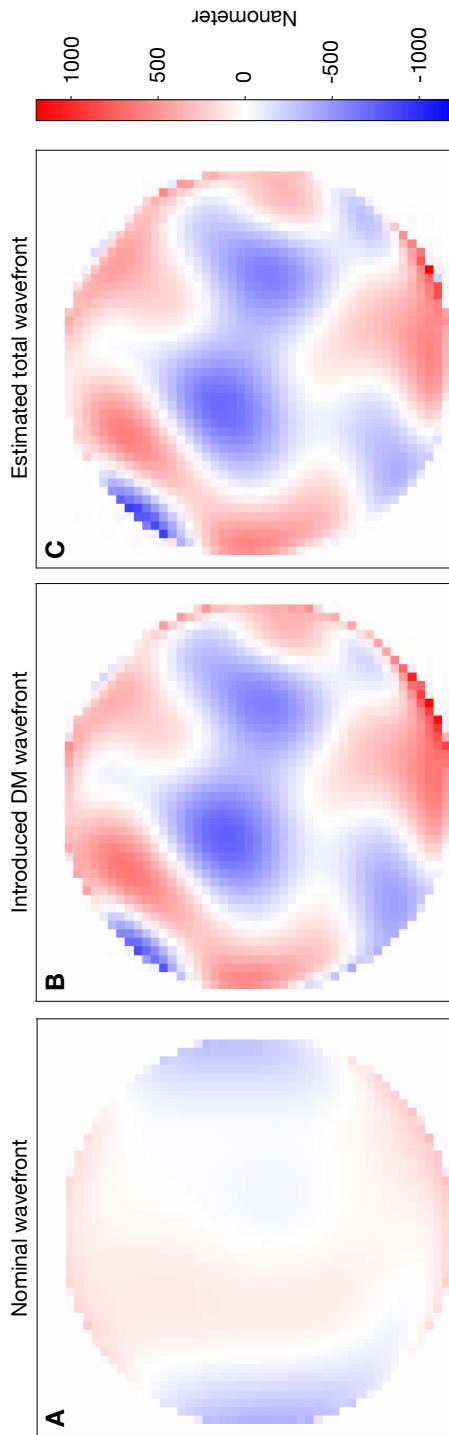


Figure 2.10: (a) Estimated wavefront of the nominal SCExAO system using the internal source and reconstructed by combining the estimated modal coefficients of the 30 Zernike modes. The estimated WFE is ~ 100 nm RMS. (b) Introduced and (c) estimated wavefront from closed-loop tests with the internal source. The introduced wavefront (b), consisting of 50 Zernike modes, has a RMS WFE of ~ 293 nm. The estimated wavefront (c), using the same 50 Zernike modes, with an RMS WFE of ~ 311 nm. The estimated wavefront also includes other WFE already present in the system.

did not investigate the amplitude of the individual error terms.

2.5.4 On-sky demonstration

On 11 January 2019 we observed Regulus ($m_H = 1.57$; Ducati 2002) during a SCE_xAO engineering night to test the vAPP FPWFS on-sky, to evaluate the performance with an incoherent background due to residual turbulence and long exposure images, and to demonstrate the true end-to-end optical system. Observing conditions were good (the seeing was $\sim 0.2'' - 0.4''$) and predictive control was running during the tests (Guyon & Males, 2017). We conducted tests similar to those with the internal source. The top row of Figure 2.11 shows the results after five iterations of closed-loop with a gain=0.5 with the nominal SCE_xAO system when estimating 30 Zernike modes. The five iterations took approximately 4 minutes. Qualitatively, the first Airy ring of the leakage PSF becomes more rounded and symmetric, the coronagraphic PSFs are more similar, the edge of the dark hole becomes better defined, and some speckles in the dark hole are removed. The gain in peak flux of the leakage PSF is 6%. In Figure 2.11 c the contrast gain is moderate, improving by a factor ~ 2 between 2.5 and 4 λ/D . The estimated wavefront is shown in Figure 2.12 a and the WFE is ~ 187 nm RMS. A notable structure in this estimated wavefront is the sharp increase in phase at the edges of the pupil. It is thought that this phase ring is a relatively static and real structure that originates from the upstream AO188 system; the PYWFS reference offset contains a similar structure as well. The bottom row shows the correction of low-order quasi-static errors from the instrument on-sky plus and additional 150 nm RMS WFE that was added to the DM consisting of 30 Zernike modes. After five iterations (gain = 0.5), shown in Figure 2.11 e, the algorithm recovers a similar PSF in a time similar to that for the correction of the nominal system (Figure 2.11 c), both in morphology and in achieved raw contrast (see Figure 2.11 f). In Figure 2.12 b-d the introduced, estimated, and residual wavefronts are shown, with the WFE being respectively ~ 146 nm, ~ 244 nm, and ~ 78 nm RMS. The residual wavefront was determined by subtracting the introduced and initial wavefronts from the estimated wavefront. This gives an estimate of the remaining wavefront error in the system. As discussed with the internal source results, the residual wavefront consists of evolved NCPA between measurements, DM calibration errors and algorithm errors. We note that the reported raw contrasts in Figure 2.11 c and f are worse than in Figure 2.9 c and f due to the incoherent speckle background created by the uncorrected residual atmospheric wavefront errors.

2.6 Discussion and conclusion

We showed in section 7.2 that an asymmetry in the pupil amplitude enables the vAPP coronagraphic PSFs to measure both even and odd pupil phase modes, generalizing the Asymmetric Pupil Fourier Wavefront Sensor (APF-WFS; Martinache 2013) with spatial Linear Dark Field Control (LDFC; Miller et al. 2017) in the vAPP. The physical model for non-linear wavefront estimation developed in section 2.3 was tested in idealized simulations (section 7.3), confirming that the vAPP currently installed at SCE_xAO can sense the even modes, but is more sensitive to odd modes. Simulations suggest that the algo-

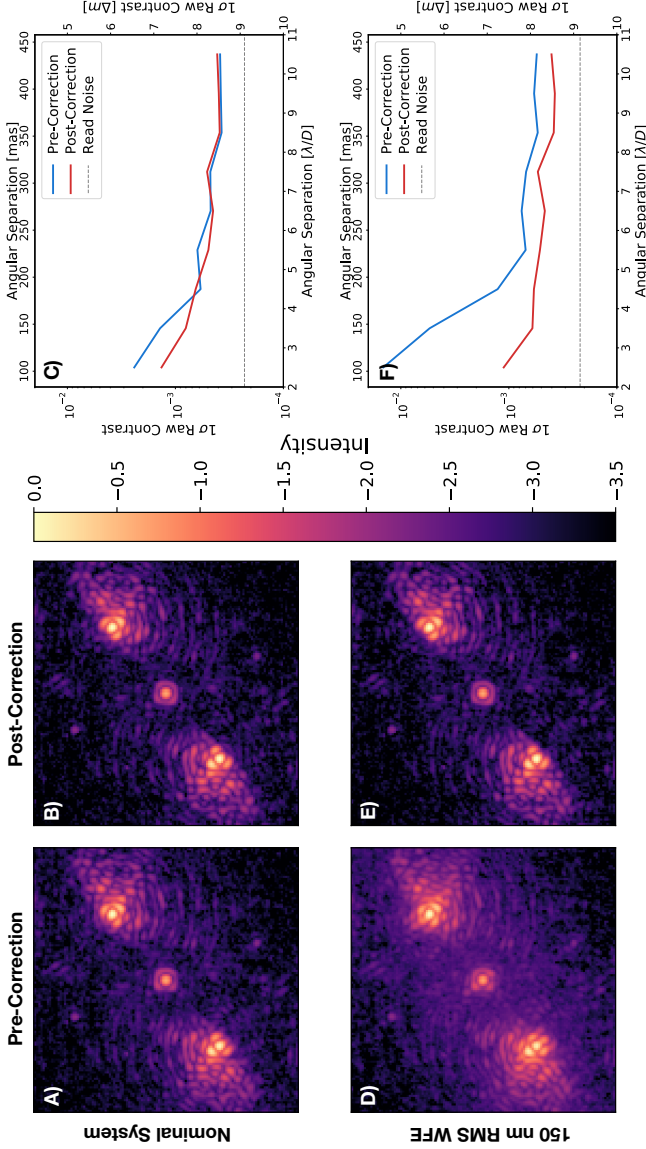


Figure 2.11: Focal-plane images and 1σ raw contrast curves pre- and post-correction during on-sky observations. (a) Pre- and (b) post-correction images for the nominal SExAO system. (c) The 1σ raw contrast curves for the correction of the nominal system. The horizontal dashed line denotes the read noise level. (d) Pre- and (e) post-correction images for an additional wavefront error of 150 nm RMS. (f) The 1σ raw contrast curves for the correction of the system with the additional 150 nm RMS wavefront error, with again the horizontal dashed line denoting the read noise.

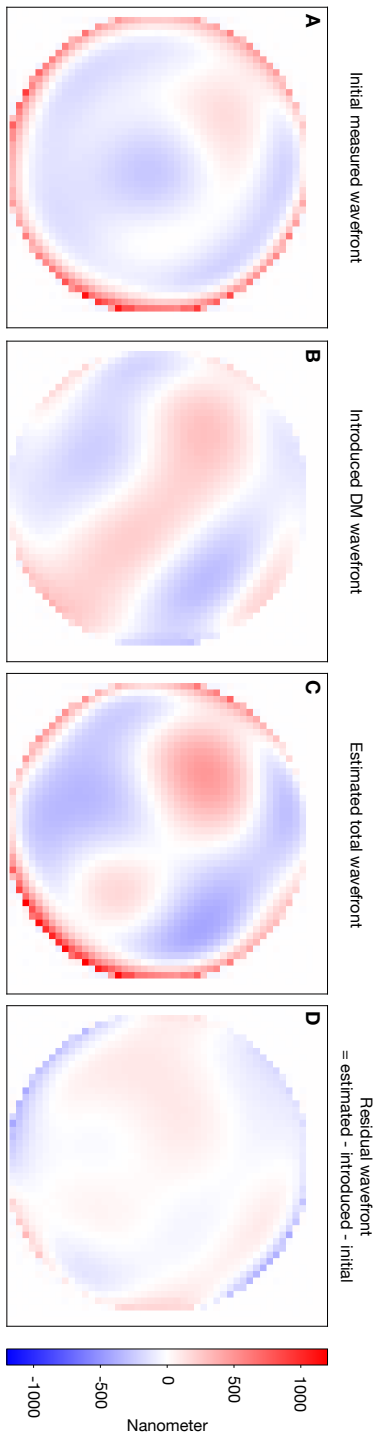


Figure 2.12: (a) Estimated wavefront of the nominal SCEXAO system during on-sky observations and reconstructed by combining the estimated modal coefficients of the 30 Zernike modes. The estimated WFE is ~ 187 nm RMS. The (b) introduced, (c) estimated, and (d) residual wavefront from closed-loop tests during on-sky observations. (b) The introduced wavefront, consisting of 30 Zernike modes, with an RMS WFE of ~ 146 nm. (c) The estimated wavefront, using the same 30 Zernike modes, with an RMS WFE of ~ 244 nm. (d) The residual wavefront (introduced minus estimated and nominal wavefronts); the RMS WFE is ~ 78 nm.

gorithm should be able to reach one-shot correction resulting in a $< \lambda/1000$ nm RMS WFE with approximately 10^7 photons, and that with one iteration it should be able to correct up to $\sim \lambda/8$ of RMS WFE. In section 6.3, we demonstrated the principle with the vAPP in SCEXAO, both with the internal source and on-sky, by measuring and controlling the 30 lowest Zernike modes and improving the raw contrast between 2.5 and $4 \lambda/D$ by a factor ~ 2 . Furthermore, we showed that the algorithm can correct WFEs of 300 nm and 150 nm RMS with the internal source and on-sky, respectively. Although the contrast gains, both with the internal source and on-sky, are moderate, it does demonstrate that the coronagraphic PSFs of the vAPP can be used for wavefront sensing.

The FPWFS performance of the SCEXAO vAPP can be improved in various ways: 1) better model calibration to increase the contrast gain, 2) measuring more and higher spatial frequency modes to increase the area of correction, and 3) improving the convergence speed of the algorithm. For this demonstration the model was calibrated ad hoc by tuning the pupil undersizing, rotation, and the detector pixel scale by hand. These parameters should be more accurately measured or be part of the fitted parameters. To measure more and higher spatial frequency modes we want to replace the current Zernike mode basis with a pixel-mode basis (Paul et al., 2013a). This should also reduce the effect of unsensed modes on the estimation, when estimating a truncated mode basis (Paul et al., 2013b). Improving the convergence speed of the algorithm would result in a higher correction cadence or the correction of a larger mode basis in a similar time. A relatively simple improvement would be to use the multi-processing capabilities in the latest python libraries not yet available on SCEXAO, this would enable multi-core processing and give a maximum speed improvement of a factor of 40. Theoretically, the best possible performance we can then expect is a wavefront estimation with sub 1 nm WFE every six seconds for targets down to a $m_H = 8$ (five seconds of integration and one second for estimation). Other coronagraph model improvements include the integral field spectrograph CHARIS, an accurate model of the focal-plane filter and the incoherent background due to residual turbulence effects. This is because science observations with the SCEXAO vAPP are done with CHARIS. Preventing detector saturation due to bright fields of the vAPP requires a focal-plane neutral density filter that attenuates the bright fields. Therefore, exposures with the focal-plane filter in place will have a larger dynamic range. This increase in dynamic range will make the incoherent background, which is due to uncorrected atmospheric turbulence, a more prominent feature in the image compared to the current on-sky results. Thus, the incoherent background needs to be included within the coronagraph model as well (Herscovici-Schiller et al., 2017), also including any asymmetries in this background (Cantalloube et al., 2018).

In this article we focused on a FPWFS based on a grating-vAPP. We operated it only in narrowband mode or in an integral field spectrograph. Therefore, the FPWFS algorithm does not have to operate over broad wavelength ranges and the current coronagraph model would suffice. However, there are broadband imaging vAPP implementations foreseen, as is detailed in Bos et al. (2018). These coronagraphs are more complicated in their optical design and therefore require a more advanced coronagraph model. For such broadband coronagraphs, the coronagraph model also needs to be extended to handle broadband FPWFS to take full advantage of the coronagraph. This can be done by evaluating the model at multiple wavelengths (Seldin et al., 2000) and would come at an increased computa-

tional cost. Operating in broadband mode would increase the sensitivity as there is more light available, but speckles at larger λ/D would be washed out and therefore higher frequency aberrations would be harder to measure.

In this paper we discussed only FPWFS for vAPPs that generate asymmetric dark holes. But FPWFS with pupil-plane coronagraphs that create symmetric dark holes such as the 360° vAPP (Otten et al., 2014) and the shaped pupil (Kasdin et al., 2007) are desirable as well. Optimal designs of vAPPs with symmetric dark holes consist of only 0 and π phase structures (Por, 2017). This results in a purely real pupil-plane electric field (Equation 2.2), and thus if the aperture is symmetric the focal-plane electric field of such a vAPP will be completely imaginary (Table 2.1) and will not support a FPWFS. Therefore, similar to one-sided dark holes, FPWFSing is enabled when an amplitude asymmetry is introduced. A similar argument can be given for shaped pupil coronagraphs, as these manipulate pupil-plane amplitude and thus only have a real pupil-plane electric field. A more important difference with one-sided dark hole PSFs is that such coronagraphs will not have a bright field in the other polarization that covers the dark hole of the coronagraph and thus does not directly probe the region of interest.

Future work will investigate optimization of the aperture asymmetry to enhance the wavefront sensing capabilities of the coronagraph. This also has implications for the APF-WFS and spatial LDFC controlling dark holes dug with other methods than the vAPP. With the current implementation of the vAPP and algorithm we can only sense phase aberrations. Uncorrected amplitude errors due to the atmosphere and instrumental errors will limit the raw contrast to $\sim 10^{-5}$ (Guyon, 2018). This is at a level that is not yet reached by the vAPP, and therefore only sensing phase aberrations is sufficient for now. When this raw contrast is met it would be necessary to sense both pupil amplitude and phase aberrations. It is expected that the two coronagraphic PSFs alone do not contain sufficient diversity to estimate both in one image. For the current SCEXAO vAPP design, an additional classical phase diversity image will likely provide the required diversity to enable amplitude estimation (Herscovici-Schiller et al., 2018), but will lower the science duty cycle. A better solution for future FPWFS vAPPs would be the addition of two strong phase diversity holograms, which would keep the science duty cycle at 100% at the cost of science throughput. Another use of FPWFS with the vAPP could be the fine co-phasing of multi-mirror telescopes from the image plane (Pope et al., 2014), such as for the upcoming Giant Magellan Telescope.

Integration of FPWFS with coronagraphy is a crucial step in the system wide integration of all optical modalities (e.g., spectroscopy and polarimetry) to get the best possible performance of high-contrast imaging instruments. The major advantages are that NCPA can be measured up to the science focal plane and a 100% science duty cycle as science observations do not have to be interrupted to probe the dark hole. The vAPP has now shown that it is able to combine both FPWFS and coronagraphy in one optic.

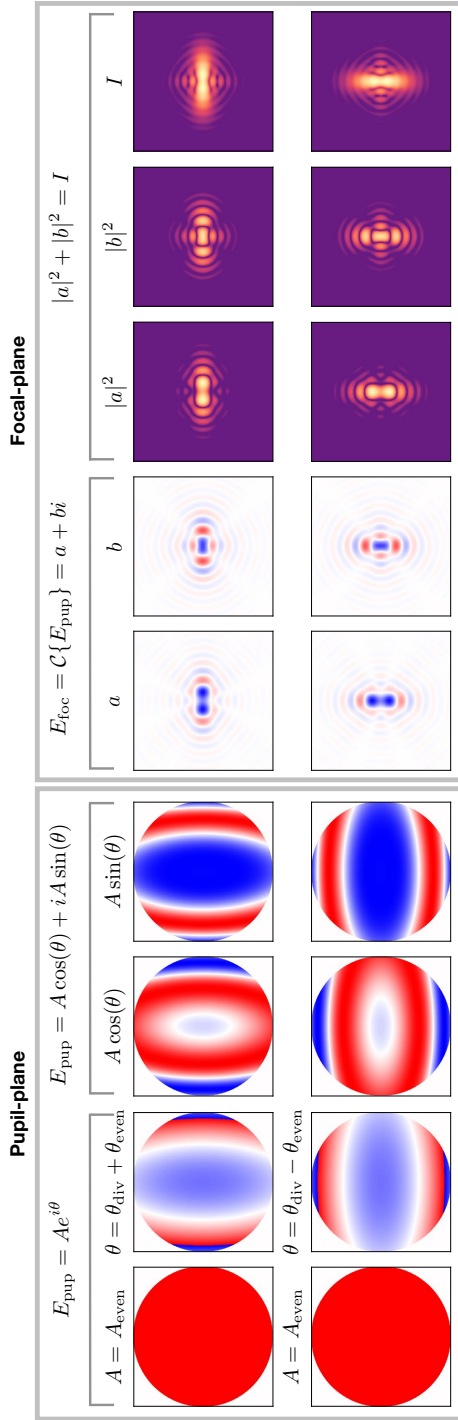


Figure 2.13: Focal- and pupil-plane quantities for a static diversity phase (defocus) with an even phase aberration (astigmatism) that has an alternating sign between the rows. The columns in the pupil-plane box show (from left to right) the amplitude, phase, and real and imaginary electric fields. In the focal-plane box, the columns show the real and imaginary electric fields, the power in the real and imaginary electric fields, and the total power.

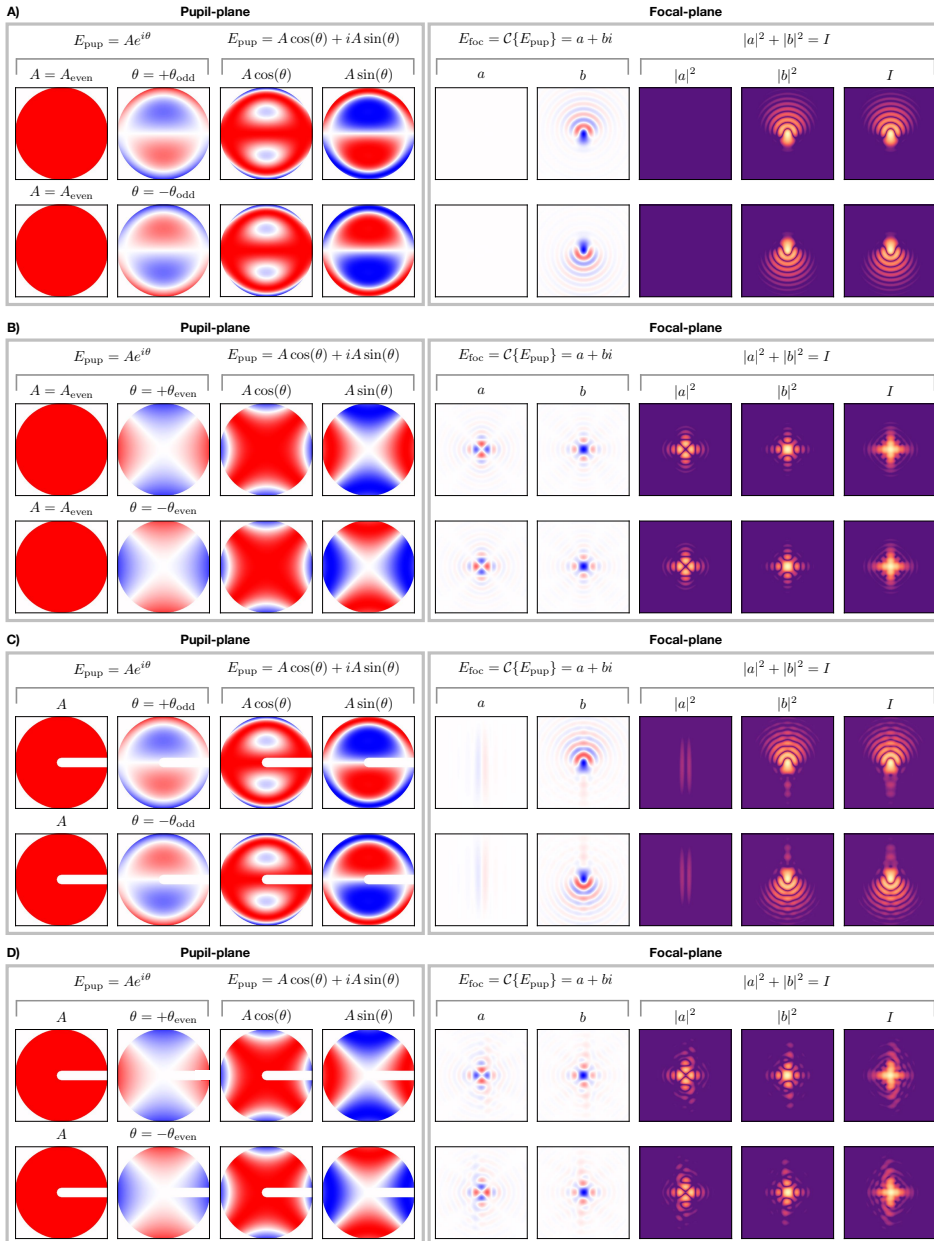


Figure 2.14: Focal- and pupil-plane quantities for different combinations of pupil symmetries and phase aberrations with alternating signs. (a) Symmetric aperture with odd aberration coma. (b) Symmetric aperture with even aberration astigmatism. (c) Asymmetric aperture with odd aberration coma. (d) Asymmetric aperture with even aberration astigmatism. The columns in the pupil-plane box show (from left to right) the amplitude, phase, and the real and imaginary electric fields. In the focal-plane box the columns show the real and imaginary electric fields, the power in the real and imaginary electric fields, and the total power.

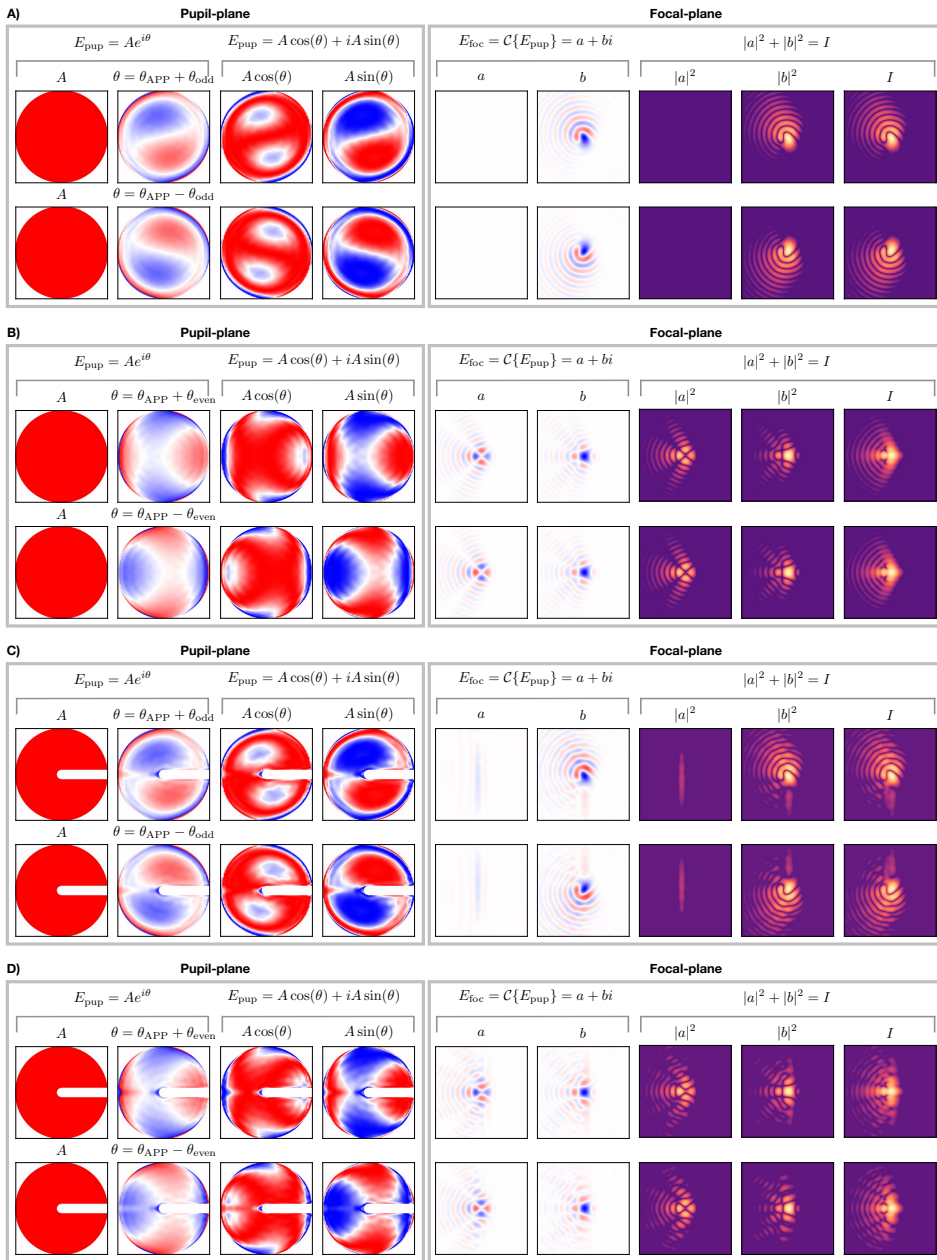


Figure 2.15: Focal- and pupil-plane quantities for APPs designed for different pupil symmetries subjected to phase aberrations with alternating sign. (a) Symmetric aperture with odd aberration coma. (b) Symmetric aperture with even aberration astigmatism. (c) Asymmetric aperture with odd aberration coma. (d) Asymmetric aperture with even aberration astigmatism. The columns in the pupil-plane box show (from left to right) the amplitude, phase, and real and imaginary electric fields. In the focal-plane box, the columns show the real and imaginary electric fields, the power in the real and imaginary electric fields, and the total power.

2.7 Appendix

2.7.1 Phase retrieval examples

In section 7.2 we explained how the sign of even phase aberrations can be retrieved using an asymmetric pupil amplitude. In this appendix we give a more complete set of examples of how pupil symmetries, and APPs designed for them, respond to even and odd aberrations.

In the top row of Figure 2.14 a we visually present Equations (2.1) to (2.7) for an even aperture ($A = A_{\text{even}}$) and the odd coma aberration ($\theta = \theta_{\text{odd}}$). The real part of the pupil-plane electric field, $A \cos(\theta)$, is completely even and contains no sign information due to $\cos(-\theta) = \cos(\theta)$; the imaginary part, $iA \sin(\theta)$, is completely odd. Therefore, propagation to the focal plane will result in a fully imaginary electric field ib (see Table 2.1) that has even and odd components. The bottom row of Figure 2.14 a shows the same images but for a flipped sign of the phase ($\theta = -\theta_{\text{odd}}$), equivalent to conjugating the pupil-plane electric field. Thus the phase conjugation results in a flipped PSF, and due to the odd component of E_{foc} , it results in a morphological change that can be measured, which is clearly visible in Figure 2.14 a.

Figure 2.14 b shows similar figures, but for the even astigmatism aberration ($\theta = \theta_{\text{even}}$) and again, the top and bottom rows show opposite signs of the aberration. As expected, both the real and imaginary parts of the pupil-plane electric field, $A \cos(\theta)$ and $iA \sin(\theta)$, are even. Again, the sign information is encoded in the imaginary pupil electric field term $iA \sin(\theta)$. This term propagates, in contrast to the odd phase aberration, to the real part of the focal-plane electric field a . Therefore, all sign information of the even phase aberration is encoded in the real focal-plane electric field. Because the aberration is even, this does not result in morphological changes in the total intensity measurement I_{foc} , and thus sign information of the even aberration cannot be measured.

This well-known sign ambiguity (Gonsalves 1982; Paxman et al. 1992) is often broken by introducing a static, known diversity phase that results in a known real focal-plane electric field. This real electric field can interfere with the sign information carrying real electric fields resulting from the even phase aberrations, which enables unique intensity changes for sign changes. Figure 2.13 shows the case of defocus as a static phase diversity and the even astigmatism aberration used in Figure 2.13. It shows a significant morphology change in both the real and imaginary focal-plane power $|a|^2$ and $|b|^2$ that can be used to determine sign changes.

In section 7.2 we explained how the Asymmetric Pupil Fourier Wavefront Sensor (Martinache, 2013) breaks the sign ambiguity in a similar way using odd pupil amplitude. In Figure 2.14 c the response of an asymmetric aperture to sign changes in odd phase aberrations is shown. It shows that, as expected, the ability of measuring odd phase modes is not affected. Figure 2.14 d has an even phase aberration, again the top and bottom rows differ in the sign. In contrast to Figure 2.14 b, the PSF for an asymmetric aperture does show a morphological change when the sign of the even aberration changes, and therefore allows the retrieval of the complete pupil-plane phase.

Now we show that wavefront sensing with APPs will give similar results. In Fig-

ure 2.15 a and b the focal-plane intensity responses are shown to an odd and even pupil-plane phase aberration for an APP designed for a symmetric aperture. As in Figure 2.14, the APP shows an intensity morphology change for a sign change in the odd phase aberration (Figure 2.15 a), but for a sign change in the even phase aberration there is no intensity morphology change (Figure 2.15 b).

This changes for an APP designed for an asymmetric aperture, as shown in Figure 2.15 c and d. Figure 2.15 d shows the focal-plane intensity response to an odd pupil-plane phase aberration and Figure 2.15 d the response to an even pupil phase aberration. For both phase aberrations there is an intensity morphology change when the sign of the aberration changes.

2.7.2 Implications for spatial LDFC

Above we discussed the principle behind FPWFS in the context of the coronagraphic PSFs of the APP, but the same principle applies to maintaining the contrast in the dark hole, such as electric field conjugation (Groff et al., 2015), speckle nulling (Bordé & Traub, 2006), or spatial Linear Dark Field Control (LDFC; Miller et al. 2017). Spatial LDFC maintains the contrast in the dark hole by monitoring the intensity of the bright field, which can be shown to have a linear response to small phase aberrations. Suppose the focal-plane electric field E_{foc} consists of the nominal electric field in the bright field E_0 disturbed by the electric field of the aberration E_{ab} :

$$E_{\text{foc}} = E_0 + E_{\text{ab}}, \quad (2.32)$$

$$I_{\text{foc}} = |E_{\text{foc}}|^2 \quad (2.33)$$

$$= |E_0|^2 + |E_{\text{ab}}|^2 + 2\Re\{E_0 E_{\text{ab}}^*\}. \quad (2.34)$$

Assuming that $|E_0|^2 \gg |E_{\text{ab}}|^2$, we can write the intensity change ΔI , compared to the reference image $I_0 = |E_0|^2$, due to the aberration as

$$\Delta I = I_{\text{foc}} - I_0 \quad (2.35)$$

$$= 2\Re\{E_0 E_{\text{ab}}^*\} \quad (2.36)$$

Writing the electric fields as their real and imaginary components, $E_0 = a + ib$ and $E_{\text{ab}} = c + id$, shows that in order to have a response to the complete electric field of the aberration, the bright field of the PSF should have real and imaginary components:

$$\Delta I = 2(ac + bd). \quad (2.37)$$

As discussed above, the real component a can be provided by either a known, even phase aberration such as defocus or by an amplitude asymmetry.

In Miller (2018) spatial LDFC was tested, both in simulation and in the lab, with a vAPP designed for an even aperture ($a = 0$). It was indeed observed that the LDFC loop was more stable when the vAPP image was defocused ($a \neq 0$), compared to a focused image ($a = 0$). Therefore, adding a pupil amplitude asymmetry, generating a non-zero a , would allow the LDFC loop to run with a focused vAPP image, having a comparable stability to the defocused image.

2.7.3 Derivatives objective function

The phase estimation is performed by minimizing the objective function \mathcal{L} defined in Equation 2.20. The convergence speed and accuracy of the minimization algorithm are improved when it is provided with the gradients of the parameters it is estimating. For the estimation the phase is expanded on a truncated mode basis $\{\phi_i\}$ with α_i the estimated coefficients, and thus the gradient $\partial\mathcal{L}/\partial\alpha_i$ needs to be derived. In addition to the phase estimation, the algorithm can also estimate the photon number N_p , the background level N_b , the fractional degree of circular polarization ν , and the amount of leakage L . Therefore, the gradients $\partial\mathcal{L}/\partial N_p$, $\partial\mathcal{L}/\partial N_b$, $\partial\mathcal{L}/\partial\nu$, and $\partial\mathcal{L}/\partial L$ also need to be derived.

The gradient of \mathcal{L} to X ($X = \{\alpha_i, N_p, N_b, \nu, L\}$) is given by

$$\frac{\partial\mathcal{L}}{\partial X} = \sum_x \frac{1}{\sigma_n^2} [D - M] \frac{\partial M}{\partial X} + \frac{\partial\mathcal{R}(\alpha)}{\partial X}, \quad (2.38)$$

with M the model of the system given by Equation 2.22. Here the dependency of \mathcal{L} and M on $(\alpha, N_p, N_b, \nu, L)$ is omitted for readability. The term $\mathcal{R}(\alpha)/\partial X$ is only non-zero for $X = \alpha_i$.

We start with the gradient $\partial\mathcal{L}/\partial\alpha_i$; with the first step already shown in Equation 2.38, the derivative of M is

$$\frac{\partial M}{\partial\alpha_i} = N_p \sum_{j=1}^3 a_j(\nu, L) \frac{\partial I_{\text{foc},j}}{\partial\alpha_i}, \quad (2.39)$$

where the sum is over the two coronagraphic PSFs and the non-coronagraphic leakage PSF, and $I_{\text{foc},j}$ is given in Equation 7.11. The derivative $\partial I_{\text{foc},j}(\alpha)/\partial\alpha_i$ is

$$\frac{\partial I_{\text{foc},j}(\alpha)}{\partial\alpha_i} = \frac{\partial E_{\text{foc},j}}{\partial\alpha_i} E_{\text{foc},j}^* + E_{\text{foc},j} \frac{\partial E_{\text{foc},j}^*}{\partial\alpha_i}. \quad (2.40)$$

The partial derivatives to the focal-plane electric field E_{foc} are

$$\begin{aligned} \frac{\partial E_{\text{foc},j}}{\partial\alpha_i} &= \frac{\partial}{\partial\alpha_i} C\{E_{\text{pup},j}(\alpha)\} \\ &= \frac{\partial}{\partial\alpha_i} C\{A e^{i(\theta_j + \sum_k \alpha_k \phi_k)}\} \\ &= C\{A \frac{\partial}{\partial\alpha_i} e^{i(\theta_j + \sum_k \alpha_k \phi_k)}\}, \text{ (Leibniz's integration rule)} \\ &= iC\{A \phi_i e^{i(\theta_j + \sum_k \alpha_k \phi_k)}\}. \end{aligned} \quad (2.41)$$

The partial derivatives to the focal-plane electric field E_{foc}^* is then simply

$$\frac{\partial E_{\text{foc},j}^*}{\partial\alpha_i} = -iC\{A \phi_i e^{i(\theta_j + \sum_k \alpha_k \phi_k)}\}^*. \quad (2.42)$$

Combining these results, we find for $\partial I_{\text{foc},j}(\alpha)/\partial\alpha_i$:

$$\begin{aligned} \frac{\partial I_{\text{foc},j}(\alpha)}{\partial\alpha_i} &= iC\{A \phi_i e^{i(\theta_j + \sum_k \alpha_k \phi_k)}\} C\{A e^{i(\theta_j + \sum_k \alpha_k \phi_k)}\}^* \\ &\quad - iC\{A e^{i(\theta_j + \sum_k \alpha_k \phi_k)}\} C\{A \phi_i e^{i(\theta_j + \sum_k \alpha_k \phi_k)}\}^*. \end{aligned} \quad (2.43)$$

The regularization term $\mathcal{R}(\alpha)$ that we adopted is fairly simple:

$$\mathcal{R}(\alpha) = \frac{1}{2} \sum_{k=1}^N \frac{\alpha_k^2}{k^\gamma}. \quad (2.44)$$

Here γ is a power that matches the known or assumed power-law distribution of the aberrations in the system. The derivative with respect to α_i is given by

$$\frac{\partial \mathcal{R}(\alpha)}{\partial \alpha_i} = \frac{\alpha_i}{i^\gamma}. \quad (2.45)$$

Combining the results in Equation 2.38, Equation 2.39, Equation 2.43, and Equation 2.45 gives the final expression for $\partial \mathcal{L} / \partial \alpha_i$.

Next, the derivatives of M to N_p and N_b are

$$\frac{\partial M}{\partial N_p} = \sum_{j=1}^3 a_j(v, L) I_{\text{foc},j}(\alpha), \quad (2.46)$$

$$\frac{\partial M}{\partial N_b} = 1. \quad (2.47)$$

The derivative of M to the leakage L is

$$\frac{\partial M}{\partial L} = N_p \sum_{j=1}^3 \frac{\partial a_j(v, L)}{\partial L} I_{\text{foc},j}, \quad (2.48)$$

with the derivatives $\partial a_j(v, L) / \partial L$ given by

$$\frac{\partial a_1}{\partial L} = -\frac{1+v}{2}, \quad (2.49)$$

$$\frac{\partial a_2}{\partial L} = \frac{v-1}{2}, \quad (2.50)$$

$$\frac{\partial a_3}{\partial L} = 1. \quad (2.51)$$

Finally, the derivative of M to v is

$$\frac{\partial M}{\partial v} = N_p \sum_{j=1}^3 \frac{\partial a_j(v, L)}{\partial v} I_{\text{foc},j}, \quad (2.52)$$

with the derivatives $\partial a_j(v, L) / \partial v$ given by

$$\frac{\partial a_1}{\partial v} = \frac{1-L}{2}, \quad (2.53)$$

$$\frac{\partial a_2}{\partial v} = \frac{L-1}{2}, \quad (2.54)$$

$$\frac{\partial a_3}{\partial v} = 0. \quad (2.55)$$

Bibliography

- Baudoz, P., Boccaletti, A., Baudrand, J., & Rouan, D. 2005, *Proceedings of the International Astronomical Union*, 1, 553
- Berry, M. V. 1987, *Journal of Modern Optics*, 34, 1401
- Beuzit, J.-L., Vigan, A., Mouillet, D., et al. 2019, arXiv preprint arXiv:1902.04080
- Boehle, A., Glauser, A. M., Kenworthy, M. A., et al. 2018, in *Ground-based and Airborne Instrumentation for Astronomy VII*, Vol. 10702, International Society for Optics and Photonics, 107023Y
- Bordé, P. J., & Traub, W. A. 2006, *The Astrophysical Journal*, 638, 488
- Bos, S. P., Doelman, D. S., de Boer, J., et al. 2018, in *Advances in Optical and Mechanical Technologies for Telescopes and Instrumentation III*, Vol. 10706, International Society for Optics and Photonics, 107065M
- Byrd, R. H., Lu, P., Nocedal, J., & Zhu, C. 1995, *SIAM Journal on Scientific Computing*, 16, 1190
- Cantalloube, F., Por, E., Dohlen, K., et al. 2018, *Astronomy & Astrophysics*, 620, L10
- Close, L. M., Males, J. R., Durney, O., et al. 2018, arXiv preprint arXiv:1807.04311
- Codona, J. L., & Doble, N. 2012, in *Adaptive Optics Systems III*, Vol. 8447, International Society for Optics and Photonics, 84476R
- Côté, O., Allain, G., Brousseau, D., et al. 2018, in *Ground-based and Airborne Instrumentation for Astronomy VII*, Vol. 10702, International Society for Optics and Photonics, 1070248
- Davies, R., Alves, J., Clénet, Y., et al. 2018, in *Ground-based and Airborne Instrumentation for Astronomy VII*, Vol. 10702, International Society for Optics and Photonics, 107021S
- De Kok, R., Stam, D., & Karalidi, T. 2011, *The Astrophysical Journal*, 741, 59
- Doelman, D. S., Auer, F. F., Escuti, M. J., & Snik, F. 2019, *Optics letters*, 44, 17
- Doelman, D. S., Snik, F., Warriner, N. Z., & Escuti, M. J. 2017, in *Techniques and Instrumentation for Detection of Exoplanets VIII*, Vol. 10400, International Society for Optics and Photonics, 104000U
- Ducati, J. 2002, *VizieR Online Data Catalog*, 2237
- Feautrier, P., Gach, J.-L., Greffe, T., et al. 2017, in *Image Sensing Technologies: Materials, Devices, Systems, and Applications IV*, Vol. 10209, International Society for Optics and Photonics, 102090G
- Galicher, R., Baudoz, P., & Rousset, G. 2008, *Astronomy & Astrophysics*, 488, L9
- Gonsalves, R. A. 1982, *Optical Engineering*, 21, 215829
- Goodman, J. W. 2005, *Introduction to Fourier optics* (Roberts and Company Publishers)
- Groff, T. D., Riggs, A. E., Kern, B., & Kasdin, N. J. 2015, *Journal of Astronomical Telescopes, Instruments, and Systems*, 2, 011009
- Groff, T. D., Kasdin, N. J., Limbach, M. A., et al. 2014, in *Ground-based and Airborne Instrumentation for Astronomy V*, Vol. 9147, International Society for Optics and Photonics, 91471W
- Guyon, O. 2005, *The Astrophysical Journal*, 629, 592
- . 2018, *Annual Review of Astronomy and Astrophysics*, 56, 315
- Guyon, O., & Males, J. 2017, arXiv preprint arXiv:1707.00570
- Guyon, O., Miller, K., Males, J., Belikov, R., & Kern, B. 2017, arXiv preprint arXiv:1706.07377
- Guyon, O., Sevin, A., Ltaief, H., et al. 2018, in *Adaptive Optics Systems VI*, Vol. 10703, International Society for Optics and Photonics, 107031E
- Haffert, S., Bohn, A., de Boer, J., et al. 2019, *Nature Astronomy*, 1
- Haffert, S., Wilby, M., Keller, C., et al. 2018, in *Adaptive Optics Systems VI*, Vol. 10703, International Society for Optics and Photonics, 1070323
- Herscovici-Schiller, O., Mugnier, L. M., Baudoz, P., et al. 2018, *Astronomy & Astrophysics*, 614,

A142

- Herscovici-Schiller, O., Mugnier, L. M., & Sauvage, J.-F. 2017, *Monthly Notices of the Royal Astronomical Society: Letters*, 467, L105
- Hoeijmakers, H., Schwarz, H., Snellen, I., et al. 2018, *Astronomy & Astrophysics*, 617, A144
- Jones, E., Oliphant, T., & Peterson, P. 2014
- Jovanovic, N., Martinache, F., Guyon, O., et al. 2015, *Publications of the Astronomical Society of the Pacific*, 127, 890
- Jovanovic, N., Absil, O., Baudoz, P., et al. 2018, in *Proc. SPIE*, Vol. 10703, *Adaptive Optics Systems VI*
- Kanseri, B., Bisht, N. S., Kandpal, H., & Rath, S. 2008, *American Journal of Physics*, 76, 39
- Kasdin, N. J., Vanderbei, R. J., & Belikov, R. 2007, *Comptes Rendus Physique*, 8, 312
- Kenworthy, M. A., Absil, O., Carlomagno, B., et al. 2018, in *Ground-based and Airborne Instrumentation for Astronomy VII*, Vol. 10702, *International Society for Optics and Photonics*, 10702A3
- Lozi, J., Guyon, O., & et al. 2018, in *Adaptive Optics Systems VI*, Vol. 10703, *International Society for Optics and Photonics*
- Macintosh, B., Graham, J. R., Ingraham, P., et al. 2014, *Proceedings of the National Academy of Sciences*, 111, 12661
- Males, J. R., Close, L. M., Miller, K., et al. 2018, in *Adaptive Optics Systems VI*, Vol. 10703, *International Society for Optics and Photonics*, 1070309
- Marois, C., Lafreniere, D., Doyon, R., Macintosh, B., & Nadeau, D. 2006, *The Astrophysical Journal*, 641, 556
- Martinache, F. 2013, *Publications of the Astronomical Society of the Pacific*, 125, 422
- Martinache, F., Jovanovic, N., & Guyon, O. 2016, *Astronomy & Astrophysics*, 593, A33
- Martinez, P., Kasper, M., Costille, A., et al. 2013, *Astronomy & Astrophysics*, 554, A41
- Martinez, P., Loose, C., Carpentier, E. A., & Kasper, M. 2012, *Astronomy & Astrophysics*, 541, A136
- Mazoyer, J., Baudoz, P., Galicher, R., Mas, M., & Rousset, G. 2013, *Astronomy & Astrophysics*, 557, A9
- Miller, K., Guyon, O., & Males, J. 2017, *Journal of Astronomical Telescopes, Instruments, and Systems*, 3, 049002
- Miller, K., Males, J. R., Guyon, O., et al. 2018, in *Adaptive Optics Systems VI*, Vol. 10703, *International Society for Optics and Photonics*, 107031T
- Miller, K. L. 2018, PhD thesis, The University of Arizona
- Minowa, Y., Hayano, Y., Oya, S., et al. 2010, in *Adaptive Optics Systems II*, Vol. 7736, *International Society for Optics and Photonics*, 77363N
- Mujat, M., Dogariu, A., & Wolf, E. 2004, *JOSA A*, 21, 2414
- N'Diaye, M., Dohlen, K., Fusco, T., & Paul, B. 2013, *Astronomy & Astrophysics*, 555, A94
- N'Diaye, M., Martinache, F., Jovanovic, N., et al. 2018, *Astronomy & Astrophysics*, 610, A18
- N'Diaye, M., Vigan, A., Dohlen, K., et al. 2016, in *Adaptive Optics Systems V*, Vol. 9909, *International Society for Optics and Photonics*, 99096S
- Oh, C., & Escuti, M. J. 2008, *Optics letters*, 33, 2287
- Otten, G. P., Snik, F., Kenworthy, M. A., et al. 2014, in *Advances in Optical and Mechanical Technologies for Telescopes and Instrumentation*, Vol. 9151, *International Society for Optics and Photonics*, 91511R
- Otten, G. P., Snik, F., Kenworthy, M. A., et al. 2017, *The Astrophysical Journal*, 834, 175
- Pancharatnam, S. 1956, in *Proceedings of the Indian Academy of Sciences-Section A*, Vol. 44, Springer, 398–417
- Paul, B., Mugnier, L., Sauvage, J.-F., Dohlen, K., & Ferrari, M. 2013a, *Optics Express*, 21, 31751

- Paul, B., Sauvage, J.-F., & Mugnier, L. 2013b, *Astronomy & Astrophysics*, 552, A48
- Paul, B., Sauvage, J.-F., Mugnier, L., et al. 2014, *Astronomy & Astrophysics*, 572, A32
- Paxman, R. G., Schulz, T. J., & Fienup, J. R. 1992, *JOSA A*, 9, 1072
- Peters-Limbach, M. A., Groff, T. D., Kasdin, N. J., et al. 2013, in *Techniques and Instrumentation for Detection of Exoplanets VI*, Vol. 8864, International Society for Optics and Photonics, 88641N
- Pope, B., Cvetojevic, N., Cheetham, A., et al. 2014, *Monthly Notices of the Royal Astronomical Society*, 440, 125
- Por, E. H. 2017, in *Techniques and Instrumentation for Detection of Exoplanets VIII*, Vol. 10400, International Society for Optics and Photonics, 104000V
- Por, E. H., Haffert, S. Y., Radhakrishnan, V. M., et al. 2018, in *Proc. SPIE*, Vol. 10703, Adaptive Optics Systems VI
- Por, E. H., & Keller, C. U. 2016, in *Adaptive Optics Systems V*, Vol. 9909, International Society for Optics and Photonics, 990959
- Ruane, G., Ngo, H., Mawet, D., et al. 2019, *The Astronomical Journal*, 157, 118
- Sauvage, J.-F., Mugnier, L., Paul, B., & Villicroze, R. 2012, *Optics Letters*, 37, 4808
- Seldin, J. H., Paxman, R. G., Zarifis, V. G., Benson, L., & Stone, R. E. 2000, in *Imaging technology and telescopes*, Vol. 4091, International Society for Optics and Photonics, 48–63
- Snik, F., & Keller, C. U. 2013, in *Planets, Stars and Stellar Systems* (Springer), 175–221
- Snik, F., Otten, G., Kenworthy, M., et al. 2012, in *Modern Technologies in Space-and Ground-based Telescopes and Instrumentation II*, Vol. 8450, International Society for Optics and Photonics, 84500M
- Sparks, W. B., & Ford, H. C. 2002, *The Astrophysical Journal*, 578, 543
- Stam, D., Hovenier, J., & Waters, L. 2004, *Astronomy & Astrophysics*, 428, 663
- Traub, W. A., & Oppenheimer, B. R. 2010, *Exoplanets*, 111
- van Holstein, R. G., Snik, F., Girard, J. H., et al. 2017, in *Techniques and Instrumentation for Detection of Exoplanets VIII*, Vol. 10400, International Society for Optics and Photonics, 1040015
- Vigan, A., Gry, C., Salter, G., et al. 2015, *Monthly Notices of the Royal Astronomical Society*, 454, 129
- Vigan, A., N'Diaye, M., Dohlen, K., et al. 2018, in *Adaptive Optics Systems VI*, Vol. 10703, International Society for Optics and Photonics, 107035O
- Wilby, M. J., Keller, C. U., Snik, F., Korkiakoski, V., & Pietrow, A. G. 2017, *Astronomy & Astrophysics*, 597, A112

3 | Spatial linear dark field control on Subaru/SCEXAO

Maintaining high contrast with a vAPP coronagraph

Adapted from

K.L. Miller¹, S.P. Bos¹, J. Lozi, O. Guyon, D.S. Doelman, S. Vievard, A. Sahoo, V. Deo, N. Jovanovic, F. Martinache, F. Snik, T. Currie
Astronomy & Astrophysics, 646, A145 (2021)

One of the key challenges facing direct exoplanet imaging is the continuous maintenance of the region of high contrast within which light from the exoplanet can be detected above the stellar noise. In high-contrast imaging systems, the dominant source of aberrations is the residual wavefront error (WFE) that arises due to non-common path aberrations (NCPA) to which the primary adaptive optics (AO) system is inherently blind. Slow variations in the NCPA generate quasi-static speckles in the post-AO corrected coronagraphic image resulting in the degradation of the high-contrast dark hole created by the coronagraph. In this paper, we demonstrate spatial linear dark field control (LDFC) with an asymmetric pupil vector apodizing phase plate (APvAPP) coronagraph as a method to sense time-varying NCPA using the science image as a secondary wavefront sensor (WFS) running behind the primary AO system. By using the science image as a WFS, the NCPA to which the primary AO system is blind can be measured with high sensitivity and corrected, thereby suppressing the quasi-static speckles which corrupt the high contrast within the dark hole. On the Subaru Coronagraphic Extreme Adaptive Optics instrument (SCEXAO), one of the coronagraphic modes is an APvAPP which generates two PSFs, each with a 180° D-shaped dark hole with approximately 10^{-4} contrast at $\lambda = 1550$ nm. The APvAPP was utilized to first remove the instrumental NCPA in the system and increase the high contrast within the dark holes. Spatial LDFC was then operated in closed-loop to maintain this high contrast in the presence of a temporally-correlated, evolving phase aberration with a root-mean-square wavefront error of 80 nm. In the tests shown here, an internal laser source was used, and the deformable mirror (DM) was used both to introduce random phase aberrations into the system and to then correct them with LDFC in closed-loop operation. The results presented here demonstrate the ability of the APvAPP combined with spatial LDFC to sense aberrations in the high amplitude regime (~ 80 nm). With LDFC operating in closed-loop, the dark hole is returned to its initial contrast and then maintained in the presence of a temporally-evolving phase aberration. We calculate the contrast in $1 \lambda/D$ spatial frequency bins in both open-loop and closed-loop operation, and compare the measured contrast in these two cases. This comparison shows that, with LDFC operating in closed-loop, there is a factor of $\sim 3x$ improvement (approximately a half magnitude) in contrast across the full dark hole extent from 2 - 10 λ/D . This improvement is maintained over the full duration (10,000 iterations) of the injected temporally-correlated, evolving phase aberration. This work marks the first deployment of spatial LDFC on an active high-contrast imaging instrument. Our SCEXAO

¹K.L. Miller and S.P. Bos have contributed equally to this work.

testbed results show that the combination of the APvAPP with LDFC provides a powerful new focal plane wavefront sensing (FPWFS) technique by which high-contrast imaging systems can maintain high-contrast during long observations. This conclusion is further supported by a noise analysis of LDFC's performance with the APvAPP in simulation.

3.1 Introduction

Since the discovery of the first exoplanet over two decades ago, the field of exoplanet detection has expanded quickly. Today, one of the major goals of modern astronomy is not just the detection of, but also the direct imaging and characterization of an Earth-like exoplanet. This feat is not simple. When observed from a distance of 10 pc in the visible spectrum (0.3 - 1 μm), an Earth - Sun system analog would have an angular separation of ~ 100 mas and a difference in contrast of $\sim 10^{-10}$ (Traub & Oppenheimer, 2010). Combined, these factors present many technical instrumentation challenges. However, with today's large ground-based observatories and advances in coronagraphy and extreme adaptive optics (ExAO) systems, we can begin to address these issues.

To overcome the massive contrast between star and planet and allow for light from the planet to be visible, stellar light must be suppressed by many orders of magnitude. To achieve and maintain this precision stellar suppression, ground-based high-contrast imaging (HCI) systems must also continuously correct wavefront distortions due to the Earth's atmosphere. Modern HCI instruments, such as VLT/SPHERE (Beuzit et al., 2019), Magellan Clay/MagAO-X (Males et al. 2018; Close et al. 2018), Gemini/GPI (Macintosh et al., 2014), and Subaru/SCEXAO (Jovanovic et al., 2015), deploy advanced coronagraphs to suppress star light and also host ExAO systems consisting of wavefront sensors (WFSs) and deformable mirrors (DMs) with high actuator counts to measure and correct wavefront errors. Even after these systems, the dominant noise source for most HCI observations comes from uncorrected wavefront aberrations which generate a quasi-static speckle background in the science image.

Wavefront errors that are non-common path to the main WFS are among the primary limitations that prevent the current generation of HCI instruments from achieving higher contrast at smaller separations. Non-common path aberrations (NCPA) originate from instrumental aberrations downstream of the main WFS, and are therefore unsensed and left uncorrected. These NCPA, and therefore the quasi-static speckles generated in the science image, slowly evolve during observations as a function of instrumental changes in temperature, humidity and the gravitational vector (Martinez et al., 2013, 2012). These speckles limit the contrast achieved by the HCI instrument and consequently reduce the ability to detect and characterize exoplanets (Racine et al., 1999). It has been shown that the contrast can be improved in post-processing by exploiting diversity in the data to calibrate and subtract the speckle background. There are several forms of diversity which can be utilized by choosing an appropriate observing technique, some of which also provide characterization diagnostics. These include angular differential imaging (ADI; Marois et al. 2006), reference star differential imaging (RDI; Ruane et al. 2019), spectral differential imaging (SDI; Sparks & Ford 2002), and polarimetric differential imaging (PDI; Kuhn et al. 2001). These techniques have enabled the current state-of-the-art HCI system performance on SPHERE, which can obtain a contrast of $\sim 10^{-6}$ at 200 mas in the near-infrared (NIR; Vigan et al. 2015). While these post-processing techniques are effective at improving the contrast in the final science images, they are still limited by raw contrast through photon noise and coherent amplification of speckles. Both RDI and ADI rely on

the long-term stability of the PSF, but are limited by the quasi-static nature of NCPA to remove the resulting speckles in post-processing. PDI relies on the polarized signature of the target, which is usually a small fraction of the total light. And SDI does not have much leverage at small angular separations. For these reasons, in order to detect and characterize companions at small angular separations, it is necessary to actively sense and suppress these aberrations in real time during observations. The ideal solution is therefore a focal-plane wavefront sensor (FPWFS) which uses the science image as a secondary WFS to measure the NCPA.

FPWFS is fully common-path and is capable of sensing the quasi-static speckles to which the primary WFS is blind. This also eliminates potential chromatic wavefront errors that could occur between the main WFS and the science focal plane. Using the science image as its own WFS provides many other benefits as well. Unlike other WFS such as the modulated pyramid (PyWFS), the curvature (CWFS) and the Shack-Hartmann (SHWFS), FPWFSs do not suffer from low sensitivity to low-order modes due to photon noise. FPWFSs maintain constant sensitivity across all separations, allowing for the correction of low and high-spatial frequencies with equal efficiency (Guyon, 2005). FPWF-Sing methods which do not require probing can also operate simultaneously with science observations, resulting in a science duty cycle close to 100%. This means that valuable exposure time can be fully devoted to science measurements.

Many different FPWFS solutions have been developed, each with their own specific requirements and performance limitations (Jovanovic et al., 2018). Many of these techniques provide full phase solutions which require wavefront estimation. To perform this estimation, many solutions require some version of modulation, which can interrupt the science observations. Techniques requiring DM modulation, which includes speckle nulling, COFFEE, and pair-wise probing (Bordé & Traub 2006; Paul et al. 2013; Groff et al. 2015; Give'on et al. 2007), pollute the dark hole during estimation and cannot be combined with simultaneous science observations. Other methods can only operate with specific coronagraph designs. This includes the asymmetric pupil Fourier wavefront sensor, the Zernike phase-mask sensor, the quadrant analysis of coronagraphic images for tip-tilt sensing (QACITS), and Fast & Furious (Bos et al., 2020; Huby et al., 2015; Martinache, 2013; N'Diaye et al., 2013). Other techniques rely on specific modifications to the optical system, such as the holographic modal wavefront sensor (hMWFS) (hMWFS; Wilby et al. 2017), which requires an optic that generates holographic wavefront sensing PSFs, and the self-coherent camera (SCC; Baudoz et al. 2005) which utilizes a pinhole. Some of these methods, including SCC, the hMWFS, QACITS, as well as phase sorting interferometry (PSI), and the Frazin algorithm utilizing short exposure images, operate with a 100% science duty cycle (Baudoz et al. 2005; Codona et al. 2008; Wilby et al. 2016; Frazin 2013). The methods described above either require temporal modulation that lowers the science duty cycle, or have additional hardware requirements that complicate their implementation. A robust FPWFS would require no hardware beyond the AO system's DM and science camera and be compatible with multiple coronagraph architectures. Ideally, it would also not require modulation that can interrupt science observations. To this end, low-order wavefront sensing (LOWFS; Singh et al. 2015) was developed, which

re-images the starlight rejected by the coronagraph to estimate and control low-order aberrations. Unlike previously mentioned techniques, LOWFS does not directly estimate the wavefront and instead drives the wavefront back to a reference state. LOWFS operates with light split off from the science optical path and thus does not interrupt the science observations. As its name suggests, LOWFS is only used for the measurement of low-order aberrations and cannot be used for sensing higher spatial frequencies. The FPWFS method we demonstrate here, spatial linear dark field control (LDFC; Miller et al. 2017, 2018; Miller 2018; Miller et al. 2019), is an expansion of the LOWFS technique that can control higher-order aberrations, operate in the science focal plane without interrupting science observations, and is compatible with multiple coronagraph designs.

Spatial LDFC utilizes a region of the unsuppressed speckle field opposite the dark hole to measure variations in intensity induced by small phase aberrations in the pupil. This region spans the same spatial frequency extent as the dark hole itself and is referred to as the bright field. Spatial LDFC is not coronagraph-dependent; it requires only a one-sided dark hole with an unsuppressed bright field on the opposite side of the PSF. The dark hole can be derived by various methods such as pair-wise probing (electric field conjugation) or with a coronagraph. In this work we implemented LDFC with the vector-Apodizing Phase plate (vAPP; Snik et al. 2012, Otten et al. 2017), a pupil-plane coronagraph that manipulates the phase to dig one-sided dark holes in the point-spread function (PSF), leaving the other side of the PSF unocculted. This makes the vAPP excellently suited for the implementation of LDFC. As a pupil-plane coronagraph, the vAPP is placed in a relayed pupil plane conjugate to the optical system's entrance pupil just as a Lyot stop is placed in a more traditional Lyot coronagraph. The vAPP optic is a half-wave liquid crystal layer with varying fast-axis orientation that induces the same but opposite phase on opposite circular polarization states through the achromatic geometric phase (Pancharatnam 1956; Berry 1987). As the two circular polarization states receive the opposite phase, it results in two PSFs with dark holes on opposite sides. The most common implementation integrates a polarization-sensitive grating (Oh & Escuti 2008; Otten et al. 2014) in the design to spatially separate the PSFs. Due to manufacturing errors, an extra, on-axis, non-coronagraphic PSF is generally generated, we refer to this as the leakage PSF. Recently, we have developed vAPPs that integrate FPWFS by including the Asymmetric pupil Fourier wavefront sensor (Martinache 2013; Martinache et al. 2016) in the design (Bos et al., 2019). It is this model of vAPP, referred to as an Asymmetric Pupil vAPP (APvAPP), that is implemented at SCEXAO. In section 7.2 we provide a review of the theory behind LDFC and FPWFS with the APvAPP, that improves this technique's sensitivity. In section 6.3 we layout the parameters of our tests of LDFC with the APvAPP installed at SCEXAO. We present the results of LDFC's operation using the internal source and implementing quasi-static aberrations by applying an evolving phase screen on the DM. We conclude with a discussion of the results in section 3.5.

Table 3.1: Variables presented in section 7.2.

Variable	Description
E_{pup}	Pupil-plane electric field.
A	Pupil-plane amplitude.
θ	Pupil-plane phase.
E_{foc}	Focal-plane electric field.
$C\{\cdot\}$	Fraunhofer propagation operator.
E_0	Nominal coronagraph focal-plane electric field.
E_{ab}	Aberrated focal-plane electric field.
I_{BF}	Bright field intensity.
I_0	Nominal focal-plane intensity.
ΔI	LDFC intensity signal.
a	Nominal, real focal-plane electric field.
b	Nominal, imaginary focal-plane electric field.
c	Aberrated, real focal-plane electric field.
d	Aberrated, imaginary focal-plane electric field.
R_{Had}	Hadamard focal plane response matrix.
R_{eigen}	Eigenmode focal plane response matrix.
G_{eigen}	Eigenmode control matrix.
S_γ	Tikhonov regularization factor.

3.2 Combining spatial LDFC with an APvAPP

3.2.1 Spatial LDFC

As previously mentioned, spatial LDFC is a successor to the LOWFS technique which was designed to maintain high Strehl by sensing and correcting low-order aberrations, which predominately affect the PSF core. LDFC operates along similar principles as the LOWFS but extends the operational spatial frequency domain out to high spatial frequencies where coronagraphs such as the APvAPP generate a region of high contrast in which light from an exoplanet could be detected. The goal of LDFC is to monitor intensity variations within this spatial frequency regime to sense and correct higher-order aberrations, which degrade the contrast within the dark hole. Spatial LDFC maintains the contrast within the dark hole by monitoring the intensity of the bright field across the same spatial frequencies, which the dark hole spans. The variables used in this section are summarized in Table 7.1.

For small phase aberrations, the response of the bright field in intensity is linearly related to the electric field of the pupil-plane aberration (Miller et al., 2017). To demonstrate this, we begin with the equation of a pupil-plane electric field E_{pup} :

$$E_{pup} = Ae^{i\theta}, \quad (3.1)$$

with A the pupil-plane amplitude and θ the pupil-plane phase. In the small phase aberration regime, we can assume that $\theta \ll 1$. The pupil plane electric field can therefore be

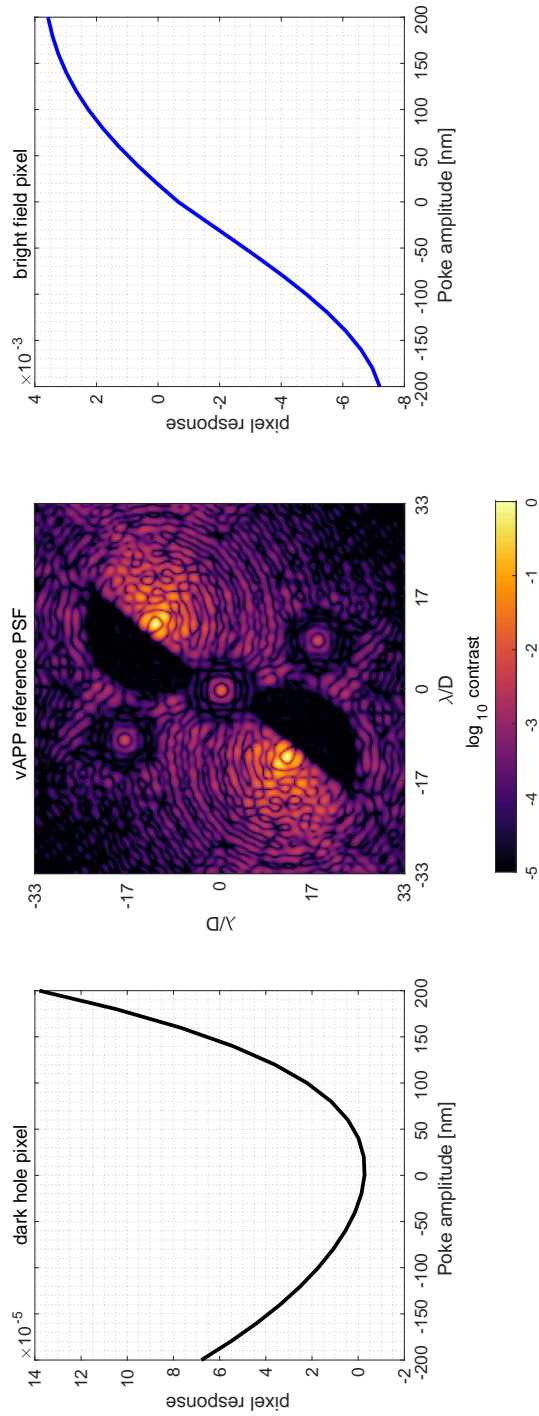


Figure 3.1: Response of both a pixel in the dark hole and a pixel in the bright field to the same low-amplitude perturbation introduced in the pupil plane. Note, the expected quadratic response within the dark hole and the monotonic response of the bright field to the same perturbation. This monotonic bright field response allows for the construction of a closed-loop control system around the bright field.

reduced to a first order approximation.

$$E_{\text{pup}} \approx A(1 + i\theta) \quad (3.2)$$

The focal plane electric field response is then the Fraunhofer propagation of this pupil-plane electric field, with the propagation operator written as $C\{\cdot\} \propto \frac{1}{i} \mathcal{F}\{\cdot\}$ (Goodman, 2005). The resulting focal-plane electric field (E_{foc}) can then be written as

$$E_{\text{foc}} = C\{E_{\text{pup}}\}, \quad (3.3)$$

$$= C\{A\} + C\{Ai\theta\}, \quad (3.4)$$

where $C\{A\}$ is the nominal electric field (E_0) generated across from the dark hole by the APvAPP coronagraph, and $C\{Ai\theta\}$ is the electric field of some small phase aberration (E_{ab}). This equation for the focal-plane electric field can therefore be rewritten as:

$$E_{\text{foc}} = E_0 + E_{\text{ab}}. \quad (3.5)$$

The resulting focal-plane intensity is then the modulus squared of the focal-plane electric field:

$$I_{\text{foc}} = |E_{\text{foc}}|^2, \quad (3.6)$$

$$= |E_0|^2 + |E_{\text{ab}}|^2 + 2\Re\{E_0 E_{\text{ab}}^*\}. \quad (3.7)$$

In the bright field, we can assume that $|E_0|^2 \gg |E_{\text{ab}}|^2$. The intensity specifically within the bright field can therefore be simplified to

$$I_{\text{BF}} = |E_0|^2 + 2\Re\{E_0 E_{\text{ab}}^*\} \quad (3.8)$$

where $|E_0|^2$ can be rewritten as I_0 , which is the reference image derived under ideal conditions. The change in intensity in the bright field ΔI due to an aberration can then be simplified to

$$\Delta I = I_{\text{BF}} - I_0 \quad (3.9)$$

$$= 2\Re\{E_0 E_{\text{ab}}^*\} \quad (3.10)$$

This ΔI is the signal used by spatial LDFC, and its linear dependence on the electric field of the pupil-plane aberration therefore makes spatial LDFC a linear algorithm. An example of the the bright field intensity response as well as the dark hole intensity response to the same pupil plane aberration is shown in Figure 3.1.

For maintaining dark hole contrast, spatial LDFC presents several benefits over other methods such as pair-wise probing and speckle nulling (Groff et al. 2015; Bordé & Traub 2006). This technique does not require DM modulation or field probing as it does not rely on any form of phase estimation. Spatial LDFC relies only on single science images to measure ΔI and calculate the pupil-plane aberration electric field. For these reasons, spatial LDFC therefore can run with nearly 100% duty cycle and does not interrupt science observations. This algorithm is able to run fast enough to address not just quasi-static NCPA, but also faster-moving atmospheric turbulence residuals. However, when running with the science image at focus, spatial LDFC can suffer from sign ambiguity for even modes. In the next subsection we describe how the sign ambiguity is overcome.

3.2.2 FPWFS with the APvAPP

In Equation 3.10 we derived the signal that LDFC uses to estimate the pupil-plane aberration. However, we have to consider that both E_0 and E_{ab} are complex quantities, and in order to extract the complete signal from E_{ab} , we have to set requirements on E_0 . This is also extensively covered in Bos et al. (2019), and therefore we will give only a short overview here.

We start by expanding the electric fields to their real and imaginary components:

$$E_0 = a + ib, \quad (3.11)$$

$$E_{ab} = c + id. \quad (3.12)$$

Using these expansions, we can rewrite Equation 3.10 as:

$$\Delta I = 2(ac + bd), \quad (3.13)$$

which shows, in order to generate a measurable signal for c and d , that a and b have to be non-zero. When phase-only aberrations are assumed, as shown in Bos et al. (2019), we understand that c is generated by even aberrations, while d is generated by odd aberrations. For E_0 , which is controlled by the coronagraph design, we find that a can be generated by a pupil-plane amplitude asymmetry or even pupil-plane phase (e.g. defocus for phase diversity), and b is generated by even pupil-plane amplitude and odd pupil-plane phase. Regular PSFs and vAPPs generally have $a = 0$ due to the geometry of the pupil-plane amplitude (Bos et al., 2019), making them insensitive to even pupil-plane phase aberrations (i.e. the sign ambiguity for even phase modes). However, APvAPPs are designed with a pupil-plane amplitude asymmetry, which gives them a non-zero a and therefore sensitivity to even modes. A non-zero a could also be realized by adding a defocus term to the system, but this cannot be combined with simultaneous coronagraphic observations.

3.3 Deploying LDFC on SCEXAO

We deployed LDFC on Subaru Telescope's Subaru Coronagraphic Extreme Adaptive Optics instrument (SCEXAO)(SCEXAO; Jovanovic et al. 2015), which marks the algorithm's first deployment on an active high-contrast imaging instrument. In this section, we will discuss the parameters of our tests at the SCEXAO, and the full process of deploying LDFC on this system. We describe SCEXAO and the basics of our set up in subsection 3.3.1, and the methods by which we derive a good reference PSF in subsection 3.3.2. Bright pixel selection and the process by which the modal basis set and control matrix are derived are explained in subsection 3.3.3 and subsection 3.3.4. In subsection 3.3.5, we describe how quasi-static speckles are introduced into the science image and how LDFC is deployed in closed-loop. An overview of the parameters used in the SCEXAO LDFC implementation is shown in Table 3.2.

Table 3.2: Parameters of the SCExAO LDFC implementation presented in section 6.3.

Variable	Description
Central wavelength	1550 nm
Filter width	25 nm
Poke amplitude	40 nm
Normalized brightness threshold	$\geq 10^{-4}$
Control loop gain	0.1
Normalized regularization value	$6 \cdot 10^{-2}$
Modal gain step	mode 150
Modal gain above step	1
Modal gain below step	0.1

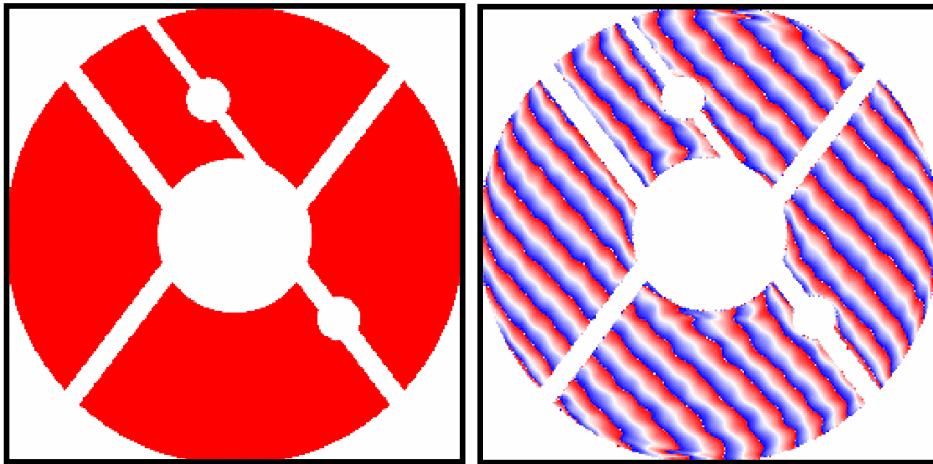
3.3.1 Instrument parameters

SCExAO is located downstream of the AO188 instrument (Minowa et al., 2010) at the Nasmyth platform of the Subaru telescope. SCExAO hosts a Boston Micromachines (BMC) 2K DM with 45 actuators across the pupil diameter, corresponding to a $22.5 \lambda/D$ control radius in the focal plane. The system’s primary wavefront sensor is a Pyramid wavefront sensor (Lozi et al., 2019) which operates in the 600-900 nm wavelength range. The instrument is run by the Compute and Control for Adaptive Optics (CACAO; Guyon et al. 2018) package which handles the real-time wavefront control. The instrument hosts multiple coronagraphs architectures, one of which is an APvAPP, used in this demonstration (Doelman et al., 2017). The SCExAO APvAPP was designed for a raw contrast of 10^{-5} between 2 to $11 \lambda/D$. Additionally, two phase diversity holograms were also added for wavefront sensing purposes, which can be seen in the center panel of Figure 3.1. The amplitude and phase design of the APvAPP are shown in Figure 3.2, which shows that a natural amplitude asymmetry occurs because a dead actuator has to be blocked. The APvAPP was designed for the JHK bands in which the integral-field spectrograph, CHARIS, (Groff et al., 2014) downstream of SCExAO, operates. The internal NIR camera, a C-RED 2, (Feautrier et al., 2017) was used as the FPWFS detector with a narrowband filter ($\Delta\lambda = 25$ nm) centered around 1550 nm. Each image was 192×192 pixels in size and was acquired with a frame rate of 1.5 kHz. The LDFC algorithm was implemented on SCExAO in Python and utilized functions within the HCIPy package (Por et al., 2018).

3.3.2 Deriving the reference PSF

LDFC does not provide an absolute phase measurement; instead, it measures intensity variations relative to an initial reference image. LDFC does not generate the dark hole; the purpose of this algorithm is to maintain the dark hole contrast achieved in the reference image. The contrast within the reference image dark hole is considered to be the ideal case. With LDFC running in closed-loop, the goal is to drive the measured contrast within the dark hole in the presence of aberrations back to the contrast measured in the

Pupil-plane Amplitude Pupil-plane Phase



3

Figure 3.2: SCExAO APvAPP amplitude and phase design. The design includes a natural pupil amplitude asymmetry to block a dead actuator. This enables FPWFS with the APvAPP.

dark hole of the reference image, thereby gaining back the contrast in the reference image. The deepest contrast recoverable by LDFC is therefore set by the contrast achieved in the reference image. For this reason, it is imperative to derive a reference image with minimal aberrations, thereby providing LDFC with the deepest possible contrast to maintain. We derive this reference PSF by performing an initial wavefront calibration with the method presented in Bos et al. (2019). This method utilizes a non-linear, model-based algorithm that derives an absolute wavefront measurement using a modal basis set consisting of the 30 lowest disk harmonics. We run this method for 5 iterations in closed loop with a loop gain of 0.5 before the LDFC calibration is performed. In five iterations, the raw contrast in the $2-3 \lambda/D$ spatial frequency bin is improved by a factor ~ 2 from $6 \cdot 10^{-4}$ to $3 \cdot 10^{-4}$. This algorithm derives the stable reference used by LDFC, as shown in Figure 3.3, where the DM command for this reference is also shown with an RMS WFE of 78 nm.

3.3.3 Bright pixel selection

The linear response of the bright field is what allows us to build a closed-loop control system, and for this reason, only the bright field pixels are selected from the image to be used as the WFS. With the SCExAO APvAPP coronagraph, two coronagraphic PSFs are generated as well as a non-coronagraphic leakage term whose peak intensity is roughly 6% of the maximum intensity of the coronagraphic PSFs and two phase diversity PSFs with peak intensities of $\leq 1\%$ of the coronagraphic PSFs. The bright field of both coronagraphic PSFs are used as the WFS as well as the leakage term and phase diversity PSFs.

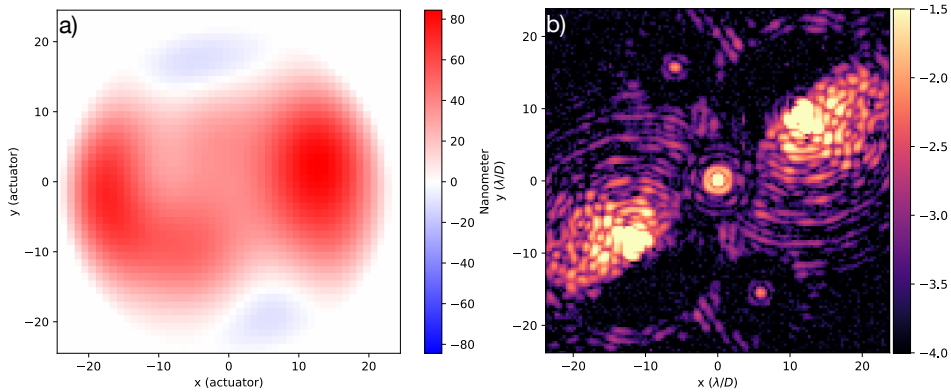


Figure 3.3: (a) DM shape derived by the non-linear WFS algorithm with the APvAPP to remove static, low-order instrumental NCPA, and (b) the resulting corrected focal plane image used as the reference for spatial LDFC. The colorbar shows normalized intensity.

3

To increase the SNR of the signal at higher spatial frequencies, the exposure time is increased; however this leads to saturation at the PSF core for the coronagraphic PSFs. The saturated pixels within the cores are then removed from the field selected for the WFS, which results in a loss of sensitivity to low-order modes. By using the much dimmer, unsaturated leakage term and phase diversity PSFs, we can then regain access to the low-order modes as well. We also limit our bright field to the control radius of the DM which, for SCExAO’s BMC 2K DM, is $22.5 \lambda/D$. Outside of the saturated PSF cores and within the DM control radius, pixels with a normalized value $\geq 10^{-4}$ are selected for use in the response matrix. The full map of bright field pixels used as the LDFC WFS is shown in Figure 3.4.

3.3.4 Modal basis set and control matrix

The modal basis set for LDFC is a set of modes derived independently for each system on which it is deployed. It is not a simple Zernike or Fourier mode set. Since the goal of LDFC is to precisely control a range of spatial frequencies across the full expanse of the dark hole, we derive a set of orthogonal modes based on the focal plane response to a series of Hadamard modes M_{Had} (Kasper et al., 2004). Unlike single influence functions, Hadamard modes have a high variance-to-peak ratio. The focal plane SNR response strength goes with variance (not peak), and the limited linear range of LDFC limits the peak value that can be applied. For these reasons, we use Hadamard modes rather than influence functions to ‘poke’ the DM and register the response in the focal plane to build the Hadamard response matrix (R_{Had}). For this work, a poke amplitude (a_p) of 40 nm was

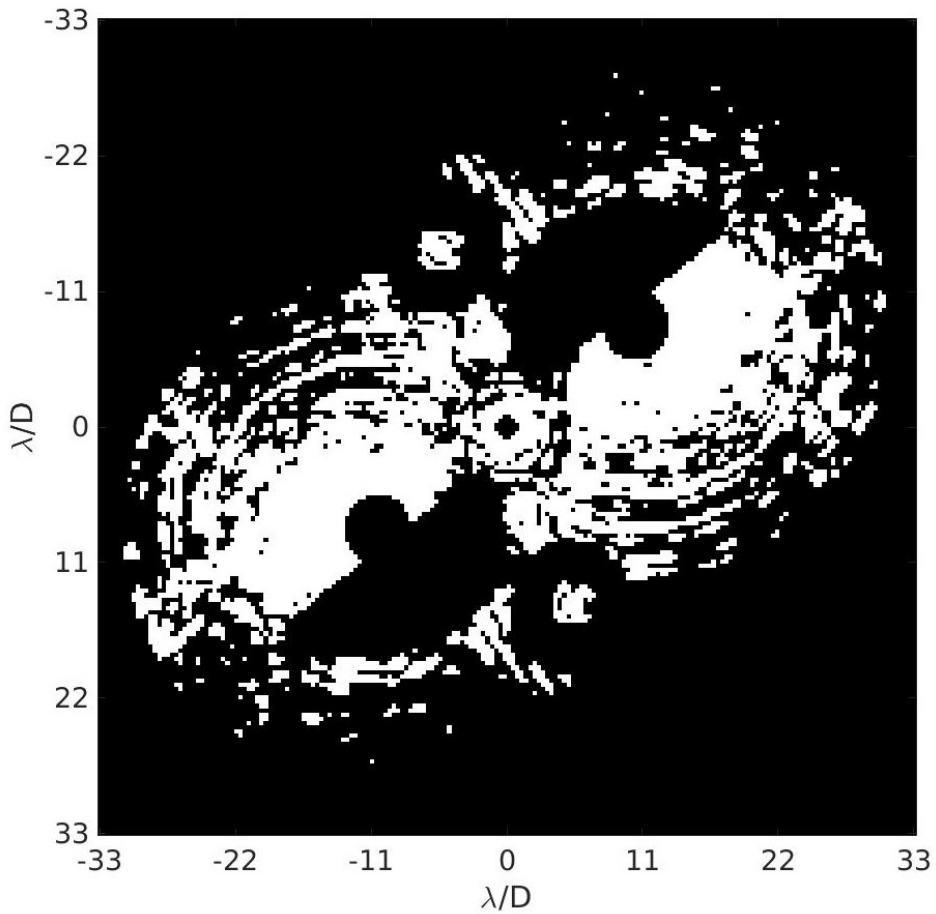


Figure 3.4: Bright field pixels used for the LDFC WFS. These pixels were chosen on three criteria: for being unsaturated, within the DM control radius, and for their linear response to small phase aberrations in the pupil.

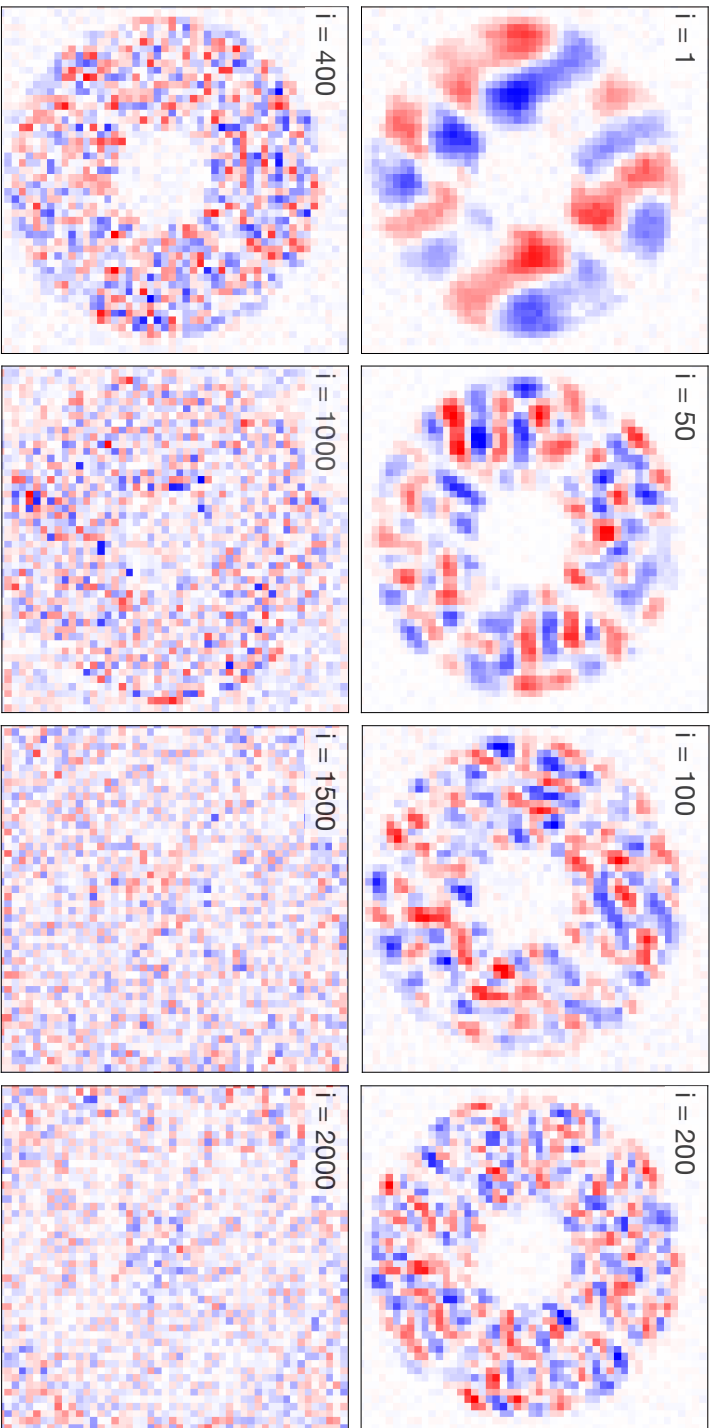


Figure 3.5: DM eigenmodes derived on the SCEXAO instrument with the APvAPP. The spatial frequency content of the modes increases with the mode number. Until mode ~ 400 the active pupil on the DM is clearly visible, at mode ~ 1000 the pupil is still visible, but noisy modes outside of the pupil begin to dominate. All subfigures are shown with the colorbar at the same, arbitrary scales.

chosen. The Hadamard response matrix is then determined by:

$$\Delta I_i = \frac{I_i^+ - I_i^-}{2a_p}, \quad (3.14)$$

$$R_{had} = \begin{pmatrix} | & & | \\ \Delta I_1 & \dots & \Delta I_N \\ | & & | \end{pmatrix}, \quad (3.15)$$

with I_i^+ and I_i^- the flattened focal-plane intensities, selected by the bright pixel map, for the positive and negative actuations of the i^{th} Hadamard mode, respectively, and ΔI_i the subsequent differential intensity response to the i^{th} mode. The modal basis set for LDFC, which we refer to as eigenmodes (M_{eigen}), is then derived from the singular value decomposition (SVD) of R_{Had} such that:

$$R_{Had} = U_{Had} S_{Had} V_{Had}^*, \quad (3.16)$$

$$M_{eigen} = M_{Had} V_{Had}^*. \quad (3.17)$$

These eigenmodes are then an orthogonal modal basis set ordered by spatial frequency (from lowest to highest frequency) from which we can then select the frequencies we wish to control. This is particularly useful when the control radius set by the number of actuators across the DM is larger than the outer working angle (OWA) of the coronagraph; in other words, when the highest spatial frequency the DM control exceeds the greatest spatial frequency spanned by the dark hole. This is the case with the SCEXAO APvAPP where the DM control radius is $22.5\lambda/D$, and the OWA of the APvAPP is only $11\lambda/D$.

With this set of eigenmodes, we then derive the response matrix R_{eigen} used for LDFC closed-loop operation. The DM is ‘poked’ with the eigenmodes, and the resulting focal plane images recorded in a process similar to Equation 3.14 and Equation 3.15. Examples of these eigenmodes are shown in Figure 3.5. The same bright pixel map is again used to select only pixels above a set intensity threshold, which sets the maximum spatial frequency that we control. This series of filtered focal images in response to the eigenmodes is then the final LDFC response matrix R_{eigen} . From this response matrix, the control matrix is then derived.

To build the control matrix, G_{eigen} , the response matrix R_{eigen} is inverted via SVD with the implementation of a Tikhonov regularization scheme to suppress the noisier higher spatial frequency modes. The singular value decomposition of R_{eigen} can be written as:

$$R_{eigen} = U_{eigen} S_{eigen} V_{eigen}^*, \quad (3.18)$$

with U_{eigen} the WFS eigenmodes, S_{eigen} a diagonal matrix with along the diagonal the singular values of the eigenmodes, and V_{eigen} the DM eigenmodes. The pseudo-inverse is therefore:

$$R_{eigen}^\dagger = V_{eigen} S_\gamma U_{eigen}^*, \quad (3.19)$$

where S_γ is the Tikhonov regularization term which suppresses singular value components that are small relative to the selected α . This regularization term is written as:

$$S_\gamma = \text{diag} \left\{ \frac{s_i^2}{s_i^2 + \gamma} \frac{1}{s_i} \right\}, \quad (3.20)$$

with s_i the i^{th} singular value, and this simply becomes the pseudo-inverse S^\dagger when $\gamma = 0$. In this process, the singular values of the SVD are plotted (as shown in Figure 3.6), and from these values, we select a modal cutoff point; modes beyond this cutoff are suppressed in the inversion. For this work we set $\gamma = 6 \cdot 10^{-2}$, which regularizes the modes above mode number 436. This value for γ was determined empirically by observing the stability of LDFC during closed-loop tests.

As the SNR drops off further out from the PSF core, the DM shape correction derived by LDFC to cancel an aberration can be distorted by noise in the lower SNR, higher frequency modes. To overcome this issue, we implement modal gain binning. As previously mentioned, the eigenmode basis set M_{eigen} , is ordered from low to high spatial frequency modes. For this reason, it is simple to implement a gain vector which gives more weight to the correction generated by the higher SNR, low-order modes and less weight to the lower SNR, high-order modes. In this way, we can mitigate issues caused by erroneous, low SNR measurements derived at the higher spatial frequencies. In these tests, our modal gain vector was set to give full weighting ($g_{\text{modal}} = 1$) to the first 150 modes in our basis set, and a weighting of 0.1 to the rest of the modes. Note that this modal gain vector is not the final gain. The modal gain vector is multiplied by a total loop gain as well which, for these tests was set to be $g_{\text{loop}} = 0.1$.

3.3.5 LDFC closed-loop operation

As described in the previous subsections, the procedure for setting up and calibrating LDFC proceeds as follows: generating the reference image, selecting the bright pixels for use as the WFS, deriving the modal basis set, and finally, building the control matrix. Once this calibration was completed, the next step was to attempt to run the algorithm in closed-loop with realistic atmospheric phase residuals. For our demonstration of LDFC, we generated quasi-static speckles in the science image plane using the BMC 2K DM. The DM was therefore both the aberration generator as well as the aberration corrector. By using the DM in this way, we were able to control the spatial frequency content of the induced aberrations and ensure the formation of speckles across the full extent of the dark hole. This technique also gave us access to both the injected aberration as well as the LDFC-derived correction. This allowed us to track the RMS wavefront error (WFE) of the open-loop aberration and compare this to the residual RMS WFE while running in closed-loop. This comparison is discussed further in section 4.3.

To simulate realistic atmospheric phase residuals, we generated a random, temporally evolving phase aberration which we applied on the DM. This aberration was generated as a cube in which each slice was the next step in the aberration evolution. Implementing the phase aberration in this way allowed us to set the temporal correlation between each step as well as the spatial frequency content. In order to emulate atmospheric residuals rather than telescope jitter, the evolving aberration was generated with a $\frac{1}{f^\alpha}$ power spectrum, where $\alpha = 4$, giving the aberration sequence high temporal correlation. Control over the spatial frequency content allowed us to ensure that quasi-static speckles were generated

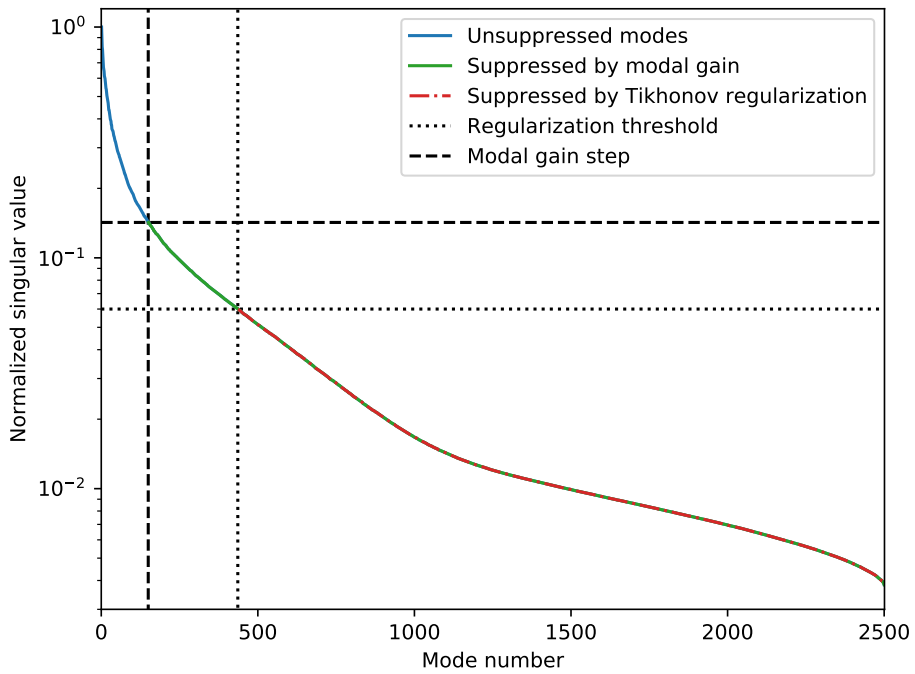


Figure 3.6: Normalized singular values for all 2500 modes generated by the SVD of the eigenmode response matrix R_{eigen} . All modes that have a normalized singular value below $6 \cdot 10^{-2}$ are suppressed by the Tikhonov regularization. In implementing modal gain binning a gain $g_{modal} = 1$ was given to the first 150. All modes above mode 150 were given a modal gain $g_{modal} = 0.01$.

across the full dark hole. The spatial frequency content was defined by a PSD given by $\frac{1}{k^\beta}$ law with $\beta = 1.1$. The aberration was given an RMS amplitude of ~ 80 nm; these tests were therefore in the high amplitude regime for atmospheric residuals and just within the linear regime limit for LDFC which is at ~ 100 nm. CACAO has 12 software channels on which a shape can be written. These channels are then summed, and the summed total is the shape that is then applied to the DM surface. Our aberration was implemented on one software channel on the DM and allowed to run first in open-loop with no correction for comparison. The same aberration was implemented in closed-loop with LDFC actively sensing the aberration and applying the proper correction to a separate channel on the DM. To demonstrate LDFC closed-loop operation, the aberration was applied on one DM channel. Ten images were taken at the science camera and averaged, the LDFC correction was derived, and the correction was then written on a separate channel of the DM. The following section shows results of these closed-loop tests over the course of a 10,000 step evolving phase aberration.

3

3.3.6 Noise analysis for LDFC with the SCExAO APvAPP

In the following figures, we present a noise analysis in simulation for LDFC with the SCExAO APvAPP. The same parameters used for the tests described previously in this section were used to generate Figure 3.7 and Figure 3.8. In these simulations, a model of the SCExAO APvAPP and the BMC 2k DM were implemented, the latter with 50 actuators across the full diameter. Hadamard modes were projected onto this DM model and used to build the eigenmode basis set. The resulting 2500 eigenmode basis set was then truncated to 436 modes as was done in the bench tests. This smaller modal basis was used to build the simulated response matrix R_{eigen} and control matrix G_{eigen} just as on the SCExAO bench. Modal gain binning was then implemented as well, with gain $g_{modal} = 1$ applied to the first 150 modes, and gain $g_{modal} = 0.01$ applied to all subsequent modes. The total loop gain, g_{loop} , was set to 1 for this simulation in order to allow for faster convergence. The same bright pixel map was chosen for the simulation tests as well.

This analysis was completed for a series of incident photon numbers (N_p) ranging from 10^3 to 10^8 . For these tests, N_p was set, and the LDFC algorithm was then calibrated and tuned with the parameters described above. A random aberration consisting of a linear sum of eigenmodes was generated and implemented on the model DM. LDFC was then run in closed-loop at a speed of 1 kHz for 20 iterations, long enough to allow the loop to converge. For each N_p , 100 different random aberrations, all with an 80 nm RMS WFE, were generated, and the loop given 20 iterations to run. The results of these tests are shown in Figure 3.7 and Figure 3.8.

In Figure 3.7, the average residual RMS WFE per closed-loop iteration from all 100 randomly generated aberrations is plotted for each N_p level. The error bars give the standard deviation of the average residual RMS WFE at each loop iteration across the set of 100 random aberrations. This plot shows that, for values of N_p between $10^8 - 10^6$, LDFC converges to ≤ 1 nm RMS WFE. This should be noted that this is an ideal case as the

induced aberrations consist solely of linear sums of modes from the eigenmode basis set.

In Figure 3.8, the data from Figure 3.7 is further reduced to show the average residual RMS WFE to which the loop converged for each N_p level over all 100 aberration tests. The error bars denote the standard deviation in the residual RMS WFE to which the loop converges across all 100 aberration cases. Plotted alongside the measured data RMS WFE data is the function $\frac{1}{\sqrt{N_p}}$, representing pure photon noise. This plot clearly shows that the measured residual RMS WFE vs N_p fits the $\frac{1}{\sqrt{N_p}}$ line. LDFC with the SCEXAO APvAPP is therefore photon noise-limited. Bos et al. (2019) performed a very similar analysis for the SCEXAO APvAPP, but with a non-linear model-based wavefront sensing algorithm reconstructing the thirty lowest Zernike modes. The results presented in Figure 3.8 closely match what was found in Bos et al. (2019), with some small differences in residual RMS WFE due to the differences in implementation between the two algorithms.

It should be noted here that this analysis was performed using the same parameters as the SCEXAO bench tests and models of the bench hardware (e.g. the APvAPP and the DM), but in an ideal case where the only source of noise was photon noise. In this simulation-based analysis, the loop speed was set to 1 kHz. This is not the speed at which the loop runs in the tests presented in this paper. The reason for this is not a theoretical limitation. The Python implementation of the algorithm is currently limited to a loop speed of ~ 2 Hz due to the slow image co-alignment algorithm currently being used. New code adaptations will soon allow for increased speed in the deployment of LDFC on SCEXAO.

This analysis was done for an ideal case where the introduced aberration is a linear sum of the eigenmode basis set. In this case, the residual RMS WFE is sub-nanometer for high flux ($N_p = 10^8$). When the aberration introduced is random and not a linear sum of eigenmodes, as is the case for the results shown in section 4.3, the residual RMS WFE does not converge to the same point, even though the dark hole contrast does return to the contrast achieved in the reference. It is hypothesized that this is due to the existence of high-spatial frequencies in the random introduced aberration that fall outside of the selected bright field and are therefore poorly-sensed or unsensed by LDFC. It will be shown in section 4.3 that this does not affect LDFC's ability to control and maintain the contrast within the OWA of the APvAPP coronagraph.

3.4 Results

The results presented here demonstrate the ability of spatial LDFC to sense and correct evolving aberrations in the high amplitude regime (~ 80 nm) behind an AO system with an APvAPP coronagraph. With LDFC operating in closed-loop, the dark hole, degraded by the introduction of quasi-static speckles, is returned to the ideal contrast of the reference image and maintained in the presence of a temporally-evolving phase aberration. To demonstrate the power of LDFC to sense and suppress quasi-static speckles, in Figure 3.9 a and b we show two images for comparison, each an average of 10,000 images.

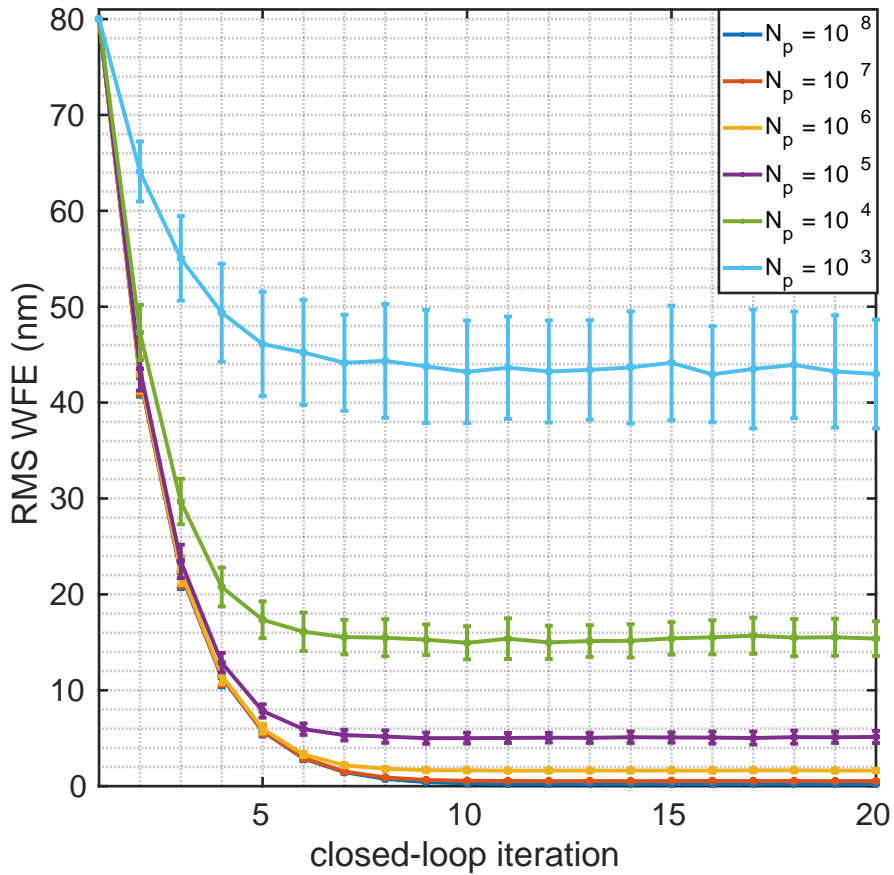


Figure 3.7: Closed-loop performance for each N_p level showing the average residual RMS WFE over all 100 randomly generated aberrations vs loop iteration. The error bars give the standard deviation of the average residual RMS WFE at each loop iteration across the set of 100 random aberrations. As expected, as N_p increases, the average residual RMS WFE, as well as the stand deviation from the mean, decreases. For values of N_p between $10^3 - 10^6$, the RMS WFE converges to ≤ 1 nm.

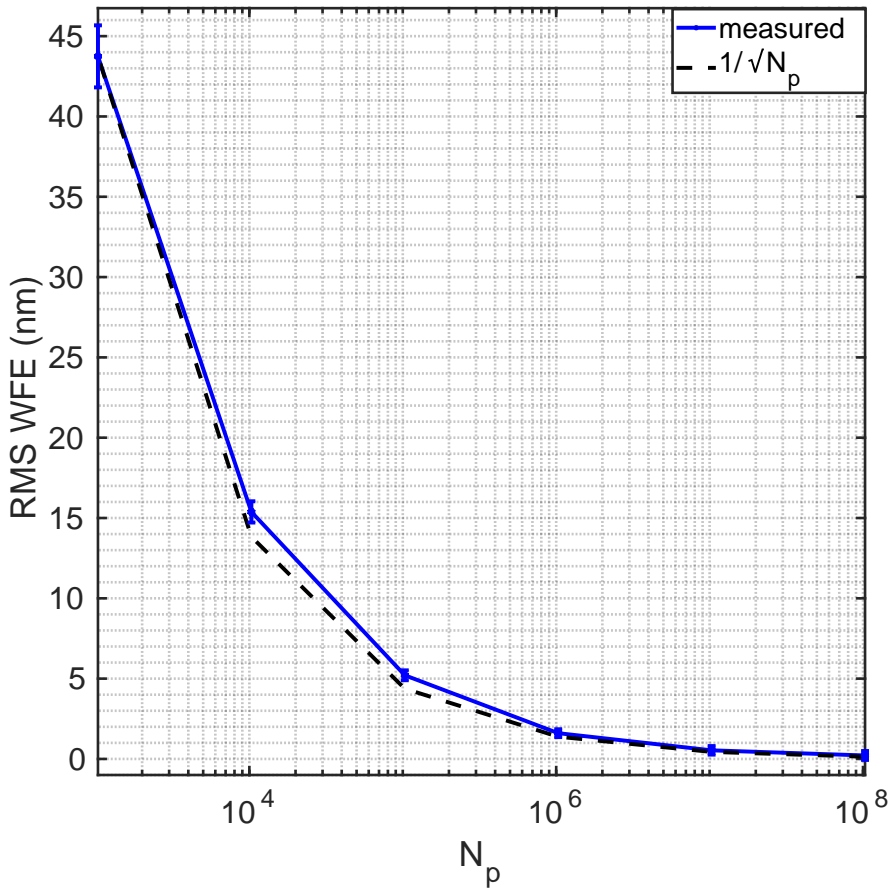


Figure 3.8: Average residual RMS WFE as a function of N_p . Error bars denote the standard deviation in the residual RMS WFE across all 100 aberration cases. The dotted line plots the pure photon noise case $\frac{1}{\sqrt{N_p}}$. The fit of this function to the measured data shows that LDFC with the SCExAO APvAPP is photon noise-limited.

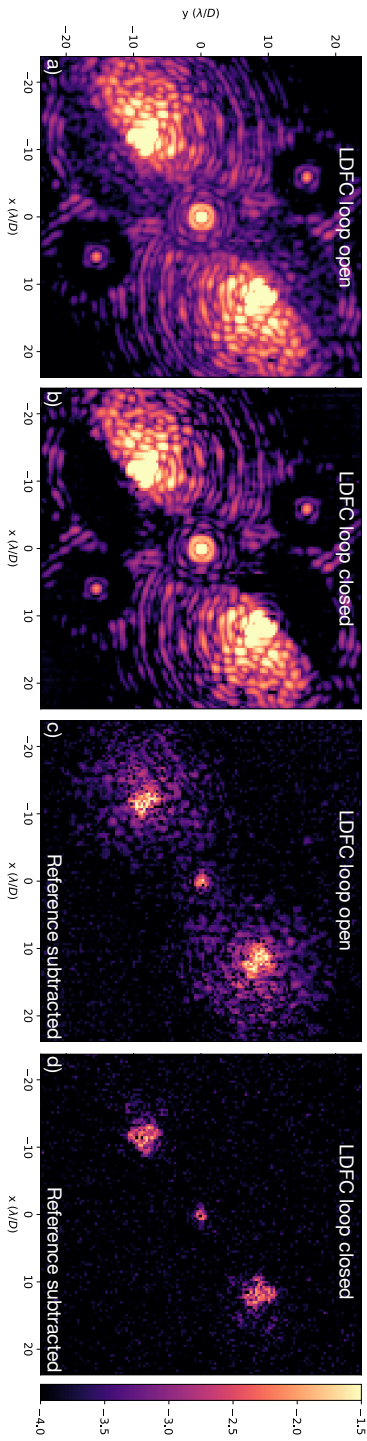


Figure 3.9: Averages of 10,000 images that show the resulting coronagraphic PSFs when the LDFC loop is closed and open. (a) The average PSF when the LDFC loop is open. (b) The average PSF when the LDFC loop is closed. (c) The average PSF when the LDFC loop is open and the reference PSF is subtracted. (d) The average PSF when the LDFC loop is closed and the reference PSF is subtracted. The colorbar shows the normalized intensity in logarithmic scale and is equal for all subfigures.

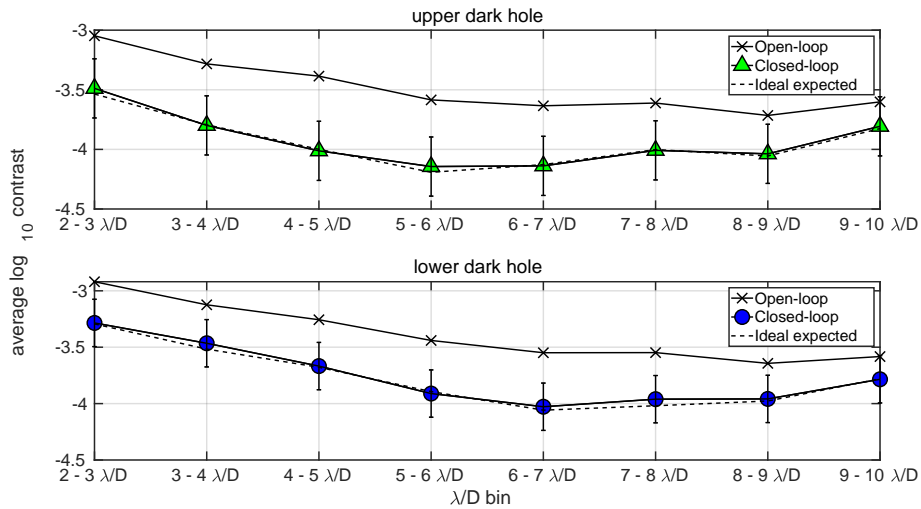


Figure 3.10: The average contrast over the full 10,000 iterations calculated for each $1 \lambda/D$ hemispherical bin in both the upper and lower dark holes. The plots show the average contrast per spatial frequency bin in the aberrated open-loop state, post-LDFC correction in closed-loop, and the ideal contrast measurement expected from the reference image. Error bars are given for the closed-loop LDFC contrast measurements denoting the standard deviation of the contrast measured in each $1 \lambda/D$ bin for the full 10,000 iterations. This plot clearly shows that running LDFC in closed-loop drives the dark hole contrast back to its initial state as measured in the reference image.

Figure 3.9 a shows the average in open-loop with our temporally evolving phase aberration induced on the DM. While in Figure 3.9 b we show the average of 10,000 images taken with the same aberration being induced on the DM, but now in closed-loop with LDFC operating. It can be seen in the comparison of these two images that the quasi-static speckles are greatly reduced in the closed-loop case. The difference between the two cases is even more pronounced when the reference image is subtracted from both averaged images. The reference subtracted is shown in Figure 3.9 c and d, where all that is left in each image are the speckles averaged over 10,000 images in the open-loop and closed-loop cases. Here it becomes very clear how well LDFC reduces the speckles within the unsaturated regions of the image within the dark hole.

To analyze the algorithm's performance by spatial frequency, the dark hole was divided into $1 \lambda/D$ spatial frequency bins. The contrast was calculated separately in each bin for both open-loop and closed-loop operation. The closed-loop performance can then be compared to open-loop at low, intermediate, and high spatial frequencies across the dark hole. Analyzing the average contrast in the averaged images shown in Figure 3.9 reveals that, with LDFC operating in closed-loop, there is a factor of $\sim 3x$ improvement (approximately a half magnitude) in contrast across the full dark hole extent from 2 -

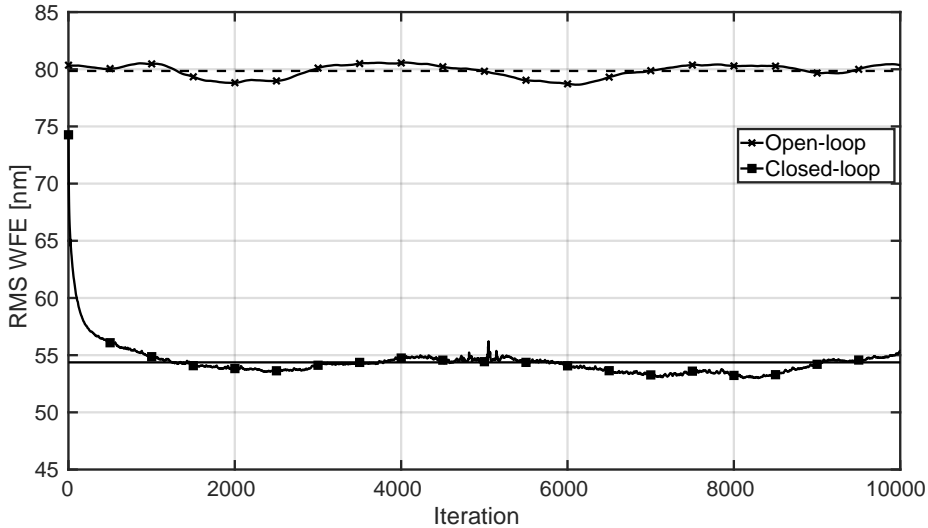


Figure 3.11: Reduction and stabilization of the RMS wavefront error in the pupil plane following compensation for bench drift. The test presented here took approximately 1 hour and 24 minutes to complete (loop speed was ~ 2 Hz).

10 λ/D . The improvement in contrast is shown per spatial frequency across the averaged images in Figure 3.10. This improvement is maintained over the full duration (10,000 iterations) of the injected temporally-correlated, evolving phase aberration. The LDFC implementation presented in this work has a loop speed of ~ 2 Hz, which means that these tests took approximately 1 hour and 24 minutes to complete. To demonstrate temporal stability of the dark hole contrast, we divided the dark hole into spatial frequency bins and measured the contrast at each step of the 10,000 iterations. These results are presented in Figure 3.12, where a single spatial frequency has been selected as a representative of the performance at low, mid, and high spatial frequencies. These results show that LDFC is capable of suppressing quasi-static speckles and stabilizing the dark hole contrast over the course of an observation. We also show this stability by analyzing the aberrations and corrections applied to the DM. In Figure 3.11 we plot the RMS WFE of both the open-loop aberration applied as well as the RMS WFE in closed-loop. The initial aberration has an RMS WFE of 80 nm which is reduced by LDFC to an average of 55 nm. The RMS WFE of the LDFC-corrected wavefront holds steady across the full 10,000 iterations.

3.5 Discussion and Conclusions

Spatial linear dark field control and asymmetric pupil vector-Apodizing Phase Plate coronagraphs make up a class of powerful new FPWFS techniques that will allow the large

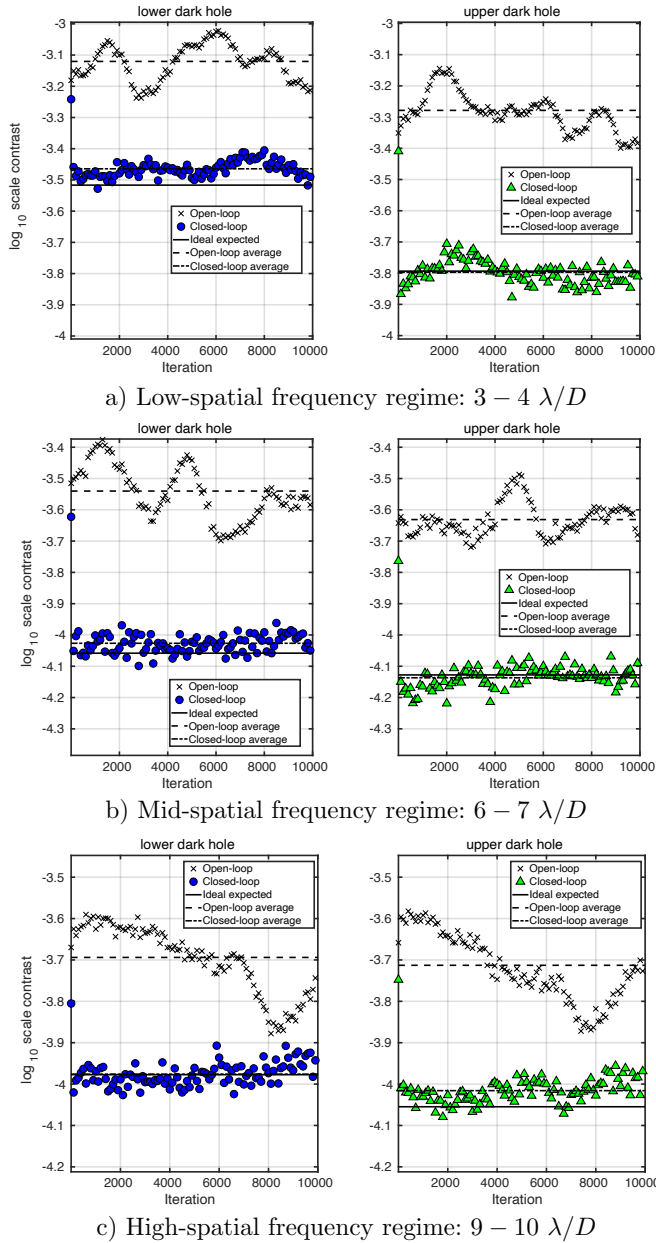


Figure 3.12: Temporal evolution of the contrast level showing the convergence and stabilization of the dark hole contrast in closed-loop over 10,000 iterations of a temporally-correlated and evolving phase aberration. The three figures show the performance of the algorithm at 3 spatial frequencies within the dark hole: in a low-spatial frequency regime ($3 - 4 \lambda/D$), at mid-spatial frequencies ($6 - 7 \lambda/D$), and at high-spatial frequencies ($9 - 10 \lambda/D$) near the OWA of the dark hole.

ground-based telescopes of today and the ELT's of tomorrow to achieve the high-contrast imaging milestones for which they were designed. Combining spatial LDFC with APvAPPs on SCExAO, we have demonstrated here that these two complementary techniques are capable of sensing the quasi-static speckles in the final focal plane that are generated by low-amplitude, temporally-evolving non-common path errors to which the primary AO system is blind. Without FPWFS, these quasi-static speckles would dominate within the dark hole and degrade the high-contrast delivered by the vAPP coronagraph within the static dark hole.

These promising results on SCExAO in the high amplitude aberration regime are complemented by similar tests in the low amplitude aberration regime demonstrated recently in the lab at NASA Ames. Spatial LDFC was shown to work in a stable lab environment at deeper contrast levels ($\sim 10^{-7} - 10^{-6}$) for phase aberrations with varying spatial frequency content (Currie et al., 2020). The results from SCExAO show that a combination of the APvAPP with spatial LDFC is not only a powerful, but very robust wavefront sensing tool which can be deployed on multiple instruments in their current state. The list of instruments includes Subaru/SCExAO (Doelman et al., 2018), Magellan Clay/MagAO-X (Miller et al., 2018) and VLT/ERIS (Boehle et al., 2018), all of which host APvAPPs as one of their coronagraphic mode.

To prevent spectral smearing by the integrated polarization-sensitive gratings in most of the current vAPP designs, they are mainly used with narrowband filters or integral-field spectrographs. For example, the results presented in this work were obtained with a $\Delta\lambda = 25$ nm filter (around 1550 nm). However, due to the faint nature of exoplanets it is preferred to observe them in broadband filters to maximize the sensitivity. Therefore, next steps for this work include implementing broadband wavefront control with spatial LDFC behind vAPPs that can operate in broadband filters (Bos et al., 2018). The current Python implementation of the algorithm is limited to a loop speed of ~ 2 Hz, which was sufficient for the results presented here, but needs to be improved for on-sky deployment. As was shown in the noise analysis presented in subsection 3.3.6, this is not a theoretical limitation. LDFC with an APvAPP is a photon noise-limited algorithm and can, in theory, run at least at 1 kHz under the conditions presented in this paper. We therefore expect future software upgrades to greatly increase the loop speed. Increasing the speed will also allow us to address not only NCPA, but faster moving chromatic terms in residual atmospheric turbulence as well. We also intend to implement spatial LDFC within the compute and control for adaptive optics (CACAO) open source package, thereby making it available to observers in the future. Use of the open source CACAO package will also allow for easy deployment of this algorithm on other systems such as MagAO-X on the Magellan Clay Telescope and the Keck Planet Imager and Characterizer (KPIC; Jovanovic et al. 2019) on the Keck Telescope. The results shown here establish that the combination of the APvAPP with spatial LDFC provides a powerful new FPWFS technique by which high-contrast imaging systems can maintain high-contrast during long observations, and marks the first deployment to an active instrument. On-sky results at Subaru will follow soon, and deployment on MagAO-X is expected in the coming year.

Bibliography

- Baudoz, P., Boccaletti, A., Baudrand, J., & Rouan, D. 2005, *Proceedings of the International Astronomical Union*, 1, 553
- Berry, M. V. 1987, *Journal of Modern Optics*, 34, 1401
- Beuzit, J.-L., Vigan, A., Mouillet, D., et al. 2019, arXiv preprint arXiv:1902.04080
- Boehle, A., Glauser, A. M., Kenworthy, M. A., et al. 2018, in *Ground-based and Airborne Instrumentation for Astronomy VII*, Vol. 10702, International Society for Optics and Photonics, 107023Y
- Bordé, P. J., & Traub, W. A. 2006, *The Astrophysical Journal*, 638, 488
- Bos, S. P., Doelman, D. S., de Boer, J., et al. 2018, in *Advances in Optical and Mechanical Technologies for Telescopes and Instrumentation III*, Vol. 10706, International Society for Optics and Photonics, 107065M
- Bos, S. P., Doelman, D. S., Lozi, J., et al. 2019
- Bos, S. P., Vievard, S., Wilby, M. J., et al. 2020, *A&A*, 639, A52, doi: [10.1051/0004-6361/202037910](https://doi.org/10.1051/0004-6361/202037910)
- Close, L. M., Males, J. R., Durney, O., et al. 2018, arXiv preprint arXiv:1807.04311
- Codona, J. L., Kenworthy, M. A., & Lloyd-Hart, M. 2008, in *Adaptive Optics Systems*, Vol. 7015, International Society for Optics and Photonics, 70155D
- Currie, T., Pluzhnik, E., Guyon, O., et al. 2020, *Publications of the Astronomical Society of the Pacific*, 132, 104502
- Doelman, D. S., Snik, F., Warriner, N. Z., & Escuti, M. J. 2017, in *Techniques and Instrumentation for Detection of Exoplanets VIII*, Vol. 10400, International Society for Optics and Photonics, 104000U
- Doelman, D. S., Por, E. H., Bos, S. P., et al. 2018, in *Adaptive Optics Systems VI*, Vol. 10703, International Society for Optics and Photonics
- Feautrier, P., Gach, J.-L., Greffe, T., et al. 2017, in *Image Sensing Technologies: Materials, Devices, Systems, and Applications IV*, Vol. 10209, International Society for Optics and Photonics, 102090G
- Frazin, R. A. 2013, *The Astrophysical Journal*, 767, 21
- Give'on, A., Kern, B., Shaklan, S., Moody, D. C., & Pueyo, L. 2007, *AAS*, 211, 135
- Goodman, J. W. 2005, *Introduction to Fourier optics* (Roberts and Company Publishers)
- Groff, T. D., Riggs, A. E., Kern, B., & Kasdin, N. J. 2015, *Journal of Astronomical Telescopes, Instruments, and Systems*, 2, 011009
- Groff, T. D., Kasdin, N. J., Limbach, M. A., et al. 2014, in *Ground-based and Airborne Instrumentation for Astronomy V*, Vol. 9147, International Society for Optics and Photonics, 91471W
- Guyon, O. 2005, *The Astrophysical Journal*, 629, 592
- Guyon, O., Sevin, A., Ltaief, H., et al. 2018, in *Adaptive Optics Systems VI*, Vol. 10703, International Society for Optics and Photonics, 107031E
- Huby, E., Baudoz, P., Mawet, D., & Absil, O. 2015, *Astronomy & Astrophysics*, 584, A74
- Jovanovic, N., Martinache, F., Guyon, O., et al. 2015, *Publications of the Astronomical Society of the Pacific*, 127, 890
- Jovanovic, N., Absil, O., Baudoz, P., et al. 2018, in *Proc. SPIE*, Vol. 10703, Adaptive Optics Systems VI
- Jovanovic, N., Delorme, J.-R., Bond, C. Z., et al. 2019, arXiv preprint arXiv:1909.04541
- Kasper, M., Fedrigo, E., Looze, D. P., et al. 2004, *JOSA A*, 21, 1004
- Kuhn, J., Potter, D., & Parise, B. 2001, *The Astrophysical Journal Letters*, 553, L189
- Lozi, J., Jovanovic, N., Guyon, O., et al. 2019, *Publications of the Astronomical Society of the*

- Pacific, 131, 044503
- Macintosh, B., Graham, J. R., Ingraham, P., et al. 2014, *Proceedings of the National Academy of Sciences*, 111, 12661
- Males, J. R., Close, L. M., Miller, K., et al. 2018, in *Adaptive Optics Systems VI*, Vol. 10703, International Society for Optics and Photonics, 1070309
- Marois, C., Lafreniere, D., Doyon, R., Macintosh, B., & Nadeau, D. 2006, *The Astrophysical Journal*, 641, 556
- Martinache, F. 2013, *Publications of the Astronomical Society of the Pacific*, 125, 422
- Martinache, F., Jovanovic, N., & Guyon, O. 2016, *Astronomy & Astrophysics*, 593, A33
- Martinez, P., Kasper, M., Costille, A., et al. 2013, *Astronomy & Astrophysics*, 554, A41
- Martinez, P., Loose, C., Carpentier, E. A., & Kasper, M. 2012, *Astronomy & Astrophysics*, 541, A136
- Miller, K., Guyon, O., & Males, J. 2017, *Journal of Astronomical Telescopes, Instruments, and Systems*, 3, 049002
- Miller, K., Males, J. R., Guyon, O., et al. 2018, in *Adaptive Optics Systems VI*, Vol. 10703, International Society for Optics and Photonics, 107031T
- Miller, K. L. 2018, PhD thesis, The University of Arizona
- Miller, K. L., Males, J. R., Guyon, O., et al. 2019, *Journal of Astronomical Telescopes, Instruments, and Systems*, 5, 1, doi: 10.1117/1.JATIS.5.4.049004
- Minowa, Y., Hayano, Y., Oya, S., et al. 2010, in *Adaptive Optics Systems II*, Vol. 7736, International Society for Optics and Photonics, 77363N
- N'Diaye, M., Dohlen, K., Fusco, T., & Paul, B. 2013, *Astronomy & Astrophysics*, 555, A94
- Oh, C., & Escuti, M. J. 2008, *Optics letters*, 33, 2287
- Otten, G. P., Snik, F., Kenworthy, M. A., et al. 2014, in *Advances in Optical and Mechanical Technologies for Telescopes and Instrumentation*, Vol. 9151, International Society for Optics and Photonics, 91511R
- Otten, G. P., Snik, F., Kenworthy, M. A., et al. 2017, *The Astrophysical Journal*, 834, 175
- Pancharatnam, S. 1956, in *Proceedings of the Indian Academy of Sciences-Section A*, Vol. 44, Springer, 398–417
- Paul, B., Mugnier, L., Sauvage, J.-F., Dohlen, K., & Ferrari, M. 2013, *Optics Express*, 21, 31751
- Por, E. H., Haffert, S. Y., Radhakrishnan, V. M., et al. 2018, in *Proc. SPIE*, Vol. 10703, Adaptive Optics Systems VI
- Racine, R., Walker, G. A., Nadeau, D., Doyon, R., & Marois, C. 1999, *Publications of the Astronomical Society of the Pacific*, 111, 587
- Ruane, G., Ngo, H., Mawet, D., et al. 2019, *The Astronomical Journal*, 157, 118
- Singh, G., Lozi, J., Guyon, O., et al. 2015, *Publications of the Astronomical Society of the Pacific*, 127, 857
- Snik, F., Otten, G., Kenworthy, M., et al. 2012, in *Modern Technologies in Space-and Ground-based Telescopes and Instrumentation II*, Vol. 8450, International Society for Optics and Photonics, 84500M
- Sparks, W. B., & Ford, H. C. 2002, *The Astrophysical Journal*, 578, 543
- Traub, W. A., & Oppenheimer, B. R. 2010, *Exoplanets*, 111
- Vigan, A., Gry, C., Salter, G., et al. 2015, *Monthly Notices of the Royal Astronomical Society*, 454, 129
- Wilby, M., Keller, C. U., Haffert, S., et al. 2016, in *Adaptive Optics Systems V*, Vol. 9909, International Society for Optics and Photonics, 990921
- Wilby, M. J., Keller, C. U., Snik, F., Korkiakoski, V., & Pietrow, A. G. 2017, *Astronomy & Astrophysics*, 597, A112

4 | First on-sky demonstration of spatial Linear Dark Field Control with the vector-Apodizing Phase Plate at Subaru/SCEXAO

Adapted from

S.P. Bos, K.L. Miller, J. Lozi, O. Guyon, D.S. Doelman, S. Vievard, A. Sahoo, V. Deo, N. Jovanovic, F. Martinache, T. Currie, F. Snik
submitted to *Astronomy & Astrophysics*

One of the key noise sources that currently limits high contrast imaging observations for exoplanet detection is quasi-static speckles. Quasi-static speckles originate from slowly evolving non-common path aberrations (NCPA). NCPA are related to the different optics encountered in the wavefront sensing path and the science path, and also have a chromatic component due to the difference in the wavelength between the science camera and the main wavefront sensor. These speckles degrade the contrast in the high-contrast region (or dark hole) generated by the coronagraph and are challenging to calibrate in post-processing. The purpose of this work is to present a proof-of-concept on-sky demonstration of spatial Linear Dark Field Control (LDFC). The ultimate goal of LDFC is to stabilize the PSF by addressing NCPA using the science image as additional wavefront sensor. We combine spatial LDFC with the Asymmetric Pupil vector-Apodizing Phase Plate (APvAPP) on the Subaru Coronagraphic Extreme Adaptive Optics system at the Subaru Telescope. To allow for rapid prototyping and easy interfacing with the instrument LDFC was implemented in Python. This limited the speed of the correction loop to approximately 20 Hz. With the APvAPP, we derive a high-contrast reference image to be utilized by LDFC. LDFC is then deployed on-sky to stabilize the science image and maintain the high-contrast achieved in the reference image. In this paper, we report the results of the first successful proof-of-principle LDFC on-sky tests. We present results from two types of cases: (1) Correction of instrumental errors and atmospheric residuals plus artificially induced static aberrations introduced on the deformable mirror and (2) correction of only atmospheric residuals and instrumental aberrations. When introducing artificial static wavefront aberrations on the DM, we find that LDFC can improve the raw contrast by a factor 3–7 over the dark hole. In these tests, the residual wavefront error decreased by ~ 50 nm RMS, from ~ 90 nm to ~ 40 nm RMS. In the case with only residual atmospheric wavefront errors and instrumental aberrations, we show that LDFC is able to suppress evolving aberrations that have timescales of < 0.1 – 0.4 Hz. We find that the power at 10^{-2} Hz is reduced by factor ~ 20 , 7, and 4 for spatial frequency bins at 2.5, 5.5, and $8.5 \lambda/D$, respectively. We have identified multiplied challenges that have to be overcome before LDFC can become an integral part of science observations. The results presented in this work show that LDFC is a promising technique for enabling the high-contrast imaging goals of the upcoming generation of extremely large telescopes.

4.1 Introduction

Direct imaging of exoplanets is an exciting and rapidly developing research field but has many technical challenges that still need to be solved. Current ground-based high-contrast imaging (HCI) systems, such as Subaru/SCExAO (Jovanovic et al., 2015), VLT/SPHERE (Beuzit et al., 2019), Gemini/GPI (Macintosh et al., 2014), and Magellan Clay/MagAO-X (Males et al., 2018), are complex instruments that deploy extreme adaptive optics (XAO) systems to correct wavefront aberrations from the Earth’s atmosphere and advanced coronagraphs to suppress star light. The goal of these systems is to reveal exoplanets at small angular separations ($< 1''$) and high contrast ($< 10^{-4}$). An XAO system consists of a primary wavefront sensor (WFS), such as the Shack-Hartman (Platt & Shack, 2001) or Pyramid (Ragazzoni, 1996) WFS, and a deformable mirror (DM) with high actuator count for wavefront correction. The current state-of-the-art performance in the near-infrared (NIR) is a post-processed contrast of $\sim 10^{-6}$ at 200 milliarcseconds by VLT/SPHERE (Vigan et al., 2015). The current HCI systems are capable of imaging young jovian planets on outer solar system-like scales around nearby stars (Chauvin et al., 2017; Macintosh et al., 2015; Marois et al., 2008).

4

However, one of the limitations of these systems are aberrations that originate from manufacturing limitations and misalignments in the optics downstream of the main WFS, and can therefore not be sensed by this WFS. We refer to these aberrations as non-common path aberrations (NCPA). During observations, the temperature, humidity, and gravitational vector slowly change, and with them the NCPA slowly evolve, resulting in quasi-static speckles in the science image (Martinez et al., 2013, 2012; Milli et al., 2016). These quasi-static speckles are a noise source (referred to as speckle noise; Racine et al. 1999) that prevent HCI instruments from reaching their full contrast at small angular separations as current observation strategies and post-processing methods have trouble completely removing them. Furthermore, as the wavelength of the science observations is generally different from the sensing wavelength of the main WFS, the residual wavefront error can also have a chromatic component (Guyon et al., 2018a). The ideal solution is to utilize the science image as a focal plane wavefront sensor (FPWFS) to measure the NCPA. Many different FPWFSs have been developed, and an overview is presented in Jovanovic et al. (2018).

In this work we present the first on-sky proof-of-principle demonstration of such a focal-plane wavefront sensing algorithm: spatial Linear Dark Field Control (LDFC; Miller et al. 2017, 2021, 2019). There is also a spectral LDFC variant (Guyon et al., 2017), which is not considered here, and therefore we will refer to spatial LDFC as LDFC. LDFC is a PSF stabilization technique that aims to lock the wavefront and maintain the deepest possible contrast achieved within the dark hole (DH; the region in which star light is suppressed by the coronagraph and XAO system) of a reference image. One major advantage is that speckle noise, the current limiting noise source in HCI, is suppressed, which can lead to tremendous gains in post-processed contrasts. LDFC monitors the light outside of the DH in the area we refer to as the bright field (BF), and uses intensity variations in the BF to derive corrections that remove the wavefront aberrations that would otherwise pol-

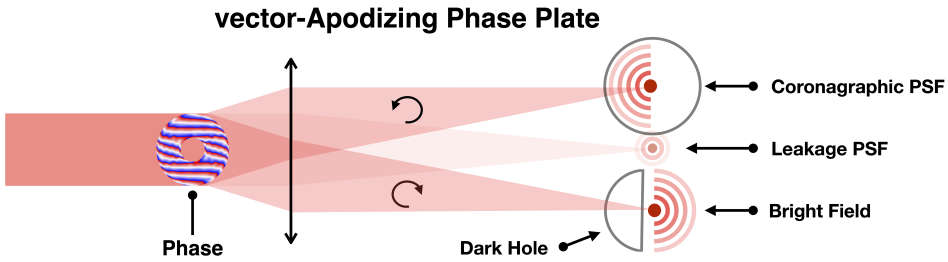


Figure 4.1: Schematic of the vAPP coronagraph. A pupil-plane optic that manipulates phase to generate two coronagraphic PSFs with opposite dark holes. Due to manufacturing errors, an extra, on-axis, non-coronagraphic leakage PSF is generated as well. Figure adapted from Bos et al. (2019).

lute the DH. It has several benefits over other techniques like pair-wise probing (Give'on et al., 2011) and speckle nulling (Bordé & Traub, 2006): 1) it is more time efficient, as it does not require multiple DM commands to derive the appropriate correction, and 2) it only monitors the BF and does not need to perturb the DH to derive a wavefront estimate (contrary to pair-wise probing and speckle nulling). For example, Currie et al. (2020a) demonstrated in lab experiments, under circumstances representative for space-based observatories, that LDFC recovers the initial contrast in 2-5 fewer iterations and 20-50 less DM commands compared to classical speckle nulling.

We implemented LDFC with the vector-Apodizing Phase Plate coronagraph (vAPP; Snik et al. 2012) installed on SCEXAO (Doelman et al., 2017). The vAPP is a pupil-plane coronagraph that manipulates phase to generate one-sided dark holes in the PSF and retains the BF, as shown in Figure 4.1. It is implemented as a liquid crystal half-wave retarder optic that has a varying fast-axis orientation which introduces the apodizing phase by means of the achromatic geometric phase (Pancharatnam 1956; Berry 1987). Due to the geometric phase, the opposite circular polarization states will receive opposite phase (Kim et al., 2015), and therefore the vAPP will generate two PSFs that have DHs on opposite sides, which are separated by integrating polarization sensitive gratings in the design (Otten et al., 2014). Note that the two coronagraphic PSFs have opposite circular polarization, and that, when the degree of circular polarization is non-zero, these two PSFs will not have the same brightness. Due to inevitable retardance errors in the half-wave retarder design, a third but small, non-coronagraphic, on-axis PSF is generated, which is generally referred to as the leakage PSF. To enable FPWFS, we use the Asymmetric Pupil vAPP (APvAPP) variant that integrates a pupil-plane amplitude asymmetry in the design (Bos et al., 2019). The pupil-plane amplitude asymmetry (Martinache, 2013) lifts the well-known sign ambiguity of even pupil-plane phase aberrations (Gonsalves, 1982; Paxman et al., 1992), and therefore allows LDFC to measure both odd and even pupil-plane phase aberrations.

The outline of this paper is as follows. In section 4.2 we present a short introduction

Table 4.1: Variables presented in section 4.2.

Variable	Description
E_{foc}	Focal-plane electric field.
E_0	Nominal coronagraph focal-plane electric field.
E_{ab}	Aberrated focal-plane electric field.
I_{BF}	Bright field intensity.
I_{DH}	Dark hole intensity.
I_0	Nominal focal-plane intensity.
ΔI	LDFC intensity signal.
G_{eigen}	Eigen mode control matrix.
M_{had}	Hadamard mode basis.
M_{eigen}	Eigenmode mode basis.
R_{Had}	Hadamard focal plane response matrix.
R_{eigen}	Eigen mode focal plane response matrix.
S_γ	Tikhonov regularization matrix.
γ	Regularization value.
s_i	Singular value of mode i .

to LDFC and how it is implemented on SCExAO. Then in section 4.3 we present and analyze the first proof-of-principle on-sky results. We discuss the results and conclude in section 4.4. All important variables used in this article are summarized in Table 7.1.

4.2 LDFC at SCExAO

4.2.1 Principle

LDFC relies on the linear response of the focal-plane intensity to phase aberrations in the pupil over a finite range of amplitudes to build a closed-loop control system. Specifically, it focuses on maintaining contrast within the entire DH, which requires LDFC to measure a response over the spatial frequencies that cover the DH. Here we show, in short, which regions in the focal-plane are selected by LDFC. A more extensive discussion is presented in Miller et al. (2021). In the small aberration regime (phase $\ll 1$ radian) we can write the focal-plane intensity I_{foc} as:

$$I_{foc} = I_0 + I_{ab} + 2\Re\{E_0 E_{ab}^*\}, \quad (4.1)$$

with E_0 and $I_0 = |E_0|^2$ the nominal focal-plane electric field and intensity respectively, E_{ab} and $I_{ab} = |E_{ab}|^2$ the electric field and intensity generated by the aberrations, and $\Re\{E\}$ the real part of E . Note that E_0 and E_{ab} are complex quantities. As in the DH the nominal focal-plane electric field is strongly suppressed by the coronagraph, we can assume that $E_{ab} \gg E_0$, and therefore the intensity I_{DH} is given by:

$$I_{DH} = |E_{ab}|^2 + 2\Re\{E_0 E_{ab}^*\}, \quad (4.2)$$

which has a quadratic response to aberrations and is therefore unsuitable to be used by LDFC. In the BF, which is the region outside of the DH, we can assume that $E_0 \gg E_{ab}$, resulting in the intensity I_{BF} :

$$I_{BF} = I_0 + 2\Re\{E_0 E_{ab}^*\}, \quad (4.3)$$

which has a linear response to changes in E_{ab} . Subtracting an unaberrated reference image I_0 from Equation 4.3 gives the signal that can be used to build a closed-loop control system:

$$\Delta I = I_{BF} - I_0 \quad (4.4)$$

$$= 2\Re\{E_0 E_{ab}^*\} \quad (4.5)$$

However, as discussed in Bos et al. (2019) and Miller et al. (2021), Equation 4.5 will only give a response to both odd and even wavefront aberrations when E_0 has real and imaginary components. The APvAPP integrates a pupil-plane amplitude asymmetry in its design (Bos et al., 2019), therefore has a E_0 with real and imaginary components, and is one of the most suitable coronagraphs to be used with LDFC.

4.2.2 SCExAO

We implemented LDFC on the Subaru Coronagraphic Extreme Adaptive Optics (SCExAO; Jovanovic et al. 2015) system, which is a HCI instrument located on the Nasmyth platform of the 8.2 meter Subaru telescope. It operates downstream of the AO188 system (Minowa et al., 2010), which provides an initial, low-order correction to the incoming wavefront. The main WFS of SCExAO is a visible Pyramid wavefront with an operational wavelength range of 600-900 nm (Lozi et al., 2019). SCExAO's DM is a Boston Micromachines DM with 45 actuators across the pupil, giving the instrument the ability to correct at separations up to $22.5\lambda/D$ ($\sim 1''$ at $1.65 \mu\text{m}$) in the focal plane. SCExAO can reach residual root-mean-square (RMS) wavefront errors (as reported by the AO telemetry) as good as ~ 70 nm (Currie et al., 2018). The real-time control is handled by the Compute and Control for Adaptive Optics (CACAO; Guyon et al. 2018b) package. It has 12 software channels to write DM commands to, which can be used by additional WFSs (like LDFC) or to apply static wavefront aberrations for testing purposes. CACAO automatically calculates reference offsets at high speed (~ 2 kHz) to prevent the Pyramid WFS from correcting the additional DM commands.

In addition to enabling high-contrast science (e.g. Goebel et al. 2018; Lawson et al. 2020; Currie et al. 2020b), SCExAO is serving as a technology demonstration testbed and tested many different FPWFSs on-sky (Martinache et al. 2014; Martinache et al. 2016; N'Diaye et al. 2018; Bos et al. 2019; Vievard et al. 2019; Bos et al. 2020). We use the vAPP coronagraph (Doelman et al. 2017; Miller et al. 2021) for the tests presented in this work. It was designed to provide a raw contrast of 10^{-5} between 2 and $11 \lambda/D$ for J-, H-, and K-band. To prevent spectral smearing by the polarization grating in the design, the vAPP can only operate with narrowband filters or an integral-field spectrograph (IFS). For FPWFS tests we use the narrowband filter ($\lambda = 1550$ nm; $\Delta\lambda = 25$ nm), and science

observations use the IFS CHARIS (Groff et al., 2014) that operates in J- to K-band. FP-WFS with this vAPP is enabled by two phase diversity holograms encoded in the design, as well as the pupil-plane amplitude asymmetry that was added to block a dead actuator (Bos et al., 2019). The camera used for LDFC was the internal NIR camera (C-RED 2; Feautrier et al. 2017) and was set to provide images with a size of 128×128 pixels. The pixel scale of the detector is 15.6 milliarcseconds per pixel, and therefore the PSF was sampled at ~ 2.6 pixels per λ/D . The images are aligned with a numerical reference PSF to eliminate tip/tilt errors. LDFC is implemented in Python, which allows for rapid prototyping and easy interfacing with the instrument, and uses the HCIPy package (Por et al., 2018). The current implementation of LDFC runs at approximately 20 Hz, limited by the speed of the algorithm used for co-aligning each image and the matrix-vector multiplication in the wavefront control loop. This speed is still sufficient for on-sky demonstration and stabilization of slowly evolving aberrations. The control loop is implemented with a leaky integrator (Hardy, 1998).

4.2.3 Static wavefront error calibration

Before starting LDFC tests, we measure and correct any static wavefront errors that exist in the system. Reducing the static aberrations present in the system is important for two reasons. Firstly, as the reference image is derived on-sky, it is imperative that static aberrations be removed before the reference is built. Secondly, the equations in subsection 4.2.1 only hold in the linear regime (wavefront error $\lesssim 100$ nm RMS for H-band). Without reducing static aberrations, LDFC operation would be forced outside the linear regime, thereby affecting the performance and stability of the wavefront control loop. As LDFC does not provide absolute wavefront measurements, another algorithm is required to do this. We use a non-linear, model-based wavefront sensing algorithm (Bos et al., 2019) that measures and corrects the 30 lowest Zernike modes. The results of this calibration, performed on-sky immediately before the results presented in section 4.3, is shown in Figure 4.2. As shown by the leakage PSF in Figure 4.2a the low order aberrations are well-corrected, but there are still some higher order wavefront aberrations that remain uncorrected as seen by speckle structure in the DH hole of the upper coronagraphic PSF. The low-order wavefront correction derived by the algorithm is shown in Figure 4.2b, and has a 42 nm root-mean-square (RMS) and 250 nm peak-to-valley (PtV) wavefront error (WFE). The DM command has a notable structure, namely a relatively strong increase in phase at the edge of the pupil. This structure has been observed during other tests as well, and is thought to be a real structure that originates from the upstream AO188 system (Bos et al., 2019).

4.2.4 Reference image and bright pixel selection

The ΔI measurement in Equation 4.4 that drives the LDFC loop is calculated by subtracting a reference image I_0 from each aberrated science image, resulting in an image containing only the term $2\Re\{E_0 E_{ab}^*\}$ (Equation 4.5). The goal of LDFC is to drive this term to zero and thus, by extension, the aberrated image back to the reference image I_0 . It is then clear that the deepest recoverable contrast by LDFC is set by the contrast in the

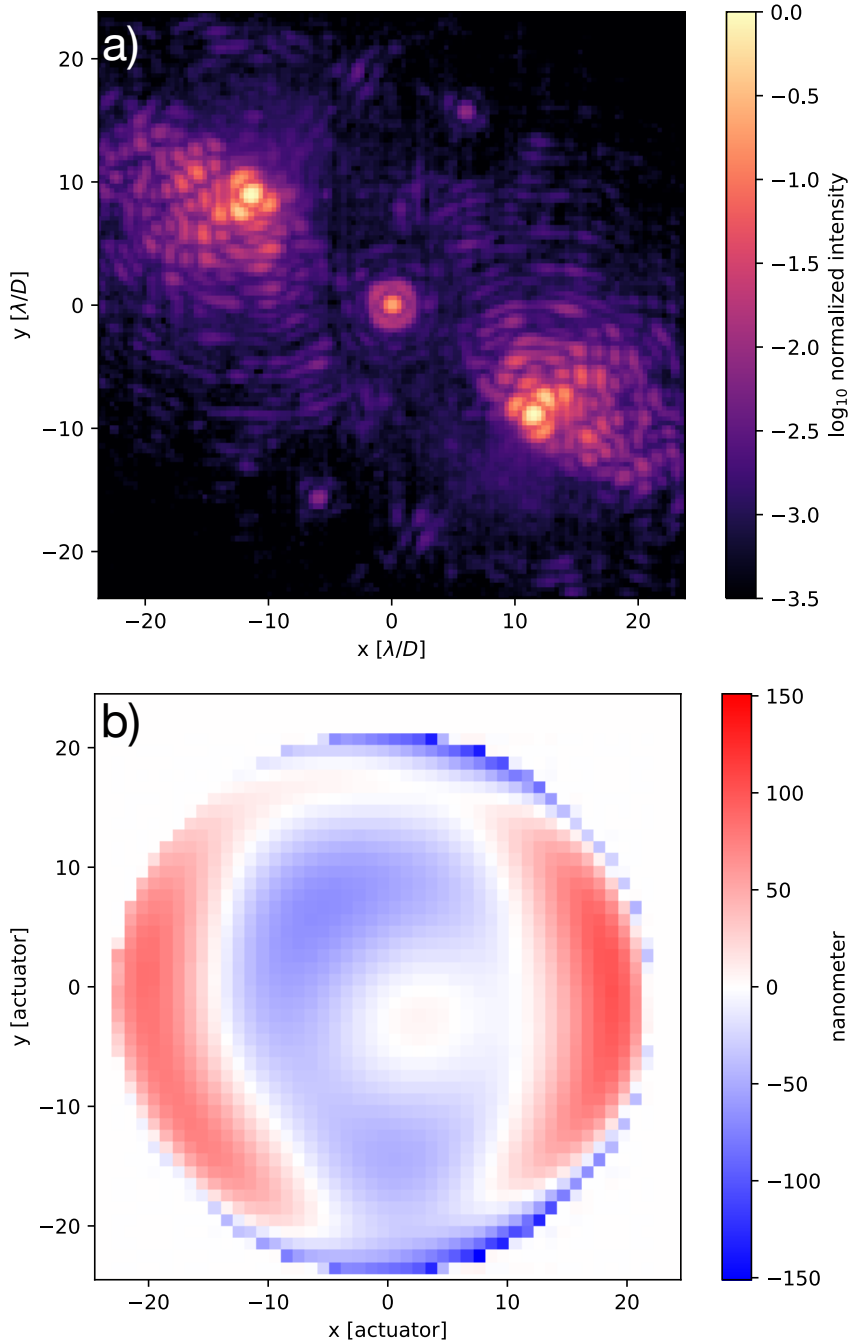


Figure 4.2: Calibrating static wavefront errors in SCEXAO during on-sky observations. a) The PSF after calibration. b) The derived DM command that corrects low-order statics.

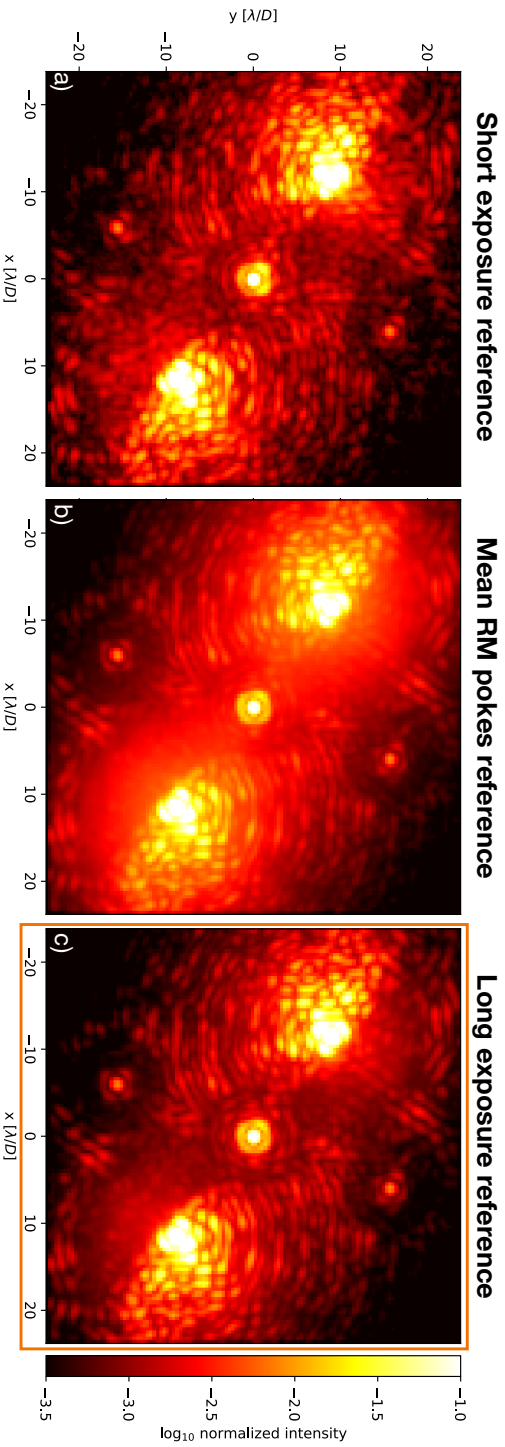
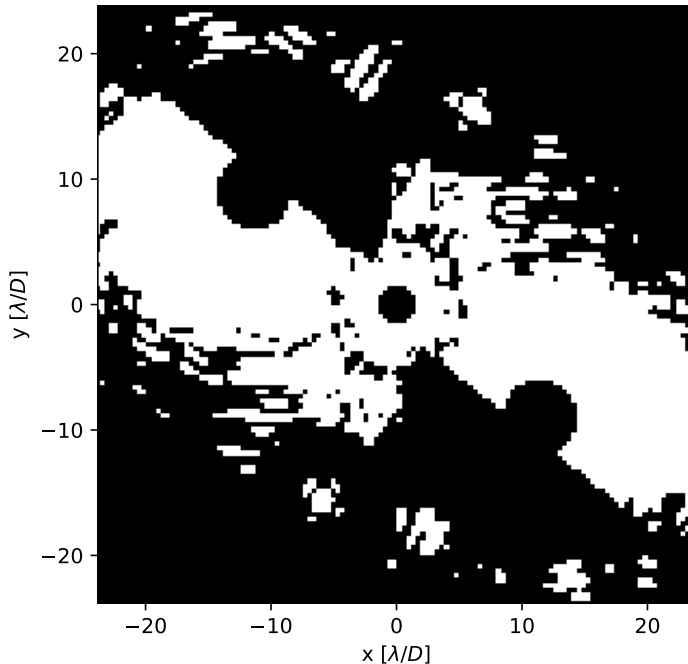


Figure 4.3: Reference images derived by various methods. All images are plotted with the same colorbar, which is shown on the right. The orange box denotes the reference that was used for the on-sky tests. a) Reference image calculated by taking the mean of 40 short exposure images taken in quick succession. b) Reference image measured by the calculating the mean of all images used for deriving the on-sky RM. c) Reference image calculated by taking the mean of 4000 short exposure images taken over ~ 5 minutes.

reference image. For tests on the bench using only the internal source and aberrations artificially introduced by the DM, it is trivial to acquire a good reference image after removing the static aberrations, as only a few co-added short exposure images are sufficient. For on-sky tests, it is not possible to use this reference image. This is due to the non-zero degree of circular polarization of the light emitted by the internal source, which can lead to a difference in intensity between the two coronagraphic PSFs of up to $\sim 10\text{-}20\%$. This difference in intensity between the PSFs does not exist during on-sky observations due to the unpolarized nature of stellar light, and thus a reference image utilizing both coronagraphic PSFs derived with the internal source will lead the LDFC loop to diverge if used on-sky. An obvious solution would be to individually normalize the coronagraphic PSFs. However, as the bright fields of the two coronagraphic PSFs partly overlap, it might not be as trivial as it seems. During the design process of a vAPP there is a constraint preventing the bright field of one coronagraphic PSF polluting the dark hole of the other. However, there is not (yet) a constraint that prevents the two bright fields of the two coronagraphic PSFs from overlapping. To prevent possible issues during normalization of the individual PSFs we did not pursue this solution yet. Therefore, we decided that the reference image used for on-sky implementation must also be measured during the observations. Other solutions to this problem are discussed in section 4.4.

The derivation of this on-sky reference image is non-trivial. During the internal source tests presented in Miller et al. (2021), it was sufficient to average a few short exposure images taken in a short timespan. This method will not work for on-sky operation because XAO residual wavefront aberrations will be present and distort the PSF. Figure 4.3a shows a reference image that consists of the mean of 40 short exposure images ($t_{int} \sim 1$ millisecond) that were taken in quick succession within one or two seconds. If this reference image were to be used by LDFC, it would drive the PSF back to this state, which is undesirable. To properly average out the effects of XAO residuals in the reference image, it should be calculated as the mean of hundreds to thousands images taken over the timespan of a few minutes. We want to keep this process and the process of acquiring the response matrix (RM; detailed in subsection 4.2.5) as efficient as possible to maximize the time available for science observations. The RM maps the DM commands to WFS measurements and is required for the LDFC wavefront control system. It is measured by poking many different DM modes and recording their focal-plane response. It would be most efficient if the RM and the reference image could be acquired simultaneously, especially because the RM acquisition process takes a few minutes and that would be sufficient time to average out XAO residuals. In Figure 4.3b we show a reference image that is the average of all of the images that were taken during the response matrix acquisition process. As shown in this figure, this method leads to a strong halo in the reference image, because the individual images are distorted by DM pokes. This halo strongly degrades the contrast, making this method unsuitable as well. To mitigate this effect, we came up with the following solution. During the RM acquisition process, there is for every DM mode a positive and negative poke (subsection 4.2.5). Between these opposite pokes we now add a short break (a few tens of milliseconds) where we do not poke the DM for LDFC, and during this time we record an image of the PSF. This will allow us to record thousands of images, that are not (or minimally) distorted by DM pokes, over a timespan of a few



4

Figure 4.4: The bright pixel map used for on-sky tests. The white region shows the pixels that are monitored by LDFC. The cores of the coronagraphic and leakage PSFs are blocked as they are saturated. The DHs are blocked as these pixels do not have a linear response to wavefront aberrations. Furthermore, we select only pixels that lie within the control radius ($22.5\lambda/D$) and have a normalized intensity of $\geq 10^{-3}$.

minutes without significantly interrupting the RM acquisition process. Figure 4.3c shows a reference image acquired in this way by averaging 4000 images taken over the span of ~ 5 minutes. The resulting reference image shows two well-defined DHs, with only a faint halo visible. The brightness of this halo is directly related to the level of XAO residuals, which means (as we will see in section 4.3) that, when the XAO correction improves compared to when the reference image was measured, the performance of LDFC will be affected. At the time of these tests, this was the best method to generate a reference image and was therefore the method we used.

After measuring the reference image, we derive the bright pixel map that selects the regions within the image that will be used by LDFC. Specifically, it will select pixels that have 1) a linear response, and 2) have a sufficient signal-to-noise ratio (SNR). The first step is to select pixels within the BF that have a linear response and lie within the control radius ($22.5\lambda/D$) of the DM. To boost the SNR at higher spatial frequencies, the PSF cores are strongly saturated and are subsequently not selected. Furthermore, we only select the

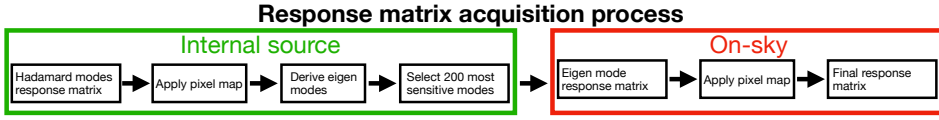


Figure 4.5: Process of acquiring the response matrix for on-sky operation. It is divided into a part that is done with the internal source before observations, and a part that is done during observations.

pixels that are sufficiently bright, and for this work have a normalized intensity of $\geq 10^{-3}$ with respect to the peak flux of the unsaturated PSF core. This threshold was empirically determined to work well for on-sky tests during various observation runs. The resulting bright pixel map used for the results presented in section 4.3 is shown in Figure 4.4.

4.2.5 Response and control matrix

The empirical relationship between changes in the focal plane intensity ΔI and DM shape is measured and stored as the response matrix (RM). The process of acquiring the RM for on-sky operation still relies on measurements taken with the internal source to derive the modal basis set to be used in closed-loop control on-sky (Miller et al., 2021). The full process for deriving the LDFC RM is shown in Figure 4.5. The first step in this process is to derive the LDFC modal basis set using the internal source and the DM, where we probe all the DM’s degrees of freedom (DoF) at high SNR using the Hadamard mode basis (M_{had} ; Kasper et al. 2004) to measure the Hadamard RM. The main advantage of using the Hadamard modes is that they have a high variance-to-peak ratio. This is important because the ΔI response strength scales with variance, and LDFC’s linearity limits the peak value that can be applied. Each mode in the basis is poked with a 40 nm RMS amplitude (a_p). The Hadamard RM (R_{had}) is measured as:

$$\Delta I_i = \frac{I_i^+ - I_i^-}{2a_p}, \quad (4.6)$$

$$R_{Had} = \begin{pmatrix} | & & | \\ \Delta I_1 & \dots & \Delta I_N \\ | & & | \end{pmatrix}, \quad (4.7)$$

with I_i^+ and I_i^- , the focal-plane intensities for the positive and negative actuations of mode i , multiplied with the binary bright pixel map (subsection 4.2.4). ΔI_i is the focal-plane response, and is reshaped from a 2D image to a 1D vector, and subsequent measurements form the columns of R_{had} . To improve the SNR of the focal-plane images I_i^+ and I_i^- , we average ten images. Measuring a high SNR Hadamard RM with the internal source, probing every mode once, takes around 20-25 minutes with the current implementation. The modal basis set used by LDFC, which we refer to as eigenmodes (M_{eigen}), is then derived by taking the singular value decomposition (SVD) of R_{had} such that:

$$R_{Had} = U_{Had} S_{Had} V_{Had}^*, \quad (4.8)$$

$$M_{eigen} = M_{Had} V_{Had}^*, \quad (4.9)$$

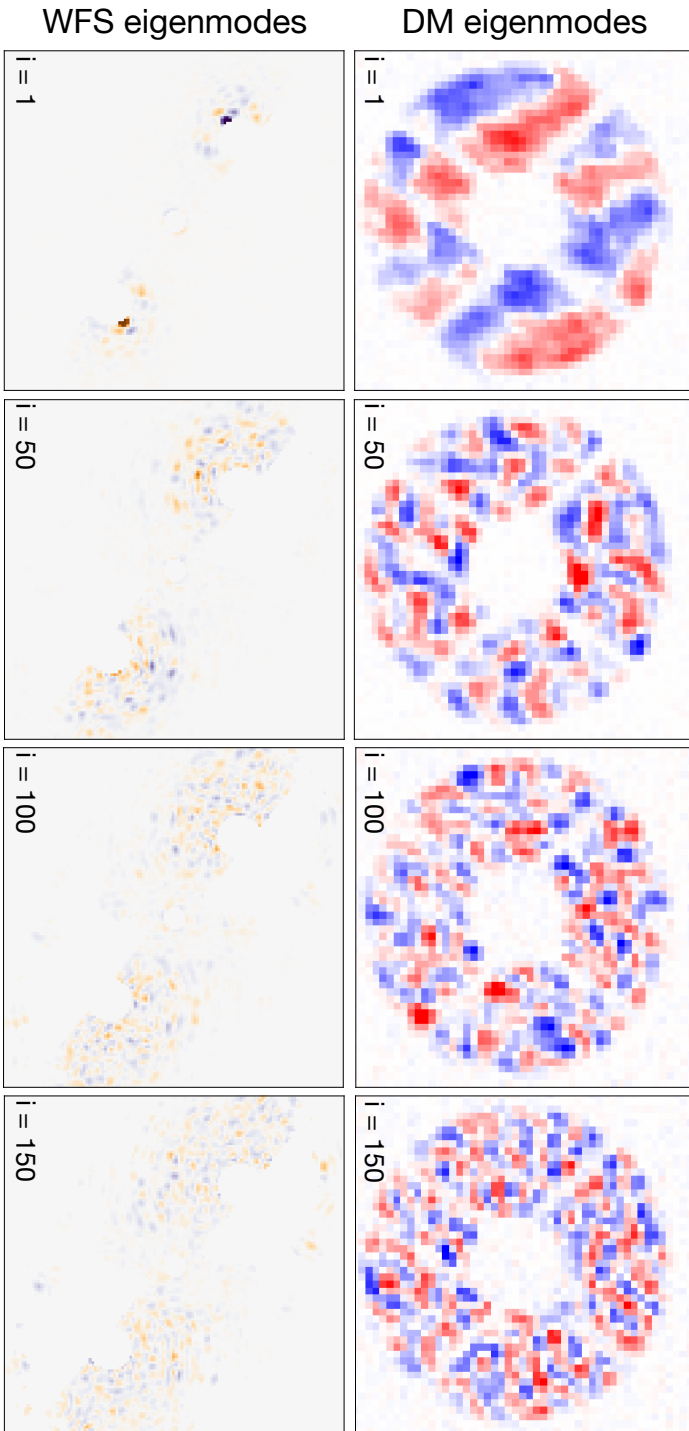


Figure 4.6: DM and WFS eigenmodes derived from R_{eigen} , which was acquired on-sky. The colorbars of the DM and WFS eigenmodes are the same for all subfigures. Note that for the WFS eigenmodes the bright pixel map of Figure 4.4 is applied.

with U_{Had} the WFS eigenmodes, S_{Had} a diagonal matrix with the singular values of the eigenmodes, and V_{Had} the DM eigenmodes. The eigenmodes form an orthogonal basis set that is ordered from high to low sensitivity, which also corresponds to a sorting from low to high spatial frequency that follows the structure of the PSF. An example of the eigenmodes, derived with the internal source, and the resulting focal plane response on-sky is shown in Figure 4.6 and clearly shows the ordering by spatial frequency.

Building the on-sky RM is more challenging due to the added noise by the post-XAO wavefront error residuals. To average out these effects, we probe every mode twenty times in quick succession. To do this for all DoF in the DM would put the total RM acquisition time well above one hour. This would be unacceptably long as it would take away time for science observations, and increase the chance that different modes are measured under different post-XAO residuals, adding more noise to the RM. Therefore, we decided to limit the modes in our modal basis set to the first 200 modes in M_{eigen} . This reduces the on-sky RM acquisition time to approximately 5 minutes. We chose the first 200 modes because: 1) these are the most sensitive modes in the mode basis, and 2) we found during tests with the internal source that this number of modes gives a good balance between acquisition speed and coverage of the dark hole. With this selected subset of eigenmodes, we then build the on-sky RM (R_{eigen}) by the same process as in Equation 4.6 and Equation 4.7 using M_{eigen} . This RM is then used for the LDFC control loop. Before any RM acquisition process, for either the Hadamard modes with the internal source or for the eigenmodes on-sky, we calibrate the static wavefront aberration with the method discussed in subsection 4.2.3.

For wavefront control we calculate the control matrix (G_{eigen}) by a numerical pseudo-inversion of R_{eigen} . We invert the matrix by a SVD with Tikhonov regularization, which suppresses noise from the more noisy high-order modes. The SVD of R_{eigen} is:

$$R_{eigen} = U_{eigen} S_{eigen} V_{eigen}^*, \quad (4.10)$$

with U_{eigen} the WFS eigenmodes, S_{eigen} a diagonal matrix with the singular values, and V_{eigen} the DM eigenmodes. The pseudo-inverse is therefore:

$$R_{eigen}^\dagger = V_{eigen} S_\gamma U_{eigen}^*, \quad (4.11)$$

with S_γ the Tikhonov regularization term. This term is written as:

$$S_\gamma = \text{diag} \left\{ \frac{s_i^2}{s_i^2 + \gamma} \frac{1}{s_i} \right\}, \quad (4.12)$$

with s_i the singular value of mode i , and γ the regularization value. By studying the singular value curve as plotted in Figure 4.7 (e.g. by looking at the point where the singular values steeply drop), and observing the stability of the LDFC control loop, we determine an appropriate value for γ . For the results presented in section 4.3 we set $\gamma = 0.1$. As an additional measure to ensure loop stability, we also implemented a modal gain. Higher order modes applied in the pupil plane correspond to higher spatial frequencies in

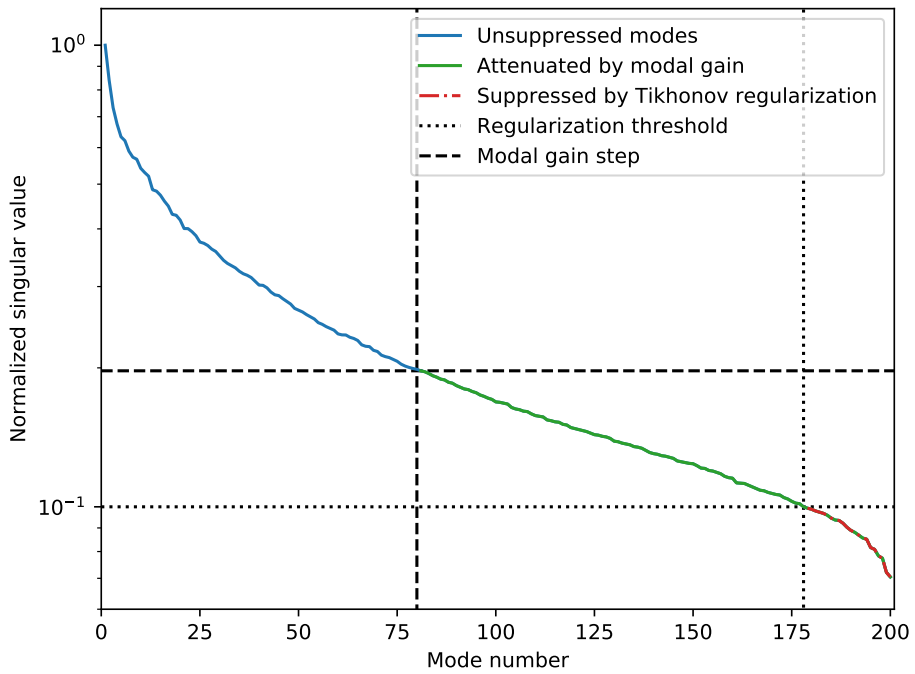


Figure 4.7: Singular value decomposition curve for the on-sky measured RM (R_{eigen}) showing the modal suppression and attenuation thresholds implemented by both Tikhonov regularization and modal gain.

the focal plane, as shown in Figure 4.6, and therefore have a lower SNR than the lower order modes. To counter this effect, we gave full weighting to the first 80 modes, and the other 120 modes had a weighting of 0.1. This is also plotted in Figure 4.7. Note that the modal gain is not the final gain; the modal gain is also multiplied by a loop gain. More appropriate weightings and a smoother modal gain function, instead of a step function, would likely improve the loop stability even more. This is left for future work.

4.3 On-sky demonstration

In the early morning of 17 September 2020, we tested LDFC on-sky during a SCEXAO engineering night. We observed the bright star Mirach ($m_H = -1.65$) in medium to good atmospheric conditions (seeing was reported to be $\sim 0.5'' - 0.8''$). As the target is very bright in H band, the exposure time of the NIR camera was set to 0.996 milliseconds. No other modules besides the NIR camera were used. The purpose of these tests was to demonstrate LDFC's performance in two specific cases: (1) in the presence of a static aberration consisting of random linear combinations of eigenmodes (Figure 4.6), and (2) in the presence of only atmospheric residual wavefront errors and naturally evolving NCPA. We present here the results of four different tests: two tests with different static aberrations induced on the DM (test A and B), and two tests with only on-sky atmospheric residuals to investigate the DH stabilization capabilities of the current implementation of LDFC (test C and D).

4

4.3.1 Static eigenmode aberration

First we demonstrate the ability of LDFC to correct for a static aberrations that are introduced on the DM. The introduced aberrations are much stronger than what generally occurs in HCI instruments, and therefore these tests should be considered to be a proof-of-concept for LDFC. They consist of a random linear combination of the eigenmodes following a flat power spectrum, and have a RMS WFE of ~ 90 nm. This RMS WFE is close to the non-linear regime for LDFC, which starts at ~ 100 nm RMS, and therefore we ran LDFC during these tests with a relatively low gain of 0.01. We chose for test A a duration of 2000 iterations (~ 110 sec) for both the open- and closed-loop datasets. For tests B we increased the number of iterations to 3000 (~ 160 sec) to investigate whether or not LDFC would converge towards a lower residual wavefront error compared to test A. There was approximately 15 minutes between the start of test A and B.

Here we present the results of two tests (test A and test B). Each test consists of a LDFC closed-loop dataset and an open-loop dataset, which were taken right after each other. Figure 4.8 and Figure 4.9 plot the mean open- and closed-loop PSF during the tests, and the introduced aberration. In both cases, LDFC dramatically improves the quality of the PSF, but does not completely bring it back to the reference state, which is shown in Figure 4.3c. LDFC is correcting low-order aberrations, as is clearly seen by comparing the leakage PSF for open- and closed-loop results. Control of the mid- and high-order spatial frequencies is shown by the removal of speckles throughout the DH. Figure 4.8d and

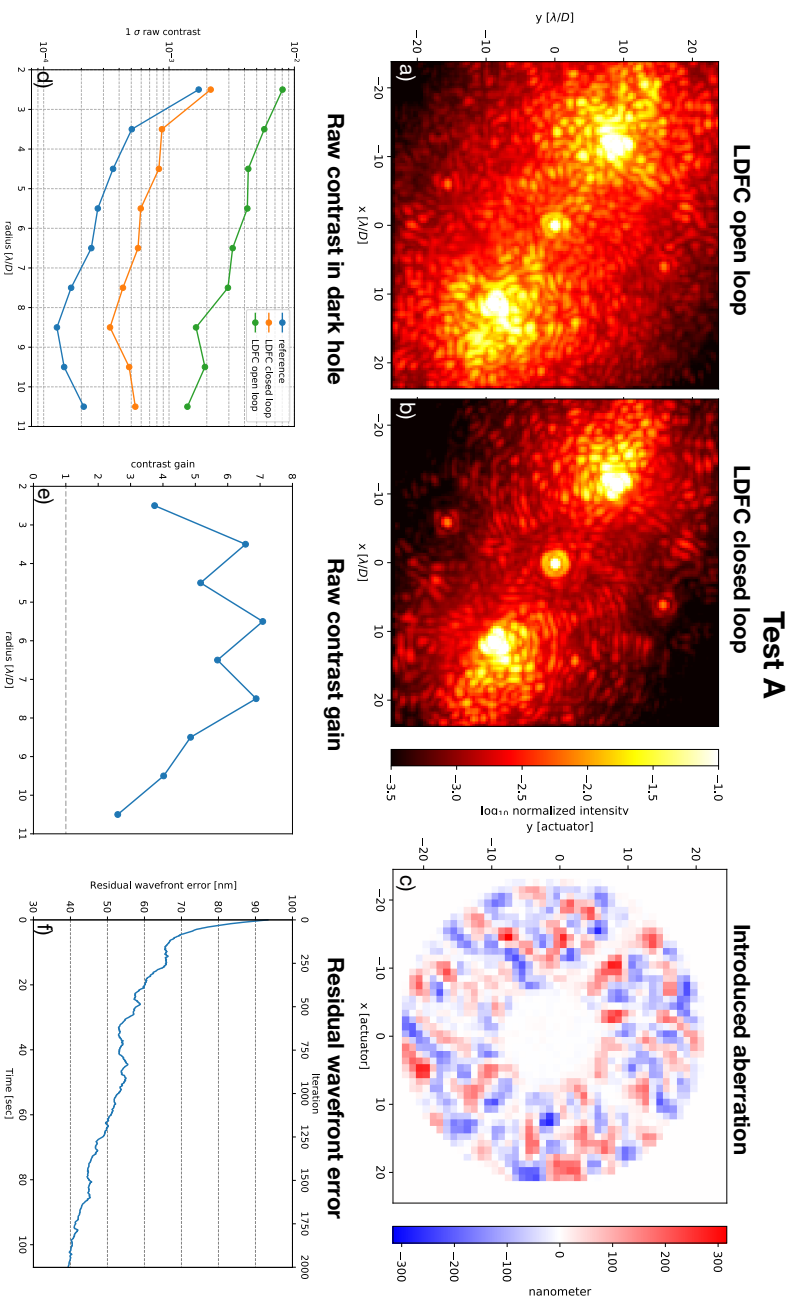


Figure 4.8: Mean PSF of open and closed-loop LDFC datasets with a static aberration introduced on the DM, and quantification of the raw contrast and residual wavefront error improvements. a) The open-loop PSF. b) The closed-loop PSF. c) The aberration introduced by the DM. d) The 1σ raw contrasts as a function of spatial frequency in the DH of the reference PSF, and the mean of the open and closed-loop LDFC dataset. e) The gain in raw contrast over the spatial frequencies in the DH. f) The residual wavefront error, calculated by adding the introduced aberration to the derived LDFC correction.

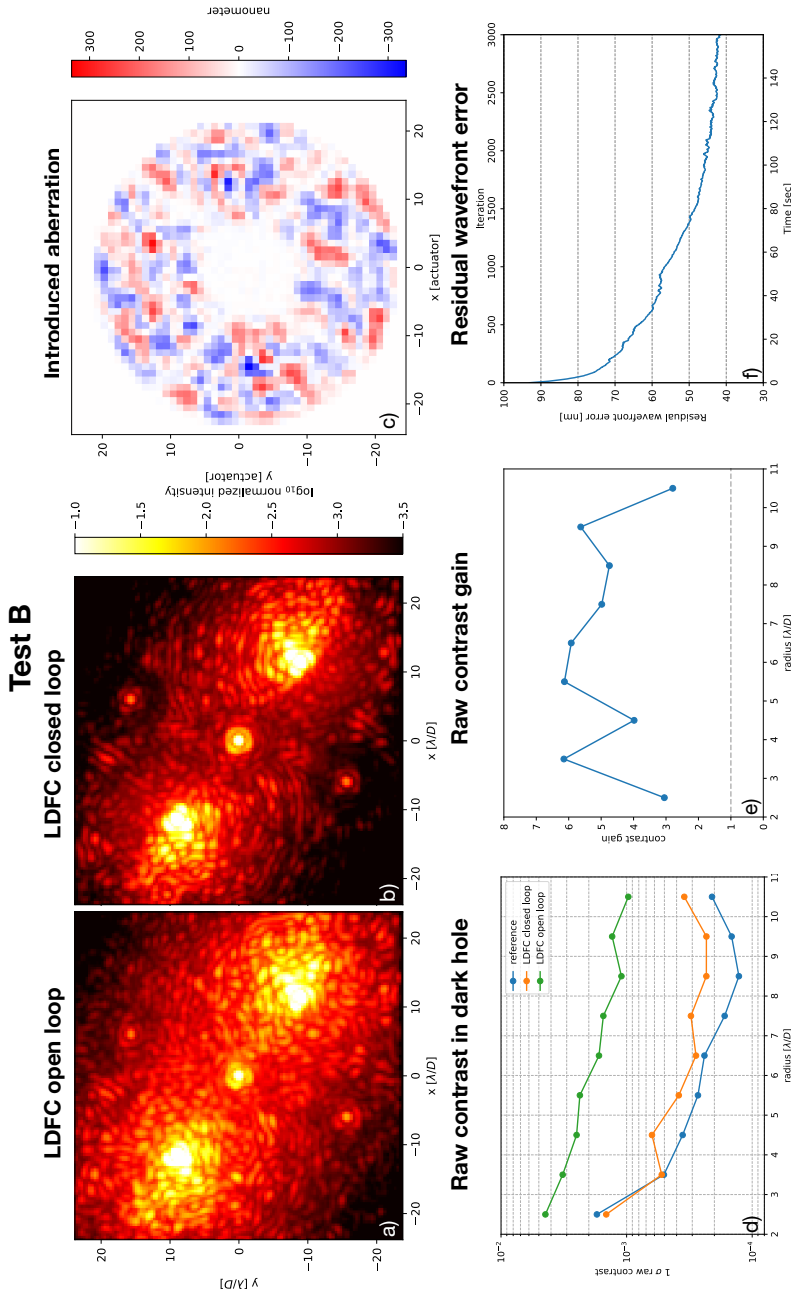


Figure 4.9: Mean PSF of open and closed-loop LDFC datasets with a static aberration introduced on the DM, and quantification of the raw contrast and residual wavefront error improvements. Note that a different aberration has been injected by the DM compared to Figure 4.8. a) The open-loop PSF. b) The closed-loop PSF. c) The aberration introduced by the DM. d) The 1σ raw contrasts as a function of spatial frequency in the DH of the reference PSF, and the mean of the open and closed-loop LDFC dataset. e) The gain in raw contrast over the spatial frequencies in the DH. f) The residual wavefront error, calculated by adding the introduced aberration to the derived LDFC correction.

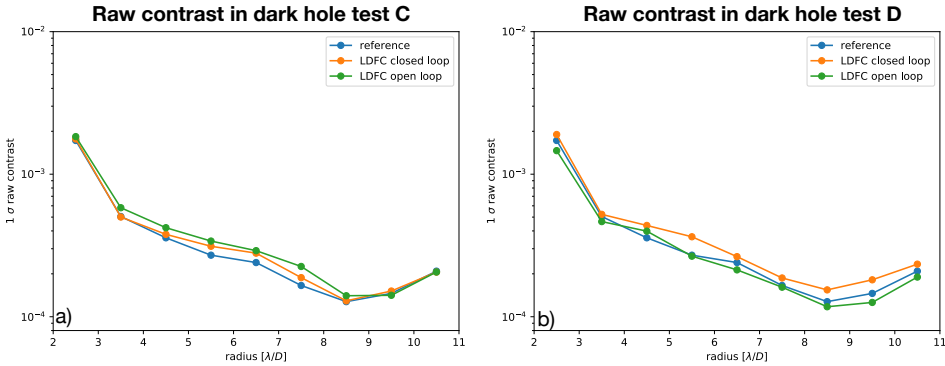


Figure 4.10: Raw contrast in the DH for the reference PSF, and the mean PSF of the open- and closed-loop LDFC data for the two sets of tests. No static aberration was introduced on the DM.

4

Figure 4.9d plot the raw contrast of the reference PSF, the mean open-loop PSF and the mean closed-loop PSF, and shows that LDFC is able to greatly increase the raw contrast. We define the raw contrast as the spatial variations in intensity in the DH by determining at a given distance from the star the standard deviation of the intensity inside $1 \lambda/D$ wide annuli covering the DHs of both coronagraphic PSFs. Note that the contrast metric adopted here provides optimistic contrast estimates at small distances from the star as the small sample statistics are not properly taken into account (Jensen-Clem et al., 2017; Mawet et al., 2014). The contrast gain is between a factor 3 and 7 and is plotted per spatial frequency in Figure 4.8e and Figure 4.9e. Especially Figure 4.9d shows that LDFC is able to almost return the PSF to its initial raw contrast. Figure 4.8f and Figure 4.9f show the residual wavefront error, which was calculated by summing the DM channel with the introduced aberration and the DM channel with the derived correction. These graphs show that LDFC is clearly correcting the aberration and is able to reduce the RMS WFE from ~ 90 nm RMS to ~ 40 nm RMS, which seems to be approximately the convergence point of both tests. It is likely that the reason for the convergence point is the noise caused by fast changing XAO residuals. In short exposure images, as were used in these tests, the XAO residuals do not average out and change too quickly for LDFC to correct, which makes it hard for LDFC to measure the artificially injected static WFE by the DM. In future on-sky tests this interpretation can be tested by performing similar tests under different levels of XAO correction to see if the convergence point changes as well. The slight difference in convergence speed can be explained by changes in the XAO correction in the 15 minutes between the two tests.

4.3.2 On-sky atmospheric residuals

The stability of the PSF during observations is important for the post-processed contrast. An ultra-stable, temporally well correlated PSF enables more accurate removal using post-processing (e.g. Soummer et al. 2011). Here we show the ability of the cur-

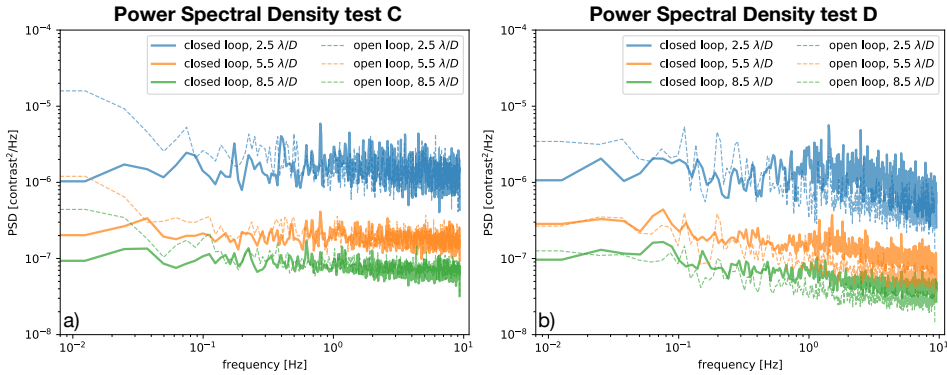


Figure 4.11: Power spectral density (PSD) of the PSF stability during the open- and closed-loop LDFC tests in three different spatial frequency bins in the DH. Subfigure a) shows the results for tests C, and subfigure b) for tests D.

rent LDFC implementation to stabilize the PSF with atmospheric turbulence and evolving NCPA (so no artificially induced wavefront error). We present two tests (test C and D); each tests consists of an open- and closed-loop LDFC dataset that were conducted successively in the same atmospheric conditions. Test C was done ten minutes after measuring the reference image, and the open- and closed-loop dataset each have a duration of 110 seconds. Test D was done approximately twenty minutes later (thirty minutes after acquiring the reference image) with the open- and closed-loop dataset each spanning a duration of ~ 210 seconds. This allows us to evaluate the effect of a closed LDFC loop on the PSF stability. The gain for these tests was set to 0.1.

First we compare the average PSF computed over the entire open- and closed-loop datasets to the reference PSF. In Figure 4.10, the 1σ raw contrast in the DH is plotted for the reference PSF, and the mean of the LDFC open- and closed-loop data. The results for test C are shown in Figure 4.10a. It shows that the open-loop data is slightly worse than the reference PSF, and that when the LDFC loop is closed the raw contrast slightly improves compared to the open-loop data. In Figure 4.10b we show the results of test D. During these tests (twenty minutes later), the XAO correction improved compared to test C, making the mean of the open-loop data slightly better than the reference PSF. When the LDFC loop closed, the raw contrast slightly degraded, because LDFC tried to drive the image back to the reference image which was more aberrated than the open-loop images.

As LDFC is meant to be a stabilization technique, it is also interesting to analyze the temporal stability of the DH. To this end, we calculated the normalized mean intensity of three different spatial frequency bins ($2.5, 5.5, 8.5 \lambda/D$) in the DH throughout these tests. It is calculated for every individual iteration, and the resulting values are subsequently averaged over 50 iterations to reduce the effect of high temporal frequency variations. Table 4.2 shows the average and 1σ standard deviation of these time series (specifically, using the 50 iteration averages). In test C, the table shows that both the average and the

Table 4.2: Average and 1σ standard deviation of the normalized mean intensity time series during the tests with on-sky atmospheric residuals.

Spatial frequency bin	Test C		Test D	
	Open loop	Closed loop	Open loop	Closed loop
2.5 λ/D	$4.64 \cdot 10^{-3} \pm 6.7 \cdot 10^{-4}$	$4.31 \cdot 10^{-3} \pm 3.0 \cdot 10^{-4}$	$2.95 \cdot 10^{-3} \pm 3.6 \cdot 10^{-4}$	$4.00 \cdot 10^{-3} \pm 2.4 \cdot 10^{-4}$
5.5 λ/D	$1.75 \cdot 10^{-3} \pm 2.0 \cdot 10^{-4}$	$1.64 \cdot 10^{-3} \pm 1.3 \cdot 10^{-4}$	$1.03 \cdot 10^{-3} \pm 1.1 \cdot 10^{-4}$	$1.38 \cdot 10^{-3} \pm 9 \cdot 10^{-5}$
8.5 λ/D	$1.18 \cdot 10^{-3} \pm 1.3 \cdot 10^{-4}$	$1.11 \cdot 10^{-3} \pm 9 \cdot 10^{-5}$	$7.2 \cdot 10^{-4} \pm 7 \cdot 10^{-5}$	$9.4 \cdot 10^{-4} \pm 6 \cdot 10^{-5}$

1σ standard deviation improved when the LDFC loop closed. This means that not only the intensity in DH improved, but also the temporal stability (i.e. less variability). The values presented in Table 4.2 for test D were calculated using only the values in the second half of the open- and closed-loop datasets. This is because when the LDFC loop closed it took roughly half the dataset to converge to a stable correction (determined by analyzing the LDFC DM telemetry). The table shows that for test D, the mean of the time series degraded when the LDFC loop closed, but that the 1σ deviation improved. This means that the intensity in the DH degraded, because LDFC tried to drive the image back to the reference image (which has a higher intensity in the DH), but that the stability improved. These tests show that LDFC is able to stabilize the mean intensity in the DH, and that a good reference image is very important to also improve the intensity in the DH.

However, it is most relevant to analyze the PSF variations during these tests. This is because these variations are hard to calibrate in post-processing, and therefore will determine the eventual post-processed raw contrast. To this end, we plot the Power Spectral Density (PSD) in the same spatial frequency bins as above for the open- and closed-loop LDFC data in Figure 4.11. These curves were calculated as follows: the mean PSF was subtracted from all images in the data set; then, for every pixel, the PSD was calculated using the Welch method (Welch, 1967). These PSDs were subsequently averaged per spatial frequency bin to reduce the effects of noise. For tests C (Figure 4.11a) the results are quite clear: LDFC successfully removes power in the lower temporal frequencies ($\lesssim 0.2$ Hz for 5.5 and 8.5 λ/D , and $\lesssim 0.4$ Hz for 2.5 λ/D). Specifically, the power at $\sim 10^{-2}$ Hz decreased by a factor ~ 20 , 7, and 4 at 2.5, 5.5, and 8.5 λ/D , respectively. This decrease in performance for higher spatial frequencies can be explained by the lower SNR at these positions in the focal plane. Again, for test D we only include the second half of the dataset, because in the first half LDFC is still converging. The results for test D (Figure 4.11b) are less clear than what we found for test C. The low temporal frequencies were not as dominant, so only in the 2.5 λ/D bin do we observe that LDFC reduces the power at frequencies $\lesssim 0.05$ Hz. Also, for the 2.5 λ/D bin there are peaks at 0.1, 0.2 and 0.3 Hz which are suppressed by LDFC. For all spatial frequency bins there is more power in high temporal frequencies ($\gtrsim 0.5$ Hz) for the closed-loop data compared to the open-loop data. The current hypothesis to explain this is that LDFC added intensity to the DH to match the reference image. This led to an increase in speckle noise, because the atmospheric speckles now interfere with a higher intensity structure in the DH.

We did not experience any events during which the XAO correction degraded compared to test C. In such a case, we expect that there would be a slight improvement in contrast for the closed-loop data compared to the open-loop data, because the LDFC loop would suppress slowly evolving variations. A result similar to the results presented in test C. However, in the current implementation of LDFC the loop speed is limited to 20 Hz and therefore not capable of lowering the high temporal frequency XAO residuals. That would mean that the contrast in the closed-loop data would still be (much) worse compared to the reference image.

4.4 Discussion and conclusion

The work presented in this paper concludes the first successful proof-of-concept on-sky demonstration of spatial LDFC with the APvAPP at Subaru/SCEXAO. The results show that LDFC is a promising technique for correcting NCPA, stabilizing the PSF, and maintaining raw contrast during HCI observations, which will dramatically improve the post-processed contrast. In this paper, we present a new, faster process to efficiently acquire a high-SNR RM for on-sky operation in which we build our eigenmodes first with the internal source. Integrated within this process is the simultaneous measurement of a long exposure reference image. The current LDFC implementation at SCEXAO uses the narrowband filter at 1550 nm ($\Delta\lambda = 25$ nm), is coded in Python and runs at ~ 20 Hz in closed loop.

We have demonstrated that LDFC can partially correct static aberrations introduced with the DM while on-sky. We have shown, for the examples presented here, that the raw contrast increases by a factor 3 – 7 over the dark hole (DH), and that the RMS WFE decreases by ~ 50 nm from 90 nm to 40 nm. The reason that LDFC converged to a WFE of 40 nm RMS is likely the noise caused by fast changing XAO residuals. In short exposure images, as were used in these tests, the XAO residuals do not average out and change too quickly for LDFC to correct. This makes it hard for the current implementation of LDFC to measure and correct these artificially injected aberrations. Singh et al. (2019) studied this effect in simulation, and their results qualitatively match with what we find here. Furthermore, we have tested LDFC with just residual atmospheric aberrations and naturally evolving NCPA. We have shown that the current LDFC implementation is able to stabilize the mean intensity in the DH. We also showed, when analyzing the PSF stability, that LDFC suppresses evolving aberrations that have timescales of < 0.1 – 0.4 Hz, which is expected considering the 20 Hz loop speed. In the situation that XAO residuals were comparable to when the reference image was measured, closing the LDFC loop reduced the power at 10^{-2} Hz by a factor of ~ 20 , 7, and 4 for spatial frequency bins at 2.5, 5.5, and $8.5 \lambda/D$, respectively. When the XAO correction improved compared to the reference image measurement, we found smaller power improvements for temporal frequencies < 0.4 Hz. In this case, the LDFC loop degraded the contrast in the DH, because it tried to drive the image back towards the reference image. This led to an increase in power for temporal frequencies > 0.4 Hz. Due to the limited durations of these tests (~ 100 – 200 seconds) we could not conclusively determine if we succeeded in the stabilization of quasi-static speckles caused by NCPA as our measurements are dominated by XAO residuals. Therefore, open- and closed-loop tests of longer duration (tens of minutes) are required to fully understand to what extent LDFC can stabilize NCPA.

We refined our methods during multiple SCEXAO engineering nights, the latest results being presented in this work, and we have identified the following challenges that have to be overcome before LDFC can be offered as observing mode for SCEXAO. The tests that corrected static, injected wavefront aberrations were limited by the effect of XAO residuals on short exposure images. We conclude that there are two solutions to overcome this problem: (1) Instead of using single, short exposure images in the LDFC control loop,

use the average of hundreds to thousands of images measured over timescales of tens of seconds to minutes to average out the XAO residuals. This would significantly lower the control loop speed, but to a level that should still be sufficient to control quasi-static aberrations. The current implementation of LDFC can be used to test this solution.

(2) Improve the loop speed to several hundred to a thousand Hz to allow LDFC to directly control the XAO residuals. This would enable LDFC to simultaneously address chromatic residual wavefront errors from the XAO system. The current limiting factors in loop speed are the matrix-vector multiplication of G_{eigen} and ΔI , and the image alignment. The matrix-vector multiplication is currently processed on the CPU, and we plan to move this to the GPU. For the image alignment, we currently compare the entire image (128×128 pixels) to a centered, reference image to determine the offset. It is actually not required to use all information in the image to determine this, and moving forward we plan to select only the leakage PSF in a 32×32 pixel window. Together, we hope that these upgrades allow for a loop speed of ~ 200 Hz. Further improvements of the loop speed would require more optimization of the code and full integration into the real-time control software CACAO (Guyon et al., 2020).

As discussed in subsection 4.2.4, a good reference image is of utmost importance. It sets the contrast levels to which LDFC will converge, and determines the stability of the loop. Ideally, it would be best to match the reference image to the images used in the LDFC control loop, which depends on the speed of the LDFC control loop as discussed above.

In the case of a fast ($> 0.1 - 1$ kHz) LDFC loop using short exposure images, the best solution is an internal source reference image as that will not contain the XAO halo and thus provide the best possible contrast. As discussed in subsection 4.2.4, this is currently problematic as there is an intensity imbalance between the two coronagraphic PSFs of the vAPP due to a non-zero degree of circular polarization with internal source measurements. This can be resolved by either using an unpolarized light source, a new vAPP design that is not sensitive to the degree of circular polarization (Bos et al., 2020), or more sophisticated PSF normalization methods that correct for this. Another solution is to run LDFC on a single coronagraphic PSF. The major disadvantage of this solution is that it increases the null space of the algorithm by allowing for a subset of aberrations (cross-talk between amplitude and phase aberrations) that pollute the dark hole and are not measurable in the BF of a single PSF (Sun, 2019). Whether this increased null space will have a significant impact on on-sky operations will have to be further explored.

A slow (< 1 Hz) LDFC loop that uses long exposure images is best combined with a long exposure reference image as both contain a XAO halo. In this work we have found, when atmospheric conditions change and the reference PSF becomes worse than the LDFC open-loop PSF, that LDFC degrades the DH to match the reference PSF, and in the worst cases leads to loop divergence. This means that we need a reference PSF that is always better than the open-loop LDFC PSF. A promising solution for re-measuring the reference PSF is the Direct Reinforcement Wavefront Heuristic Optimization algorithm (DR WHO; Vievard et al. 2020). DR WHO continuously monitors the PSF quality, and selects from continuous image streams the most suitable reference image update by evaluating a performance metric of choice. In the case of LDFC this performance metric could be the

contrast in the DH.

In this work we have shown that when practical reasons prevent the use of either of the above described ideal solutions, a mix of both solutions can also work. We combined a long exposure reference image with short exposure images in a relatively slow control loop. As discussed above, this reference image will also have to be continuously updated when the XAO residuals change. The extent to which such a combined solution degrades the best possible performance of LDFC will have to be investigated in future work.

Besides mitigation of the major challenges posed by the XAO residuals noise and reference images, there are also other, more minor upgrades that we have identified for the current LDFC implementation. During SCEXAO engineering nights we regularly encounter “low-wind effect” events (Sauvage et al. 2015; Milli et al. 2018), that heavily distort the PSF. In its current form, LDFC is not able to fully sense and correct these effects as they appear as piston, tip, and tilt aberrations across the four quadrants of the telescope pupil separated by the spiders. These modes are not currently included in our eigenmode basis set. In order to operate during such events we will test two solutions: a) include the appropriate modes (piston, tip, and tilt modes for the segments in the telescope pupil) in the mode basis that LDFC controls, and b) run the Fast and Furious (Bos et al., 2020) focal-plane wavefront sensing algorithm on the leakage PSF simultaneously with LDFC.

4

Results presented in this work were obtained with the C-RED 2 camera (Feautrier et al., 2017). Recently, SCEXAO acquired a C-RED One as an additional NIR camera, which is particularly exciting for FPWFS as it offers strongly reduced read-out noise ($< 1 e^-$ versus $< 30 e^-$) and dark current ($80 e^-/\text{pixel}/\text{sec}$ versus $600 e^-/\text{pixel}/\text{sec}$) compared to the C-RED 2. SCEXAO also feeds the z- to J-bands (800 - 1400 nm) to the MKID Exoplanet Camera (MEC; Walter et al. 2020), which utilizes the Microwave Kinetic Inductance Detector (MKID) technology for high-contrast imaging. This camera provides read noise free, and fast time domain images at a spectral resolution of 5-7. Future LDFC tests will therefore either use the C-RED One or MEC.

As soon as we have addressed the above mentioned challenges and upgrades, we intend to offer LDFC as an observing mode for SCEXAO. We foresee two possible observing modes: (a) The C-RED One as the science camera and FPWFS, which limits the observations to narrow bandwidths to prevent spectral smearing by the polarization grating integrated in the vAPP design. This solution would completely eliminate the non-common path and thus, in theory, should be able to provide the best wavefront correction. (b) The C-RED One as the FPWFS and the IFS CHARIS (Groff et al., 2014) as the science camera. Both cameras would share the light, with the C-RED One providing wavefront sensing and control with LDFC, while CHARIS would do simultaneous science observations in J-, H-, and K-band. This solution would strongly reduce the non-common path, but not completely eliminate it. The improvement in contrast in this mode would depend on the number and specifications of the optical elements in both paths. We did not consider using CHARIS for focal-plane wavefront sensing, because of the long readout times of its HAWAII-2RG detector.

In this paper, we have shown through on-sky tests that spatial LDFC combined with an APvAPP is a promising focal-plane wavefront sensor for high-contrast imaging instruments to directly image exoplanets. We have identified and provided solutions to multiple challenges that have to be overcome before LDFC can effectively sense NCPA, suppress quasi-static speckles, and stabilize the PSF. We are currently working towards offering LDFC as an observing mode on SCExAO which would enable FPWFS to be used regularly during observations and result in gains in the post-processed contrast.

Bibliography

- Berry, M. V. 1987, *Journal of Modern Optics*, 34, 1401
- Beuzit, J.-L., Vigan, A., Mouillet, D., et al. 2019, arXiv preprint arXiv:1902.04080
- Bordé, P. J., & Traub, W. A. 2006, *The Astrophysical Journal*, 638, 488
- Bos, S. P., Doelman, D. S., Miller, K. L., & Snik, F. 2020, in *Adaptive Optics Systems VII*, Vol. 11448, International Society for Optics and Photonics, 114483W
- Bos, S. P., Doelman, D. S., Lozi, J., et al. 2019, *Astronomy & Astrophysics*, 632, A48
- Bos, S. P., Vievard, S., Wilby, M. J., et al. 2020, *A&A*, 639, A52, doi: 10.1051/0004-6361/202037910
- Chauvin, G., Desidera, S., Lagrange, A.-M., et al. 2017, *Astronomy & Astrophysics*, 605, L9
- Currie, T., Brandt, T. D., Uyama, T., et al. 2018, *The Astronomical Journal*, 156, 291
- Currie, T., Pluzhnik, E., Guyon, O., et al. 2020a, *Publications of the Astronomical Society of the Pacific*, 132, 104502
- Currie, T., Brandt, T. D., Kuzuhara, M., et al. 2020b, *The Astrophysical Journal Letters*, 904, L25
- Doelman, D. S., Snik, F., Warriner, N. Z., & Escuti, M. J. 2017, in *Techniques and Instrumentation for Detection of Exoplanets VIII*, Vol. 10400, International Society for Optics and Photonics, 104000U
- Feautrier, P., Gach, J.-L., Greffe, T., et al. 2017, in *Image Sensing Technologies: Materials, Devices, Systems, and Applications IV*, Vol. 10209, International Society for Optics and Photonics, 102090G
- Give'on, A., Kern, B. D., & Shaklan, S. 2011, in *Techniques and Instrumentation for Detection of Exoplanets V*, Vol. 8151, International Society for Optics and Photonics, 815110
- Goebel, S., Currie, T., Guyon, O., et al. 2018, *The Astronomical Journal*, 156, 279
- Gonsalves, R. A. 1982, *Optical Engineering*, 21, 215829
- Groff, T. D., Kasdin, N. J., Limbach, M. A., et al. 2014, in *Ground-based and Airborne Instrumentation for Astronomy V*, Vol. 9147, International Society for Optics and Photonics, 91471W
- Guyon, O., Mazin, B., Fitzgerald, M., et al. 2018a, in *Adaptive Optics Systems VI*, Vol. 10703, International Society for Optics and Photonics, 107030Z
- Guyon, O., Miller, K., Males, J., Belikov, R., & Kern, B. 2017, arXiv preprint arXiv:1706.07377
- Guyon, O., Sevin, A., Ltaief, H., et al. 2018b, in *Adaptive Optics Systems VI*, Vol. 10703, International Society for Optics and Photonics, 107031E
- Guyon, O., Sevin, A., Ferreira, F., et al. 2020, in *Adaptive Optics Systems VII*, Vol. 11448, International Society for Optics and Photonics, 114482N
- Hardy, J. W. 1998, *Adaptive optics for astronomical telescopes*, Vol. 16 (Oxford University Press on Demand)
- Jensen-Clem, R., Mawet, D., Gonzalez, C. A. G., et al. 2017, *The Astronomical Journal*, 155, 19
- Jovanovic, N., Martinache, F., Guyon, O., et al. 2015, *Publications of the Astronomical Society of the Pacific*, 127, 890
- Jovanovic, N., Absil, O., Baudoz, P., et al. 2018, in *Proc. SPIE*, Vol. 10703, Adaptive Optics Systems VI
- Kasper, M., Fedrigo, E., Looze, D. P., et al. 2004, *JOSA A*, 21, 1004
- Kim, J., Li, Y., Miskiewicz, M. N., et al. 2015, *Optica*, 2, 958
- Lawson, K., Currie, T., Wisniewski, J. P., et al. 2020, *The Astronomical Journal*, 160, 163
- Lozi, J., Jovanovic, N., Guyon, O., et al. 2019, *Publications of the Astronomical Society of the Pacific*, 131, 044503
- Macintosh, B., Graham, J. R., Ingraham, P., et al. 2014, *Proceedings of the National Academy of Sciences*, 111, 12661

- Macintosh, B., Graham, J., Barman, T., et al. 2015, *Science*, 350, 64
- Males, J. R., Close, L. M., Miller, K., et al. 2018, in *Adaptive Optics Systems VI*, Vol. 10703, International Society for Optics and Photonics, 1070309
- Marois, C., Macintosh, B., Barman, T., et al. 2008, *science*, 322, 1348
- Martinache, F. 2013, *Publications of the Astronomical Society of the Pacific*, 125, 422
- Martinache, F., Jovanovic, N., & Guyon, O. 2016, *Astronomy & Astrophysics*, 593, A33
- Martinache, F., Guyon, O., Jovanovic, N., et al. 2014, *Publications of the Astronomical Society of the Pacific*, 126, 565
- Martinez, P., Kasper, M., Costille, A., et al. 2013, *Astronomy & Astrophysics*, 554, A41
- Martinez, P., Loose, C., Carpentier, E. A., & Kasper, M. 2012, *Astronomy & Astrophysics*, 541, A136
- Mawet, D., Milli, J., Wahhaj, Z., et al. 2014, *The Astrophysical Journal*, 792, 97
- Miller, K., Guyon, O., & Males, J. 2017, *Journal of Astronomical Telescopes, Instruments, and Systems*, 3, 049002
- Miller, K., Bos, S., Lozi, J., et al. 2021, *Astronomy & Astrophysics*, 646, A145
- Miller, K. L., Males, J. R., Guyon, O., et al. 2019, *Journal of Astronomical Telescopes, Instruments, and Systems*, 5, 1, doi: 10.1117/1.JATIS.5.4.049004
- Milli, J., Banas, T., Mouillet, D., et al. 2016, in *Adaptive Optics Systems V*, Vol. 9909, International Society for Optics and Photonics, 99094Z
- Milli, J., Kasper, M., Bourget, P., et al. 2018, in *Adaptive Optics Systems VI*, Vol. 10703, International Society for Optics and Photonics, 107032A
- Minowa, Y., Hayano, Y., Oya, S., et al. 2010, in *Adaptive Optics Systems II*, Vol. 7736, International Society for Optics and Photonics, 77363N
- N'Diaye, M., Martinache, F., Jovanovic, N., et al. 2018, *Astronomy & Astrophysics*, 610, A18
- Otten, G. P., Snik, F., Kenworthy, M. A., et al. 2014, in *Advances in Optical and Mechanical Technologies for Telescopes and Instrumentation*, Vol. 9151, International Society for Optics and Photonics, 91511R
- Pancharatnam, S. 1956, in *Proceedings of the Indian Academy of Sciences-Section A*, Vol. 44, Springer, 398–417
- Paxman, R. G., Schulz, T. J., & Fienup, J. R. 1992, *JOSA A*, 9, 1072
- Platt, B. C., & Shack, R. 2001, *Journal of refractive surgery*, 17, S573
- Por, E. H., Haffert, S. Y., Radhakrishnan, V. M., et al. 2018, in *Proc. SPIE*, Vol. 10703, Adaptive Optics Systems VI
- Racine, R., Walker, G. A., Nadeau, D., Doyon, R., & Marois, C. 1999, *Publications of the Astronomical Society of the Pacific*, 111, 587
- Ragazzoni, R. 1996, *Journal of modern optics*, 43, 289
- Sauvage, J.-F., Fusco, T., Guesalaga, A., et al. 2015, in *Adaptive Optics for Extremely Large Telescopes 4—Conference Proceedings*, Vol. 1
- Singh, G., Galicher, R., Baudoz, P., et al. 2019, *Astronomy & Astrophysics*, 631, A106
- Snik, F., Otten, G., Kenworthy, M., et al. 2012, in *Modern Technologies in Space-and Ground-based Telescopes and Instrumentation II*, Vol. 8450, International Society for Optics and Photonics, 84500M
- Soummer, R., Hagan, J. B., Pueyo, L., et al. 2011, *The Astrophysical Journal*, 741, 55
- Sun, H. 2019, PhD thesis, Princeton University
- Vievard, S., Bos, S., Cassaing, F., et al. 2019, arXiv preprint arXiv:1912.10179
- Vievard, S., Bos, S. P., Cassaing, F., et al. 2020, in *Adaptive Optics Systems VII*, Vol. 11448, International Society for Optics and Photonics, 114486D
- Vigan, A., Gry, C., Salter, G., et al. 2015, *Monthly Notices of the Royal Astronomical Society*, 454, 129

- Walter, A. B., Fruitwala, N., Steiger, S., et al. 2020, Publications of the Astronomical Society of the Pacific, 132, 125005
- Welch, P. 1967, IEEE Transactions on audio and electroacoustics, 15, 70

5 | The polarization-encoded self-coherent camera

Adapted from

S.P. Bos

Astronomy & Astrophysics, 646, A177 (2021)

The exploration of circumstellar environments by means of direct imaging to search for Earth-like exoplanets is one of the challenges of modern astronomy. One of the current limitations are evolving non-common path aberrations (NCPA) that originate from optics downstream of the main wavefront sensor. Measuring these NCPA with the science camera during observations is the preferred solution for minimizing the non-common path and maximizing the science duty cycle. The self-coherent camera (SCC) is an integrated coronagraph and focal-plane wavefront sensor that generates wavefront information-encoding Fizeau fringes in the focal plane by adding a reference hole (RH) in the Lyot stop. However, the RH is located at least 1.5 pupil diameters away from the pupil center, which requires the system to have large optic sizes and results in low photon fluxes in the RH. Here, we aim to show that by featuring a polarizer in the RH and adding a polarizing beamsplitter downstream of the Lyot stop, the RH can be placed right next to the pupil. This greatly increases the photon flux in the RH and relaxes the requirements on the optics size due to a smaller beam footprint. We refer to this new variant of the SCC as the polarization-encoded self-coherent camera (PESCC). We study the performance of the PESCC analytically and numerically, and compare it, where relevant, to the SCC. We look into the specific noise sources that are relevant for the PESCC and quantify their effect on wavefront sensing and control (WFSC). We show analytically that the PESCC relaxes the requirements on the focal-plane sampling and spectral resolution with respect to the SCC by a factor of 2 and 3.5, respectively. Furthermore, we find via our numerical simulations that the PESCC has effectively access to ~ 16 times more photons, which improves the sensitivity of the wavefront sensing by a factor of ~ 4 . We identify the need for the parameters related to the instrumental polarization and differential aberrations between the beams to be tightly controlled – otherwise, they limit the instrument’s performance. We also show that without additional measurements, the RH point-spread function (PSF) can be calibrated using PESCC images, enabling coherent differential imaging (CDI) as a contrast-enhancing post-processing technique for every observation. In idealized simulations (clear aperture, charge two vortex coronagraph, perfect DM, no noise sources other than phase and amplitude aberrations) and in circumstances similar to those of space-based systems, we show that WFSC combined with CDI can achieve a 1σ raw contrast of $\sim 3 \cdot 10^{-11} - 8 \cdot 10^{-11}$ between 1 and $18 \lambda/D$. The PESCC is a powerful, new focal-plane wavefront sensor that can be relatively easily integrated into existing ground-based and future space-based high-contrast imaging instruments.

5.1 Introduction

The direct imaging of exoplanets is a rapidly growing research field as it offers exciting opportunities in comparison to indirect methods such as the transit and radial velocity method. The star and exoplanet light are spatially separated and this therefore allows for the direct characterization of the exoplanet and (eventually) the search for biomarkers. Furthermore, it can target exoplanets at wider separations than practically attainable with indirect methods and does not suffer from diminishing sensitivity when the exoplanet's orbit is not edge-on. However, the direct imaging of exoplanets is not a trivial task and many technical challenges still have to be solved. For example, when observing an Earth-like exoplanet around a Solar-type star at 10 pc, the angular separation is expected to be ~ 100 milliarcseconds and the contrast $\sim 10^{10}$ in the visible (0.3 - 1 μm ; Traub & Oppenheimer 2010).

Modern ground-based high-contrast imaging (HCI) instruments (VLT/SPHERE Beuzit et al. 2019; Subaru/SCEXAO Jovanovic et al. 2015; Gemini/GPI Macintosh et al. 2014; Magellan Clay/MagAO-X Males et al. 2018, Close et al. 2018) deploy extreme adaptive optics (XAO) systems to correct for wavefront errors caused by the turbulent Earth's atmosphere, coronagraphs to suppress starlight, and additional imaging, spectroscopic, and polarimetric post-processing techniques to further remove the speckle background. The current suite of observing and post-processing techniques consists of: angular differential imaging (ADI; Marois et al. 2006), reference star differential imaging (RDI; Ruane et al. 2019), spectral differential imaging (SDI; Sparks & Ford 2002), polarimetric differential imaging (PDI; Kuhn et al. 2001), and coherent differential imaging (CDI; Guyon 2004). Both ADI and RDI are observing techniques that are relatively easy to implement, but have been suffering from temporal stability issues that prevent them to reach high contrasts at small separations. In addition, SDI has been shown to be ineffective at smaller inner working angles, as the radial movement of speckles by spectral diversity is minimal at these separations. However, PDI has achieved impressive results (van Holstein et al., 2017) and can be simultaneously used for exoplanet characterization; still, exoplanets are never 100% polarized, making this technique not the most efficient discovery method. With CDI, the light in the image is separated into its coherent and incoherent parts. As the exoplanet's light is by definition completely incoherent with the surrounding starlight, CDI can use 100% of the exoplanet's light for the detection. This makes it a very promising technique, but it has thus far seen limited on-sky tests (Bottom et al., 2017).

Typically, the XAO system consists of a deformable mirror (DM) with a high actuator count and a sensitive wavefront sensor, such as the Shack-Hartmann or Pyramid wavefront sensor, and delivers a high Strehl point-spread-function (PSF) to the instrument. There is a non-common optical path difference between the science camera and the wavefront sensor split-off, in which aberrations occur due to misalignments and manufacturing errors. These so-called non-common path aberrations (NCPA) are not sensed by the main wavefront sensor and therefore left uncorrected. Due to changing temperature, humidity and gravity vector during observations, the NCPA slowly evolve, making them difficult to calibrate in post-processing and one of the current limitations in high-contrast imaging

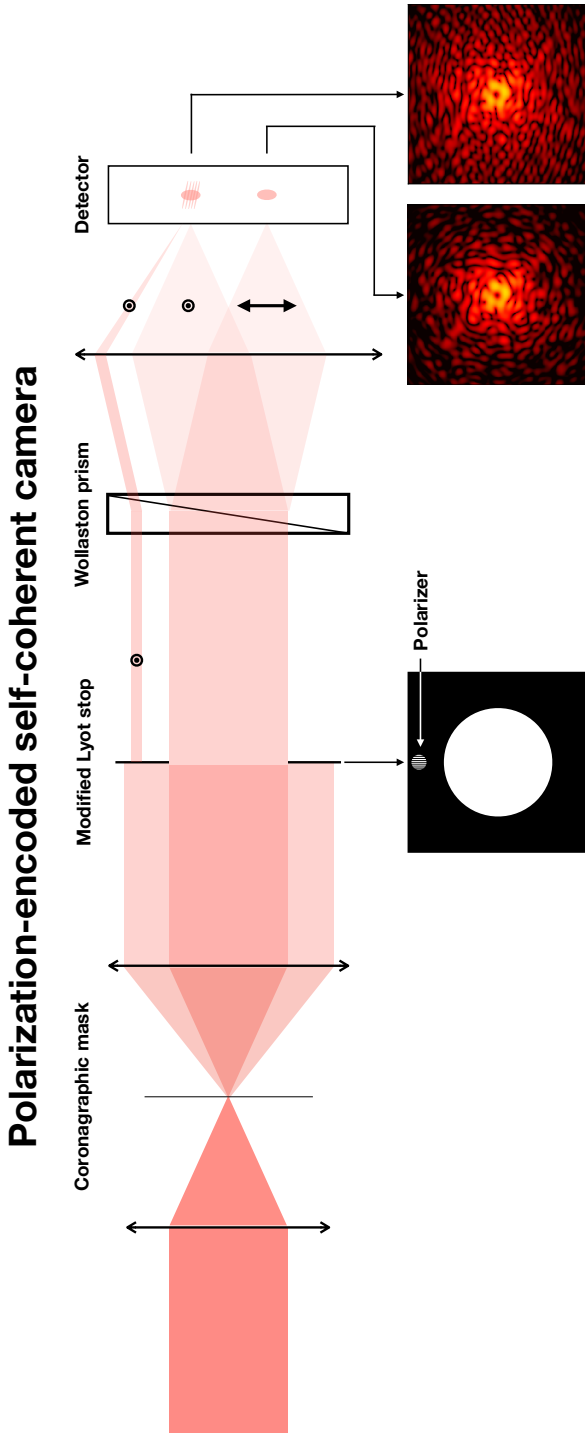


Figure 5.1: Overview of the system architecture of the PESCC. A focal-plane coronagraph (in this example a charge two vortex mask) diffracts the starlight out of the geometric pupil. A reference hole (RH) with polarizer is placed in the Lyot stop and lets a polarized reference beam through. The polarization state of the reference beam is pointing away from the page. Prior to the focal-plane, a Wollaston prism (or any other polarizing beamsplitter) splits the two orthogonal polarization states. The image with a polarization state that matches the RH polarizer has fringes that encode the wavefront information, while the orthogonal polarization state remains unmodulated by fringes.

(Martinez et al. 2012; Martinez et al. 2013; Milli et al. 2016). One solution is to apply a focal-plane wavefront sensor (FPWFS) that uses the science images to measure the wavefront aberrations, which can subsequently be corrected by the DM. Ideally, the FPWFS is integrated with the coronagraph to enable simultaneous wavefront measurements and scientific observations. A host of different FPWFSs have been developed and tested on-sky (Jovanovic et al., 2018), but only a subset has a 100% science duty cycle ((Bos et al., 2019; Codona & Kenworthy, 2013; Guyon et al., 2017; Huby et al., 2017; Miller et al., 2019; Wilby et al., 2017)).

The FPWFS that is most relevant to this work is the self-coherent camera (SCC; Baudoz et al. 2005). The SCC places a reference hole (RH) in the Lyot stop of a coronagraph in an off-axis location. The RH transmits light that is diffracted by the coronagraph outside of the geometric pupil that would have otherwise been blocked by the Lyot stop. This light will propagate to the focal-plane, interfere with the on-axis beam, and generate high-spatial frequency fringes. The focal plane's electric field is spatially modulated and directly available by calculating the Fourier transform (FT) of the image. This operation results in the optical transfer function (OTF) of the image. The OTF of the SCC consists of three components: the central peak that is the PSF, and two sidebands, which are generated by the cross-talk between the fringes and PSF and which contain the electric field estimate. However, for the FT of the image to properly show the electric field estimate, the RH needs to be at least 1.5 times the pupil diameter from the center of the pupil. This requires the system hosting the SCC to have large-diameter optics to contain both the reference and the central beam, and for the detector to have a high pixel density to properly sample the fringes in the focal plane. The technique has been extensively tested in simulations (Galicher et al., 2010) and in the lab (Mazoyer et al., 2013, 2014); in the latter case, it has reached contrast levels of $\sim 5 \cdot 10^{-9}$ in narrow spectral bands (Potier et al., 2020). The SCC also enables CDI as post-processing technique (Galicher & Baudoz, 2007), but requires additional flux measurements of the RH beam to calibrate the brightness of the RH PSF. It was shown in the lab (Singh et al., 2019) and on sky (Galicher et al., 2019) that the SCC is able to increase the contrast to by correcting the (quasi-)static aberrations during long exposure images with residual wavefront errors from the XAO system. The major disadvantage of the SCC is the minimum distance of the RH at 1.5 times the pupil diameter, making it: 1) difficult to implement in existing instruments, as their optics do not have the required size; and 2) there is a little amount of light left this far from the on-axis beam, resulting in long exposure times for obtaining sufficient sensitivity.

The Fast Atmospheric Self-coherent Camera Technique (FAST; Gerard et al. 2018) tackles the second problem by modifying the focal-plane mask of the coronagraph to inject specifically more light into the RH. This provides the sensitivity to FAST for running at much shorter exposure times and enables it to correct for the rapidly changing residual wavefront errors from the XAO system. This technique was tested in simulation with a Lyot coronagraph, and more recently, with a vortex coronagraph (Gerard & Marois, 2020). A lab test validated the coronagraph designs for the FAST concept (Gerard et al., 2019). Another recently developed concept is the fast-modulated SCC (FMSCC; Martinez 2019), which aims to address the other major disadvantage of the SCC. The

FMSCC places the RH right next to the pupil, breaking the original minimum distance of 1.5 pupil diameters. In order to separate the sidebands from the central peak, which are now overlapping, in the OTF, two images are taken in quick succession with the RH blocked in one of the images. The OTF of this second image only contains the central peak, and when it is subtracted from the first image, the two sidebands are revealed. For the subtraction to successfully reveal the sidebands on ground-based systems with the rapidly changing atmosphere, the system needs to either block the RH at high temporal frequency (\sim kHz) to "freeze" the atmosphere or to split the post-coronagraphic light into two beams: one with and one without RH. The first solution can only work for bright targets due to the high switching speeds, and the second solution is prone to differential aberrations between the two beams. This concept bears great similarities with the differential OTF WFS (dOTF; Codona 2013), which extracts wavefront information by subtracting the OTFs of two PSFs, one of which is formed by an aperture with a small amplitude asymmetry.

Here, we present the polarization-encoded self-coherent camera (PESCC), which is a variant of the FMSCC. The PESCC features a polarizer in the RH that generates a polarized reference beam, which, in turn, generates fringes in one polarization state, while the orthogonal polarization state is unmodulated by fringes. This is a concept that is very similar to the polarization differential OTF wavefront sensor (Brooks et al., 2016). When the beam is split into two channels by a Wollaston prism just before the science camera, it ensures that there are minimal differential aberrations between the two polarization states. See Figure 5.1 for an overview of the system architecture. The two polarization states can be imaged simultaneously, allowing for longer integration times and, therefore, fainter stars can be used as targets. For the images of the two polarization states, the OTF can then be calculated and subtracted to reveal the aberrated electric field (similar to the FMSCC analysis). This process is shown in Figure 5.2. Furthermore, as we show in section 7.2, the measurements also contain direct measurements of the RH, ensuring that the CDI is possible for every observation without additional measurements. We also show that because the RH is placed closer to the pupil, the PESCC relaxes the requirements on focal-plane sampling and this allows it to operate over broader wavelength ranges. Another advantage is that one of the two channels does not contain the reference beam and, therefore, it is not polluted by extra photon noise from the reference PSF.

In section 7.2, we present the theory of the PESCC, including the CDI with the PESCC. We also carry out an analytical study of the performance of the PESCC compared to the SCC. In section 7.3, we present the simulation results, specifically the wavefront sensing in subsection 5.3.1, wavefront control in subsection 5.3.2, and CDI in subsection 5.3.3. In section 7.5, we discuss the results and present our conclusions.

5.2 Theory

In this section, we focus on the theory behind the PESCC and perform an analytical study of its performance. We first derive the necessary equations in subsection 5.2.1. In

Table 5.1: Variables presented in section 7.2.

Variable	Description
β	Factor that builds in safety margins in ϵ_0 .
γ	Ratio of the pupil diameter and reference hole diameter.
$\delta\theta$	Misalignment angle of the RH polarizer.
ϵ_0	Distance of the RH to the center of the pupil.
λ	The wavelength of light.
$\Delta\lambda$	The spectral bandwidth.
d_r	Diameter of the reference hole.
p	The strength of the instrumental polarization.
t	The relative polarization leakage.
D	Diameter of the pupil.
E_p	The central beam pupil-plane electric field after the modified Lyot stop.
E_{ref}	The pupil-plane electric field of the RH.
$\mathcal{F}\{\cdot\}$	The Fourier transform operator.
I_0	The focal-plane intensity of the central peak in the OTF.
I_{ic}	The focal-plane intensity of the incoherent contribution (e.g., an exoplanet).
I_{ct}	The focal-plane intensity of both sidebands in the OTF.
I_i	Focal-plane intensity image of channel i .
I'_i	Focal-plane intensity image of channel i with companion.
I_{ref}	The focal-plane intensity of the RH.
I'_{ref}	The focal-plane intensity of the RH corrected for polarizer leakage.
I_{sb}	The focal-plane intensity of one sideband in the OTF.
N_{act}	Number of actuators along one axis in the pupil.
N_{pix}	Number of pixels per λ/D .
OTF_i	The OTF of channel i .
R_λ	The spectral resolution.
S	The detector sampling in units of pixels per λ/D .

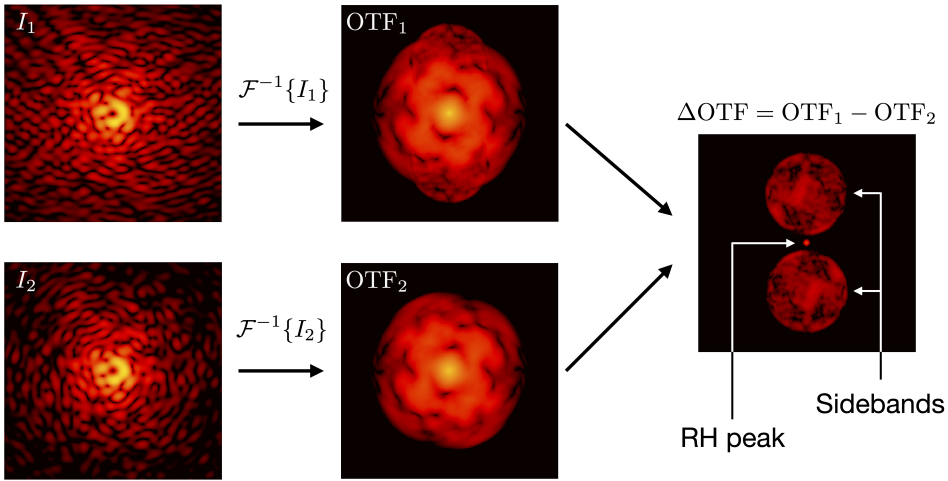


Figure 5.2: Example of sideband extraction with the PESCC. For the images of channels 1 and 2 (I_1 and I_2) in Figure 5.1, the OTFs are calculated. The OTF_1 contains the two sidebands with wavefront information and the RH peak, but these are overwhelmed by the central peak. When OTF_2 , which only contains the central peak, is subtracted from OTF_1 , the two sidebands and RH peak are revealed.

subsection 5.2.2 and subsection 5.2.3 we present the maximal RH diameter and its minimal distance from the pupil center. Using the equations derived in subsection 5.2.3, we study how the smaller RH distance effects the focal-plane sampling constraints (subsection 5.2.4) and the spectral bandwidth limitations (subsection 5.2.5). Then we investigate the effects of instrumental polarization and polarizer leakage in subsection 5.2.6 and subsection 5.2.7. Subsequently, we develop CDI with the PESCC in subsection 5.2.8. The variables presented in this section are defined in Table 7.1.

5.2.1 Polarization-encoded self-coherent camera

Here, we derive the working principle of the PESCC. We adopt the setup as shown in Figure 5.1. The starlight first encounters a focal-plane coronagraph that diffracts it outside of the geometric pupil. The subsequent modified Lyot stop blocks most of the light and the RH, which contains a polarizer, transmits a fully polarized reference beam with an electric field, E_{ref} , with a diameter, d_r . The electric field of the central beam, directly after the Lyot stop, is given by E_p and has a diameter, D . A polarizing beamsplitter (PBS) splits the beam into two channels that have orthogonal linear polarization states. The polarizer in the RH transmits a polarization state that is parallel to the polarization state of one of the channels. One of channels contains the reference beam and feature fringes in the focal-plane, the other does not. For now, we assume that the starlight is unpolarized, and that the polarizer featured in the RH and the polarizing beamsplitter (PBS) are perfect (i.e., they split the light perfectly into two orthogonal polarization states and do

not introduce wavefront aberrations). In later subsections, we analytically and numerically investigate the consequences when these assumption do not hold. For simplicity, but without loss of generality, we also assume monochromatic, one-dimensional electric fields. The focal-plane intensities of channel 1 (I_1 ; with reference beam) and channel 2 (I_2 ; without reference beam), are given by:

$$I_1 = I_0 + I_{ref} + I_{ct}, \quad (5.1)$$

$$I_2 = I_0, \quad (5.2)$$

with $I_0 = |\mathcal{F}\{E_p\}|^2$ as the PSF of the coronagraphic system, $I_{ref} = |\mathcal{F}\{E_{ref}\}|^2$ as the PSF of the RH, $I_{ct} = 2\Re\{\mathcal{F}\{E_p\}\mathcal{F}\{E_{ref}\}^*\}$ as the cross-talk term between the RH and the central beam, and $\mathcal{F}\{\cdot\}$ as the Fourier transform. Here, E^* denotes the complex conjugate of E . The wavefront information of E_p is encoded in I_{ct} , but is hidden behind the much stronger I_0 term. To retrieve the wavefront, we calculate the OTF of I_1 and I_2 with the inverse Fourier transform:

$$\text{OTF}_1 = \mathcal{F}^{-1}\{I_1\}, \quad (5.3)$$

$$= E_p * E_p^* + E_{ref} * E_{ref}^* + \quad (5.4)$$

$$E_p * E_{ref}^* * \delta(x + \epsilon_0) + E_p^* * E_{ref} * \delta(x - \epsilon_0),$$

$$\text{OTF}_2 = \mathcal{F}^{-1}\{I_2\}, \quad (5.5)$$

$$= E_p * E_p^*, \quad (5.6)$$

with $*$ the convolution operator. The OTF_1 consists of four terms, which are convolution combinations of the pupil-plane electric fields E_p and E_{ref} . The term $E_p * E_p^*$ is the central peak in the OTF and is generated by the main beam in the system, its width in the OTF is $2D$. The RH ($E_{ref} * E_{ref}^*$) also creates a peak at the same location as the main beam, but is much fainter than the central peak, and is smaller with a width of $2d_r$. The cross-talk between the RH beam and the central beam generates two lateral peaks or sidebands in the OTF located at $\pm\epsilon_0$, both with a width of $D + d_r$. As the RH is placed close to the pupil ($\epsilon_0 < D$), the two sidebands still partly overlap with the central peak. See Figure 5.2 for a two-dimensional example that visualizes this. To reveal the sidebands, which contain the wavefront information, we subtract the OTF_2 from OTF_1 :

$$\Delta\text{OTF} = E_{ref} * E_{ref}^* + E_p * E_{ref}^* * \delta(x + \epsilon_0) + E_p^* * E_{ref} * \delta(x - \epsilon_0). \quad (5.7)$$

If ϵ_0 has been appropriately chosen (subsection 5.2.3), the three remaining peaks in the OTF are well separated. It is essential that differential aberrations between the two channels are minimal, otherwise the $E_p * E_p^*$ term does not completely cancel in the subtraction. Extracting, centering and Fourier transforming one of the sidebands gives an estimation of the focal-plane speckle field I_{sb} (Mazoyer et al., 2014):

$$I_{sb} = \mathcal{F}\{E_p * E_{ref}^*\}, \quad (5.8)$$

$$= \mathcal{F}\{E_p\}\mathcal{F}\{E_{ref}^*\}. \quad (5.9)$$

This term is used with wavefront sensing and control, as shown in subsection 5.3.2. We note that I_{sb} is a complex quantity, which becomes completely real when the other sideband is included. For CDI we also have to extract other information from the ΔOTF .

Selecting the RH peak and calculating its Fourier transform gives an estimate of the RH PSF:

$$I_{ref} = \mathcal{F}\{E_{ref} * E_{ref}^*\}. \quad (5.10)$$

It is also important to have an estimate of the cross-talk intensity term I_{ct} . This term can be estimated by extracting both sidebands and calculating their Fourier transform:

$$I_{ct} = \mathcal{F}\{E_p * E_{ref}^* * \delta(x + \epsilon_0) + E_p^* * E_{ref} * \delta(x - \epsilon_0)\}, \quad (5.11)$$

$$= 2\Re\{\mathcal{F}\{E_p\}\mathcal{F}\{E_{ref}'\}^*\}. \quad (5.12)$$

5.2.2 Reference hole diameter

The diameter of the RH (d_r) directly depends on the size of the dark hole. The dark hole size is set by the maximum spatial frequency that can be controlled by the DM and is given by $\sqrt{2}N_{act}\lambda/(2D)$ (Mazoyer et al., 2013), with D as the diameter of the pupil, N_{act} the number of actuators along one axis in the pupil, and λ the observed wavelength. The factor of $\sqrt{2}$ is included to account for the higher number of actuators along the diagonal compared to the sides of a square grid of actuators in a DM. To make sure that the DM can actually remove the speckles within the dark hole, the electric field of the speckles needs to be accurately measured. This can only happen when the focal-plane electric field of the RH is non-zero over the dark hole. The position of the first dark ring of the RH PSF is located at $1.22\lambda/d_r$. Therefore, the diameter (d_r) is given by (Mazoyer et al., 2014):

$$d_r \leq 1.22 \sqrt{2} \frac{D}{N_{act}}. \quad (5.13)$$

Often, the ratio between the pupil diameter and reference hole diameter is used, $\gamma = D/d_r$. Then the Equation 5.13 becomes:

$$\gamma \geq \frac{N_{act}}{1.22 \sqrt{2}}. \quad (5.14)$$

5.2.3 Reference hole distance

For the SCC, the minimum distance of the reference hole (ϵ_0) with respect to the center of the pupil was derived in Galicher et al. (2010). It ensures that the sidebands would not overlap with the central peak in the OTF (see Figure 5.3 a), and is given by:

$$\epsilon_0 = \frac{\beta}{2} \left(3 + \frac{1}{\gamma} \right) D, \quad (5.15)$$

with β a factor that cannot be lower than unity and usually set to 1.1 to include some extra margin. However, for the PESCC the sidebands can overlap with the central peak in the OTF as the central peak is subtracted out. The only constraint is that the sidebands do not overlap with one another or the peak from the RH, otherwise the wavefront information

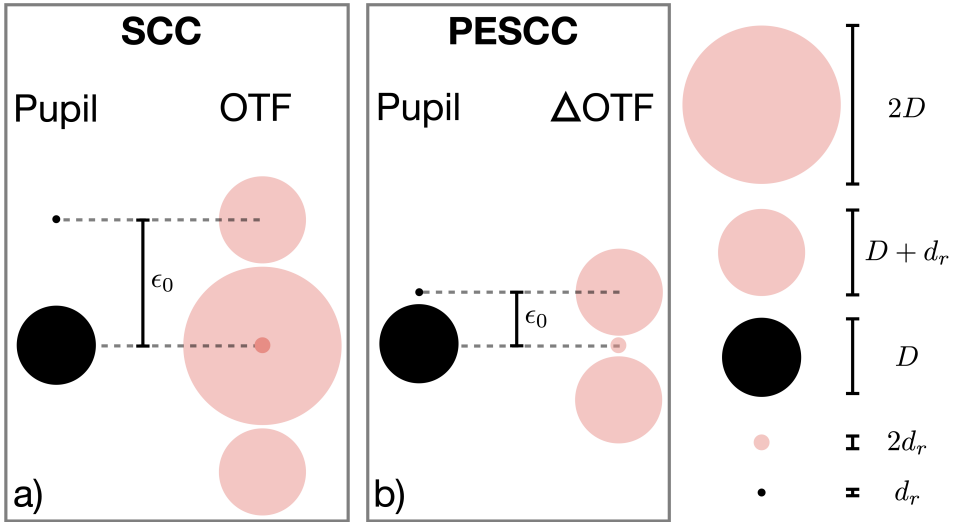


Figure 5.3: Explanation of how the geometry of the pupil relates to the geometry of the OTF. This figure shows that the minimum distance of the RH of (a) the SCC is much larger than that of (b) the PESCC.

cannot be completely extracted, which is shown in Figure 5.3 b. For the PESCC, this leads to the following reference hole distance law:

$$\epsilon_0 = \frac{\beta}{2} \left(1 + \frac{2}{\gamma} \right) D. \quad (5.16)$$

Now we investigate in the ideal case how much closer the reference hole can be placed for the PESCC compared to the SCC. We set $\beta = 1$ and assume an infinitely small reference hole $d_r \rightarrow 0$ ($\gamma \rightarrow \infty$). We then find for the SCC (Equation 5.15) that $\epsilon_0 = 1.5D$. For the PESCC (Equation 5.16) we find $\epsilon_0 = 0.5D$. This means that the PESCC can be placed three times closer to the center of the pupil than the SCC. This results in access to more light in the RH, as the focal-plane masks of coronagraphs diffracts more light closer to the geometric pupil, and, as shown in the following sections, it relaxes the focal-plane sampling constraints and allow for broader spectral bandwidths.

5.2.4 Focal-plane sampling constraints

As the RH of the PESCC can be positioned significantly closer to the pupil, the constraints on the focal-plane sampling can be relaxed. In this subsection, we investigate what the sampling constraints are for the PESCC. For an unobstructed telescope pupil, the sampling (\mathcal{S}), in units of pixels (N_{pix}) per λ/D , is given by:

$$\mathcal{S} = \frac{N_{pix}}{\lambda/D}, \quad (5.17)$$

with λ as the wavelength. To be Nyquist sampled in the focal-plane, it is required that $N_{pix} \geq 2$, and is usually set to $N_{pix} = 3$ or $N_{pix} = 4$. For the (PE)SCC, the combined diameter of the pupil and RH becomes $D \Rightarrow D + \epsilon_o - D/2 + d_r/2$ (Figure 5.3). This results in the following sampling constraint:

$$\mathcal{S} = \frac{N_{pix}}{\lambda/[(D + d_r)/2 + \epsilon_o]}. \quad (5.18)$$

When substituting the value of ϵ_o for the SCC (Equation 5.15) in this equation, we can rewrite it as:

$$\mathcal{S} = \frac{(1 + \beta)(1 + 1/\gamma) + 2\beta N_{pix}}{2} \frac{N_{pix}}{\lambda/D}. \quad (5.19)$$

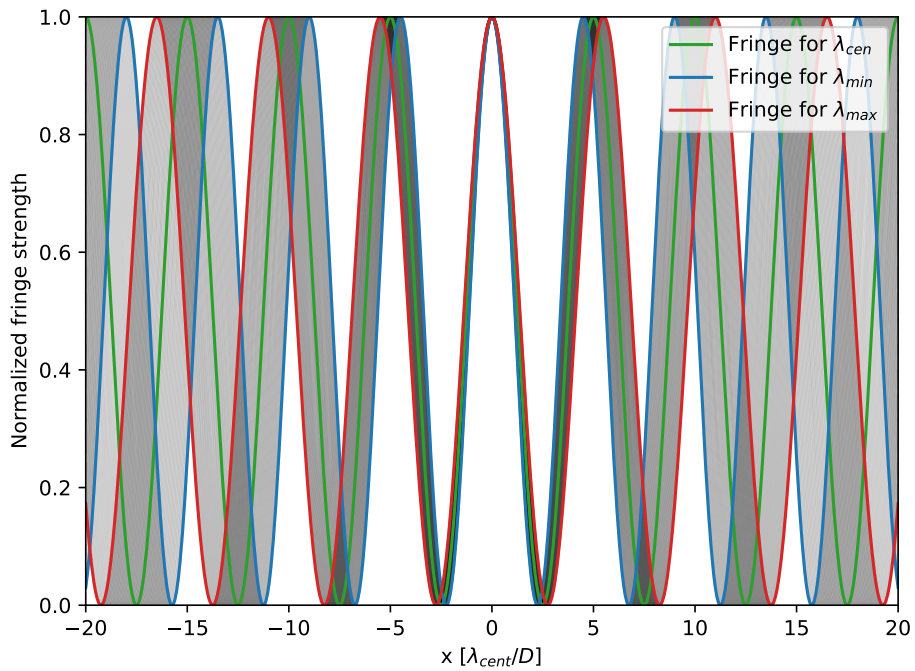
For the PESCC (Equation 5.16) we find:

$$\mathcal{S} = \frac{(1 + \beta)(1 + 1/\gamma) + \beta/\gamma N_{pix}}{2} \frac{N_{pix}}{\lambda/D}. \quad (5.20)$$

As in subsection 5.2.3, we explore in an idealized example the gain in focal-plane sampling is for the PESCC. Again, we assume that $\beta = 1$, and that $d_r \rightarrow 0$ ($\gamma \rightarrow \infty$). We set N_{pix} to 2 pixels to meet the Nyquist sampling constraint. For the SCC, we find that $\mathcal{S} = 4$ pixels per λ/D , which means that the sampling should be twice as high compared to the unobscured pupil. On the other hand, the PESCC has a sampling of $\mathcal{S} = 2$ pixels per λ/D , which is equal to the case of the unobscured pupil. This is because in this idealized example, the RH is infinitely small and can be placed right on the edge of the pupil. This shows that the PESCC significantly relaxes the sampling requirements as the total number of pixels on the detector can be reduced, in the ideal case, by a factor of four.

5.2.5 Spectral bandwidth limitations

Exoplanets are preferably observed over broad wavelength ranges ($\Delta\lambda$) to maximize the signal-to-noise ratio. However, the PSF is not constant, changing its size with wavelength ($\propto \lambda/D$). This means that the fringes introduced by (PE)SCC also increase their size and period with wavelength. Close to the center of the image these chromatic effects are not that pronounced, but after a few periods the fringes of the lowest and highest wavelengths in the filters start to significantly shift with respect to each other. An example of this is shown in Figure 5.4. After a certain distance from the image center the fringes are blurred to a level that it severely impacts the wavefront sensing performance. However, in the direction orthogonal to the fringe, the smearing is minimal and therefore the wavefront sensing in that direction is still relatively accurate. Here, we study the bandwidth for (PE)SCC solutions with one RH. Broadband solutions for the SCC with multiple RHs do exist (Delorme et al., 2016), but require even larger optics than the SCC to accommodate the additional reference beams. This is because for SCC solutions with one DH, the constraint on the optics diameter can be somewhat mitigated by moving the central pupil from the center of the optics. The RH beam and the main beam will then both pass through off-axis positions in the optics. However, for the broadband solutions with three RHs presented by Delorme et al. (2016), this is not the case because the RHs are evenly



5

Figure 5.4: Example of fringe smearing by spectral bandwidth. Fringes are plotted for many wavelengths within a broadband filter ($R_\lambda = 5$). All are plotted with a period of $5 \lambda/D$, but due to the changing wavelength the physical fringe periods in the focal plane change as well. This results in significant fringe blurring after only a few periods from the center.

distributed around the central pupil such that it cannot be moved any more to reduce the optics diameter. Galicher et al. (2010) derived the minimal spectral resolution ($R_\lambda = \lambda_0/\Delta\lambda$) required for the spectral smearing or chromatism not to impact the control region of the DM (or dark hole size):

$$R_\lambda = \sqrt{2}N_{act} \frac{\epsilon_0}{D} - \frac{1}{2}. \quad (5.21)$$

For the SCC (Equation 5.15), this becomes:

$$R_\lambda = \frac{\beta N_{act}}{\sqrt{2}} \left(3 + \frac{1}{\gamma} \right) - \frac{1}{2}. \quad (5.22)$$

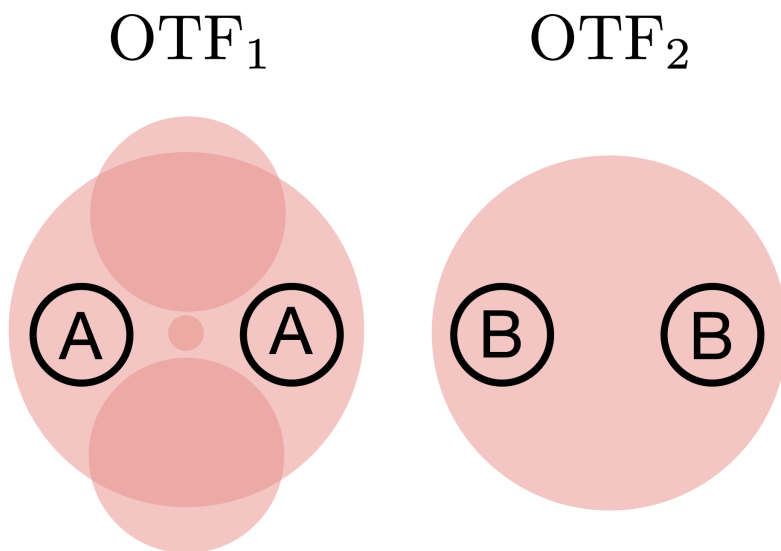
For the PESCC (Equation 5.16), R_λ is given by:

$$R_\lambda = \frac{\beta N_{act}}{\sqrt{2}} \left(1 + \frac{2}{\gamma} \right) - \frac{1}{2}. \quad (5.23)$$

We again go through our idealized example where we set $\beta = 1$, $N_{act} = 40$, and $d_r \rightarrow 0$ ($\gamma \rightarrow \infty$). For the SCC, we find that $R_\lambda \approx 84$, which is consistent with the examples in Galicher et al. (2010). Then, for the PESCC, we find $R_\lambda \approx 24$. Thus, the PESCC can operate over bandwidths that are ~ 3.5 times wider than the SCC. This result can be understood as follows. The period of the fringes is determined by ϵ_0 : when the RH is further away from the pupil, the period of fringes becomes shorter. For a fixed spectral bandwidth the number of fringe periods before the blurring becomes too strong is also fixed. Because the PESCC has a smaller ϵ_0 than the SCC, the PESCC fringe periods are longer and the blurring becomes too strong at larger physical distances. Turning it around, when the size of the dark hole and thus the distance at which the blurring can occur are fixed, the PESCC can operate over broader bandwidths than the SCC.

5.2.6 Instrumental polarization

When the starlight is polarized, it is possible that the performance of the PESCC is affected. This is because the central peaks in the two channels (I_0 in Equation 5.1 and Equation 5.2) will not end up having an equal intensity and when the Δ OTF is calculated, they will not be completely canceled out in the subtraction. We are mainly concerned with the polarization introduced by the telescope and instrument because starlight is generally unpolarized (e.g., the integrated polarization signal of the Sun is $< 10^{-6}$; Kemp et al. 1987). The instrumental polarization has been measured to be non-negligible for VLT/SPHERE and is on the level of $\sim 10^{-2}$ (Van Holstein et al., 2020). For the PESCC, we only have to account for the polarization states in which the PBS splits the light. We describe the instrumental polarization's strength by $p = (I_{0,1} - I_{0,2})/(I_{0,1} + I_{0,2})$ ($-1 \leq p \leq 1$), with $I_{0,x}$ as the intensity of the central peak in channel, x . If $p = 1$, then the light is polarized such that all the light is in channel 1; if $p = -1$, all the light is in channel 2; and when $p = 0$, both channels have equal amounts of light. This can be viewed as a normalized Stokes parameter. Here, we explore the effect of a non-zero p . We rewrite Equation 5.7 such that



5

Figure 5.5: Regions in the OTF_1 and OTF_1 that are not contaminated by the sidebands or the RH. Therefore, regions A and B are suitable to measure p .

it includes these polarization effects:

$$\Delta\text{OTF} = pE_p * E_p^* + \frac{1+p}{2}E_{ref} * E_{ref}^* + (1+p) \cdot [E_p * E_{ref}^* * \delta(x + \epsilon_0) + E_p^* * E_{ref} * \delta(x - \epsilon_0)]. \quad (5.24)$$

The major problem at hand is the residual of the central peak ($pE_p * E_p^*$), as it will overlap with the sidebands and affect the wavefront estimate, particularly because the central peak is much brighter than the sidebands. The $1 + p$ factor that affects the RH peak and the sidebands will put more photons in these terms when $p > 0$ and fewer photons when $p < 0$, and therefore it will affect the wavefront sensing sensitivity by decreasing or increasing the photon noise. However, as p is expected to be around 10^{-2} , this effect will have less of an impact than the residuals of the central peak.

If the value of p is known, then it is possible to compensate for its effects in post-processing by dividing OTF_1 and OTF_2 with, respectively, $1 + p$ and $1 - p$. This removes the detrimental effects of the first term in Equation 5.24, but it does not affect the sensitivity of the other terms as it cannot correct the fundamental effects of photon noise. Much effort has already gone in understanding the polarization effects of high-contrast imaging instruments (De Boer et al. 2020; Van Holstein et al. 2020). Therefore, a detailed model that describes the instrumental polarization at a given configuration of the telescope and instrument could help to mitigate these effects. It is also possible to directly measure p in OTF_1 and OTF_2 . As shown in Figure 5.5 by the circles A and B, it is possible to selection regions in the OTFs without contamination of the sidebands or the RH. By calculating the flux in region A (F_A) and B (F_B), it is possible to estimate p :

$$p = \frac{F_A - F_B}{F_A + F_B}. \quad (5.25)$$

5.2.7 Polarization leakage

In subsection 5.2.1, we assume that the RH polarizer and the PBS would perfectly split the two polarization states. However, polarizers are not perfect and can be misaligned with respect to each other, which makes the reference beam leak from channel 1 into channel 2. Channel 2 will then also form (weaker) fringes in the focal-plane image, which results in the sidebands in the OTF. When calculating ΔOTF , as in Equation 5.7, these sidebands in channel 2 will remove the signal from the sidebands in channel 1, affecting the wavefront estimates. We rewrite Equation 5.7 such that it includes the polarization leakage:

$$\Delta\text{OTF} = \frac{1-t}{2}E_{ref} * E_{ref}^* + (1 - \sqrt{t}) \cdot [E_p * E_{ref}^* * \delta(x + \epsilon_0) + E_p^* * E_{ref} * \delta(x - \epsilon_0)], \quad (5.26)$$

with t ($0 \leq t \leq 1$) the relative level of polarization leakage, which simulates the extinction ratio of the polarizer as $1/t$, and the effect of a misaligned polarizer as:

$$t = 2 \sin^2(\delta\theta), \quad (5.27)$$

with the misalignment angle $\delta\theta$. Equation 5.26 shows that the central peak is always be subtracted out in this case, which is not surprising because the main effect of polarization leakage is the reference beam leaking into channel 2. It also shows that the accuracy of the sideband estimate is now proportional to $1 - \sqrt{t}$, effectively reducing the response of the wavefront sensor, which will eventually lower the gain of the wavefront control loop. The accuracy with which the flux in the reference hole can be estimated scales more favorably with $(1 - t)$ and is therefore less affected. When, for example, the RH polarizer has an extinction ratio of 100:1, that is, $1/t = 100 \rightarrow t = 10^{-2}$, then the wavefront estimate is 90% of its true value, while the reference hole flux is 99% of the truth. If the extinction ratio is accurately known, for example by measurements before installing the modified Lyot mask, this effect can be corrected for during post-processing or wavefront control. Another effect to take into account, especially with CDI as discussed in subsection 5.2.8, is that the polarization leakage also contaminates the second channel. This introduces an extra source of photon noise during post-processing with CDI. Therefore, although the effects on the wavefront control can be calibrated, a high performance polarizer with low leakage is desirable. As discussed in section 7.5, a prime candidate for the RH polarizer are wire grids polarizers. These can be manufactured to have an extinction ratio of 1000:1 - 10,000:1 (George et al., 2013), which would result in $t = 10^{-3} - 10^{-4}$. When the PBS is implemented as a Wollaston prism, which we foresee to be used, the extinction ratio exceeds 100,000:1 (King & Talim, 1971), which is equivalent to $t \leq 10^{-5}$ and thus negligible compared to the wire grid polarizer performance. A rotational misalignment between the RH polarizer and PBS gives a polarization leakage dictated by Equation 5.27. For misalignments of 1° , 3° , and 5° , we find $t \approx 6 \cdot 10^{-4}$, $t \approx 5 \cdot 10^{-3}$, and $t \approx 2 \cdot 10^{-2}$, respectively. Therefore, it is likely that rotational misalignments will dominate the polarization leakage.

5.2.8 Coherent differential imaging

In this subsection, we investigate how CDI is performed with the PESCC. If we consider adding the light of an unpolarized, incoherent circumstellar environment (e.g., an exoplanet, or circumstellar disk), the measurements in channel 1 and 2 become:

$$I'_1 = I_1 + I_{ic}, \quad (5.28)$$

$$I'_2 = I_2 + I_{ic}, \quad (5.29)$$

with I_1 and I_2 given by Equation 5.1 and Equation 5.2, and I_{ic} the incoherent contribution. We assume that $p = 0$ and $t = 0$. Deriving the I_c term is slightly different for the two channels, as only one has the RH beam interfering. For channel 1 we find I_{ic} as (Galicher & Baudoz, 2007):

$$I_{ic} = I'_1 - I_{ref} - I_{sb}^2/I_{ref} - I_{ct}, \quad (5.30)$$

with I_{ref} given by Equation 5.10, I_{sb} given by Equation 5.8, and I_{ct} given by Equation 5.11. For channel 2 we find I_{ic} as:

$$I_{ic} = I'_2 - I_{sb}^2/I_{ref}. \quad (5.31)$$

We note that the second channel does not contain the RH PSF, and is therefore not affected by photon noise from this term. These equations only hold for the perfect system. When

Table 5.2: Simulation parameters for section 7.3.

Variable	Value
λ	1550 nm
Pupil diameter	7 mm
Aperture	Clear
Coronagraph	Charge two vortex
Lyot stop diameter	0.99 pupil diameter
Deformable mirror	40 × 40 actuators
β	1.1
d_r	0.3 mm
γ	23.2
ϵ_0 PESCC	4.2 mm
ϵ_0 SCC	11.7 mm
Focal-plane sampling PESCC	2.24 pixels per λ/D
Focal-plane sampling SCC	4.39 pixels per λ/D

there are system inaccuracies present, the CDI performance will degrade significantly. However, inaccuracies such as p and t can be accounted for in the post-processing step if the correct values are known. As shown in subsection 5.2.6, it is possible to measure p in the OTF_1 and OTF_2 . For t , it would have to be measured preferably before the modified Lyot stop is installed. When correcting for these effects, Equation 5.30 and Equation 5.31 become:

$$I_{ic} = I''_1 - I'_{ref} - I'^2_{sb}/I'_{ref} - I'_{ct}, \quad (5.32)$$

$$I_{ic} = I''_2 - t^2 I'_{ref} - I'^2_{sb}/I'_{ref} - t I'_{ct}, \quad (5.33)$$

with $I''_1 = I_1/(1+p)$ and $I''_2 = I_2/(1-p)$ the images corrected for instrumental polarization effects, $I'_{ref} = I_{ref}/(1-t^2)$, $I'_{sb} = I_{sb}/(1-t)$, and $I'_{ct} = I_{ct}/(1-t)$ the correction for polarizer leakage of respectively the RH beam, the intensity of the sideband, and the intensity of the cross-talk term.

5.3 Simulations

In this section, we investigate the performance of the PESCC in numerical simulations, and compare it to the SCC where relevant. The effects of photon noise, differential aberrations, instrumental polarization, polarizer leakage, and spectral resolution on wavefront sensing and control are explored. The simulations are performed in Python using the HCIPy package (Por et al., 2018), which includes polarization propagation with Jones matrices necessary for this work. We simulate an idealized HCI system with static wavefront aberrations. The system operates at 1550 nm and consists of a clear aperture, an

idealized DM (e.g., no actuator cross-talk, or quantization errors) with a 40×40 square grid of actuators located in the pupil plane, a charge two vortex coronagraph, a (PE)SCC Lyot stop, a polarizing beamsplitter and detector. The diameter of the pupil before the vortex coronagraph is 7 mm. The wavefront aberrations that are looked at are induced by an out-of-plane phase aberration following a power spectral density with a power law exponent of -3. Fresnel propagation from this plane to the pupil creates both phase and amplitude aberrations. This results in a wavefront error (WFE) of $2.9 \cdot 10^{-2}$ ($\pm 8 \cdot 10^{-3}$) λ root mean square (RMS), and intensity variations over the pupil of 16 ($\pm 1\%$) RMS (measured over 100 random aberrations). The Lyot is undersized by 1% compared to the pupil diameter. The diameter of the RH is determined by Equation 5.13 and for this specific system it is set to 0.3 mm ($\gamma = 23.2$). The RH distance is determined by Equation 5.15 and Equation 5.16 for the SCC and PESCC respectively. For $\beta = 1.1$, the RH distance is 11.7 mm for the SCC and 4.2 mm for the PESCC. This automatically sets the focal-plane sampling to 4.39 pixels per λ/D for the SCC (Equation 5.19) and 2.24 pixels per λ/D for the PESCC (Equation 5.20). The simulation parameters are summarized in Table 7.2.

First, we investigate the wavefront sensing performance in subsection 5.3.1. Subsequently, we look into wavefront sensing and control in subsection 5.3.2. Finally, we test the CDI with the PESCC in an idealized system in subsection 5.3.3. As the wavefront aberrations considered here remain static during the simulations, the conditions and results are more representative for space-based observatories. They mainly serve as proof of principle, and in a future work, we will investigate more realistic conditions for ground-based observatories.

5

5.3.1 Wavefront sensing

In this subsection, we investigate how the wavefront sensing capabilities of the PESCC compare to the SCC and how they degrade due to various noise sources. To estimate the wavefront sensing performance, we calculate, from the two channels images, the ΔOTF as in Equation 5.7 when the noise source is applied. Subsequently, we select one of the sidebands and center it. This sideband is the pupil-plane electric field convolved with the pupil-plane RH electric field, and we consider that to be the pupil-plane electric field estimate. Similarly, a noiseless pupil-plane electric estimate is calculated for the same wavefront aberration. The residual RMS wavefront error, which is the WFE common to both channels, is calculated by subtracting the phase of the noiseless electric field estimate from the estimate with noise, and is converted from units of radians to relative units of fractional λ . We simulate various levels of every noise source, and for every level, we simulate a hundred random wavefront aberration instances.

Photon noise performance

As discussed in subsection 5.2.3, the RH of the PESCC can be positioned much closer to the pupil compared to the RH of the SCC. This provides access to a greater number of photons for wavefront sensing as the coronagraph's focal-plane mask scatters most light close to the geometric pupil. In Figure 5.6, we plot the fractional power of the RH (ratio of the power in the RH and the total power available) as function of the distance to the

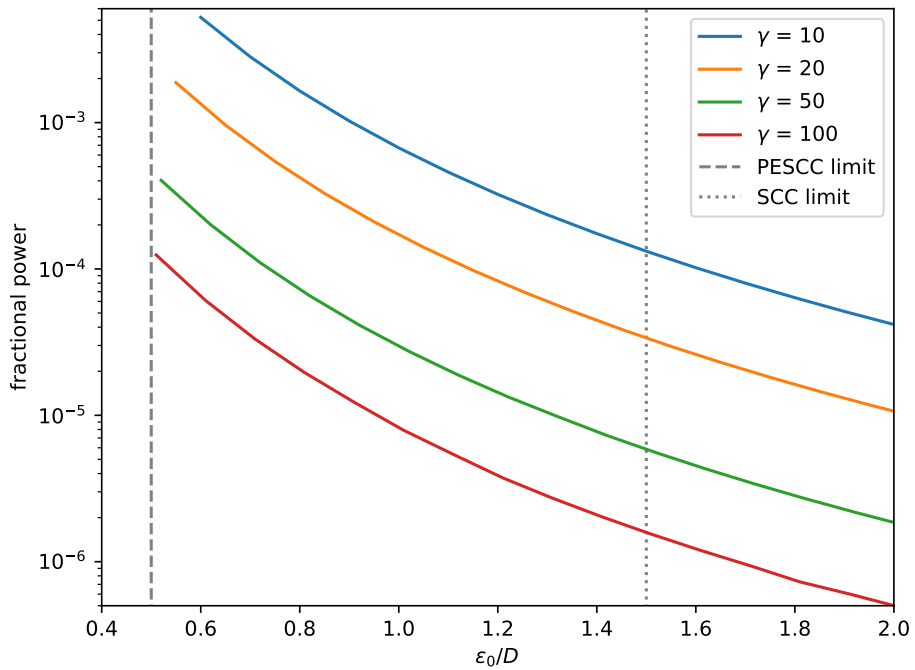
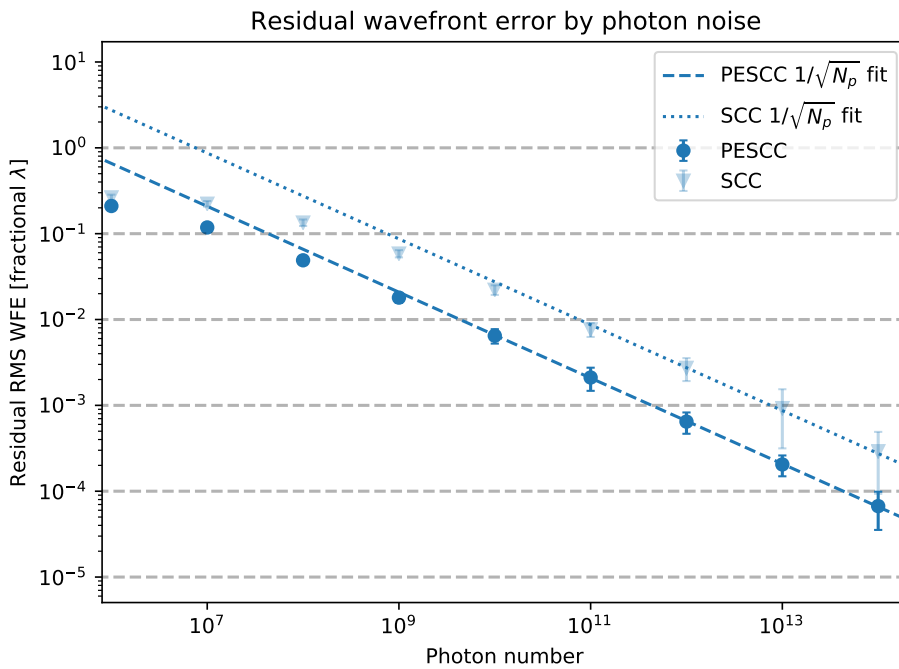


Figure 5.6: Fractional power in the RH (ratio of the power in the RH and total power in pupil plane before Lyot stop) as function of distance from the center of the pupil. This was simulated using a charge two vortex coronagraph and does not include the polarizer in the RH for the PESCC to show the total power available.



5

Figure 5.7: Photon noise sensitivity of the PESCC and SCC for wavefront sensing. The reported photon number is the number of photons before the coronagraph. The error bars show the 1σ deviation over the 100 random wavefront aberration instances. The dashed and dotted lines show $1/\sqrt{N_p}$ fits for photon numbers $\geq 10^{11}$ to show the regimes in which the performance is photon noise-limited.

pupil center (ϵ_0/D) for various γ with a charge 2 vortex coronagraph. We do not include the polarizer that would be installed in the RH of the PESCC to show the total power available. This figure shows that there is a greater number of photons available for the PESCC compared to the SCC, for example, at their respective minimum ϵ_0 (shown in the figure with the vertical, dotted and dashed lines), there is a factor of ~ 64 difference (factor ~ 32 including the polarizer). However, the polarizing beamsplitter does also split the main beam into two, which effectively halves the number of photons in the main beam. Therefore, the effective increase in the photon numbers is ~ 16 . We note that this last sensitivity hit only applies to wavefront sensing and not for companion detection because in the latter case, both channels can be combined. To indicate the expected wavefront sensing performance, we plot in Figure 5.7 the wavefront sensing performance as function of the number of photons before the coronagraph. This figure shows that the PESCC consistently outperforms the SCC by a factor of four, which is to be expected as the PESCC receives ~ 16 more photons ($\sqrt{16} = 4$). This enables the PESCC to either achieve a sensitivity that is four times higher or run with wavefront control loop speed that is a 16 times higher. The dotted and dashed lines show $1/\sqrt{N_p}$ fits (N_p is the photon number) that are fitted to the data points for $N_p \geq 10^{11}$ photons. When the photon numbers become too low, then there are not enough photons in the sidebands for wavefront information to be subtracted and the noise becomes dominated by numerical artifacts, which explains the flattening of the data points. As the PESCC has access to more photons, it occurs at the lower photon number. For 10^{12} photons, the PESCC reaches a $< 10^{-3} \lambda$ RMS WFE, a similar WFE is reached by the SCC at $\sim 1.6 \cdot 10^{13}$ photons.

Differential aberrations

The principle of the PESCC is that the OTFs of the two beams can be subtracted to reveal the sidebands. However, these beams follow different optical paths in and downstream of the PBS. A converging beam propagating through a PBS such as a Wollaston prism can incur differential aberrations between the outgoing beams (Simon, 1986) and these differential aberrations can increase when the beams hit the downstream at optics at slightly different positions. These differential aberrations introduce residuals in the Δ OTF that affect the wavefront estimation. Here, we quantify the effect of these differential aberrations on the wavefront estimation. We assume that the polarizing beam splitter is one of the last elements in the optical train and that downstream optics only introduce low-order aberrations from misalignments. We simulate the differential aberrations by introducing on one beam a random combination of seven low order aberrations (starting at defocus), that have been scaled to a certain rms wavefront error ($\Delta\phi$). These low-order aberrations include differential aberrations expected by the Wollaston prism (Simon, 1986) and from the downstream optics (derived from Zemax simulations). The other beam does not get any additional aberrations, so that we make sure that we tightly control the level of differential aberrations. In Figure 5.8, we plot wavefront estimation performance as a function of the level of differential aberration. It shows that the wavefront is severely affected by differential aberrations. For $\Delta\phi \approx 5 \cdot 10^{-4} \lambda$, the residual RMS WFE is $\sim 10^{-2} \lambda$. This means that differential aberrations will have to be tightly controlled for successful operation of the PESCC. To put these values into perspective, SPHERE/IRDIS was built with

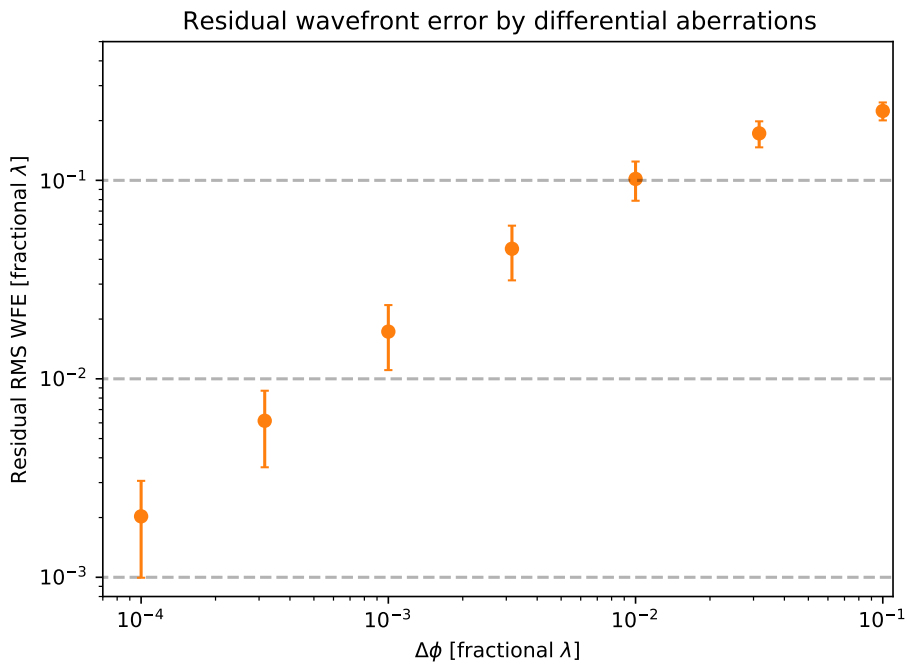


Figure 5.8: RMS differential aberrations ($\Delta\phi$) between the two beams downstream of the polarizing beamsplitter, and their effect on the wavefront reconstruction. The error bars show the 1σ deviation over the 100 random wavefront aberration instances.

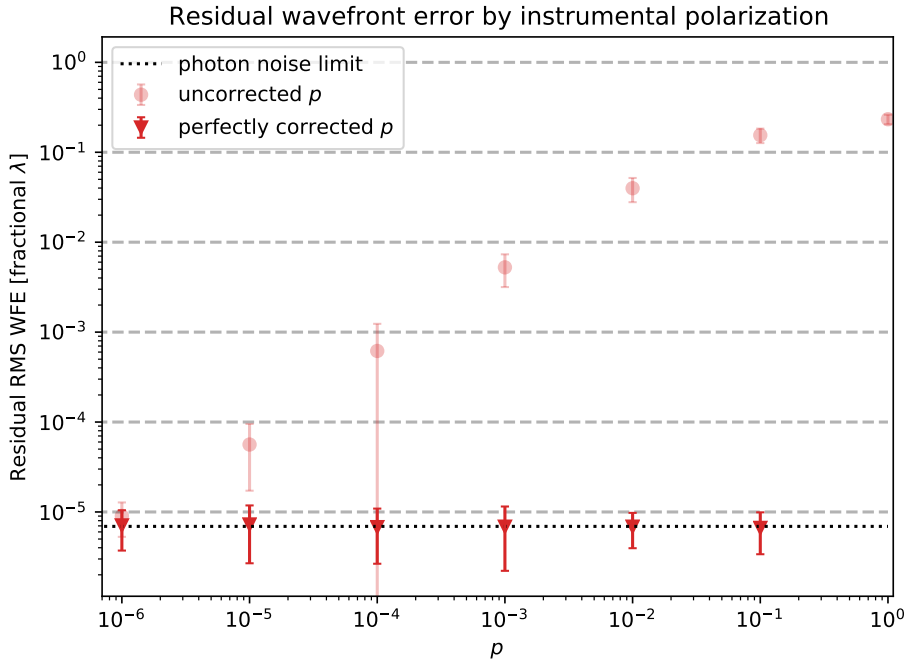
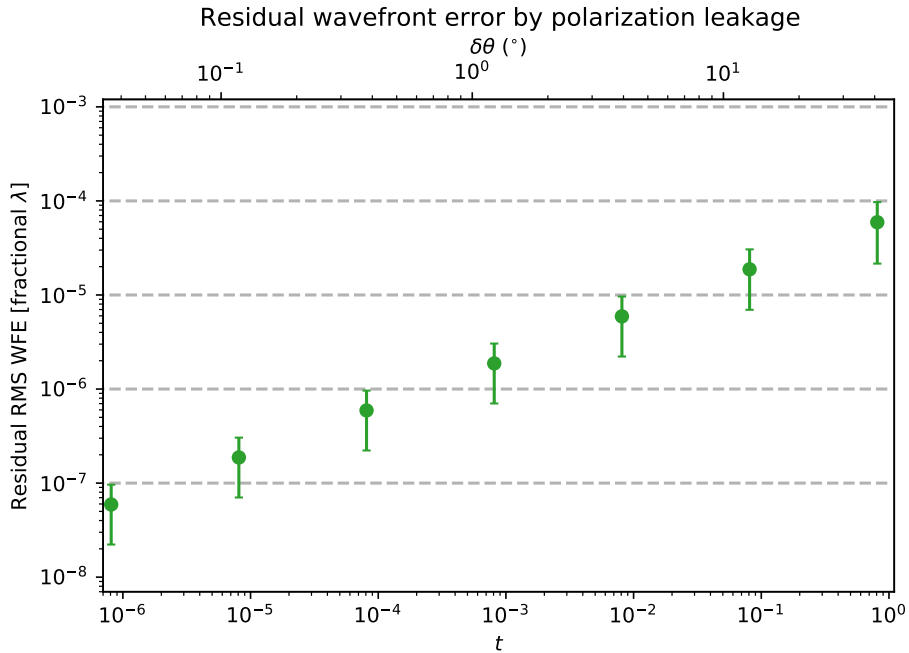


Figure 5.9: Performance of the wavefront sensing with instrumental polarization effects. The error bars show the 1σ deviation over the 100 random wavefront aberration instances. The circles show that data points where the strength of instrumental polarization (p) was not corrected and the triangles show the data points where p was corrected. The dotted lines shows the photon noise limit, which was introduced to prevent the residual wavefront error reaching numerical noise.

$\sim 6 \cdot 10^{-3}$ waves of differential aberrations (Dohlen et al., 2008) between the two beams.

Instrumental polarization

As discussed and analytically studied in subsection 5.2.6, uncorrected instrumental polarization can impact the wavefront estimation performance of the PESCC as the main peak in the OTFs does not, thus, completely cancel in the Δ OTF. Here, we quantify the effects of uncorrected and perfectly corrected instrumental polarization on the wavefront sensing. In Figure 5.9, we plot the effects of increasing p versus the wavefront sensing performance. We show the case of corrected and uncorrected p and we added photon noise (10^{16} photons before the coronagraph) because, otherwise the corrected dots would be at the numerical noise limit. This shows that when p is accurately known and corrected for, the detrimental effects can be completely amended. However, when p is left (even partially) uncorrected, it significantly impacts the wavefront sensing. For $p \approx 2 \cdot 10^{-3}$,



5 Figure 5.10: Performance of the wavefront sensing with polarization leakage. The error bars show the 1σ deviation over the 100 random wavefront aberration instances. The bottom x-axis shows polarization leakage (t), and the upper x-axis shows the equivalent rotation offset ($\delta\theta$) between the RH polarizer and PBS. We note that the right most data point is sampled at $t = 0.81$.

the residual RMS WFE is $\sim 10^{-2} \lambda$. This shows that the application of the p correction, suggested in subsection 5.2.6, is important. For SPHERE/IRDIS, the uncorrected level instrumental polarization is at the order of $\sim 10^{-2}$ (Van Holstein et al., 2020).

Polarization leakage

The polarizers are vital parts of the PESCC, and any imperfections will leak unwanted light into channel 2. As discussed in subsection 5.2.7, this will affect the wavefront estimation. This polarization leakage could be due to rotation offsets of this polarizer with regard to the polarizing beamsplitter or an imperfect blockage of the unwanted polarization state. Here, we simulate the polarization leakage and quantify its affect on the wavefront sensing performance of the PESCC. In Figure 5.10, we plot the wavefront sensing performance as function of the polarizer leakage. It clearly shows that the polarizer leakage has a relatively minor impact on the wavefront sensing since, even for $t = 0.81$, the residual RMS WFE is still below 10^{-4} fractional λ .

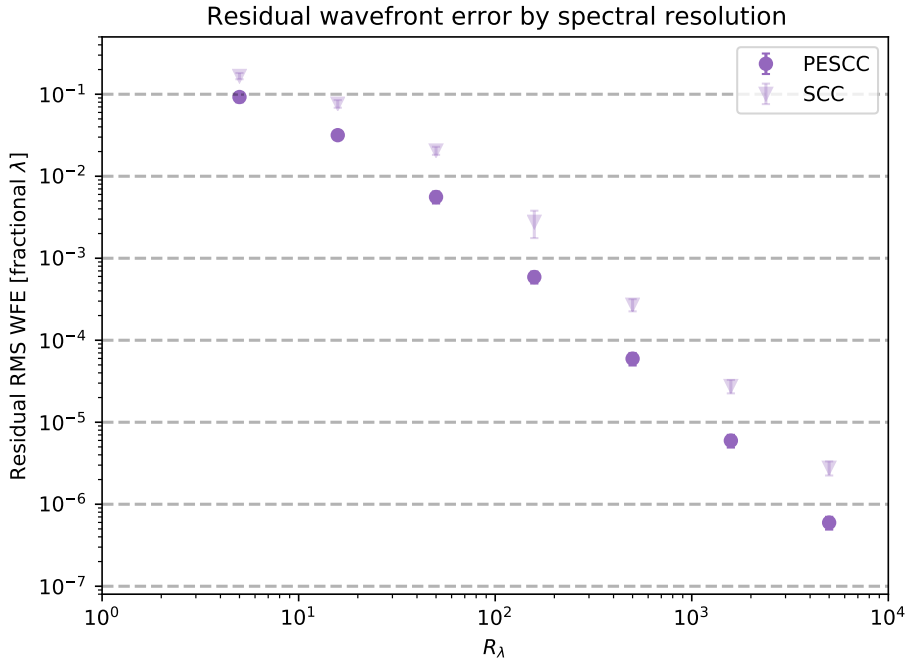


Figure 5.11: Performance of the wavefront sensing with varying spectral resolution (R_λ). The error bars show the 1σ deviation over the 100 random wavefront aberration instances. The circles show the performance of the PESCC and the triangles the performance of the SCC.

Spectral resolution

Astronomical observations always have a finite R_λ , and, as was analytically studied in subsection 5.2.5, this affects the performance of the PESCC. Specifically, it was determined when Equation 5.22 and Equation 5.23 are not satisfied, respectively, the SCC and PESCC, accurate wavefront sensing in the entire control region of the DM is not possible. Here we simulate the effects of spectral resolution on the wavefront sensing. The broadband effects are simulated by sampling seven wavelengths over the wavelength range defined by the spectral resolution, calculating the PSF for each wavelength, and incoherently adding the resulting PSFs. Due to the spectral effects, the sidebands in the Δ OTF are smeared, affecting the wavefront information. We use the position and size of the RH at the central wavelength to generate an aperture that is applied to the Δ OTF for wavefront sensing. In Figure 5.11, the results of the simulation are shown. It shows that $< 10^{-2} \lambda$ RMS WFE is achieved for $R_\lambda \approx 30$ for the PESCC and $R_\lambda \approx 90$ for the SCC.

5.3.2 Wavefront sensing & control

In this subsection, we study how the noise sources in subsection 5.3.1 affect the wavefront sensing and control when the goal is to cancel residual starlight in the region of interest (ROI). When the goal is to minimize the electric field of the starlight in the ROI, it was shown (Mazoyer et al., 2014) that minimizing I_{sb} (Equation 5.8) is equivalent. We assume that we are in the small phase regime and can therefore say that there is a linear relationship between DM actuation and changes in I_{sb} . The response matrix, which dictates this linear relationship, can now be calibrated by actuating modes on the DM (actuator pokes or sine/cosine modes) and recording the changes in I_{sb} . We find the focal-plane response to DM mode i by:

$$\Delta I_{sb}^i = \frac{I_{sb+}^i - I_{sb-}^i}{2a^2}, \quad (5.34)$$

with a the poke amplitude that was set to $10^{-3} \cdot \lambda$, and I_{sb+}^i and I_{sb-}^i the images flattened to 1D vectors that corresponds to the positive and negative actuations of the mode, respectively. The response matrix R is then constructed by stacking the responses to the N modes that are controlled:

$$R = \begin{pmatrix} \Re\{\Delta I_{sb}^1\} & \Im\{\Delta I_{sb}^1\} \\ \vdots & \vdots \\ \Re\{\Delta I_{sb}^N\} & \Im\{\Delta I_{sb}^N\} \end{pmatrix}^T, \quad (5.35)$$

with $\Re\{\cdot\}$ and $\Im\{\cdot\}$ the real and imaginary components. In the simulations there is only one DM, which is set in a pupil-plane and, therefore, we can only hope to correct for phase and amplitude errors in a one-sided dark hole. Therefore, we chose a ROI given by $5 \lambda/D < x < 10 \lambda/D$ and $-5 \lambda/D < y < -5 \lambda/D$. We use a sine/cosine mode basis to directly probe this region (Poyneer & Véran, 2005) to calibrate the response matrix. The control matrix C is then calculated by inverting the response matrix using the singular-value decomposition method with Tikhonov regularization. In closed-loop operation for the wavefront control (WFC), we use a simple integral controller with a loop gain of 0.5.

As a comparison to WFC tests with the various noise sources, we first simulate the WFC for 20 iterations without any noise sources present. The PSFs of this test are shown in Figure 5.12. It shows that a dark hole is generated after the WFC in the ROI. In channel 1, the intensity of the RH is clearly visible as it limits the achieved contrast. When the RH is blocked, the contrast in the ROI is the same for both channels. The convergence of the algorithm is shown in Figure 5.13. The contrast of the two channels is plotted, which shows that the channel with the RH PSF plateaus at $\sim 10^{-7}$ before the RH is blocked, and the other channel converges to $\sim 2 \cdot 10^{-9}$ within ten iterations. When the RH is blocked at iteration 21, the contrast in channel 1 also converges to $\sim 2 \cdot 10^{-9}$.

The results presented in Figure 5.13 serve as benchmark for the test with noise sources to quantify the performance loss. For all the noise sources tested in subsection 5.3.2, we use the values that give approximately a 10^{-1} , 10^{-2} , 10^{-3} fractional λ RMS WFE to test with WFC.

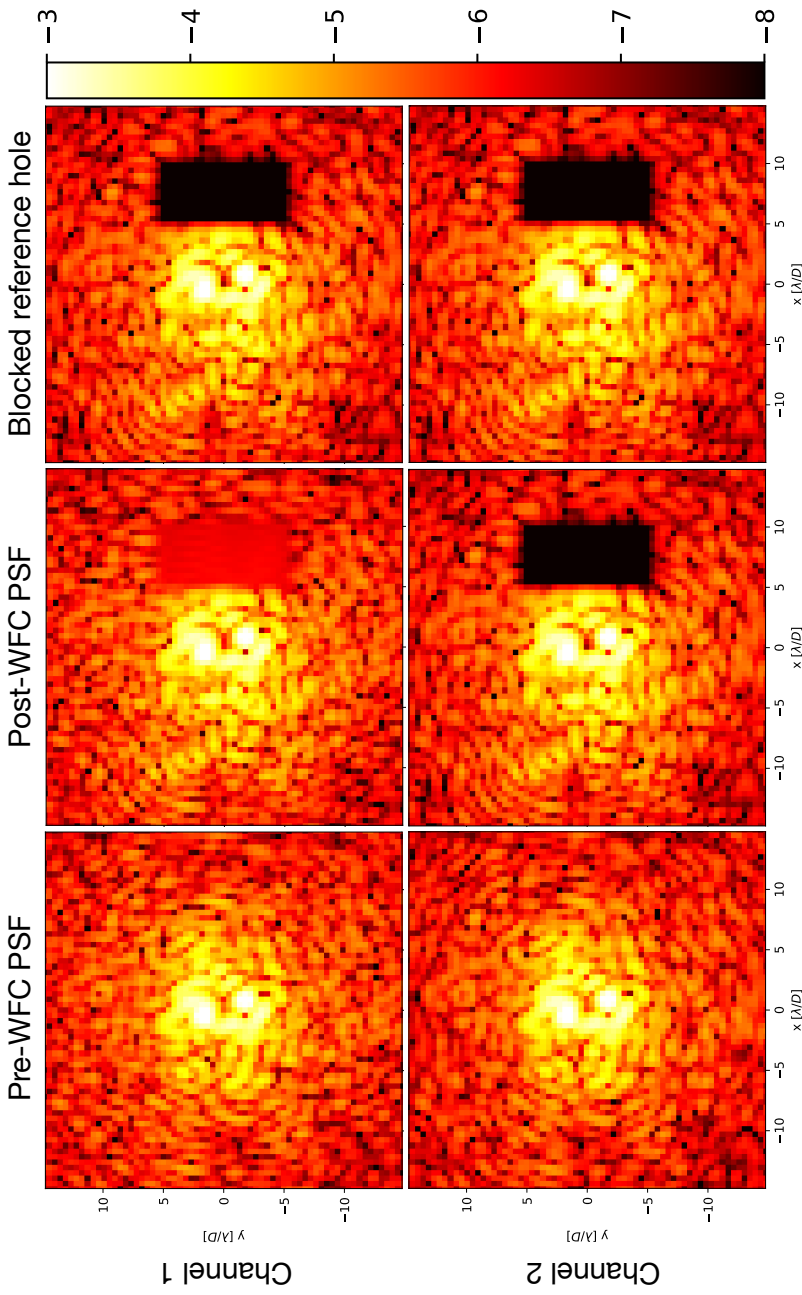


Figure 5.12: WFC example with the PESCC without noise sources present. The subfigures in the two rows show the PSFs of the two channels. The columns show, respectively, the PSFs before WFC, the PSFs after twenty iterations of the WFC, and the PSFs after the WFC with the RH blocked. The colorbar shows the intensity in logarithmic scale and is equal for all subfigures.

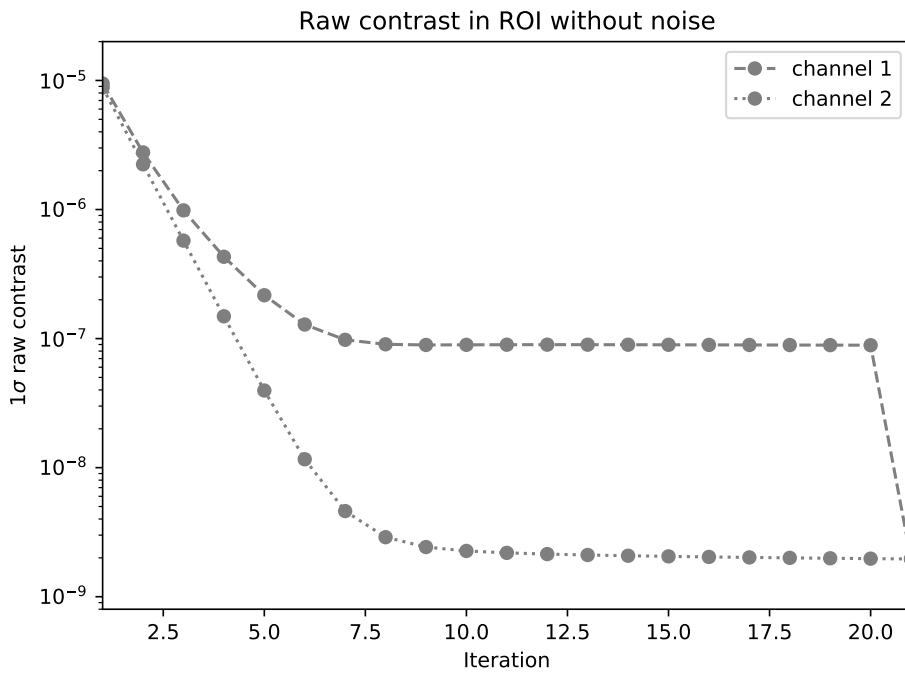


Figure 5.13: Raw contrast as function of iterations in the ROI for WFC example with noise sources. At iteration 21, the RH is blocked to show that the dark holes reach similar raw contrasts.

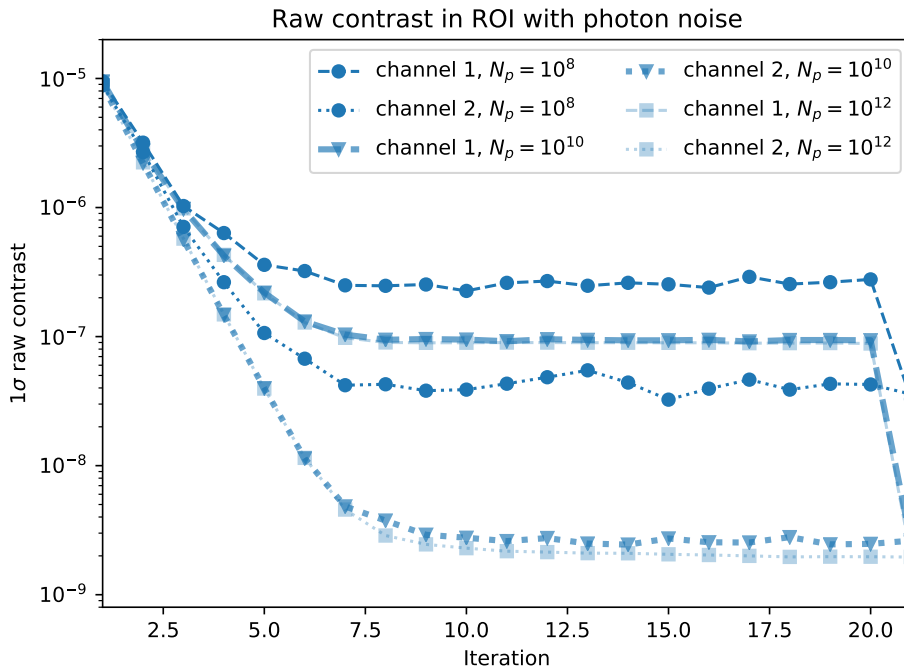
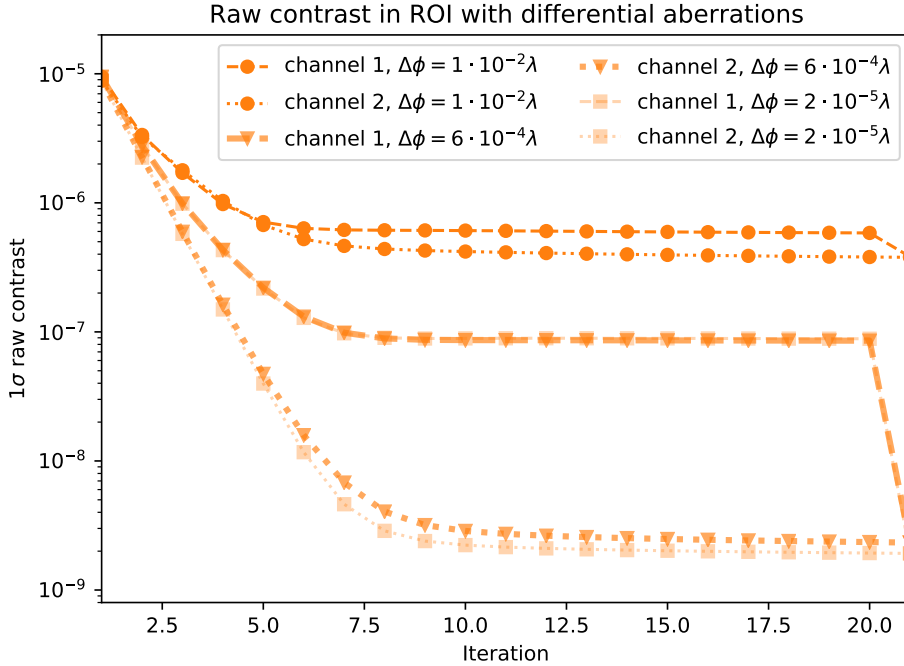


Figure 5.14: Raw contrast as function of iterations for the system with photon noise. The response matrix is acquired without photon noise. At iteration 21, the RH is blocked to compare the raw contrasts in the two channels.



5 Figure 5.15: Raw contrast as function of iterations for the system with different levels of RMS differential aberrations ($\Delta\phi$) between the beams. The response matrix is acquired with the differential aberrations present. At iteration the RH is blocked to compare the raw contrast in the two channels.

Photon noise performance

Here, we test how the wavefront control converges under photon noise. We assume that the response matrix is calibrated by observing a very bright source (e.g., an internal source within the instrument) such that photon noise is irrelevant, that is, we did not simulate photon noise while acquiring the response matrix. In Figure 5.14, the results are presented. For 10^8 photons per exposure the wavefront control converges to $\sim 4 \cdot 10^{-8}$ contrast. With 10^{10} photons, the contrast is close to that of the perfect system, at $\sim 3 \cdot 10^{-9}$. Then for 10^{12} photons, the contrast that is reached is that of the perfect system, $\sim 2 \cdot 10^{-9}$. When considering the current internal near-infrared (NIR) camera and $\Delta\lambda = 50$ nm filter at 1550 nm in SCEXAO (Jovanovic et al. 2015; Lozi et al. 2018), which is located at the 8 meter Subaru telescope on Maunakea, these photon numbers correspond to ~ 2 Hz WFC loop speed on a $m_H = 6$, $m_H = 1$, and $m_H = -4$ target, respectively.

Differential aberrations

As shown in Figure 5.3.1, differential aberrations between the two beams after the PBS severely affect the wavefront sensing. Here, we quantify to what level it limits the WFC. When calibrating the response matrix, the differential aberrations are included as they are expected to be always present in the system. In Figure 5.15, the convergence of the WFC under various levels of differential aberration is shown. For $\Delta\phi = 10^{-2} \lambda$, the PESCC converges to a contrast of $\sim 4 \cdot 10^7$. With $\Delta\phi = 6 \cdot 10^{-4} \lambda$ it converges close to the benchmark performance at $\sim 3 \cdot 10^{-9}$ contrast. For $\Delta\phi = 2 \cdot 10^{-5} \lambda$ the system converges to the benchmark system results at $\sim 2 \cdot 10^{-9}$. To put these values into perspective, the SCEXAO/CHARIS polarization mode (Lozi et al., 2019) has $\sim 7 \cdot 10^{-3}$ waves of differential aberrations¹, and SPHERE/IRDIS was built with $\sim 6 \cdot 10^{-3}$ waves of differential aberrations (Dohlen et al., 2008) (both values calculated at $\lambda = 1600$ nm). This means that if PESCC were implemented at either of these systems, it would converge to a 1σ raw contrast between $\sim 4 \cdot 10^7$ and $\sim 3 \cdot 10^{-9}$, probably closer to the former.

Instrumental polarization

Here, we test the effect of (un)corrected instrumental polarization on the WFC with the PESCC. When calibrating the response matrix the instrumental polarization effects are included when there is no correction of p in post-processing. When the instrumental polarization is corrected, the correction is also included when calibrating the response matrix. In Figure 5.16 a we show the WFC results when the instrumental polarization is not corrected. For $p = 3 \cdot 10^{-2}$, the loop is not stable because the contrast first increases, and then decreases. The final contrast achieved is $\sim 4 \cdot 10^{-6}$, which is only a slight improvement from the initial contrast. When $p = 2 \cdot 10^{-3}$, the system converges to $\sim 10^{-8}$ contrast. Then, for $p = 1.3 \cdot 10^{-4}$ the contrast achieved is $\sim 2 \cdot 10^{-9}$, equal to the benchmark results.

In Figure 5.16 b the polarization effects are corrected during WFC by the method presented in subsection 5.2.6. It shows that for all cases, the WFC converges to the contrast of the system without noise. Uncorrected instrumental polarization at SPHERE/IRDIS is at a level of $p \approx 10^{-2}$, and when corrected, using a detailed instrument polarization model, reaches $p \leq 10^{-3}$ (Van Holstein et al., 2020). As shown in the results of Figure 5.16 a, this means that the instrumental polarization have to be corrected as, otherwise, the loop would be unstable and diverge. When the instrument polarization model is used and p is corrected to a level of $\sim 10^{-3}$, then the WFC will converge to $\sim 10^{-8}$ contrast.

Polarization leakage

We investigate the effects of polarizer leakage on the WFC. As with the previous subsections, we include the polarizer leakage in the response matrix calibration. The results presented in Figure 5.3.1 show that the wavefront error is never affected more than on the level of a 10^{-4} fractional λ RMS WFE. Therefore, we decided to test $t = 10^{-2}, 10^{-4}, 10^{-6}$. The results are shown in Figure 5.17. It shows that for $t = 10^{-3}$, the contrast in channel

¹As derived from a Zemax file provided by T. Groff.

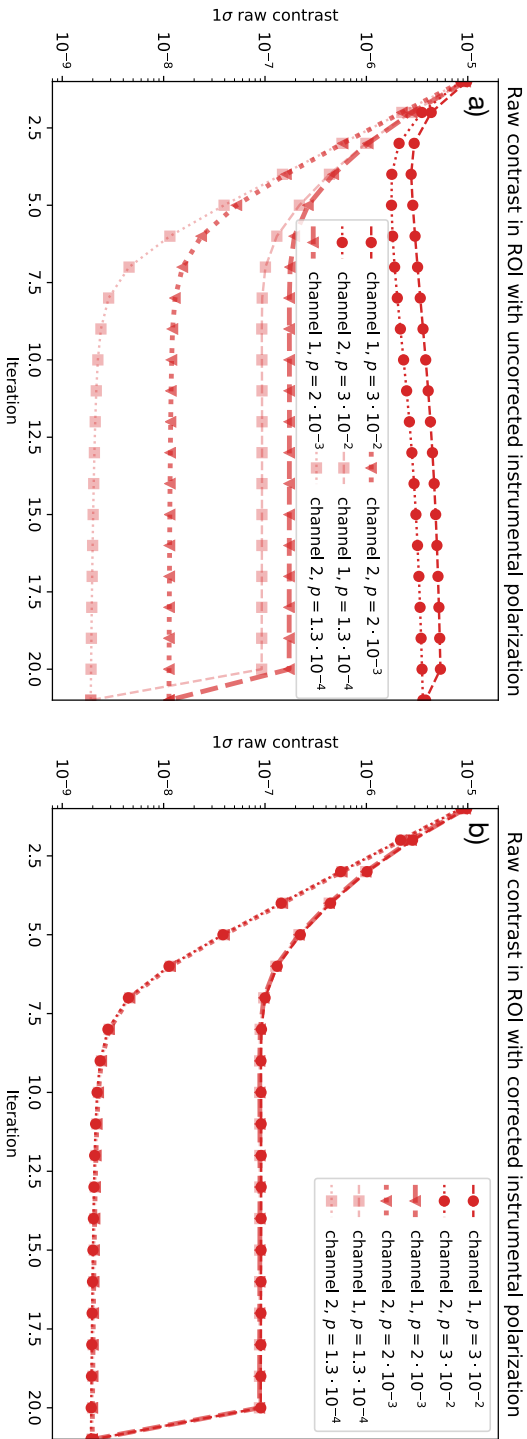


Figure 5.16: Raw contrast as function of iterations for the perfect system with instrumental polarization (p) effects. At the last iteration, the RH is blocked to compare the raw contrast in the two channels; (a) During the acquisition of the response matrix and the closed loop tests the effects of p were not corrected. (b) During all steps of the response matrix acquisition and WFC tests, p was corrected. All three tested levels of p now overlap and reach the performance level of the benchmark tests.

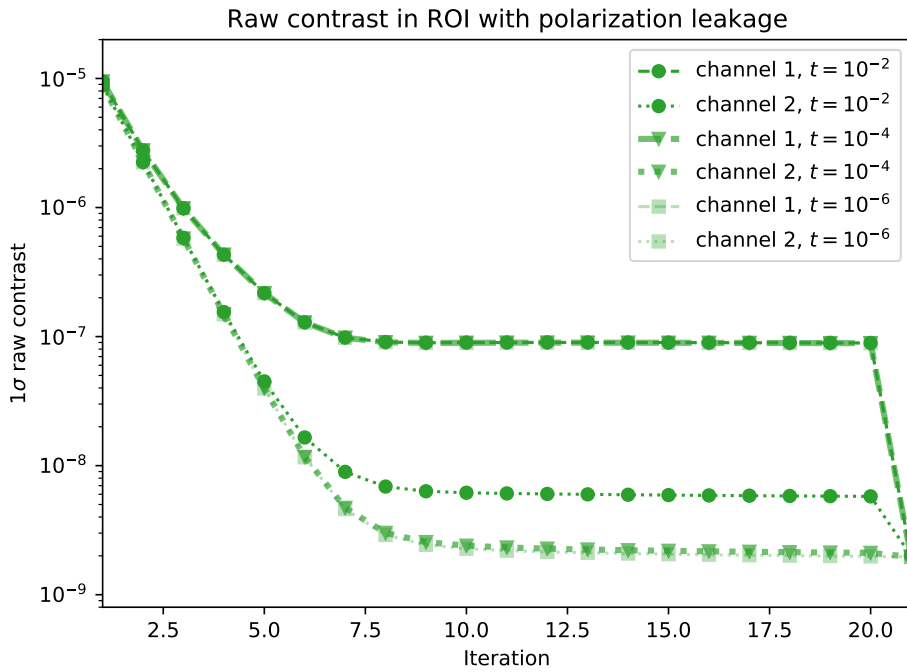
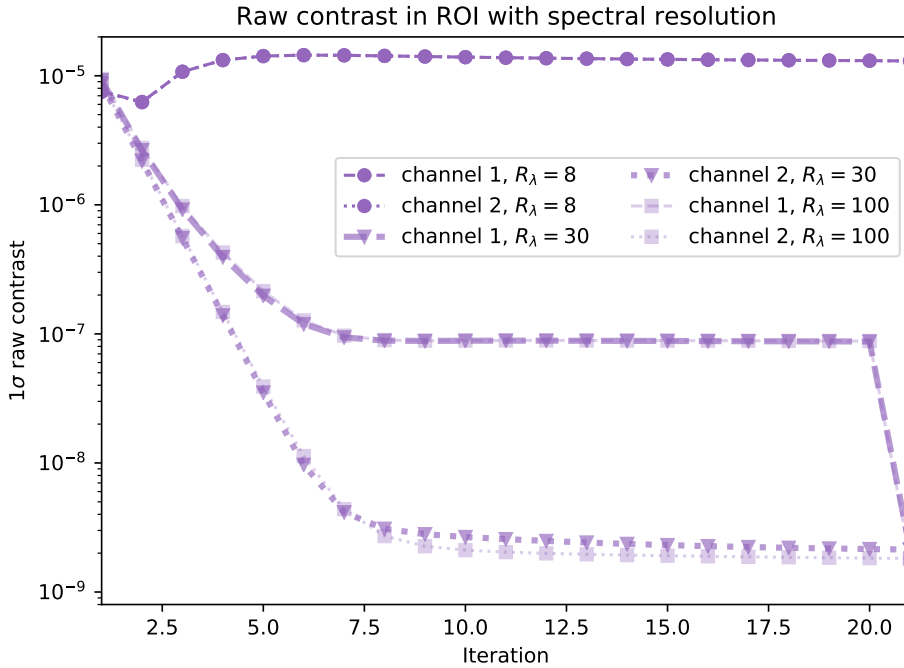


Figure 5.17: Raw contrast as function of iterations for the system with polarizer leakage. The response matrix is acquired with the polarizer leakage. At iteration 21, RH is blocked to compare the raw contrast between the two channels.



5

Figure 5.18: Raw contrast as function of iterations for the system with broadband effects. The response matrix is acquired with the broadband effects included. At iteration 21, the RH is blocked to compare the raw contrast in the two channels.

2 initially does not converge to the benchmark contrast. When the RH is blocked, then both channels converge to $\sim 2 \cdot 10^{-9}$, which shows that channel 2 was limited by leakage from the RH PSF. This proves that the WFC itself is not limited by polarizer leakage, but that the contrast in the DH could be limited by leakage from the polarizer. As discussed in subsection 5.2.7, polarization leakage is expected to be $t = 10^{-3} - 10^{-4}$, and $t \leq 10^{-5}$ for the RH polarizer and PBS, respectively, and are not expected to have an impact on WFC. When the RH polarizer and PBS are misaligned by 5° the leakage is $\sim 2 \cdot 10^{-2}$, which is also on a level that does not impact the WFC, but the contrast in channel 2 will then be limited by RH PSF to $\sim 7 \cdot 10^{-9}$.

Spectral resolution

Here, we simulate the effects of spectral resolution on WFC. The broadband effects are included when the response matrix is measured and the wavefront measurements are identical to Figure 5.3.1. Similarly as before, we sample seven wavelengths of the spectral band and add the resulting PSFs to get the broadband PSF. In Figure 5.18, we show the WFC results for various R_λ . It shows that for $R_\lambda = 8$, the WFC control diverges and that

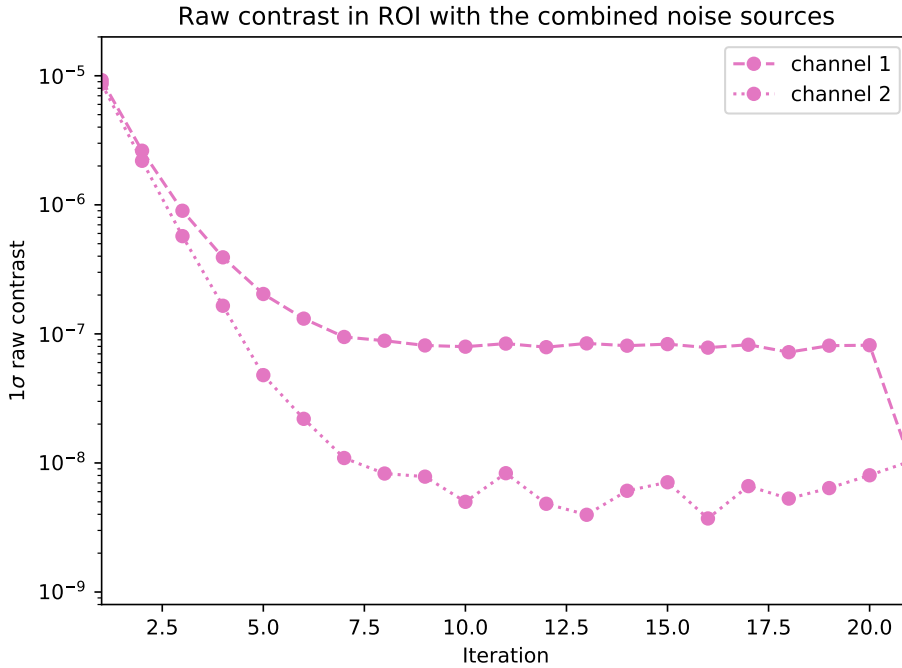


Figure 5.19: Raw contrast as function of iterations for the system with all effects. The response matrix is acquired with all effects included. At iteration 21, the RH is blocked to compare the raw contrasts in the two channels.

the contrast in the ROI becomes worse. For $R_\lambda = 30$ and $R_\lambda = 100$, the WFC converges (close) to the contrast achieved by the system without noise sources. The tested spectral resolutions are equivalent to filters with bandwidths of $0.13 \cdot \lambda_0$, $0.03 \cdot \lambda_0$, and $0.01 \cdot \lambda_0$. Therefore, as shown in Figure 5.18, the PSECC does not work with the broadband photometric filters, but with narrowband filters that have $\delta\lambda \leq 0.03 \cdot \lambda_0$ it will be able to run a WFC effectively. Operation of the PESCC with an integral field spectrograph (IFS) would be an ideal solution as it provides relatively narrowband images over broad wavelength ranges. SCEXAO/CHARIS (Groff et al., 2017) offers a low-resolution mode at $R_\lambda = 18$ and high-resolution modes at $R_\lambda \approx 70$. The PESCC is able to operate with the high-resolution modes. And SPHERE/IFS operates either with $R_\lambda = 30$ (Claudi et al., 2008) or $R_\lambda = 50$ (Mesa et al., 2015), which means that the PESCC can operate with both modes.

Combined effects

Here, we combine the tested noise sources in one simulation to investigate whether these noise sources interact with each other. For every noise source, we select the level that gives a $10^{-2} \lambda$ WFE, as described in subsection 5.3.1. All the noise sources, except the

photon noise, are included when calibrating the response matrix. During the wavefront sensing step, the instrumental polarization is measured and corrected in the frames. The results are presented in Figure 5.19. This shows that the WFC control converges to a contrast of $\sim 10^{-8}$, which is very similar to the raw contrast achieved when there were uncorrected p effects at $p \sim 2 \cdot 10^{-3}$, roughly an order of magnitude worse than the performance under the other individual noise sources. This is caused by the differential aberrations, which introduce intensity differences between the OTFs of the two channels at locations where p is measured. These intensity differences are not caused by p effects and, therefore, lead to incorrect p estimates.

5.3.3 Coherence differential imaging

In this subsection, we study the improvements in contrast that CDI could bring with the PESCC, which was developed in subsection 5.2.8. As proof of principle, we simulate a monochromatic, idealized system without any noise sources other than wavefront aberrations. The parameters as presented in Table 7.2 are used for the simulation. We compare the CDI before and after the WFC. We aim to minimize the starlight in the ROI, defined by $1 \lambda/D > r > 18 \lambda/D$ and $x > 0$. The ROI is larger than what was used in subsection 5.3.2 to show that the PESCC is not limited to a dark hole size. Unlike in subsection 5.3.2, we do not block the RH after the final WFC step. This is to estimate the effect of subtracting the terms involving the RH PSF. In Figure 5.20, the PSFs are shown before and after the WFC as well as after the CDI. It shows that the WFC improves the contrast in the ROI, as it is intended to do, while the CDI improves the entire FOV. Furthermore, it shows that CDI is not able to completely remove the PSF and bring the contrast to numerical noise. This is likely due to numerical artifacts. The PSF of the RH is clearly visible in the post-WFC PSF of channel 1, and is largely removed after the final CDI step. A radial profile of the contrast in the ROI is shown in Figure 5.21. It shows that the initial contrast in the ROI is between $\sim 4 \cdot 10^{-4}$ and $\sim 10^{-6}$. When performing CDI on the initial PSFs, the contrast is improved to $\sim 6 \cdot 10^{-8} - 3 \cdot 10^{-9}$, which is an increase of a factor of $\sim 330 - 6600$. Following the WFC, the contrast becomes $\sim 2 \cdot 10^{-7} - 3 \cdot 10^{-8}$ for channel 1, which is limited by the RH PSF, and $\sim 2 \cdot 10^{-8} - 10^{-9}$ for channel 2. A subsequent CDI step brings this to $6 \cdot 10^{-10}$ for channel 1, and $\sim 3 \cdot 10^{-11} - 8 \cdot 10^{-11}$ for channel 2, which is a factor of $\sim 100 - 300$ increase.

5.4 Discussion and conclusions

In this work, we present the PESCC, a new variant of the SCC that features a linear polarizer in the RH. When the two linear polarization states are subsequently separated by a polarizing beamsplitter, the focal-plane image of the polarization state let through by the RH polarizer is fringed, while the image of the orthogonal polarization state remains unmodulated by fringes. When the OTFs of these two images are subtracted, the sidebands containing wavefront information and the RH peak are revealed. These can be used for wavefront sensing and control in order to generate dark holes where the starlight is canceled by DM actuation. It can also be used for CDI, a post-processing technique that

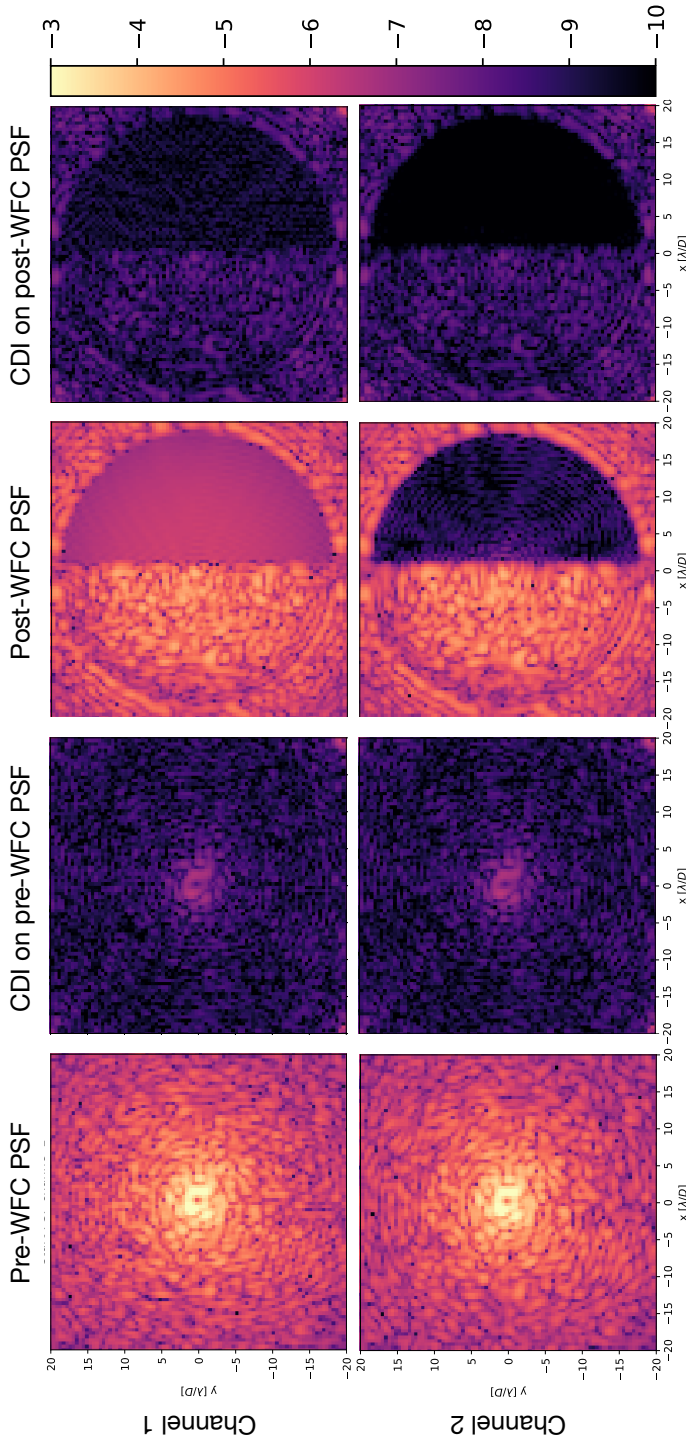


Figure 5.20: WFC and CDI example with the PESCC for a system without noise source other than wavefront aberrations. The two rows show subfigures of the two channels. The columns show the PSFs before WFC, the PSFs after WFC and after CDI, the PSFs after WFC, and the PSFs after WFC and CDI. The colorbar shows the intensity in logarithmic scale and is equal for all subfigures.

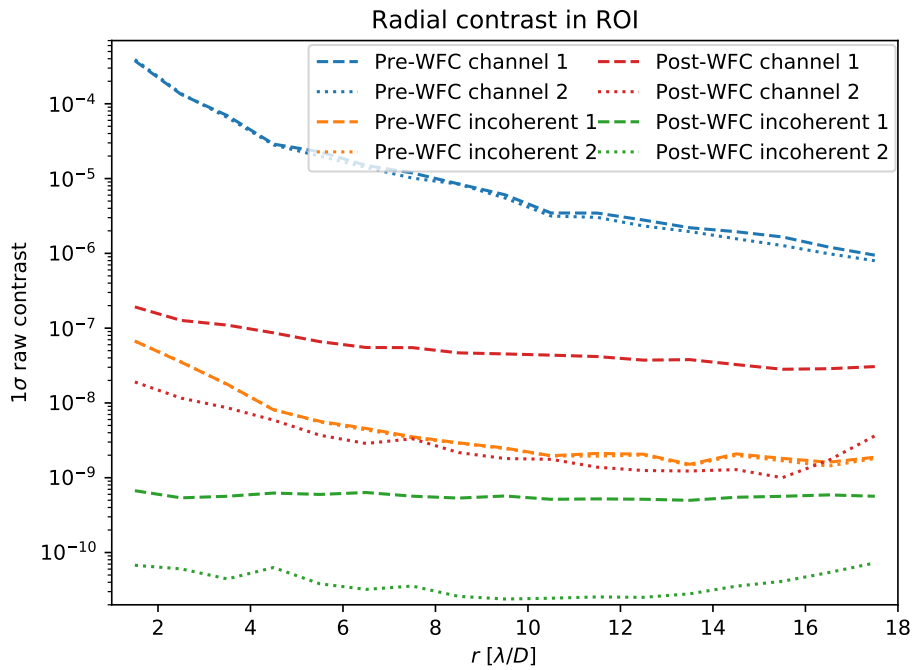


Figure 5.21: Radial contrast in the ROI for the CDI simulation. Shown are the 1σ raw contrast curves before and after WFC and CDI.

aims to remove all coherent light in the image. The PESCC has the great advantage that the RH can be placed right next to the pupil, which strongly reduces the constraints on the optics size as the total beam foot print is much smaller compared to the SCC. This makes it much easier to implement the PESCC in existing high-contrast imaging instruments such as VLT/SPHERE and Subaru/SCEXAO. As focal-plane coronagraphs diffract more light close to the edge of the pupil, this has the added advantage that the PESCC has access to more light for wavefront sensing.

We simulated an idealized HCI system with static phase and amplitude wavefront aberrations generated by an out-of-plane phase aberration. The system was operating at 1550 nm, consisting of a clear aperture, an idealized DM (e.g., no actuator cross-talk or quantization errors), with a 40×40 square grid located in the pupil plane, a charge 2 vortex coronagraph, a (PE)SCC Lyot stop, and a polarizing beamsplitter and detector. We found that the PESCC has ~ 16 times more photons available than the SCC (this includes the 50% throughput of the RH polarizer and polarizing beamsplitter). This was confirmed with additional simulations where we studied the sensitivity of the wavefront sensing with photon noise, as the PESCC reached a sensitivity ~ 4 times higher than that of the SCC. This can either be used to increase the loop speed of the WFC or reach higher sensitivities in the wavefront sensing. The RH being closer the pupil also relaxes the focal-plane sampling and spectral resolutions constraints with regard to the SCC by a factor 2 and 3.5, respectively, to 2 pixels per λ/D (which is a factor four gain in number of pixels) and $R_\lambda \approx 24$ for an infinitely small RH. The latter was confirmed with numerical simulations. Another advantage is that the PESCC automatically estimates the RH PSF, enabling CDI post-processing for all science frames. Through idealized simulations, we have shown that CDI after WFC can reach a 1σ raw contrast of $\sim 3 \cdot 10^{-11} - 8 \cdot 10^{-11}$ between 1 and $18 \lambda/D$. However, we found in the analytical and numerical studies that instrumental polarization and differential aberrations need to be tightly controlled for the PESCC to operate successfully. We have shown that it is possible to measure the degree of instrumental polarization in the OTFs of the two channels when the differential aberrations are not dominant, and this can subsequently be used to correct the images. If the differential aberrations dominate, then it is preferable to use an instrumental polarization model to predict p (Van Holstein et al., 2020). Leakage from the RH polarizer was found not to affect the wavefront sensing significantly, but it does pollute the dark hole in the other channel.

The simulations presented in section 7.3 were highly idealized and are, rather, more representative of space-based observatory conditions. They mainly serve as a proof of principle and in a future work, we will use more realistic simulations to investigate the performance of the PESCC on ground-based systems. This would include realistic residual wavefront errors after an XAO system that will limit the achievable raw contrast to $\sim 10^{-5}$ (Guyon, 2018), while simultaneously creating an incoherent speckle ground that reduces the effectivity of CDI. Also, more realistic telescope apertures and coronagraphs, such as the standard Lyot coronagraph and Vector Vortex Coronagraph (Mawet et al., 2009), need to be included. Furthermore, recent studies have shown that there are also limitations coming from DM(s) location(s) as well as DM actuator number and quanti-

zation errors (Beaulieu et al., 2017, 2020; Ruane et al., 2020). Therefore, we need to add more realistic DM models in future simulations. Finally, CDI was studied without any noise sources present other than wavefront aberrations. Additional simulations that include these noise sources are needed to accurately predict the gain in contrast that CDI could realistically offer.

Thus far, we have not discussed how the PESCC Lyot mask with RH polarizer would actually be implemented. Unfortunately, it is not as trivial as putting a wire grid polarizer on a substrate in front or behind the RH. The main problem is the coherence length L of light, which is defined by (Wolf et al., 2007) as:

$$L = \frac{\lambda^2}{\Delta\lambda}. \quad (5.36)$$

If the optical path difference between the main beam and the beam propagating through the RH polarizer exceeds L , then the RH beam becomes incoherent and will not interfere. This means that the PESCC would then lose its wavefront sensing capabilities. Supposing $\lambda = 1550$ nm and $\Delta\lambda = 50$ nm, then L would only be $48 \mu\text{m}$, which sets very tight requirements on the thickness of the RH polarizer. For an initial lab demonstration with a laser source, a film or wire grid RH polarizer would be sufficient, as the coherence length of lasers sources is much longer than several meters. The implementation in an actual instrument would need other solutions as the bandwidth would otherwise be unacceptably small. We envision two possible solutions: 1) reflective Lyot stops with the RH polarizer also operating in reflection; and 2) a simultaneously lithographically etched wire grid polarizer and Lyot stop on thin a glass substrate that covers the entire pupil. The former solution will probably be affected by a lower quality of the reflected beam from the polarizer (Baur, 2003) and is not easily implemented in existing systems as they generally don't have reflective Lyot stops. Therefore, the latter solution is more appealing as it could be more easily implemented. The pixelated polarizer technology offered by Moxtek² looks especially promising, but it will have to be investigated more closely to determine the feasibility of its application.

The PESCC is a variant of the fast-modulated SCC (FMSCC; Martinez 2019), which temporally modulates the RH. Here, we put into perspective how the PESCC stands in relation to the FMSCC. The two wavefront sensors bear great similarities and part of the simulations presented in this work apply to both (photon noise sensitivity, differential aberrations, and spectral resolution). The main difference is the domain in which the reference beam is encoded: polarization for the PESCC and temporal for the FMSCC. Both domains have their advantages and disadvantages. The PESCC is a completely static solution, important for situations when observing faint targets through the turbulent atmosphere and when moving parts are avoided to prevent vibrations. As an added bonus, polarimetry is almost automatically enabled; this is discussed in more detail below. However, it comes at the cost of added optics with their own set of requirements (e.g., coherence length, leakage, differential aberrations) and sensitivity to instrumental

²<https://moxtek.com/optics-product/pixelated-polarizer/>

polarization. The FMSCC is optically more easily implemented, as it only adds mechanics to dynamically block the RH in synchronization with camera exposure and readout. This makes it suitable for situations in which the number of optics needs to be minimized, for example, in space-based observatories. However, in situations when the camera exposure time to get sufficient signal-to-noise becomes longer than the timescale for which the evolving aberrations can be considered frozen, the FMSCC is less applicable. The temporal RH modulation might also induce vibrations that can affect the overall system performance.

Although the PESCC offers a factor of 3.5 in spectral bandwidth improvement compared to the SCC, it still does not encompass an entire broadband photometric band. Therefore, further improvements are desirable as a broader bandwidth will improve the S/N. To increase the bandwidth of the SCC the multi-reference SCC (MRSCC: Delorme et al. 2016) was introduced. The MRSCC has additional RHs, placed at different clocking angles, and has shown to reach high contrasts in broad wavelength ranges. Similarly, we can introduce the multi-reference PESCC (MRPESCC), which would be very similar to the MRSCC, but with polarizers in each RH. These additional RHs would generate fringes in different directions, which enables more accurate broadband wavefront sensing. The polarizers in the RHs could be orientated differently, making them sensitive to electric field estimates of opposite polarization states and, therefore, possibly enabling the MRPESCC to measure polarization aberrations (Breckinridge et al., 2015). Another solution for increasing the bandwidth is via numerical monochromatization of the broadband image (Huijts et al., 2020). In this method, the wavelength scaling of the PSF is inverted by a vector-matrix multiplication, with the vector the flattened broadband image, and the matrix the inverse of the monochromatic image to broadband image mapping. The monochromatized image could then be used for wavefront sensing.

Starlight is unpolarized to a very high degree, but when it is reflected by an exoplanet, it becomes polarized. Polarization differential imaging (PDI) separates polarized light from unpolarized light, making it a useful tool for discriminating between a planet and mere speckles. As the PESCC requires a polarizing beamsplitter, a natural, additional, post-processing method that could be used is the PDI, especially for longer integration times, where CDI would have trouble removing the incoherent AO speckle halo; in such a case, the PDI could help remove this unpolarized structure. Using a fast polarization modulator to freeze the atmosphere, subsequent images in one of the channels could directly be subtracted, similar to a single-beam polarimeter. If we want to combine the CDI and PDI, it has to be investigated whether, following a CDI step on the two polarization channels, it would be possible to directly subtract them (similar to a dual-beam polarimeter) or would subsequent images in one channel be subtracted after polarization modulation. The latter example would also require a fast polarization modulator (~100 - 1000 Hz) to “freeze” the atmosphere. An additional advantage of a polarization modulator right after the modified Lyot stop is that the effect of differential aberrations can be minimized. A polarization modulator can exchange the two beams between the channels, that is the polarization state with reference beam will be in channel 2 instead of channel 1. The differential aberration will now flip its sign because two beams now in-

cur the other aberrations. Combining two measurements of the ΔOTF , which had a beam exchange in between them, in time will cancel the detrimental effect of the differential aberrations. Similar techniques are used with dual-beam polarimeters to reach high polarimetric sensitivity (Snik & Keller, 2013). In any case, this could be a unique integration of a coronagraph with WFSC, CDI, and PDI.

The integration of the PESCC in current ground-based high-contrast imaging systems such as Subaru/SCEXAO and VLT/SPHERE could be relatively simple. Both systems already have focal-plane coronagraphs (Jovanovic et al. 2015; Beuzit et al. 2019) and polarizing beamsplitters (Lozi et al. 2019; De Boer et al. 2020) in place. Therefore, the only upgrade required would be the modified Lyot stop with RH and polarizer, which in a minimally invasive way could offer substantial gains in terms of focal-plane wavefront sensing and control. In the introduction, we do not discuss space-based systems, however, the simulations show that the PESCC could be applicable to them. This is even more relevant with regard to space-based systems, such as the high-contrast imaging system in HabEx (Mennesson et al., 2016) and LUVOIR (Pueyo et al., 2017), where the optics size is limited as the entire telescope is constrained in weight and volume. The PESCC might also serve as a powerful solution for such systems, as we demonstrate in this work.

Bibliography

- Baudoz, P., Boccaletti, A., Baudrand, J., & Rouan, D. 2005, *Proceedings of the International Astronomical Union*, 1, 553
- Baur, T. G. 2003, in *Polarization Science and Remote Sensing*, Vol. 5158, International Society for Optics and Photonics, 135–141
- Beaulieu, M., Abe, L., Martinez, P., et al. 2017, *Monthly Notices of the Royal Astronomical Society*, 469, 218
- Beaulieu, M., Martinez, P., Abe, L., et al. 2020, *Monthly Notices of the Royal Astronomical Society*, 498, 3914
- Beuzit, J.-L., Vigan, A., Mouillet, D., et al. 2019, arXiv preprint arXiv:1902.04080
- Bos, S. P., Doelman, D. S., Lozi, J., et al. 2019, *Astronomy & Astrophysics*, 632, A48
- Bottom, M., Wallace, J. K., Bartos, R. D., Shelton, J. C., & Serabyn, E. 2017, *Monthly Notices of the Royal Astronomical Society*, 464, 2937
- Breckinridge, J. B., Lam, W. S. T., & Chipman, R. A. 2015, *Publications of the Astronomical Society of the Pacific*, 127, 445
- Brooks, K. J., Catala, L., Kenworthy, M. A., Crawford, S. M., & Codona, J. L. 2016, in *Advances in Optical and Mechanical Technologies for Telescopes and Instrumentation II*, Vol. 9912, International Society for Optics and Photonics, 991203
- Claudi, R. U., Turatto, M., Gratton, R. G., et al. 2008, in *Ground-based and Airborne Instrumentation for Astronomy II*, Vol. 7014, International Society for Optics and Photonics, 70143E
- Close, L. M., Males, J. R., Durney, O., et al. 2018, arXiv preprint arXiv:1807.04311
- Codona, J. L. 2013, *Optical Engineering*, 52, 097105
- Codona, J. L., & Kenworthy, M. 2013, *The Astrophysical Journal*, 767, 100
- De Boer, J., Langlois, M., Van Holstein, R. G., et al. 2020, *Astronomy & Astrophysics*, 633, A63
- Delorme, J., Galicher, R., Baudoz, P., et al. 2016, *Astronomy & Astrophysics*, 588, A136
- Dohlen, K., Langlois, M., Saisse, M., et al. 2008, in *Ground-based and Airborne Instrumentation for Astronomy II*, Vol. 7014, International Society for Optics and Photonics, 70143L
- Galicher, R., & Baudoz, P. 2007, *Comptes Rendus Physique*, 8, 333
- Galicher, R., Baudoz, P., Delorme, J.-R., et al. 2019, *Astronomy & Astrophysics*, 631, A143
- Galicher, R., Baudoz, P., Rousset, G., Totems, J., & Mas, M. 2010, *Astronomy & Astrophysics*, 509, A31
- George, M. C., Bergquist, J., Wang, B., et al. 2013, in *Advanced Fabrication Technologies for Micro/Nano Optics and Photonics VI*, Vol. 8613, International Society for Optics and Photonics, 86131I
- Gerard, B. L., & Marois, C. 2020, *Publications of the Astronomical Society of the Pacific*, 132, 064401
- Gerard, B. L., Marois, C., & Galicher, R. 2018, *The Astronomical Journal*, 156, 106
- Gerard, B. L., Marois, C., Galicher, R., et al. 2019, arXiv preprint arXiv:1910.04554
- Groff, T., Chilcote, J., Brandt, T., et al. 2017, in *Techniques and Instrumentation for Detection of Exoplanets VIII*, Vol. 10400, International Society for Optics and Photonics, 1040016
- Guyon, O. 2004, *The Astrophysical Journal*, 615, 562
- . 2018, *Annual Review of Astronomy and Astrophysics*, 56, 315
- Guyon, O., Miller, K., Males, J., Belikov, R., & Kern, B. 2017, arXiv preprint arXiv:1706.07377
- Huby, E., Bottom, M., Femenia, B., et al. 2017, *Astronomy & Astrophysics*, 600, A46
- Huijts, J., Fernandez, S., Gauthier, D., et al. 2020, *Nature Photonics*, 1
- Jovanovic, N., Martinache, F., Guyon, O., et al. 2015, *Publications of the Astronomical Society of the Pacific*, 127, 890

- Jovanovic, N., Absil, O., Baudoz, P., et al. 2018, arXiv preprint arXiv:1807.07043
- Kemp, J. C., Henson, G., Steiner, C., & Powell, E. 1987, *Nature*, 326, 270
- King, R., & Talim, S. 1971, *Journal of Physics E: Scientific Instruments*, 4, 93
- Kuhn, J., Potter, D., & Parise, B. 2001, *The Astrophysical Journal Letters*, 553, L189
- Lozi, J., Guyon, O., & et al. 2018, in *Adaptive Optics Systems VI*, Vol. 10703, International Society for Optics and Photonics
- Lozi, J., Guyon, O., Jovanovic, N., et al. 2019
- Macintosh, B., Graham, J. R., Ingraham, P., et al. 2014, *Proceedings of the National Academy of Sciences*, 111, 12661
- Males, J. R., Close, L. M., Miller, K., et al. 2018, in *Adaptive Optics Systems VI*, Vol. 10703, International Society for Optics and Photonics, 1070309
- Marois, C., Lafreniere, D., Doyon, R., Macintosh, B., & Nadeau, D. 2006, *The Astrophysical Journal*, 641, 556
- Martinez, P. 2019, *Astronomy & Astrophysics*, 629, L10
- Martinez, P., Kasper, M., Costille, A., et al. 2013, *Astronomy & Astrophysics*, 554, A41
- Martinez, P., Loose, C., Carpentier, E. A., & Kasper, M. 2012, *Astronomy & Astrophysics*, 541, A136
- Mawet, D., Serabyn, E., Liewer, K., et al. 2009, *Optics Express*, 17, 1902
- Mazoyer, J., Baudoz, P., Galicher, R., Mas, M., & Rousset, G. 2013, *Astronomy & Astrophysics*, 557, A9
- Mazoyer, J., Baudoz, P., Galicher, R., & Rousset, G. 2014, *Astronomy & Astrophysics*, 564, L1
- Mennesson, B., Gaudi, S., Seager, S., et al. 2016, in *Space telescopes and instrumentation 2016: Optical, infrared, and millimeter wave*, Vol. 9904, International Society for Optics and Photonics, 99040L
- Mesa, D., Gratton, R., Zurlo, A., et al. 2015, *Astronomy & Astrophysics*, 576, A121
- Miller, K., Males, J. R., Guyon, O., et al. 2019, *Journal of Astronomical Telescopes, Instruments, and Systems*, 5, 049004
- Milli, J., Banas, T., Mouillet, D., et al. 2016, in *Adaptive Optics Systems V*, Vol. 9909, International Society for Optics and Photonics, 99094Z
- Por, E. H., Haffert, S. Y., Radhakrishnan, V. M., et al. 2018, in *Proc. SPIE*, Vol. 10703, Adaptive Optics Systems VI
- Potier, A., Baudoz, P., Galicher, R., Singh, G., & Boccaletti, A. 2020, *Astronomy & Astrophysics*, 635, A192
- Poyneer, L. A., & Véran, J.-P. 2005, *JOSA A*, 22, 1515
- Pueyo, L., Zimmerman, N., Bolcar, M., et al. 2017, in *UV/Optical/IR Space Telescopes and Instruments: Innovative Technologies and Concepts VIII*, Vol. 10398, International Society for Optics and Photonics, 103980F
- Ruane, G., Ngo, H., Mawet, D., et al. 2019, *The Astronomical Journal*, 157, 118
- Ruane, G. J., Echeverri, D., Bendek, E. A., et al. 2020, *Journal of Astronomical Telescopes, Instruments, and Systems*, 6, 045002
- Simon, M. C. 1986, *Applied optics*, 25, 369
- Singh, G., Galicher, R., Baudoz, P., et al. 2019, *Astronomy & Astrophysics*, 631, A106
- Snik, F., & Keller, C. U. 2013, in *Planets, Stars and Stellar Systems* (Springer), 175–221
- Sparks, W. B., & Ford, H. C. 2002, *The Astrophysical Journal*, 578, 543
- Traub, W. A., & Oppenheimer, B. R. 2010, *Exoplanets*, 111
- van Holstein, R. G., Snik, F., Girard, J. H., et al. 2017, in *Techniques and Instrumentation for Detection of Exoplanets VIII*, Vol. 10400, International Society for Optics and Photonics, 1040015
- Van Holstein, R. G., Girard, J. H., De Boer, J., et al. 2020, *Astronomy & Astrophysics*, 633, A64
- Wilby, M. J., Keller, C. U., Snik, F., Korkiakoski, V., & Pietrow, A. G. 2017, *Astronomy & Astro-*

physics, 597, A112

Wolf, E., et al. 2007, Introduction to the Theory of Coherence and Polarization of Light (Cambridge University Press)

6 | On-sky verification of Fast and Furious focal-plane wavefront sensing

Moving forward toward controlling the island effect at Subaru/SCEXAO

Adapted from

S.P. Bos, S. Vievard, M.J. Wilby, F. Snik, J. Lozi, O. Guyon,
B.R.M. Norris, N. Jovanovic, F. Martinache, J.-F. Sauvage,
C.U. Keller

Astronomy & Astrophysics, 639, A52 (2020)

High-contrast imaging (HCI) observations of exoplanets can be limited by the island effect (IE). The IE occurs when the main wavefront sensor (WFS) cannot measure sharp phase discontinuities across the telescope's secondary mirror support structures (also known as spiders). On the current generation of telescopes, the IE becomes a severe problem when the ground wind speed is below a few meters per second. During these conditions, the air that is in close contact with the spiders cools down and is not blown away. This can create a sharp optical path length difference (OPD) between light passing on opposite sides of the spiders. Such an IE aberration is not measured by the WFS and is therefore left uncorrected. This is referred to as the low-wind effect (LWE). The LWE severely distorts the point spread function (PSF), significantly lowering the Strehl ratio and degrading the contrast. In this article, we aim to show that the focal-plane wavefront sensing (FPWFS) algorithm, Fast and Furious (F&F), can be used to measure and correct the IE/LWE. The F&F algorithm is a sequential phase diversity algorithm and a software-only solution to FPWFS that only requires access to images of non-coronagraphic PSFs and control of the deformable mirror. We deployed the algorithm on the SCEXAO HCI instrument at the Subaru Telescope using the internal near-infrared camera in H-band. We tested with the internal source to verify that F&F can correct a wide variety of LWE phase screens. Subsequently, F&F was deployed on-sky to test its performance with the full end-to-end system and atmospheric turbulence. The performance of the algorithm was evaluated by two metrics based on the PSF quality: 1) the Strehl ratio approximation (*SRA*), and 2) variance of the normalized first Airy ring (*VAR*). The *VAR* measures the distortion of the first Airy ring, and is used to quantify PSF improvements that do not or barely affect the PSF core (e.g., during challenging atmospheric conditions). The internal source results show that F&F can correct a wide range of LWE phase screens. Random LWE phase screens with a peak-to-valley wavefront error between $0.4 \mu\text{m}$ and $2 \mu\text{m}$ were all corrected to a *SRA* $>90\%$ and an *VAR* $\lesssim 0.05$. Furthermore, the on-sky results show that F&F is able to improve the PSF quality during very challenging atmospheric conditions (1.3-1.4" seeing at 500 nm). Closed-loop tests show that F&F is able to improve the *VAR* from 0.27 to 0.03 and therefore significantly improve the symmetry of the PSF. Simultaneous observations of the PSF in the optical ($\lambda = 750 \text{ nm}$, $\Delta\lambda = 50 \text{ nm}$) show that during these tests we were correcting aberrations common to the optical and NIR paths within SCEXAO. We could not conclusively determine if we were correcting the

LWE and / or (quasi-)static aberrations upstream of SCEXAO. The F&F algorithm is a promising focal-plane wavefront sensing technique that has now been successfully tested on-sky. Going forward, the algorithm is suitable for incorporation into observing modes, which will enable PSFs of higher quality and stability during science observations.

6.1 Introduction

Current high-contrast imaging (HCI) instruments, such as SCExAO (Jovanovic et al., 2015b), MagAO-X (Males et al. 2018; Close et al. 2018), SPHERE (Beuzit et al., 2019), and GPI (Macintosh et al., 2014), are now routinely exploring circumstellar environments at high contrast ($\sim 10^{-6}$) and small angular separation (~ 200 mas) in the near-infrared or the optical (Vigan et al., 2015). These instruments detect and characterize exoplanets by means of direct imaging, integral field spectroscopy, or polarimetry (Macintosh et al. 2015; Keppler et al. 2018). Such observations help us to understand the orbital dynamics of planetary systems (Wang et al., 2018), the composition of the exoplanet's atmosphere (Hoeijmakers et al., 2018), and find cloud structures (Stam et al., 2004). To reach these extreme contrasts and angular separations, these instruments use extreme adaptive optics to correct for turbulence in the Earth's atmosphere, coronagraphy to remove unwanted star light, and advanced post-processing techniques to enhance the contrast, for example, angular differential imaging (Marois et al., 2006a), reference star differential imaging (Ruane et al., 2019), spectral differential imaging (Sparks & Ford, 2002), and polarimetric differential imaging (Langlois et al. 2014 ; van Holstein et al. 2017).

One of the limitations of the current generation of HCI instruments are aberrations that are non-common and chromatic between the main wavefront sensor arm and the science focal-plane. These non-common path aberrations (NCPA) vary on minute to hour timescales during observations, due to a changing gravity vector, humidity, and temperature (Martinez et al. 2012; Martinez et al. 2013), and are therefore difficult to remove in post-processing. Ideally, these aberrations are detected by wavefront sensors close to, or in the science focal plane and subsequently corrected by the deformable mirror (DM). Many variants of such wavefront sensors have been developed, and some of these have been successfully demonstrated on-sky (Martinache et al. 2014; Singh et al. 2015; Martinache et al. 2016; Bottom et al. 2017; Wilby et al. 2017; Bos et al. 2019; Galicher et al. 2019; Vigan et al. 2019).

Another limitation is the island effect (IE), which occurs when the telescope pupil is strongly fragmented by support structures for the secondary mirror. We refer to these fragments as segments in the rest of the paper. When these structures become too wide, conventional pupil-plane wavefront sensors (WFSs) such as the Shack-Hartmann and Pyramid poorly sense sharp discontinuities in phase aberrations across these gaps. This is because these WFSs typically measure the gradient of the wavefront in two orthogonal directions, and discontinuities can be difficult to integrate over to retrieve the wavefront itself. It is expected that the upcoming class of Giant Segmented Mirror Telescopes (GSMTs) will increasingly suffer from the IE, as the support structures will become even wider and more numerous.

For the current generation of HCI instruments, the IE mainly manifests itself as the so-called low-wind effect (LWE). The LWE occurs when the ground windspeed is very low (under a few m/s), which would typically be considered to be amongst the best observing conditions. It has now been well understood to be a form of dome seeing and is caused by thermal problems at the spiders supporting the secondary mirror (Sauvage

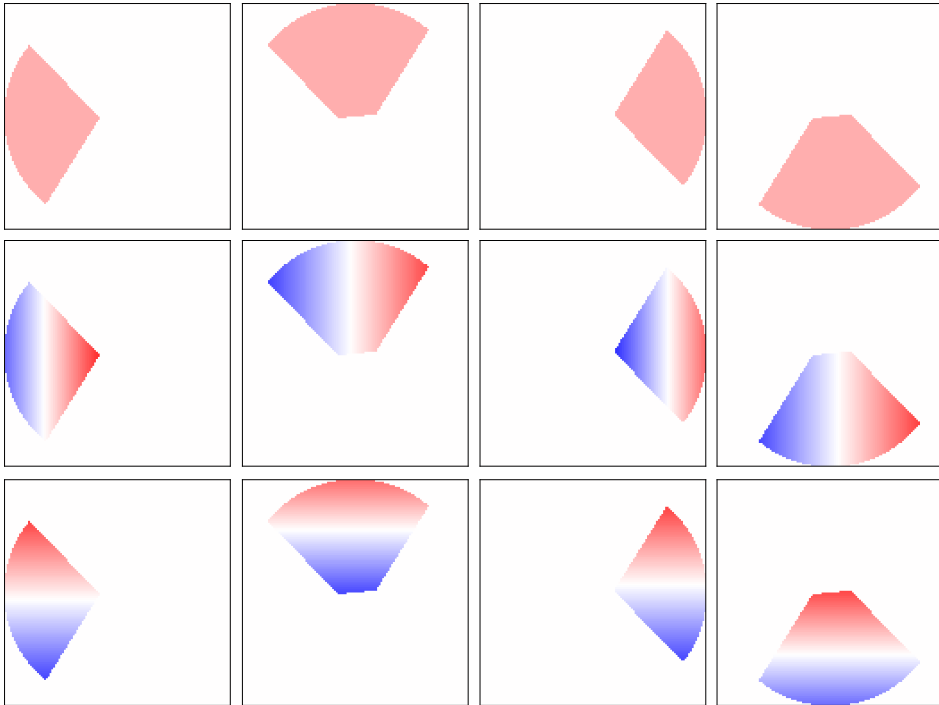


Figure 6.1: Piston-tip-tilt mode basis for SCEXAO instrument at the Subaru Telescope. The pupil of SCEXAO is fragmented into four segments due to the spiders, see Figure 6.4. For every individual segment, we define a piston, tip, and tilt mode.

et al. 2015; Sauvage et al. 2016; Milli et al. 2018). During these events, radiative cooling of the spiders lowers their temperature below that of the ambient air. The air on one side of the spider that is in close contact, and which is not blown away due to the low wind speeds, also cools down and changes its refractive index. This introduces a sharp optical path length difference (OPD) between light passing on opposite sides of a spider, which is subsequently not measured by the traditional wavefront sensor. The aberrations generated by the LWE were measured to have a peak-to-valley (P-V) wavefront error (WFE) of up to hundreds of nanometers (Sauvage et al., 2015), and can be considered to be a combination of piston-tip-tilt (PTT) phase modes across each segment. We invite the reader to see Figure 6.1 for an example of such modes in the context of the Subaru Telescope pupil. Typical consequences of the LWE are a strong distortion of the point spread function (PSF), the first Airy ring broken up into multiple side lobes, and an accompanying strong reduction in Strehl ratio (typically tens of percent). This results in a reduced relative signal from circumstellar objects and degraded raw contrasts, and thus an overall worse performance of the HCI system. Furthermore, these effects are generally quasi-static and thus become difficult to calibrate in post-processing. The LWE has been reported at the VLT and Subaru telescopes to affect 3% to 20% of the observations, while Gemini South is at < 3% (Milli et al., 2018).

Thus far, multiple solutions have been investigated that either prevent the LWE from occurring, or measure it with an additional wavefront sensor and correct it with the DM. At the VLT, the spiders were recoated with a material that has a low thermal emissivity in the infrared. This brought the occurrence rate down from 20% to a more manageable 3% (Milli et al., 2018). But it is still reported when the ground wind speed is below 1 m/s, making additional solutions that drive this down even further desirable. In the context of future instruments of GSMTs, there have also been investigations (Hutterer et al., 2018) toward changing the wavefront reconstruction of the Pyramid WFS to make it sensitive to the IE and therefore the LWE. Several focal-plane wavefront sensors have also been investigated to specifically target the LWE. For example, the Asymmetric Pupil Fourier Wavefront Sensor (APF-WFS; Martinache (2013)) was demonstrated on-sky at Subaru/SCEXAO to be able to correct the LWE (N'Diaye et al., 2018). At Subaru/SCEXAO, a host of new focal-plane wavefront sensing methods are being tested with the internal source and on-sky in the context of the IE and LWE (Vievard et al., 2019).

In this paper, we present the results of deploying one of these methods, the Fast and Furious algorithm (F&F; Keller et al. 2012; Korhikoski et al. 2012; Korhikoski et al. 2014), to the SCEXAO instrument. This algorithm is a software-only solution to focal-plane wavefront sensing and therefore easy to implement on HCI instruments. It will be more extensively discussed in section 7.2. In previous work, F&F was already explored as a way to measure the LWE in the context of the SPHERE instrument (Wilby et al. 2016; Wilby et al. 2018). Specifically, the goal was to show that the algorithm would still perform well in the low signal-to-noise environment of the differential tip-tilt sensor (Baudoz et al., 2010) within SPHERE. It showed satisfactory performance both in simulation (Wilby et al., 2016) and at the MITHIC bench (Vigan et al., 2016) in a laboratory environment (Wilby et al., 2018). Here, we study the performance of the algorithm on

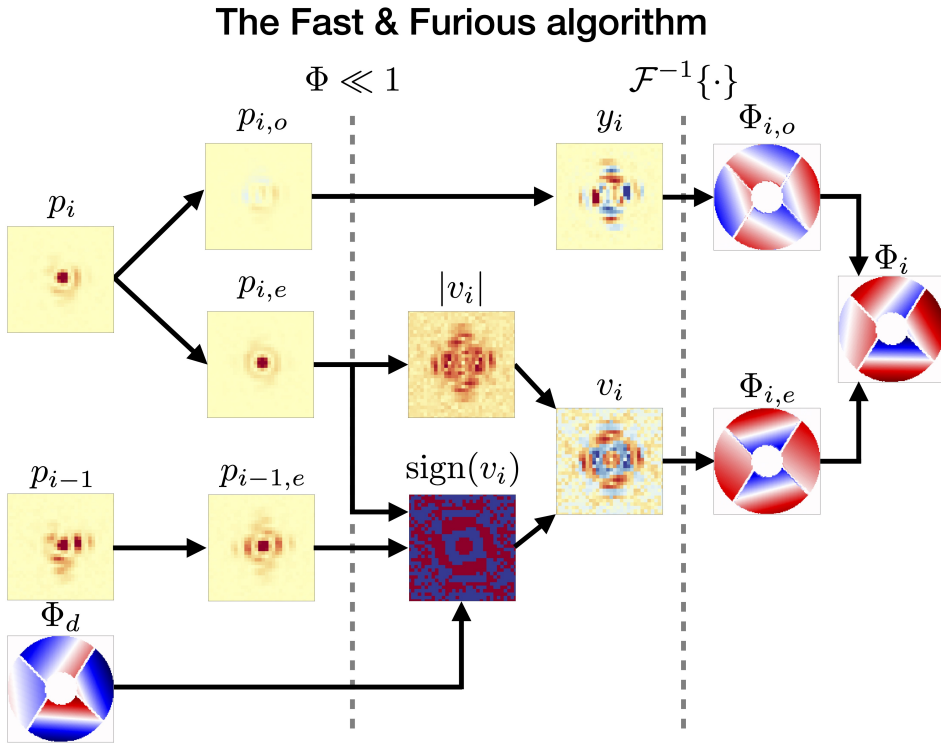


Figure 6.2: Explanation of one iteration of the Fast and Furious algorithm. At iteration i an image p_i is split into its even $p_{i,e}$ and odd $p_{i,o}$ components. The odd component can directly solve for the odd focal-plane electric field y_i (Equation 6.5). Similarly, the even component is used to solve for the absolute value of the even focal-plane electric field $|v_i|$ (Equation 6.6). To solve for the sign of v_i , the previous image p_{i-1} , that has a diversity phase Φ_d , is introduced to break the degeneracy (Equation 6.9). The estimates of y_i and v_i together give an estimate of the pupil-plane phase Φ_i (Equation 6.10).

the SCExAO instrument using the internal source, and report on the first on-sky tests in section 6.3. We discuss the results and conclude in section 7.5.

6.2 Fast and Furious algorithm

The Fast and Furious (F&F; Keller et al. 2012; Korhikoski et al. 2014) algorithm is an extension of the sequential phase diversity technique originally introduced by Gonsalves (2002). In conventional phase diversity techniques (Gonsalves 1982; Paxman et al. 1992), the degeneracy in estimating even phase modes is solved by recording two images, one in focus and another strongly out of focus. This forces the user to either split the light into two imaging channels or alternately record in- and out-of-focus images. A sequential

phase diversity algorithm uses sequential in-focus images and relies on a closed-loop system that continuously provides phase corrections that improve the wavefront and serve as diversity to solve for the even phase aberrations. Therefore, such an algorithm will never be able to give a single shot phase estimate and must always be operated in closed loop.

The F&F algorithm refers to an extension of this sequential phase diversity technique and greatly improves the dynamic range and stability (Keller et al., 2012). Focal-plane images acquired by the algorithm are split into the even and odd components. Using simple algebra, the odd component directly solves for the odd focal-plane electric field. The even component can only solve for the absolute value of the even focal-plane electric field. To acquire the sign of the even electric field, F&F uses the image and change in the phase introduced by the DM of the previous iteration to break the degeneracy. Together, these operations give an estimate of focal-plane electric field, and, by an inverse Fourier transformation, an estimate of the pupil-plane phase. As one F&F iteration only relies on simple algebra and a single Fourier transformation, the algorithm is computationally very efficient, and can in principle run at high frame rates.

An extensive discussion on the algorithm and its performance is presented in Keller et al. (2012) and Korhikoski et al. (2014). Here, we give an overview of the key F&F equations that lead to a phase estimate. A graphical overview of the algorithm is shown in Figure 6.2. For these equations, we notably assume; (i) real and symmetric pupil amplitude (which is a reasonable assumption for most telescope and instrument pupils); (ii) monochromatic light (performance of the algorithm decreases when the bandwidth increases); (iii) phase-only aberrations (an extension of F&F deals with amplitude aberrations (Korhikoski et al., 2014)); and (iv) phase aberrations can be approximated to be small ($\Phi \ll 1$ radian). The point-spread-function (PSF) of an optical system is given by:

$$p = |\mathcal{F}\{Ae^{i\Phi}\}|^2. \quad (6.1)$$

Here, p is the PSF, A and Φ the pupil-plane amplitude and phase, and $\mathcal{F}\{\cdot\}$ the Fourier transformation operator. For F&F, the assumption is that A is real and symmetric. We adopt the same notation as in Wilby et al. (2018), which means that pupil-plane quantities are denoted by upper case variables and focal-plane quantities by lower case variables. Assuming that $\Phi \ll 1$, we can expand the PSF to second order, which results in:

$$p \approx S a^2 + 2a(ia * \phi_o) + (ia * \phi_o)^2 + (a * \phi_e)^2. \quad (6.2)$$

With the electric field of the unaberrated PSF given by $a = \mathcal{F}\{A\}$, the Fourier transforms of the even and odd pupil-plane phases ($\Phi = \Phi_o + \Phi_e$) are given by $\phi_o = \mathcal{F}\{\Phi_o\}$ and $\phi_e = \mathcal{F}\{\Phi_e\}$. The normalization factor $S = 1 - \sigma_\phi^2$ can be understood as the first order Maréchal approximation of the Strehl ratio (Roberts et al., 2004), with σ_ϕ^2 the wavefront variance. This approximation becomes highly accurate when the aberrations are small. The convolution operator is denoted by $*$. It is more convenient to express Equation 6.2 in terms of the odd and even focal-plane electric fields, which are given by:

$$y = i\mathcal{F}\{A\Phi_o\} = ia * \phi_o, \quad (6.3)$$

$$v = \mathcal{F}\{A\Phi_e\} = a * \phi_e. \quad (6.4)$$

Splitting the PSF (Equation 6.2) in its odd and even components ($p = p_o + p_e$), and solving for y and v results in:

$$y = ap_o/(2a^2 + \epsilon), \quad (6.5)$$

$$|v| = \sqrt{|p_e - (Sa^2 + y^2)|}. \quad (6.6)$$

Here, ϵ is a regularization parameter for the pixels where a goes to zero that would otherwise amplify the noise. This solution only solves for $|v|$, which is a well-known sign ambiguity (Gonsalves 1982; Paxman et al. 1992). The sign of v is solved by introducing an additional image that has a known phase diversity Φ_d . This additional image is for F&F the image of the previous iteration; because it has a phase diversity with respect to the current iteration, given by the change in DM command (assuming that Φ remains constant). The PSFs of these two images can be approximated by:

$$p_i \approx Sa^2 + 2ay + y^2 + v^2, \quad (6.7)$$

$$p_{i-1} \approx Sa^2 + 2a(y + y_d) + (y + y_d)^2 + (v + v_d)^2, \quad (6.8)$$

with $y_d = i\mathcal{F}\{A\Phi_{d,o}\}$ and $v_d = \mathcal{F}\{A\Phi_{d,e}\}$ the odd and even focal-plane electric fields of the diversity. It is most robust to estimate only the sign of v (instead of the complete v) by:

$$\text{sign}(v) = \text{sign}\left(\frac{p_{i-1,e} - p_{i,e} - (v_d^2 + y_d^2 + 2yy_d)}{2v_d}\right). \quad (6.9)$$

For the first iteration of F&F, when there is no diversity image available, the most optimal guess is $\text{sign}(v) = a$. Although this guess might be wrong, it will provide sufficient diversity to make the following estimates of the even wavefront accurate. The estimate of the odd part of the wavefront is unaffected by any sign error, and therefore will be improved from the first iteration. The final pupil-plane phase estimate for this iteration is given by:

$$A\Phi = \mathcal{F}^{-1}\{\text{sign}(v)|v| - iy\}. \quad (6.10)$$

This phase estimate can be subsequently projected onto a mode basis of choice to target specific aberrations. For example, the piston-tip-tilt (PTT) mode basis shown in Figure 6.1 is designed specifically for the LWE, and/or the lowest Zernike modes for NCPA caused by optical misalignments (Wilby et al., 2018).

6.3 Demonstration at Subaru/SCExAO

6.3.1 SCExAO and algorithm implementation

We deployed F&F to the Subaru Coronagraphic Extreme Adaptive Optics (SCExAO) instrument (Jovanovic et al., 2015b), which is located on the Nasmyth platform of the Subaru Telescope downstream of the AO188 system (Minowa et al., 2010). We invite the reader to see Figure 6.3 for a schematic of the telescope, AO188, and SCExAO. The main wavefront sensor in the instrument is a pyramid wavefront sensor (PYWFS; Lozi

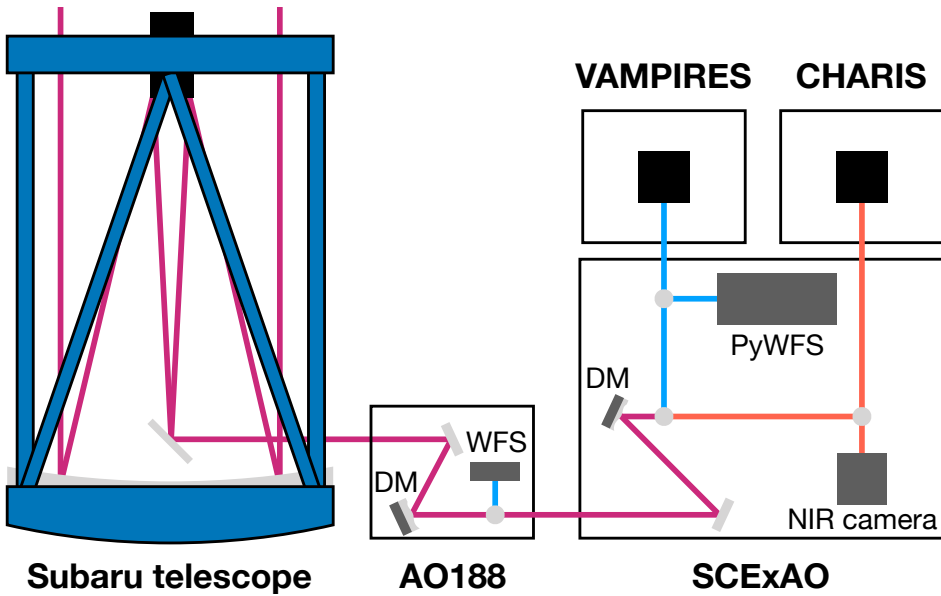


Figure 6.3: Schematic of the complete system layout. Acronyms in the figure are: deformable mirror (DM), wavefront sensor (WFS), pyramid wavefront sensor (PyWFS), near infrared (NIR).

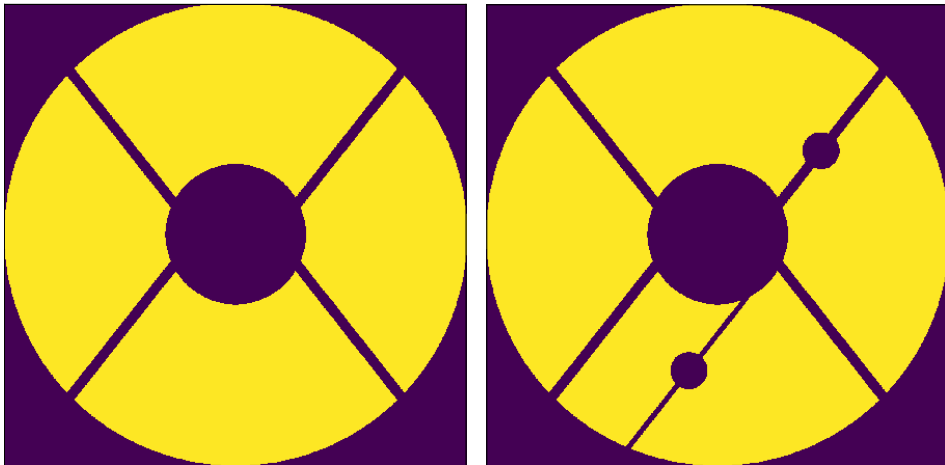


Figure 6.4: Pupil of Subaru pupil (left), and the SCExAO instrument (right). The SCExAO pupil has additional structure to block unresponsive actuators in the deformable mirror. The spiders are 23 cm wide and up to ~1 m high (Milli et al., 2018).

et al. 2019a) in the 600-950 nm wavelength range. The real-time control is handled by the Compute And Control for Adaptive Optics (CACAO) software package (Guyon et al., 2018) that sends the wavefront corrections to the 2000-actuator deformable mirror (DM). The active pupil on the DM has a diameter of 45 actuators, which gives SCExAO a control radius of $22.5 \lambda/D$. The CACAO software allows for additional wavefront corrections to be sent by other wavefront sensors, by treating their corrections on separate DM channels. It updates the PYWFS reference offset to make sure that the AO loop does not cancel commands of the other wavefront sensors. The current science modules fed by SCExAO are VAMPIRES (Norris et al., 2015) in the optical, and CHARIS (Peters-Limbach et al. 2013; Groff et al. 2014) in the near-infrared, but more are foreseen (Lozi et al. 2018; Lozi et al. 2019b; Guyon et al. 2019).

The F&F algorithm is implemented using Python and the HCIPy package (Por et al., 2018). Python has a simple interface with the instrument and allows for rapid testing. We tested F&F using the internal NIR C-RED 2 camera that has a 640×512 pixel InGaAs sensor cooled to -40°C (Feautrier et al., 2017). The images were cropped to 64×64 pixels, dark-subtracted, flat-fielded and subsequently aligned with a reference PSF from a numerical model. Alignment with the reference PSF improved the stability of F&F (or any other FPWFS algorithm), but therefore tip and tilt were no longer measured. The number of images stacked for one F&F iteration was generally between 1 and 100. The algorithm was tested using a narrowband filter ($\Delta\lambda = 25 \text{ nm}$) at 1550 nm and the H-band filter. We note that the quantum efficiency of the detector in the C-RED 2 camera rapidly decreases when the wavelength is above $\sim 1630 \text{ nm}$, and therefore the tests using the H-band filter only used approximately half of the wavelength range. As explained in section 7.2, F&F assumes a real and symmetric pupil amplitude. In Figure 6.4, we show in the left subfigure the nominal Subaru pupil and on the right subfigure the SCExAO pupil. SCExAO defines its pupil internally, because there are unresponsive actuators in the DM that need to be blocked, which is shown in the figure. Normally, we would have used the right subfigure to be the pupil amplitude for F&F, and accept that the relatively small asymmetry would introduce a bias in the wavefront estimate. But, during the tests presented in this paper, this internal mask in SCExAO was damaged (the structure blocking the dead actuator in the lower segment was broken off), and thus we assumed the nominal Subaru pupil for A . To accurately calculate $a = \mathcal{F}\{A\}$ on the detector, we had to take into account the plate scale and the rotation of the pupil with respect to the detector. We determined these parameters by fitting a simple model of the PSF to data from the instrument, using the pupil in Figure 6.4 and the rotation and plate scale as free parameters. This resulted in a plate scale of 15.45 mas/pixel and a counterclockwise rotation of 9.6° . As discussed in section 7.2, the phase estimate by F&F as shown in Equation 6.10 can be projected on a mode basis. This can have multiple advantages: first, if the goal is to just control a certain mode basis (e.g., the PTT modes or low-order Zernike modes for NCPA); second, by filtering out the (noisier) higher spatial frequency modes, the noise in the phase estimate is reduced; and third, removing any systematics due to inaccurate pupil symmetry assumptions. As the goal of this paper was to measure the LWFE using a camera downstream of the PYWFS, we projected the phase estimates of F&F on a mode basis that consisted of the PTT modes shown in Figure 6.1 and/or the lowest 50 Zernike modes (starting at defocus) for NCPA estimation. We did not estimate tip and tilt, because

all images are aligned with a reference PSF. The combined PTT and Zernike mode basis was not orthogonalized, and therefore there could have been some cross-talk. However, as we operated in closed loop, we initially expected these effects to be minimal, and in the end did not notice any significant effects. The algorithm used its own phase estimates (after the decomposition; multiplied by the loop gain) for the phase diversity. Estimates of PYWFS would not be useful as they will not see the same aberration due to NCPA, chromatic effects, and the null-space of the PYWFS. The DM command $\theta_{DM,i}$ at iteration i sent to CACAO by F&F for wavefront control was calculated by:

$$\theta_{DM,i} = c_{lf}\theta_{DM,i-1} - \frac{g}{2}\Phi_i, \quad (6.11)$$

with g the loop gain (mostly set between 0.1 and 0.3), and c_{lf} the leakage factor (generally between 0.99 and 0.999). The factor $\frac{1}{2}$ was to account for the reflection of the DM, and Φ_i the phase estimate by F&F at iteration i . We computed the DM commands as actuator displacements in micrometers, which were converted to voltages internally by CACAO. The loop speed during the tests presented in this work was generally between 4 and 25 frames per second (FPS), and depends on the image size, the number of images stacked ($N_{img\ avg}$), and the size of the mode basis on which the phase estimate is decomposed. Currently, the main limitation is $N_{img\ avg}$, because each of the images needs to be aligned, which is the most time-consuming process. The image alignment code uses the Python library Scipy (Jones et al., 2014). It is expected that if the algorithm (including the image alignment routines) were completely written in C (used by CACAO), 300 - 400 FPS would be relatively easily to achieve if that is desirable.

6.3.2 Quantifying PSF quality

We quantified the quality of the PSF by the Strehl ratio approximation. The Strehl ratio approximation (*SRA*) is estimated by comparing the data p with a numerical PSF $|a|^2$ (that has been oversampled by a factor of 16) by using a modified encircled energy metric:

$$SRA = \frac{p(r < 1.22 \lambda/D)}{p(r < 11.5 \lambda/D)} \cdot \frac{|a|^2(r < 11.5 \lambda/D)}{|a|^2(r < 1.22 \lambda/D)}. \quad (6.12)$$

The *SRA* is calculated at $\lambda = 1550$ nm. We note that it is very difficult to make an accurate Strehl measurement (Roberts et al., 2004), for example, in our metric aberrations that impact the PSF beyond $11.5 \lambda/D$ are not taken into account. Furthermore, as all images are aligned with a numerical reference PSF, the brightest peak of a severely distorted image will be aligned with the PSF core. This means that images with a low Strehl ratio (~ 0 -50%) are reported with a much higher *SRA*. We chose this metric over residual wavefront measurements, because there was not an independent WFS available that is sufficiently common-path with the C-RED 2 camera during either internal source or on-sky tests. Furthermore, at high Strehl ratios it is still a good indication of residual wavefront variance.

Some of the on-sky results were taken during challenging atmospheric conditions, for example during the tests on December 12, 2019, we recorded a 1-1.1" seeing in H-band, corresponding to 1.3-1.4" seeing at 500 nm^1 . This meant that when the F&F loop was

¹The seeing scales with $\lambda^{-1/5}$ (Hardy, 1998).

Table 6.1: Parameters of F&F and the closed-loop settings during the internal source tests.

Parameter	Value
ϵ	10^{-3}
Mode basis	Zernike or PTT
$N_{\text{img avg}}$	10
g	0.3
c_{lf}	0.999
N_{iter}	200

closed, the PSF would qualitatively improve (it became more symmetric), but the improvement was not reflected in an increased SRA . Therefore, we defined a metric that measures the quality of the first Airy ring, because the low-order nature of LWE aberrations results in strong distortions of the first Airy ring and it is easy to measure. The Variance of the normalized first Airy ring (VAR) is defined as:

$$VAR = \text{Var}\left(\frac{p(1.52\lambda/D < r < 2.14\lambda/D)}{\langle p(1.52\lambda/D < r < 2.14\lambda/D) \rangle} \cdot \frac{\langle |a|^2(1.52\lambda/D < r < 2.14\lambda/D) \rangle}{|a|^2(1.52\lambda/D < r < 2.14\lambda/D)}\right) \quad (6.13)$$

We only select the peak of the Airy ring (i.e., $1.52\lambda/D < r < 2.14\lambda/D$), as that is where the effects are the strongest. Furthermore, the Airy ring is normalized twice, first by its mean in order for us to measure relative disturbances. And subsequently, by the normalized Airy ring of a numerically calculated PSF. This is necessary because there are natural variations in brightness across the Airy ring due to the diffraction structures of the spiders that we want to divide out. An undistorted PSF will therefore have $VAR=0$, while distorted PSFs will have $VAR>0$. Based on the experiments with the internal source, a VAR of 0.03-0.05 can be considered as good. We note that the VAR is insensitive to aberrations that are azimuthally symmetric, for example, defocus and spherical aberration, as these are removed by the first normalization step.

6

6.3.3 Internal source demonstration

We conducted tests with the internal source in SCExAO. The goal was to show that F&F in closed-loop control can be used to measure and correct NCPA and the LWE. The parameters for F&F and the closed-loop settings that were used during these tests are shown in Table 6.1. There were no other AO loops running during these tests. The first test was to calibrate the static aberrations in the optical path of the NIR camera. We used the narrow band filter ($\Delta\lambda = 25$ nm) at 1550 nm. As we expected optical misalignments to dominate the NCPA, we decided to project the F&F output on the lowest 50 Zernike modes. In Figure 6.5 a and b, the pre- and post-NCPA calibration PSFs are shown. The SRA has increased from 94% to 97%, the first Airy ring becomes less distorted, which is reflected in the VAR going down from 0.15 to 0.03. This shows that F&F is suitable to correct low-order NCPA.

The next test was to introduce a severe LWE wavefront ($1.6 \mu\text{m}$ P-V) and correct it

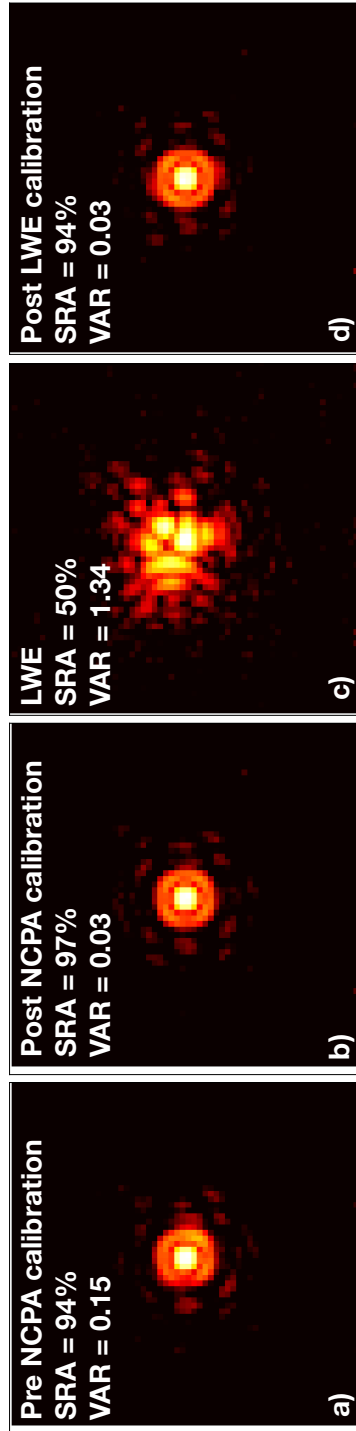


Figure 6.5: Images during tests with the internal source. PSFs are normalized to their maximum value, and are plotted in logarithmic scale. PSF before (a) and after (b) NCPA calibration. Introduction of the LWE phase screen (c) and the PSF after correction (d).

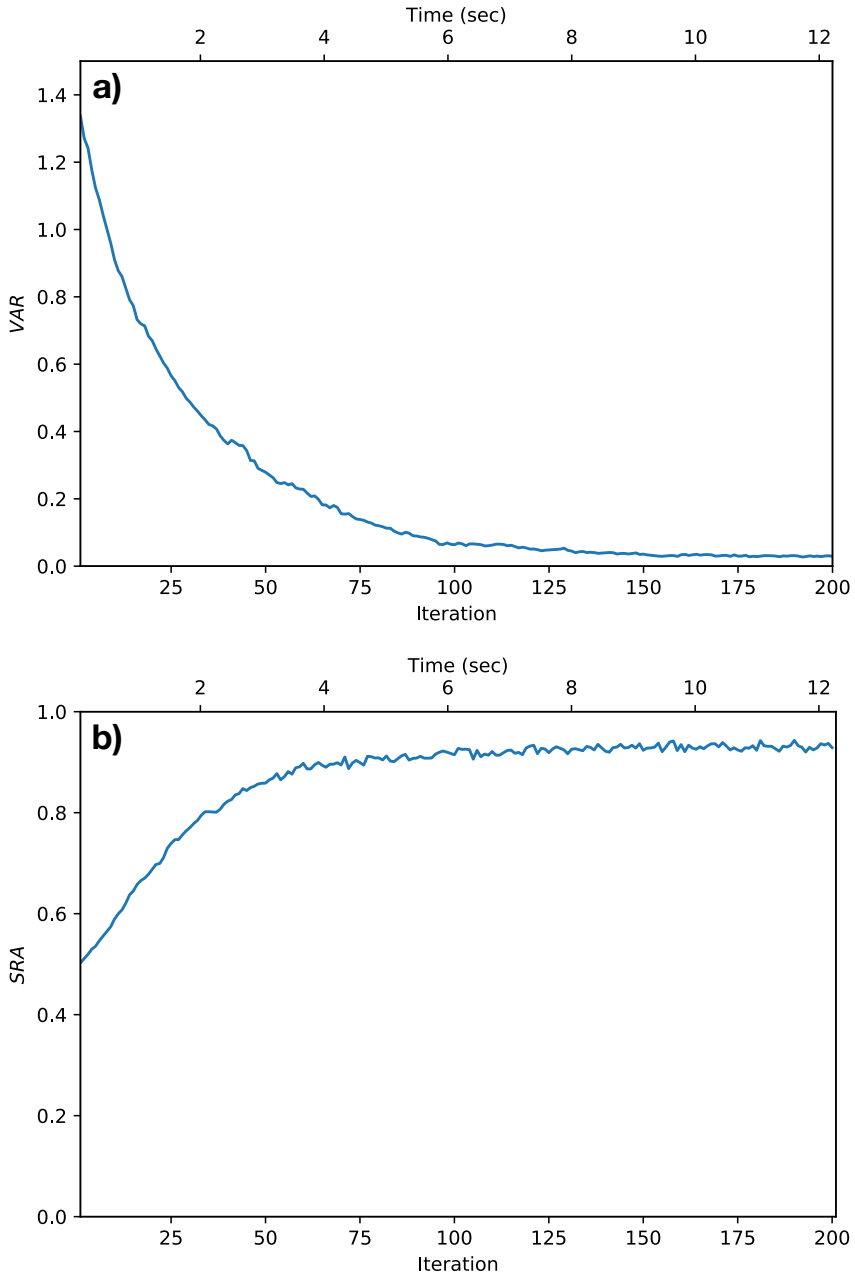


Figure 6.6: F&F performance as the iterations progress. (a) The VAR as function of iteration. (b) The SRA as function of iteration.

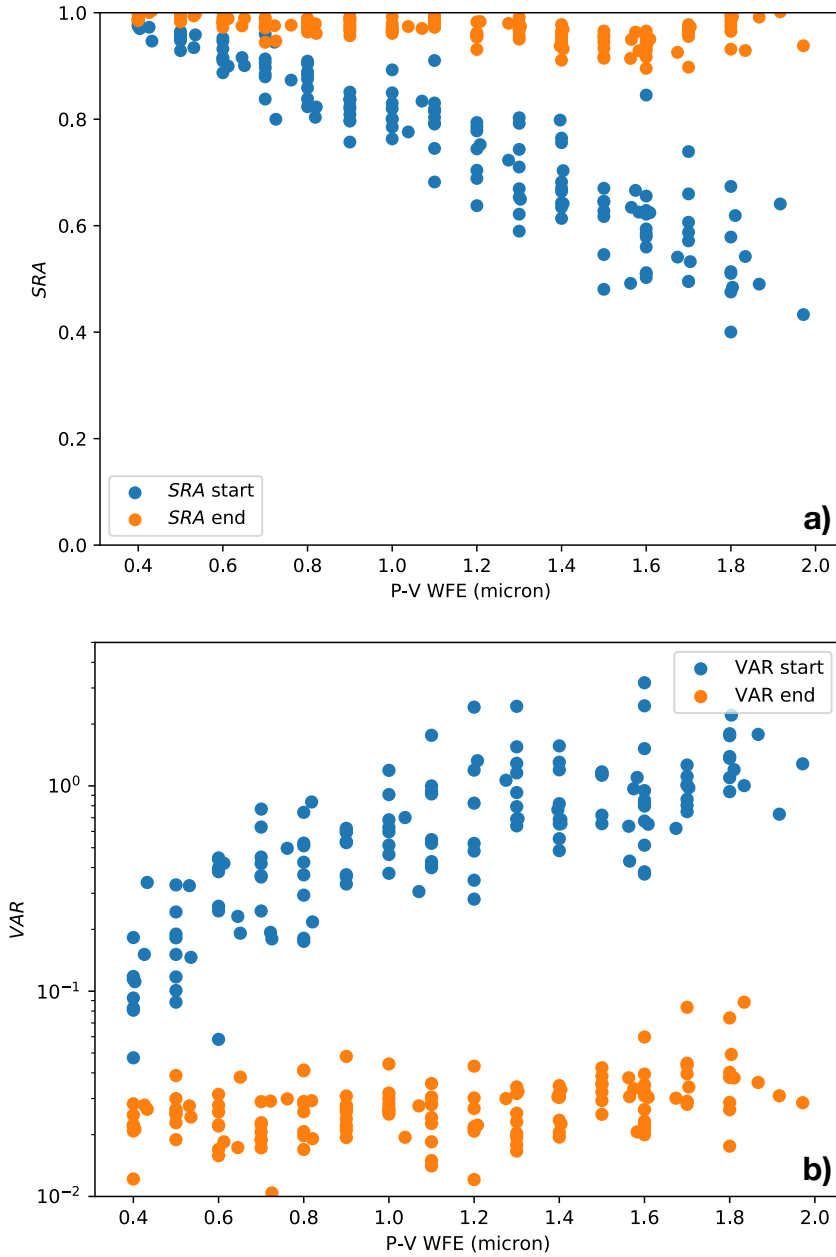


Figure 6.7: The *SRA* and *VAR* as function of the P-V WFE of the LWE for the experiments with the internal source. Shown is the distribution before and after correction by F&F.

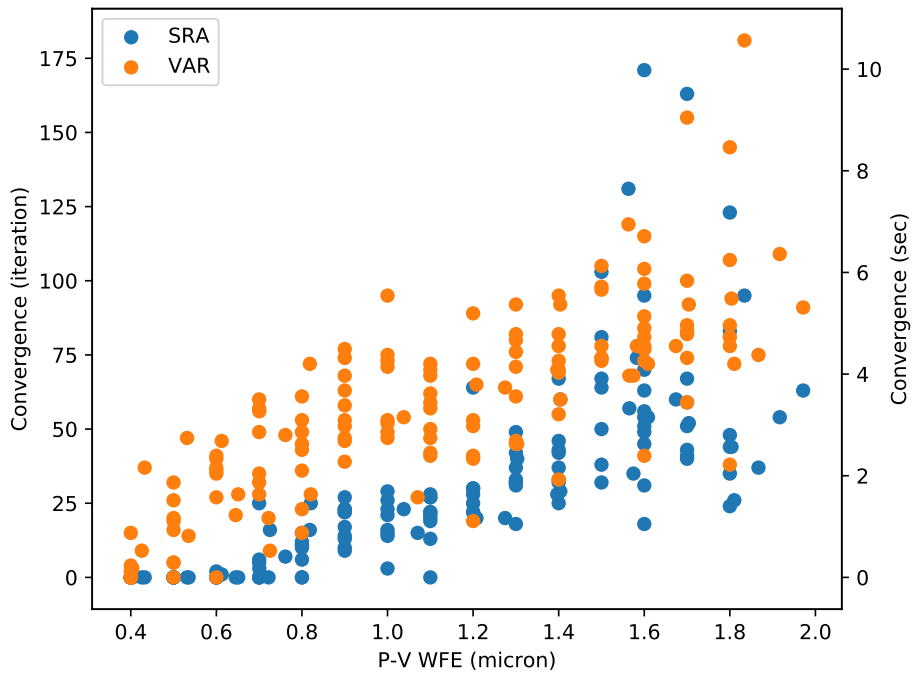


Figure 6.8: Convergence time of F&F as function of the P-V WFE of the LWE for the experiments with the internal source. The convergence time for the *SRA* and *VAR* was measured separately. The algorithm converged when the *SRA* > 90 % and the *VAR* < 0.1.

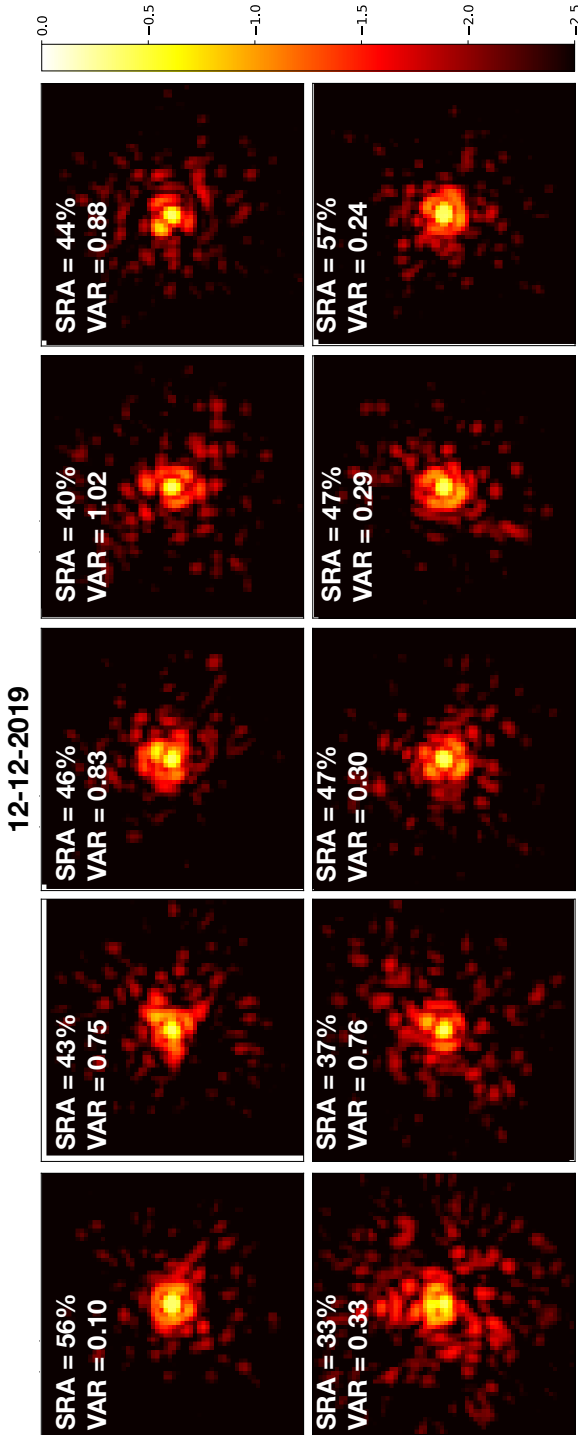


Figure 6.9: Short exposure images recorded during an open-loop test of F&F. Individual images consist of 10 aligned and stacked images, each with an integration time of $19 \mu\text{s}$, with a total integration of 0.19 ms . These show that the PSFs are severely distorted by the challenging atmospheric conditions. The first Airy ring is always broken up, and higher order diffraction structure is not visible. All PSFs are normalized to their maximum value, and are plotted in logarithmic scale.

with the algorithm. Here, we chose to project the estimated phase on the PTT mode basis, as the NCPA were already compensated by the previous test, and the PTT modes were assumed to dominate. In Figure 6.5 c and d, we show the PSF with the LWE and after the correction. When the LWE is introduced, the PSF is heavily distorted and broken up into multiple parts. This is quantified by the *SRA* of 50% and the *VAR* of 1.34. After correction, the PSF is almost restored the original aberration-free version of itself, it looks very similar to Figure 6.5 b with some slight vertical elongation due to an uncorrected aberration. Quantitatively, the *SRA* increased to 94% and the *VAR* decreased to 0.03. The evolution of the *VAR* and *SRA* during the test are shown, respectively, in Figure 6.6 a and b. The *SRA* and *VAR* have mostly converged in ~ 100 iterations and remained stable at that level.

We expanded the LWE correction test by including a set of LWE phase screens in a range P-V WFEs to verify that F&F can bring back the PSF quality. We tested 153, random, LWE phase screens with a P-V WFE between 0.4 and 2 μm . For each of these phase screens, we calculated the *SRA* and *VAR* before and after correction, the results of which are shown in Figure 6.7. These show that, for the initial, uncorrected images, the *SRA* decreases for increasing WFE. The *VAR* increases with increasing WFE, but its values have a bigger spread than the *SRA*. For example, when the WFE is 0.9 μm P-V, the *SRA* varies between 75% and 90%, while the *VAR* fluctuates between 0.3 and 0.6. Also for higher WFE, for example, at 1.8 μm P-V, the *VAR* is distributed between 1 and 2. Although the *VAR* generally increases with P-V WFE, due to the large spread, the *VAR* on its own does not seem to be a good indicator for the amount of WFE other than that there is WFE present. After correction, the distributions of the *SRA* and *VAR* flatten to above 90% and under ~ 0.05 , respectively. Thus, the LWE phase screens were successfully corrected in all the tested cases. We also measured the convergence time of F&F for each of the LWE phase screens. The convergence time was measured separately for the *SRA* and the *VAR*. The algorithm was said to have converged when the *SRA* $> 90\%$ and the *VAR* < 0.1 . In Figure 6.8, the results are shown. The convergence time goes up with increasing P-V WFE, with the *VAR* having slightly longer convergence times. For most P-V WFEs, the *SRA* converged within 75 iterations, which corresponds to ~ 4.5 seconds. For the *VAR*, most tests converged within 100 iterations, which is ~ 6 seconds. For some phase screens the convergence time is zero, which is because the phase screens were not severe enough to push the PSF out of the converged regime.

6.3.4 On-sky demonstration

We tested F&F on-sky during two SCEXAO engineering nights. The first tests were done in the first half night of December 12, 2019, while observing the bright star Mirach ($m_H = -1.65$). The tests started at 19:24 and ended at approximately 20:00 (HST). The atmospheric conditions were not ideal, seeing measurements during the F&F test were recorded to be between 1-1.1" in H-band, corresponding to 1.3-1.4" seeing at 500 nm. In less severe conditions, when SCEXAO can deliver a good AO performance, it routinely

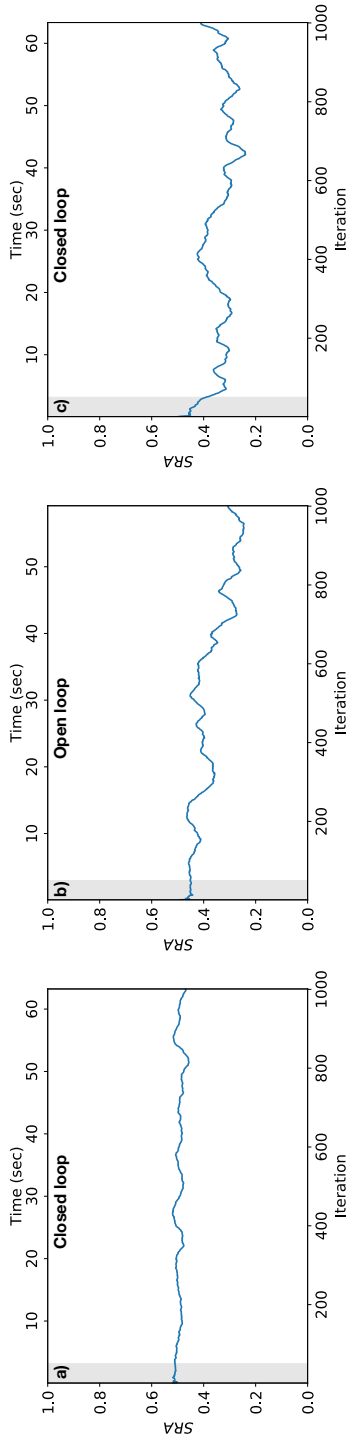


Figure 6.10: Measurements of *SRA* on running average images during three, subsequent in time, on-sky experiments. The running average image for iteration i is defined as the average of images $i - 50$ to i . The gray box denotes the iterations for which the full average of 50 images could not be calculated. (a) The measurements during the first closed-loop test. (b) The F&F loop was opened, meaning the gain was set to zero and its DM correction removed. (c) Loop was closed again.

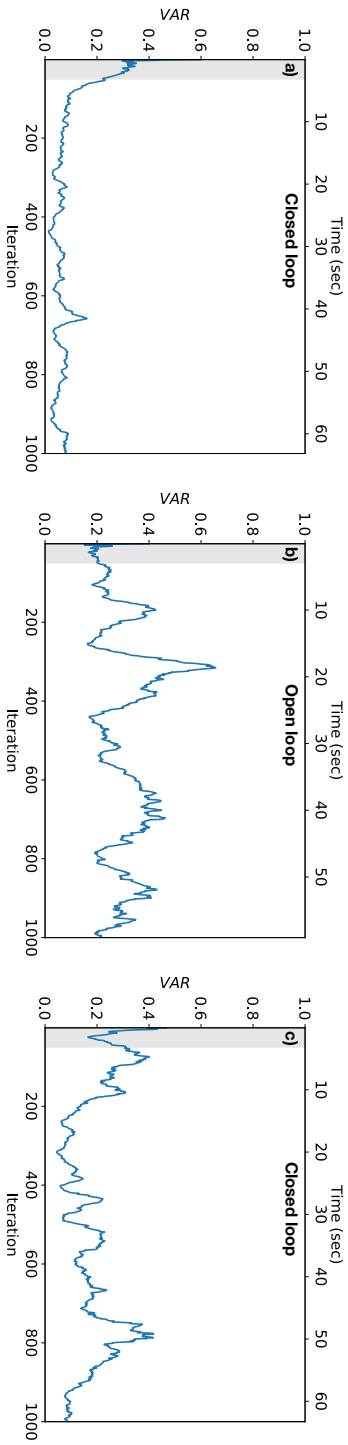


Figure 6.11: Measurements of VAR on running average images during three, subsequent in time, on-sky experiments. The running average image for iteration i is defined as the average of images $i - 50$ to i . The gray box denotes the iterations for which the full average of 50 images could not be calculated. (a) The measurements during the first closed-loop test. (b) The F&F loop was opened, i.e. gain was set to zero and its DM correction removed. (c) Loop was closed again.

Table 6.2: Parameters of F&F and the closed-loop settings during the on-sky tests.

Parameter	Value (12-12-2019)	Value (30-01-2020)
ϵ	10^{-2}	10^{-3}
Mode basis	Zernike + PTT	Zernike + PTT
$N_{\text{img avg}}$	10	10
g	0.3	0.3
c_{lf}	0.999	0.999
N_{iter}	1000	500 / 1000

achieves estimated Strehl ratios above 90%². In comparison, during these tests we report a *SRA* between 34% and 49%. The individual images (that F&F used for its phase estimates) were heavily distorted, for instance, the first Airy ring was always broken up, and higher order diffraction structure was not visible. As an example, Figure 6.9 shows images that were taken during open-loop measurements, without F&F running but with the PYWFS loop closed. The wind speed of the jet stream was forecasted to be 22.2 m/s at 20:00 (HST)³. The nearby CFHT telescope (located 750 m to the east of the Subaru Telescope) reported a wind speed between 4.5 and 7 m/s during the tests⁴. Simultaneously, the wind speed inside the dome of the Subaru Telescope was measured to be between 0 and 0.3 m/s. A further analysis of all wind speed data measured in 2019 by CFHT and within the Subaru dome revealed that these were typical conditions, and therefore cannot be considered individually to indicate LWE occurrence. In Table 6.2, the settings for F&F and the loop are shown. The F&F loop was running at 12 FPS. These experiments were performed with the H-band filter, as it was already in place when the experiments started. It was not possible to separate NCPA and LWE calibrations, and therefore we projected the F&F phase estimate on the combined Zernike and PTT mode basis to be able to simultaneously sense and correct them.

Here, we present the tests where we first closed the F&F loop, then opened it (by setting the gain to zero) and removed the DM command, and then closed the loop again. Each of these tests was conducted with 1000 iterations. As shown in Figure 6.9, the individual images were severely distorted by the atmosphere. To suppress atmospheric effects and more accurately measure the performance of F&F on long exposure images, we introduced running average images. The running average image on iteration i is defined as the average of the images $i - 50$ to i . The *SRA* estimated during these tests is shown in Figure 6.10. This figure shows that during the first closed-loop tests, the *SRA* was relatively stable around 50%, and when the F&F loop opened, it slowly deteriorated to below 40%. When the F&F loop closed again, the *SRA* varied between 30% and 50%. Roughly half way through the open loop and through the last closed-loop test, the atmospheric conditions started deteriorating, explaining the strong variations and loss in *SRA*.

²<https://www.naoj.org/Projects/SCExAO/scexaoWEB/020instrument.web/010wfsc.web/indexm.html>

³<https://earth.nullschool.net/>

⁴<http://mkwc.ifa.hawaii.edu/archive/wx/cfht/>

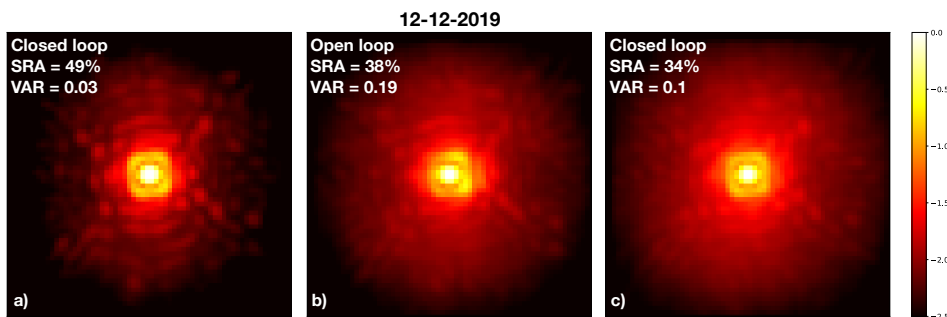


Figure 6.12: Averaged PSFs during during three, subsequent in time, on-sky experiments. All PSFs are normalized to their maximum value, and are plotted in logarithmic scale. During these experiments, the atmospheric conditions degraded, explaining the lower *SRA*. (a) The average PSF with a closed F&F loop. (b) The average PSF when the F&F loop was opened and its DM correction removed. (c) The average PSF when the F&F loop was closed again.

In Figure 6.11, we show similar plots but for the *VAR*. These figures show that the *VAR* was significantly lower during the closed-loop tests than during the open-loop test. In the first closed-loop test, the *VAR* decreased within the first hundred iterations and then remained relatively stable around 0.1. When the loop opened, the *VAR* never got under 0.2, and it even peaked at ~ 0.65 around three hundred iterations. When the loop was closed again, the *VAR* again decreased in \sim two hundred iterations. It did not remain as stable as in the first experiment, which is likely due to the deteriorated atmospheric conditions, but it is still lower than the open-loop experiment. The oscillations in *VAR* observed in all three tests could be due to changes in the *LWE*. Finally, in Figure 6.12, we show the PSFs that are averaged over all the iterations, and therefore suppress most of the atmospheric effects. These PSFs also clearly show how the deteriorating conditions, such as the halo around the PSF, which is caused by residual wavefront errors, become significantly more visible during the experiments. It shows that when the loop is closed, the *VAR* converges to 0.03 - 0.10, and when the loop is open, the *VAR* is 0.19. This clearly shows that, even when the atmospheric conditions are challenging, F&F manages to increase the symmetry of the PSF and thus corrects aberrations distorting the PSF. This was also observed in all other tests performed during this night, which are not presented in this work. However, although the circumstances seemed to be right (low ground wind speed), we cannot be sure that during these tests we corrected *LWE* aberrations, static aberrations upstream of SCEXAO, or NCPA.

We conducted more F&F on-sky tests during the first half night of January 30, 2020. We observed Rigel ($m_H = 0.2$), and the tests approximately started and ended at 23:36 and 23:48 (HST), respectively. We did not make seeing measurements, but the conditions appeared to be somewhat better than for the previous on-sky tests. The wind speed in the dome of the Subaru Telescope was again reported to be very low, between 0 and 0.2 m/s. The CFHT telescope reported a windspeed between 3 and 4 m/s. Again, typical wind

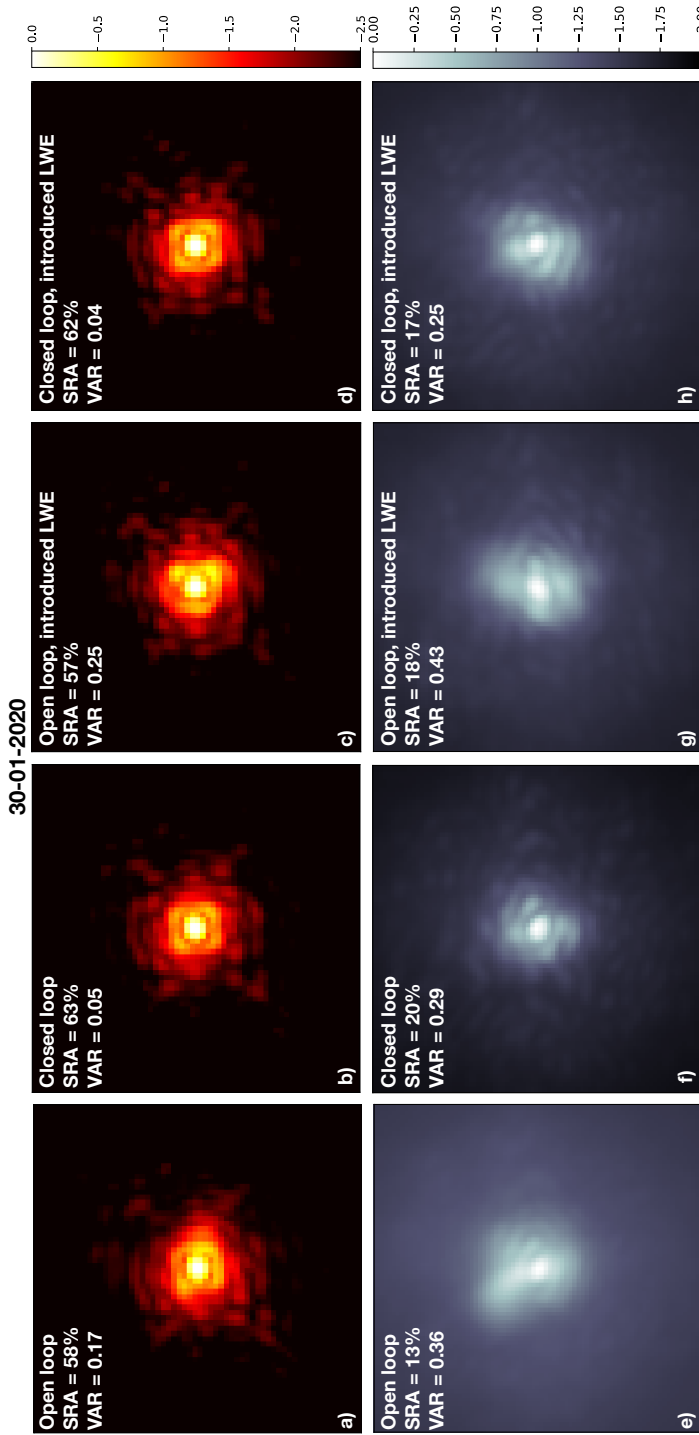


Figure 6.13: Averaged PSFs from four different on-sky experiments. The top row shows the PSFs in the NIR, while the bottom row shows the PSFs in the optical. All PSFs are normalized to their maximum value, and are plotted in logarithmic scale. (a) and (e): PSFs while the F&F loop was open and no (previous) F&F DM correction applied. The optical PSF is significantly distorted. (b) and (f): The PSFs while the F&F was closed. Both PSFs improved, a clear sign that aberrations common to both the optical and NIR path were (partially) corrected. (c) and (g): The PSFs while the F&F loop was opened and a LWE-like wavefront was applied by the DM, but no F&F correction was applied. (d) and (h): Closed loop PSFs with the LWE introduced on the DM, which was successfully corrected.

speed conditions. The jet stream wind speed was predicted to be between 11 and 22 m/s, significantly higher than the ground windspeed. The settings of the algorithm are shown in Table 6.2. The F&F loop was running at 12 FPS. During these tests, we simultaneously recorded data in the optical with the VAMPIRES instrument. The goal was, given the system layout Figure 6.3, to rule out NCPA as the corrected aberration, as a PSF improvement both in the optical and NIR would point towards corrected aberrations in the common optics. These aberrations could be (quasi-)static aberrations in the telescope and AO188, and/or the LWE. The VAMPIRES instrument was recording short exposure data at 200 FPS at 750 nm ($\Delta\lambda = 50$ nm), and its images were aligned and stacked to get an estimate of its long exposure PSF. The VAMPIRES images were also analyzed using the SRA (Equation 6.12) and VAR (Equation 6.13). The VAR and SRA were calculated at $\lambda = 750$ nm, and used a plate scale of 6.1 mas / pixel and a clockwise rotation of 68.9° .

The two first experiments were again with an open and closed F&F loop to quantify how F&F improves the nominal PSFs. These tests were done for 1000 iterations of the F&F loop and the results are shown in Figure 6.13. The NIR and optical PSFs are shown in Figure 6.13 a and e, respectively. The NIR PSF shows an asymmetric first Airy ring, and has an *SRA* of 58% and a *VAR* of 0.17. The optical PSF was heavily distorted, almost no diffraction structure was observed and was very elongated, corresponding to an *SRA* of 13% and a *VAR* of 0.36. When the F&F loop closed (Figure 6.13 b and f), the *SRA* of the NIR PSF rose to 63%, and the *VAR* dropped to 0.05. The optical PSF also significantly improved: the *SRA* became 20%, the *VAR* dropped to 0.29, the strong elongation disappeared and diffraction structure became more visible. Both PSFs have improved, which is a strong sign that aberrations in the common optics got corrected, either the LWE or statics in the telescope and AO188. During the next tests, we introduced a LWE-like wavefront on the DM ($0.8 \mu\text{m}$ P-V) after removing the previous F&F corrections, and recorded the open and closed-loop data. The main AO loop remained closed while recording this data, and the PYWFS reference was updated in such a way that the PYWFS would not correct the LWE-like wavefront (a similar offset that is used for the F&F loop). This PYWFS reference offset was calculated such that the DM command by the PYWFS was on average zero, meaning the PYWFS was only correcting wavefront errors from the free atmosphere. In the open-loop data (Figure 6.13 c and g), the NIR PSF was more distorted than before, its *SRA* was 56%, and the *VAR* was 0.25. The first Airy ring was broken up into three bright lobes, a typical signature of the LWE. The optical PSF was still heavily distorted, but its elongation rotated, and had a *SRA* of 18% and a *VAR* of 0.43. When the F&F loop closed (Figure 6.13 d and h), it restored the NIR PSF back to a *SRA* of 62% and a *VAR* of 0.04. The optical PSF also became more symmetric, as the *VAR* decreased to 0.25, the *SRA* stayed approximately the same at 17%.

6.4 Discussion and conclusion

The Fast and Furious sequential phase diversity algorithm has been deployed to the SCE-xAO instrument at the Subaru Telescope. This is in the context of measuring and cor-

recting non-common path aberrations (NCPA), the island effect (IE), and the low-wind effect (LWE). Both of these effects are considered to be limiting factors in the detection of exoplanets in high-contrast imaging observations. In this paper, we present the results of experiments both with the internal source and on-sky. We measured the quality of the PSF using two metrics: 1) the Strehl ratio approximation (*SRA*; Equation 6.12), and 2) the variance of the normalized first Airy ring (*VAR*; Equation 6.13), which measures the distortion of the first Airy ring. Using the internal source, we tested random LWE aberrations between 0.4 and 2.0 μm and show that F&F is able to correct these aberrations and bring the *SRA* above 90% and the *VAR* below 0.05. Although we only managed modest improvements in PSF quality, we demonstrated during multiple on-sky tests significant gains in PSF stability. During these tests, the F&F loop was running at 12 FPS. In the first tests, no improvement in *SRA* was observed, which we attribute to the challenging atmospheric circumstances during these tests (seeing was 1.3-1.4" at 500 nm). The *VAR*, however, did improve from 0.19 to 0.03, indicating greater PSF stability within the control region of F&F. During further on-sky tests, we did observe an *SRA* improvement of $\sim 5\%$ in the NIR, but it is unclear if it can be attributed to a correction of the LWE and/or static aberrations or to changing atmospheric conditions. The *VAR* improved from 0.17 to 0.05 during these tests. Simultaneously, we also recorded the PSF in the optical with the VAMPIRES instrument. The goal was to investigate if we were correcting aberrations common to both the optical and NIR path, or NCPA. When the F&F loop was closed, the optical PSF also significantly improved, meaning the *SRA* increased by $\sim 7\%$ and the *VAR* improved from 0.36 to 0.29. These results strongly imply that we were correcting aberrations common to both paths, which could be the LWE and/or statics upstream of SCEXAO. Although the windspeed in the dome of Subaru was low (between 0 and 0.2 m/s), we can not conclude that we actually corrected the LWE as there were no independent measurements available. These tests show that F&F is able to improve the wavefront, even during very challenging atmospheric conditions.

The characteristic timescale of the LWE was determined to be ~ 1 to 2 seconds (Savage et al. 2016; Milli et al. 2018) in context of VLT/SPHERE. It is unclear if these timescales also apply to Subaru/SCEXAO as it has a different spider geometry. If we assume that the timescales are similar, then the convergence times of F&F presented in Figure 6.8 are not sufficient. However, we foresee some improvements to the implementation of F&F at SCEXAO that would bring the convergence timescale in the regime that would allow effective LWE correction. These improvements are as follows:

1. In the work presented by Wilby et al. (2018), the algorithm converged in fewer iterations (~ 10 iterations) than the internal source results presented in this work (~ 100 iterations). In simulation work performed in context of SCEXAO, we also found similar convergence times (~ 10 iterations; Vievard et al. 2019). This means that there is an unaccounted for gain factor in the current implementation at SCEXAO. If this gain factor is resolved, the the convergence time would increase by a factor of ~ 10 .
2. As discussed in section 7.4, the current loop speed is limited by the implementation in Python, and not by the frame-rate of the NIR camera. This was also the case for

- the on-sky tests. We expect that, when the algorithm is implemented in C, 300-400 FPS would be relatively easily achievable.
3. As also discussed in section 7.4, the current bottleneck in the Python implementation is the image alignment. During the on-sky tests, we aligned and averaged 10 images for every iteration of F&F. If this is reduced to one image for every F&F iteration, the loop speed would also increase by a factor of a few.
 4. For both the internal source and the on-sky tests, the loop settings and F&F parameters (loop gain, leakage factor, and ϵ) were not optimized. For example, during the on-sky experiments ϵ (regularization parameter for odd phase modes, see Equation 6.5) was varied between 10^{-2} and 10^{-3} . This changes the algorithm sensitivity to odd modes, but it is unclear how much it affects the on-sky performance. Therefore, we expect tweaking these parameters to lead to a performance gain in terms of convergence speed.

These improvements will be tested in future work.

The experiments with the internal source were carried out with the narrowband filter at 1550 nm ($\Delta\lambda = 25$ nm). This bandwidth is relatively close to monochromatic, and thus close to the ideal performance of the algorithm as it assumes monochromatic light. However, the on-sky experiments were carried out using roughly half of the bandwidth of H-band, and still show satisfactory results. Therefore, quantifying the performance difference between narrowband and broadband filters would also be of interest.

The implementation of F&F presented in this paper assumes, and therefore only estimates, phase aberrations. Although phase aberrations are currently limiting observations, amplitude aberrations due to the atmosphere and instrumental errors will start to limit raw contrast at the $\sim 10^{-5}$ level (Guyon, 2018). Therefore, implementing the extended version of F&F presented by Korhikoski et al. (2014), which can measure both phase and amplitude will also be of interest. We only demonstrated low-order corrections by projecting the F&F phase estimate on the first 50 Zernike modes and the piston-tip-tilt modes, because we focused on correcting the IE. Higher order corrections with F&F are possible (Korhikoski et al., 2014), but will need to be tested on sky.

For F&F to be operated effectively and routinely during high-contrast imaging observations, the algorithm needs to be integrated in the system in such a way that it can run simultaneously with the coronagraphic mode. The algorithm would preferably have access to a focal plane as close as possible to the science focal plane, as it will also correct the NCPA as much as possible. The most important limitation is that F&F needs a pupil-plane electric field that is (close to) real and symmetric, and that there is no focal-plane mask. The coronagraph with which the algorithm can most easily be integrated is the shaped pupil coronagraph (Kasdin et al., 2007). This coronagraph suppresses starlight by modifying the pupil-plane electric field with symmetric amplitude masks. Therefore, F&F is expected to be able to operate on the PSF generated by a shaped pupil coronagraph. Another coronagraph in which F&F can be integrated is the vector-Apodizing

Phase Plate (vAPP; Snik et al. 2012; Otten et al. 2017). The vAPP has been deployed to multiple instruments (MagAO; Otten et al. 2017, MagAO-X; Miller et al. 2019, SCEXAO; Doelman et al. 2017, LBT; Doelman et al. 2017, and LEXI; Haffert et al. 2018). The vAPP suppresses starlight by manipulating the pupil-plane phase and creates multiple coronagraphic PSFs. However, this process is never 100% efficient, and thus there is always a non-coronagraphic PSF at a lower intensity. The morphology of the non-coronagraphic PSF would only depend on the shape of the pupil, and would therefore be suitable for F&F. Some of these vAPPs already have other implementations of wavefront sensing (Wilby et al. 2017; Bos et al. 2019; Miller et al. 2019), but F&F would be a useful addition. For coronagraphs that have focal-plane masks to block starlight, there are a few ways to implement F&F (assuming that for these coronagraphs the pupil-plane electric field stays symmetric and real). One of these, extensively discussed in Wilby et al. (2018) in the context of the SPHERE system, is to extract light for the beam just before it hits the focal-plane mask using, for example, a beam splitter. A way to circumvent the focal-plane mask would be to generate PSF copies of the star that are not affected by the focal-plane mask, using diffractive elements in the pupil (Sivaramakrishnan & Oppenheimer 2006; Marois et al. 2006b; Jovanovic et al. 2015a). These PSF copies can then serve as input PSFs for F&F.

In this paper, we show that F&F is able to increase the PSF quality, both on-sky and with the internal source in SCEXAO. Using the internal source, we show that F&F can measure and correct a wide range of LW- and IE-like aberrations. With future algorithm upgrades and further on-sky tests, we hope to conclusively show on-sky correction of the LW and IE. For future giant segmented mirror telescopes, the IE is expected to become even more significant as the support structures become wider and more numerous, and the segments have to be co-phased. Going forward, it is suitable for incorporation into observing modes, enabling PSFs of higher quality and stability during science observations.

Bibliography

- Baudoz, P., Dorn, R. J., Lizon, J.-L., et al. 2010, in *Ground-based and Airborne Instrumentation for Astronomy III*, Vol. 7735, International Society for Optics and Photonics, 77355B
- Beuzit, J.-L., Vigan, A., Mouillet, D., et al. 2019, arXiv preprint arXiv:1902.04080
- Bos, S. P., Doelman, D. S., Lozi, J., et al. 2019, *Astronomy & Astrophysics*, 632, A48
- Bottom, M., Wallace, J. K., Bartos, R. D., Shelton, J. C., & Serabyn, E. 2017, *Monthly Notices of the Royal Astronomical Society*, 464, 2937
- Close, L. M., Males, J. R., Durney, O., et al. 2018, arXiv preprint arXiv:1807.04311
- Doelman, D. S., Snik, F., Warriner, N. Z., & Escuti, M. J. 2017, in *Techniques and Instrumentation for Detection of Exoplanets VIII*, Vol. 10400, International Society for Optics and Photonics, 104000U
- Feautrier, P., Gach, J.-L., Greffe, T., et al. 2017, in *Image Sensing Technologies: Materials, Devices, Systems, and Applications IV*, Vol. 10209, International Society for Optics and Photonics, 102090G
- Galicher, R., Baudoz, P., Delorme, J.-R., et al. 2019, *Astronomy & Astrophysics*, 631, A143
- Gonsalves, R. A. 1982, *Optical Engineering*, 21, 215829
- Gonsalves, R. A. 2002, in *European Southern Observatory Conference and Workshop Proceedings*, Vol. 58, 121
- Groff, T. D., Kasdin, N. J., Limbach, M. A., et al. 2014, in *Ground-based and Airborne Instrumentation for Astronomy V*, Vol. 9147, International Society for Optics and Photonics, 91471W
- Guyon, O. 2018, *Annual Review of Astronomy and Astrophysics*, 56, 315
- Guyon, O., Sevin, A., Ltaief, H., et al. 2018, in *Adaptive Optics Systems VI*, Vol. 10703, International Society for Optics and Photonics, 107031E
- Guyon, O., Lozi, J., Vievard, S., et al. 2019, in *American Astronomical Society Meeting Abstracts# 233*, Vol. 233
- Haffert, S., Wilby, M., Keller, C., et al. 2018, in *Adaptive Optics Systems VI*, Vol. 10703, International Society for Optics and Photonics, 1070323
- Hardy, J. W. 1998, *Adaptive optics for astronomical telescopes*, Vol. 16 (Oxford University Press on Demand)
- Hoeijmakers, H., Schwarz, H., Snellen, I., et al. 2018, *Astronomy & Astrophysics*, 617, A144
- Hutterer, V., Shatokhina, I., Obereder, A., & Ramlau, R. 2018, *Journal of Astronomical Telescopes, Instruments, and Systems*, 4, 049005
- Jones, E., Oliphant, T., & Peterson, P. 2014
- Jovanovic, N., Guyon, O., Martinache, F., et al. 2015a, *The Astrophysical Journal Letters*, 813, L24
- Jovanovic, N., Martinache, F., Guyon, O., et al. 2015b, *Publications of the Astronomical Society of the Pacific*, 127, 890
- Kasdin, N. J., Vanderbei, R. J., & Belikov, R. 2007, *Comptes Rendus Physique*, 8, 312
- Keller, C. U., Korkiakoski, V., Doelman, N., et al. 2012, in *Adaptive Optics Systems III*, Vol. 8447, International Society for Optics and Photonics, 844721
- Keppler, M., Benisty, M., Müller, A., et al. 2018, *Astronomy & Astrophysics*, 617, A44
- Korkiakoski, V., Keller, C. U., Doelman, N., et al. 2012, in *Adaptive Optics Systems III*, Vol. 8447, International Society for Optics and Photonics, 84475Z
- Korkiakoski, V., Keller, C. U., Doelman, N., et al. 2014, *Applied optics*, 53, 4565
- Langlois, M., Dohlen, K., Vigan, A., et al. 2014, in *Ground-based and Airborne Instrumentation for Astronomy V*, Vol. 9147, International Society for Optics and Photonics, 91471R
- Lozi, J., Guyon, O., & et al. 2018, in *Adaptive Optics Systems VI*, Vol. 10703, International Society for Optics and Photonics

- Lozi, J., Jovanovic, N., Guyon, O., et al. 2019a, *Publications of the Astronomical Society of the Pacific*, 131, 044503
- Lozi, J., Guyon, O., Jovanovic, N., et al. 2019b
- Macintosh, B., Graham, J. R., Ingraham, P., et al. 2014, *Proceedings of the National Academy of Sciences*, 111, 12661
- Macintosh, B., Graham, J., Barman, T., et al. 2015, *Science*, 350, 64
- Males, J. R., Close, L. M., Miller, K., et al. 2018, in *Adaptive Optics Systems VI*, Vol. 10703, International Society for Optics and Photonics, 1070309
- Marois, C., Lafreniere, D., Doyon, R., Macintosh, B., & Nadeau, D. 2006a, *The Astrophysical Journal*, 641, 556
- Marois, C., Lafreniere, D., Macintosh, B., & Doyon, R. 2006b, *The Astrophysical Journal*, 647, 612
- Martinache, F. 2013, *Publications of the Astronomical Society of the Pacific*, 125, 422
- Martinache, F., Jovanovic, N., & Guyon, O. 2016, *Astronomy & Astrophysics*, 593, A33
- Martinache, F., Guyon, O., Jovanovic, N., et al. 2014, *Publications of the Astronomical Society of the Pacific*, 126, 565
- Martinez, P., Kasper, M., Costille, A., et al. 2013, *Astronomy & Astrophysics*, 554, A41
- Martinez, P., Loose, C., Carpentier, E. A., & Kasper, M. 2012, *Astronomy & Astrophysics*, 541, A136
- Miller, K., Males, J. R., Guyon, O., et al. 2019, *Journal of Astronomical Telescopes, Instruments, and Systems*, 5, 049004
- Milli, J., Kasper, M., Bourget, P., et al. 2018, in *Adaptive Optics Systems VI*, Vol. 10703, International Society for Optics and Photonics, 107032A
- Minowa, Y., Hayano, Y., Oya, S., et al. 2010, in *Adaptive Optics Systems II*, Vol. 7736, International Society for Optics and Photonics, 77363N
- N'Diaye, M., Martinache, F., Jovanovic, N., et al. 2018, *Astronomy & Astrophysics*, 610, A18
- Norris, B., Schworer, G., Tuthill, P., et al. 2015, *Monthly Notices of the Royal Astronomical Society*, 447, 2894
- Otten, G. P., Snik, F., Kenworthy, M. A., et al. 2017, *The Astrophysical Journal*, 834, 175
- Paxman, R. G., Schulz, T. J., & Fienup, J. R. 1992, *JOSA A*, 9, 1072
- Peters-Limbach, M. A., Groff, T. D., Kasdin, N. J., et al. 2013, in *Techniques and Instrumentation for Detection of Exoplanets VI*, Vol. 8864, International Society for Optics and Photonics, 88641N
- Por, E. H., Haffert, S. Y., Radhakrishnan, V. M., et al. 2018, in *Proc. SPIE*, Vol. 10703, Adaptive Optics Systems VI
- Roberts, L. C. J., Perrin, M. D., Marchis, F., et al. 2004, in *Advancements in Adaptive Optics*, Vol. 5490, International Society for Optics and Photonics, 504–515
- Ruane, G., Ngo, H., Mawet, D., et al. 2019, *The Astronomical Journal*, 157, 118
- Sauvage, J.-F., Fusco, T., Guesalaga, A., et al. 2015, in *Adaptive Optics for Extremely Large Telescopes 4—Conference Proceedings*, Vol. 1
- Sauvage, J.-F., Fusco, T., Lamb, M., et al. 2016, in *Adaptive Optics Systems V*, Vol. 9909, International Society for Optics and Photonics, 990916
- Singh, G., Lozi, J., Guyon, O., et al. 2015, *Publications of the Astronomical Society of the Pacific*, 127, 857
- Sivaramakrishnan, A., & Oppenheimer, B. R. 2006, *The Astrophysical Journal*, 647, 620
- Snik, F., Otten, G., Kenworthy, M., et al. 2012, in *Modern Technologies in Space-and Ground-based Telescopes and Instrumentation II*, Vol. 8450, International Society for Optics and Photonics, 84500M
- Sparks, W. B., & Ford, H. C. 2002, *The Astrophysical Journal*, 578, 543

- Stam, D., Hovenier, J., & Waters, L. 2004, *Astronomy & Astrophysics*, 428, 663
- van Holstein, R. G., Snik, F., Girard, J. H., et al. 2017, in *Techniques and Instrumentation for Detection of Exoplanets VIII*, Vol. 10400, International Society for Optics and Photonics, 1040015
- Vievard, S., Bos, S., Cassaing, F., et al. 2019, arXiv preprint arXiv:1912.10179
- Vigan, A., Gry, C., Salter, G., et al. 2015, *Monthly Notices of the Royal Astronomical Society*, 454, 129
- Vigan, A., Postnikova, M., Caillat, A., et al. 2016, in *Adaptive Optics Systems V*, Vol. 9909, International Society for Optics and Photonics, 99093F
- Vigan, A., N'Diaye, M., Dohlen, K., et al. 2019, *Astronomy & Astrophysics*, 629, A11
- Wang, J. J., Graham, J. R., Dawson, R., et al. 2018, *The Astronomical Journal*, 156, 192
- Wilby, M., Keller, C., Sauvage, J.-F., et al. 2016, in *Adaptive Optics Systems V*, Vol. 9909, International Society for Optics and Photonics, 99096C
- Wilby, M. J., Keller, C. U., Sauvage, J.-F., et al. 2018, *Astronomy & Astrophysics*, 615, A34
- Wilby, M. J., Keller, C. U., Snik, F., Korkiakoski, V., & Pietrow, A. G. 2017, *Astronomy & Astrophysics*, 597, A112

7 | The Vector Speckle Grid

Instantaneous incoherent speckle grid for high-precision
astrometry and photometry in high-contrast imaging

Adapted from

S.P. Bos

Astronomy & Astrophysics, 638, A118 (2020)

Photometric and astrometric monitoring of directly imaged exoplanets will deliver unique insights into their rotational periods, the distribution of cloud structures, weather, and orbital parameters. As the host star is occulted by the coronagraph, a speckle grid (SG) is introduced to serve as astrometric and photometric reference. Speckle grids are implemented as diffractive pupil-plane optics that generate artificial speckles at known location and brightness. Their performance is limited by the underlying speckle halo caused by evolving uncorrected wavefront errors. The speckle halo will interfere with the coherent SGs, affecting their photometric and astrometric precision. Our aim is to show that by imposing opposite amplitude or phase modulation on the opposite polarization states, a SG can be instantaneously incoherent with the underlying halo, greatly increasing the precision. We refer to these as vector speckle grids (VSGs). We derive analytically the mechanism by which the incoherency arises and explore the performance gain in idealised simulations under various atmospheric conditions. We show that the VSG is completely incoherent for unpolarized light and that the fundamental limiting factor is the cross-talk between the speckles in the grid. In simulation, we find that for short-exposure images the VSG reaches a $\sim 0.3\text{--}0.8\%$ photometric error and $\sim 3 - 10 \cdot 10^{-3} \lambda/D$ astrometric error, which is a performance increase of a factor ~ 20 and ~ 5 , respectively. Furthermore, we outline how VSGs could be implemented using liquid-crystal technology to impose the geometric phase on the circular polarization states. The VSG is a promising new method for generating a photometric and astrometric reference SG that has a greatly increased astrometric and photometric precision.

7.1 Introduction

Temporally monitoring directly imaged exoplanets will deliver unique insight into their rotational periods, and the distribution and dynamics of cloud structures (Kostov & Apai, 2012). For example, HST observations showed that 2M1207b has photometric variations at the 0.78-1.36% level, which allowed for the first measurement of the rotation period of a directly imaged exoplanet (Zhou et al., 2016). Furthermore, high precision astrometric monitoring of exoplanets will help determine their orbital dynamics. This was demonstrated by Wang et al. (2016), where the authors showed that β Pic b does not transit its host star, but that its Hill sphere does.

Ground-based high-contrast imaging (HCI) systems, such as SPHERE (Beuzit et al., 2019), GPI (Macintosh et al., 2014), and SCExAO (Jovanovic et al., 2015b), deploy extreme adaptive optics (AO) systems to measure and correct for the turbulence in the Earth's atmosphere. The direct photometric and astrometric reference, that is the host star, is occulted by a coronagraph to reveal the faint companions. This makes it hard to disentangle exoplanet brightness variations, due to their intrinsic rotation, from seeing and transmission changes in the Earth's atmosphere. To circumvent this problem, Marois et al. (2006) and Sivaramakrishnan & Oppenheimer (2006) simultaneously came up with diffractive methods to generate artificial speckle grids (SGs) that could serve as photometric and astrometric references. These are implemented as static masks that introduce phase or amplitude modulations in the pupil plane, and are installed before the focal-plane mask of the coronagraph. The artificial speckles are designed to fall on specific off-axis focal-plane positions and will therefore not be occulted by the coronagraph. For example, GPI implemented a square grid that acts as an amplitude grating and reports a $\sim 7\%$ photometric stability (Wang et al., 2014), and SPHERE uses a static deformable mirror (DM) modulation with a $\sim 4\%$ photometric stability (Langlois et al. 2013; Apai et al. 2016). The limiting factor of these SGs is their coherency with the time-varying speckle background, which results in interference that dynamically distorts the shape and brightness of the SGs, which in turn ultimately limits their photometric and astrometric precision. The background speckles are for example generated by uncorrected wavefront errors due to fitting, bandwidth, or calibration errors in the AO system (Sivaramakrishnan et al. 2002; Macintosh et al. (2005)), or evolving non-common path errors (Soummer et al., 2007). These background speckles have been found to decorrelate, that is, they become incoherent over timescales from seconds to minutes and hours (Fitzgerald & Graham 2006; Hinkley et al. 2007; Martinez et al. (2012); Martinez et al. (2013); Milli et al. 2016), and therefore affect the stability of the SGs during the entire observation.

Jovanovic et al. (2015a) presented a method that circumvents this problem. Their solution is a high-speed, temporal modulation that switches ($\lesssim 1$ ms) the phase of the SG between zero and π (e.g. by translating the mask). Due to the modulation, the interference averages out and the SG effectively becomes incoherent. This has been implemented at SCExAO using DM modulation and is reported to increase the stability by a factor of between approximately two and three (Jovanovic et al., 2015a). However, a dynamic, high-speed component cannot always be integrated and is not always desired in a HCI system. For an implementation by DM modulation, the SG can only be placed within the control radius of the AO, and the incoherency relies on the quality of the DM calibration.

Here, we propose the vector speckle grid (VSG). This is a SG solution that instantaneously generates incoherency by imposing opposite amplitude or phase modulation on the opposite polarization states in the pupil plane. The opposite polarization states will both generate SGs at the same focal-plane positions, but with opposite phase. Therefore, the two polarization states will interfere differently with the background speckle halo, but such that in total intensity the interference terms cancel. The VSG can be implemented as one static, liquid crystal optic that can be easily calibrated before observations. Furthermore, the speckles can be positioned anywhere in the focal plane and thus outside the scientifically interesting AO control region.

In section 7.2 we derive the theory behind the VSG. In section 7.3 we perform idealised simulations to quantify the performance increase and investigate the effect of partially polarized light. In section 7.4 we discuss how the VSGs could be implemented. Lastly, in section 7.5, we discuss the results and present our conclusions.

7.2 Theory

7.2.1 Vector phase speckle grid

Here we derive how the incoherency of VSGs arises, and focus on the vector phase speckle grid (VPSG) first. The derivation of the vector amplitude speckle grid (VASG) is presented in subsection 7.2.2. All variables used in this section are also defined in Table 7.1. We assume that the stellar point spread function (PSF) is only aberrated by phase aberrations for simplicity. However, VSGs are still incoherent when there are also amplitude aberrations present. Here, we assume a one-dimensional pupil-plane electric field $E_p(x)$:

$$E_p(x) = A(x)e^{i\theta(x)}, \quad (7.1)$$

with $A(x)$ being the amplitude of the electric field, which is described as the rectangular function, $\theta(x)$ the phase aberration distorting the PSF, and $i = \sqrt{-1}$ the unit imaginary number. The coordinate x denotes the position in the pupil and is omitted from here on. We describe starlight with a degree of polarization p , as two orthogonal polarization states (either linear or circular) using Jones calculus:

$$E_1 = \frac{1}{\sqrt{2}} \begin{pmatrix} \sqrt{1+p} \\ 0 \end{pmatrix}, \quad E_2 = \frac{1}{\sqrt{2}} \begin{pmatrix} 0 \\ \sqrt{1-p} \end{pmatrix}. \quad (7.2)$$

The VPSG is implemented by a cosine wave (with spatial frequency b) on the pupil phase, with opposite amplitude a for the two opposite polarization states. As we see below in the derivation, b determines the focal-plane position of the artificial speckles and a their relative brightness to the PSF core. The opposite amplitude eventually leads to the incoherency of the VSG.

$$E_p = \frac{Ae^{i\theta}}{\sqrt{2}} \begin{pmatrix} \sqrt{1+p} \cdot e^{ai \cos(2\pi bx)} \\ \sqrt{1-p} \cdot e^{-ai \cos(2\pi bx)} \end{pmatrix}. \quad (7.3)$$

Table 7.1: Variables presented in section 7.2.

Variable	Description
α	Real part of the aberration focal-plane electric field (Equation 7.8).
β	Imaginary part of the aberration focal-plane electric field (Equation 7.8).
θ	Pupil-plane electric field phase.
Γ	Real part of the speckle grid's focal-plane electric field (Equation 7.13).
Δ	Real part of the central PSF's focal-plane electric field (Equation 7.12).
Ω	Imaginary part of the speckle grid's focal-plane electric field (Equation 7.15).
Λ	Imaginary part of the central PSF's focal-plane electric field (Equation 7.14).
a	Amplitude of the speckle grid generating pupil-plane modulation (Equation 7.3).
b	Spatial frequency of the speckle grid generating pupil-plane modulation (Equation 7.3).
f_x	Focal-plane coordinate.
p	Degree of polarization.
x	Pupil-plane coordinate.
A	Pupil-plane electric field amplitude.
E_f	Focal-plane electric field.
E_p	Pupil-plane electric field.
$\mathcal{F}\{\cdot\}$	Fourier transform operator.
I_f	Focal-plane intensity of the PSF.
I_s	Relative intensity of the speckle grid.

We assume the Fraunhofer approximation and calculate the focal-plane electric field E_f by taking the Fourier transform ($\mathcal{F}\{\cdot\}$) of E_p :

$$E_f = \mathcal{F}\{E_p\}(f_x) \quad (7.4)$$

$$= \frac{\mathcal{F}\{A\} * \mathcal{F}\{e^{i\theta}\}}{\sqrt{2}} * \left(\frac{\sqrt{1+p} \cdot \mathcal{F}\{e^{ai \cos(2\pi bx)}\}}{\sqrt{1-p} \cdot \mathcal{F}\{e^{-ai \cos(2\pi bx)}\}} \right), \quad (7.5)$$

where $*$ is the convolution operator, and f_x the coordinate in the focal plane, which is omitted as well. As we chose $A(x)$ to be the rectangular function in Equation 7.1, its Fourier transform is:

$$\mathcal{F}\{A\}(f_x) = \text{sinc}(f_x)/f_x \quad (7.6)$$

$$= \text{sinc}(f_x). \quad (7.7)$$

We do not explicitly calculate $\mathcal{F}\{e^{i\theta}\}$ and assume that:

$$\mathcal{F}\{e^{i\theta}\} = \alpha + i\beta. \quad (7.8)$$

Writing $e^{\pm ai \cos(2\pi bx)}$ as a series expansion, we find that:

$$E_f = \frac{\text{sinc}(f_x) * (\alpha + i\beta)}{\sqrt{2}} * \left(\frac{\sqrt{1+p}[1 + \sum_{n=1}^{\infty} \frac{(i)^n a^n}{n!} \mathcal{F}\{\cos^n(2\pi bx)\}]}{\sqrt{1-p}[1 + \sum_{n=1}^{\infty} \frac{(i)^n (-a)^n}{n!} \mathcal{F}\{\cos^n(2\pi bx)\}]} \right). \quad (7.9)$$

Equation 7.9 shows that the VPSG creates an infinite number of speckles with decreasing brightness. For now, we assume that $a \ll 1$ radian and expand Equation 7.9 to first order ($n = 1$). Working out the terms in Equation 7.9, we find:

$$E_f = \frac{\alpha + i\beta}{\sqrt{2}} * \left(\frac{\sqrt{1+p}[\text{sinc}(f_x) + \frac{ai}{2}(\text{sinc}(f_x - b) + \text{sinc}(f_x + b))]}{\sqrt{1-p}[\text{sinc}(f_x) - \frac{ai}{2}(\text{sinc}(f_x - b) + \text{sinc}(f_x + b))]} \right). \quad (7.10)$$

Rearranging in the real and imaginary terms, and computing the focal-plane intensity ($I_f = E_f \cdot E_f^*$) results in:

$$I_f = \underbrace{\Delta^2 + \Lambda^2}_{\text{PSF}} + \underbrace{\frac{a^2}{4}(\Gamma^2 + \Omega^2)}_{\text{speckle grid}} + \underbrace{ap(\Delta\Gamma + \Lambda\Omega)}_{\text{cross-talk of PSF with speckle grid}}. \quad (7.11)$$

Greek symbols are used here to simplify the notation and denote the following terms:

$$\Delta = \text{sinc}(f_x) * \alpha \quad (7.12)$$

$$\Gamma = [\text{sinc}(f_x - b) + \text{sinc}(f_x + b)] * \beta \quad (7.13)$$

$$\Lambda = \text{sinc}(f_x) * \beta \quad (7.14)$$

$$\Omega = [\text{sinc}(f_x - b) + \text{sinc}(f_x + b)] * \alpha. \quad (7.15)$$

Equation 7.11 shows that the focal-plane intensity can be divided into three terms: the stellar PSF, the speckle grid, and the cross-talk between the speckle grid and the PSF. We

find that the relative intensity of the speckle grid is given by $I_s = a^2/4$. The performance of regular SGs is limited by the cross-talk term. For the VPSG, when $p = 0$ (i.e. with unpolarized light), the cross-talk term is eliminated and Equation 7.11 reduces to:

$$I_f = \Delta^2 + \Lambda^2 + \frac{a^2}{4}(\Gamma^2 + \Omega^2), \quad (7.16)$$

effectively making the VPSG incoherent with the PSF.

The remaining cross-talk that degrades the photometric and astrometric performance is the interference between the speckles themselves:

$$\begin{aligned} \Gamma^2 + \Omega^2 = & \underbrace{(\text{sinc}(f_x - b) * \alpha)^2 + (\text{sinc}(f_x - b) * \beta)^2}_{\text{speckle 1}} + \\ & \underbrace{(\text{sinc}(f_x + b) * \alpha)^2 + (\text{sinc}(f_x + b) * \beta)^2}_{\text{speckle 2}} + \\ & \underbrace{2(\text{sinc}(f_x - b) * \alpha \cdot \text{sinc}(f_x + b) * \alpha + \text{sinc}(f_x - b) * \beta \cdot \text{sinc}(f_x + b) * \beta)}_{\text{cross-talk between speckles}}. \end{aligned} \quad (7.17)$$

We have not found a method to mitigate this effect, and consider this cross-talk to be the fundamental limiting factor of the VSG. Its effect can be reduced by minimizing the number of speckles in the VSG and increasing their separation. This can be understood as follows: the distortion of an artificial speckle is determined by the relative strength of the combined electric field of the other artificial speckles (the distorting electric field) at its location, relative to its own electric field strength. If the distorting electric field becomes stronger, the cross-talk terms in Equation 7.17 become more important and the artificial speckle is more distorted. If there are fewer artificial speckles in the VSG, the distorting electric field becomes weaker. Furthermore, as the electric field an artificial speckles scales with f_x^{-1} (Equation 7.6), placing the artificial speckles further apart also reduces the distorting electric field.

We expanded Equation 7.9 to first order and ignored higher order terms; we discuss their effects here. The higher order terms can be divided into two groups: the odd orders ($n = \text{odd}$) and the even orders ($n = \text{even}$). The amplitude of the higher order terms is given by $(a)^n$. For the odd orders, n is odd, and therefore, when a flips its sign ($a \rightarrow -a$), the higher orders also have a sign flip. Which means that all the odd orders become incoherent as the cross-talk term between the PSF and the speckle grid cancels when $p = 0$. For the even orders ($n = \text{even}$), a sign flip of a does not result in a sign flip of $(a)^n$. This means that none of the even orders are incoherent as the cross-talk term does not cancel. As the even orders fall at other spatial locations and are much fainter than the first order speckles, the impact of the coherent even orders is minimal.

7.2.2 Vector amplitude speckle grid

Here we derive how the incoherency of the VASG arises. This derivation is very similar to what is presented in subsection 7.2.1 and starts with the same assumptions. The VASG

is implemented by a sine wave (with spatial frequency b) on the pupil amplitude, with opposite amplitude a for the two opposite polarization states:

$$E_p = \frac{Ae^{i\theta}}{\sqrt{2}} \left(\frac{\sqrt{1+p}[1+a\sin(2\pi bx)]}{\sqrt{1-p}[1-a\sin(2\pi bx)]} \right). \quad (7.18)$$

We calculate the focal-plane electric field E_f by taking the Fourier transform ($\mathcal{F}\{\cdot\}$) of E_p :

$$E_f = \mathcal{F}\{E_p\} \quad (7.19)$$

$$= \frac{\mathcal{F}\{A\} * \mathcal{F}\{e^{i\theta}\}}{\sqrt{2}} * \left(\frac{\sqrt{1+p}[1+a\mathcal{F}\{\sin(2\pi bx)\}]}{\sqrt{1-p}[1-a\mathcal{F}\{\sin(2\pi bx)\}]} \right). \quad (7.20)$$

Using Equation 7.8 and working out the Fourier transforms of the terms in Equation 7.20, we find:

$$E_f = \frac{\alpha + i\beta}{\sqrt{2}} * \left(\frac{\sqrt{1+p}[\text{sinc}(f_x) + \frac{ai}{2}(\text{sinc}(f_x - b) - \text{sinc}(f_x + b))]}{\sqrt{1-p}[\text{sinc}(f_x) - \frac{ai}{2}(\text{sinc}(f_x - b) - \text{sinc}(f_x + b))]} \right). \quad (7.21)$$

Rearranging this in its real and imaginary terms, and computing the focal-plane intensity ($I_f = E_f \cdot E_f^*$) results in:

$$I_f = \underbrace{\Delta^2 + \Lambda^2}_{\text{PSF}} + \underbrace{\frac{a^2}{4}(\Gamma^2 + \Omega^2)}_{\text{speckle grid}} + \underbrace{ap(\Delta\Gamma + \Lambda\Omega)}_{\text{cross-talk of PSF with speckle grid}}. \quad (7.22)$$

As in subsection 7.2.1, the Greek symbols denote the following terms:

$$\Delta = \text{sinc}(f_x) * \alpha \quad (7.23)$$

$$\Gamma = [\text{sinc}(f_x - b) - \text{sinc}(f_x + b)] * \beta \quad (7.24)$$

$$\Lambda = \text{sinc}(f_x) * \beta \quad (7.25)$$

$$\Omega = [\text{sinc}(f_x - b) - \text{sinc}(f_x + b)] * \alpha \quad (7.26)$$

In Equation 7.22 we find again that the relative intensity of the speckle grid is given by $I_s = a^2/4$, and that the VASG becomes incoherent when $p = 0$. As with the VPSG, the remaining cross-talk that degrades the photometric and astrometric performance is the interference between the speckles themselves. We also note that this implementation with a sine wave modulation of the VASG does not generate any higher order speckles. A VASG implementation comparable to the GPI amplitude grating (Wang et al., 2014) will introduce higher order speckles in a similar manner to the VPSG.

7.3 Simulations

7.3.1 Performance quantification

To validate the VSG concept and quantify the performance increase that VSGs could bring compared to regular SGs, we performed idealised numerical simulations. These

Table 7.2: Parameters in the simulations presented in section 7.3.

Parameter	Value
Outer scale	30 m at 500 nm
Seeing	[0.6", 1", 1.4"] at 500 nm
Wind speed	[4.4, 8.8, 13.2] m/s
Wavefront sensor	Noiseless
Frame rate	2 kHz
Deformable mirror	40 × 40 actuators
Lag of AO	3 frames
Loop duration	1 s
Telescope diameter	8 m
Wavelength	1220 nm
Bandwidth	Monochromatic
Coronagraph	Vector Vortex Coronagraph
Lyot stop diameter	0.95 · Telescope diameter
Speckle intensity	$5 \cdot 10^{-3}$
Speckle positions	$[\pm 25 \lambda/D, \pm 25 \lambda/D]$

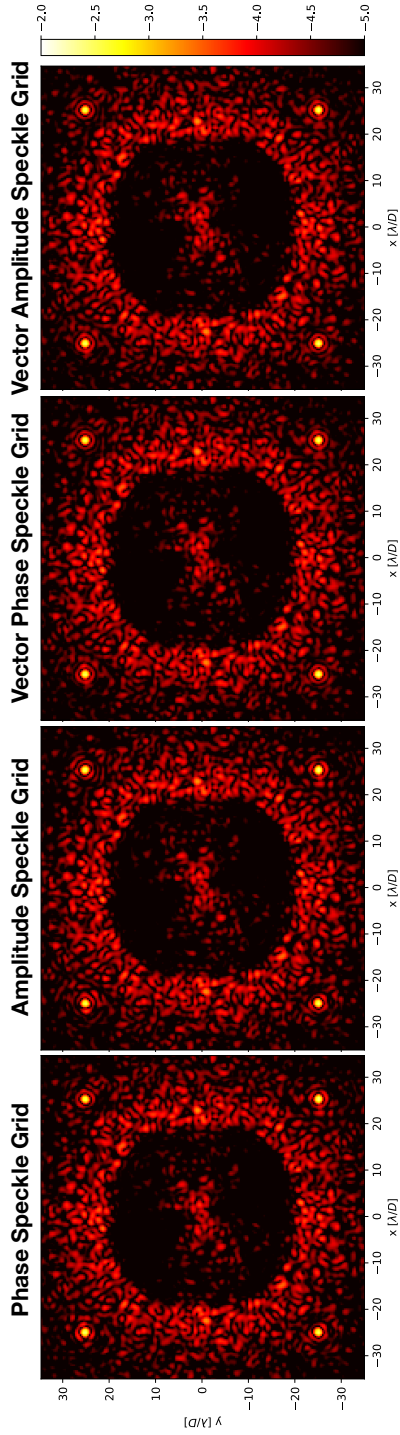
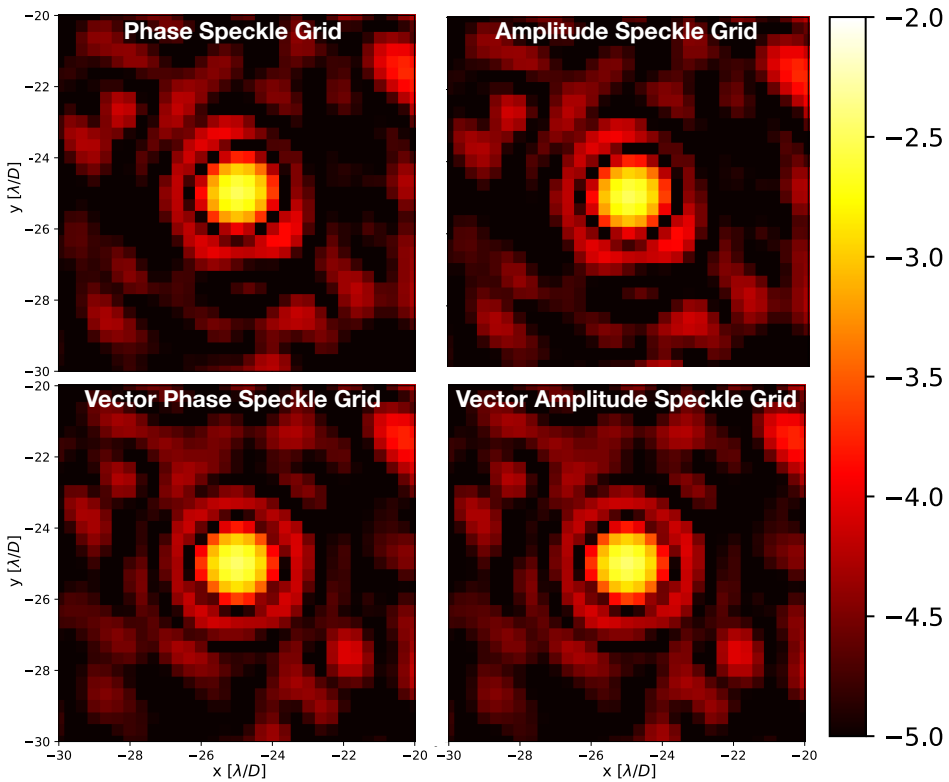


Figure 7.1: Short-exposure images at a random iteration in the simulation with the medium atmospheric conditions (seeing of 1" and wind speed of 8.8 m/s). The dark hole in the center of the images is generated by the AO system and the Vector Vortex Coronagraph. The reference speckles are located in the corners of the image at $[\pm 25 \lambda/D, \pm 25 \lambda/D]$. We note that the reference speckles generated by the VPSG and VASG are significantly less distorted and more similar to each other compared to the Phase and Amplitude Speckle Grids. The images show intensity normalized to the maximum of the star in logarithmic scale, and share the same color bar (shown at the right).



7

Figure 7.2: Zoom onto the reference speckles in the lower left corner of the panels in Figure 7.1. The VSGs are clearly less distorted compared to the regular SGs. The images show intensity normalized to the maximum of the star in logarithmic scale, and share the same color bar (shown at the right).

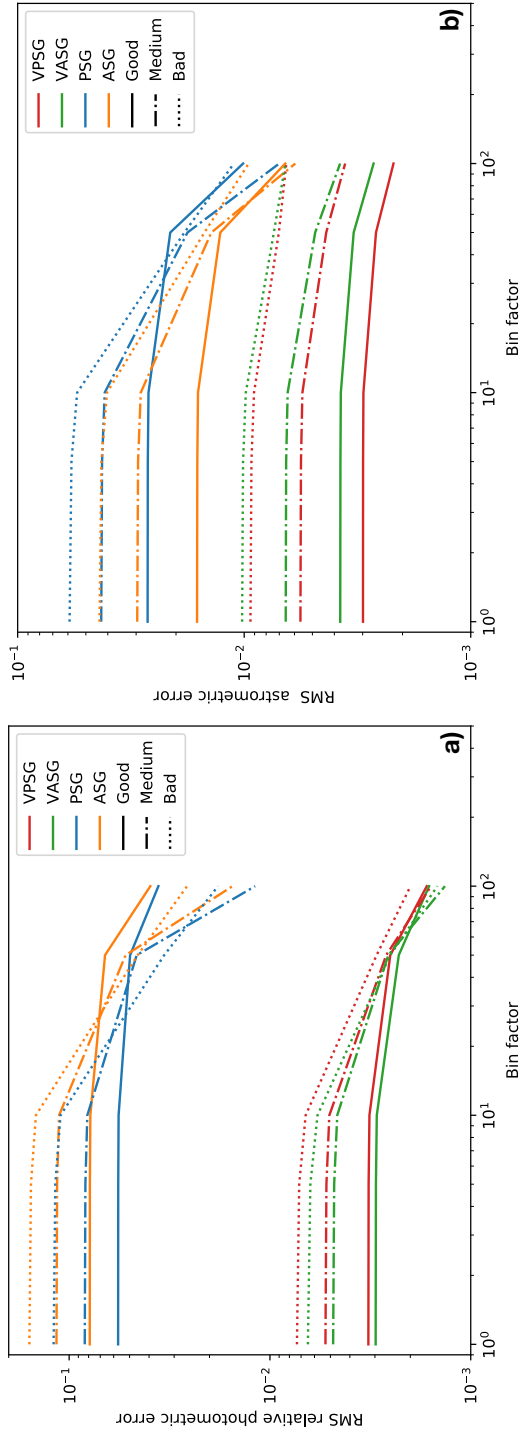


Figure 7.3: Photometric and astrometric performance of the SGs as a function of the number of frames averaged, and for various atmospheric conditions (Table 7.2). (a) The rms relative photometric error. (b) The rms astrometric error.

are performed in Python using the HCIPy package¹ (Por et al., 2018), which supports polarization propagation with Jones calculus necessary for simulating VSGs. It is notoriously hard to realistically simulate high-contrast imaging observations as not all speckle noise sources are well understood (Guyon et al., 2019), thus making it hard to predict the on-sky performance of the VSG. Therefore, we decided to limit the scope of the simulations. We simulated a general HCI instrument with coronagraph and AO system at an 8 m class telescope with a clear aperture under various atmospheric conditions, and did not include any other noise sources (e.g. detector and photon noise, evolving non-common path aberrations). An overview of the simulation parameters is shown in Table 7.2. We only considered monochromatic images as we leave broadband effects for future work. The images are recorded at a wavelength of 1220 nm, which is at the centre of J-band, a scientifically interesting band for photometric variations of exoplanets (Kostov & Apai, 2012). We considered three cases of atmospheric conditions, under which the current generation of HCI instruments regularly operate:

1. Good conditions with a seeing of 0.6'' and wind speed of 4.4 m/s.
2. Medium conditions with a seeing of 1'' and wind speed of 8.8 m/s.
3. Poor conditions with a seeing of 1.4'' and wind speed of 13.2 m/s.

These atmospheric conditions were simulated as an evolving turbulent wavefront assuming the "Frozen Flow" approximation with a von-karman power spectrum. The AO system that measures and corrects the atmospheric conditions consists of a noiseless wavefront sensor, and a deformable mirror with 40×40 actuators in a rectangular grid. The AO system runs at 2 kHz and has a three-frame lag between measurement and correction. The root mean square (rms) residual wavefront error after the AO system is respectively 44 nm, 70 nm, and 95 nm for the good, medium, and poor atmospheric conditions. Following the Maréchal approximation (Roberts et al., 2004), these residual wavefront errors correspond to Strehl ratios of 95%, 88%, and 79%, respectively (calculated at $\lambda = 1220$ nm). With this setup we only consider the speckle noise from the free atmosphere. As the decorrelation timescale for such speckles is on the order of ~ 1 second (Macintosh et al., 2005), we limited the duration of the simulation to 1 second. For longer simulations, the background speckles would effectively become incoherent with the SGs. Focal-plane images were recorded at 2 kHz. The coronagraph in this setup is the Vector Vortex Coronagraph (VVC; Mawet et al. 2005) with an accompanying Lyot stop with a 95% diameter. The VVC is a focal-plane mask that removes starlight and operates on the vector state of light. The reason for implementing the VVC in this simulation is twofold: first, for a clear aperture, the performance of the VVC is close to that of the perfect coronagraph (Cavarroc et al., 2006), and second, as the VVC also operates on the vector state of light, we show that the performance of the VSG will not be affected by such optics. The SGs are placed at $[\pm 25\lambda/D, \pm 25\lambda/D]$, which is well beyond the control radius of the AO system. The intensities of the SGs relative to the PSF core are $5 \cdot 10^{-3}$, making them ~ 150 , 63, and 35 times brighter than the background speckle halo for the good, medium, and poor atmospheric conditions, respectively. We compare the phase speckle grid (PSG) and

¹<https://hcipy.org>

the amplitude speckle grid (ASG) to the VPSG and the VASG. We did not include any temporally modulated SGs because, when assuming an instantaneous modulation, their performance is equal to the VSG. The VPSG and VASG are implemented on the circular polarization state. The simulations were performed with the same wavefronts for all the SGs. We also performed the same simulations without a SG for accurate background estimation.

In Figure 7.1 we show images of the SGs at a random iteration in the simulation for medium atmospheric conditions. The coronagraph and AO system removed the central stellar light and generated the dark hole, which is clearly visible. The idealistic AO system gives an optimistic contrast in the dark hole. Outside of the dark hole and control region, the speckle background is clearly visible. This background is generated by residual wavefront errors and evolves during the simulation. It will strongly interfere with the SGs, affecting their photometric and astrometric accuracy. The reference speckles of the SG are located in the corners of the images ($\pm 25 \lambda/D$, $\pm 25 \lambda/D$). The VPSG and VASG are significantly less distorted and more similar to each other compared to the PSG and ASG. This shows the effect of the incoherency of the VSG. Zooming in on the lower left reference speckles as shown in Figure 7.2 demonstrates this as well.

To quantify the performance increase offered by the VSGs, we calculate the rms photometric error and the rms astrometric error. These are calculated on the individual frames, and images that are averages of 5, 10, 50, and 100 frames to simulate longer exposure times. The photometric performance is calculated by carrying out the following steps:

1. Measure the photometry of the SG with an aperture with a diameter of $2.44 \lambda/D$.
2. Measure the background by aperture photometry in the simulation without SG at the same positions.
3. Subtract the background estimate from the SG photometry.
4. Remove the general photometric fluctuations by dividing the SG photometry by the mean photometry of the four speckles.
5. Calculate the rms photometry error per speckle.
6. Determine the final rms photometric error by calculating the mean of the four speckles individual rms photometric errors.

The astrometric performance is calculated by carrying out the following steps:

1. Measure the position of the individual speckles by cross-correlation with an unaberrated PSF.
2. Calculate the distance between the speckles.
3. Calculate the rms of these distances over all images.
4. Calculate the mean rms astrometric error over all the distances, which gives the final rms astrometric error.

In Figure 7.3 we plot the photometric and astrometric performance of the SGs as a function of the number of averaged frames (bin factor) and for the different atmospheric conditions. Figure 7.3 a shows that the VASG and the VPSG outperform the ASG and PSG in photometric error by a factor of ~ 10 -20 (depending on the bin factor and atmospheric conditions). The VASG and VPSG reach a ~ 0.3 -0.8% photometric error for individual frames, which drops to $\sim 0.2\%$ when the bin factor increases. The ASG and PSG on the other hand start at ~ 6 -15% photometric error and decrease to ~ 1.5 -4%. Figure 7.3 b also shows a performance increase for the astrometric performance. The VASG and VPSG improve the astrometric error by a factor of ~ 3 -5 with respect to the ASG and PSG. At a bin factor of one, the VSGs reach an astrometric error of $\sim 3 - 10 \cdot 10^{-3} \lambda/D$, and slightly improve for a bin factor of 100. The ASG and PSG start at $\sim 1.5 - 6 \cdot 10^{-2} \lambda/D$ and improve to $\sim 7 - 16 \cdot 10^{-3} \lambda/D$. These results clearly demonstrate that VSGs greatly improve the photometric and astrometric precision with respect to their non-vector counterparts.

For poorer seeing conditions, the performance of all SGs decreases. For the ASG and PSG, this is due to the increased speckle background halo that interferes with the SG (Equation 7.11), while for the VSGs this is due to the increased cross-talk between the reference speckles (Equation 7.17). When the wind speed increases, the performance of the SGs increases more rapidly with bin factor. This is because the decorrelation timescale of background speckles scales with the inverse of the windspeed (Macintosh et al., 2005). Therefore, for higher wind speeds, the interference between the background speckles and SGs will decrease with increasing bin factor, improving their performance.

7.3.2 Degree of polarization effects

As discussed in section 7.2, the incoherency of the VSGs depends on the degree of polarization (p ; Equation 7.2) of the light passing through the VSG (specifically the polarization state on which the VSG operates). As starlight is generally unpolarized to a very high degree (e.g. the integrated p of the Sun is $< 10^{-6}$; Kemp et al. 1987), we are mainly concerned with polarization introduced by the telescope and instrument. For VLT/SPHERE, the linear p has been measured to be on the order of a few percent (Van Holstein et al., 2020) and the circular p is expected to be even lower. To study the effect of p , we repeat the simulations of Figure 7.3 with the medium atmospheric conditions for the VSGs but with increasing levels of p . The simulations are performed with the same wavefronts as in Figure 7.3. Therefore, for $p = 0$, we expect exactly the same results, while for $p = 1$ the performance of the VSGs should reduce to that of the ASG and PSG. Figure 7.4 (a) shows the photometric performance and Figure 7.4 (b) the astrometric performance. Both figures indeed show that the performance of the VASG and VPSG degrade to that of the ASG and PSG when $p = 1$, and are optimal for $p = 0$. They also show that up to a p of 0.05 there is barely a performance degradation. The performance degrades close to linearly as a function of p , which is what we expect from Equation 7.11.

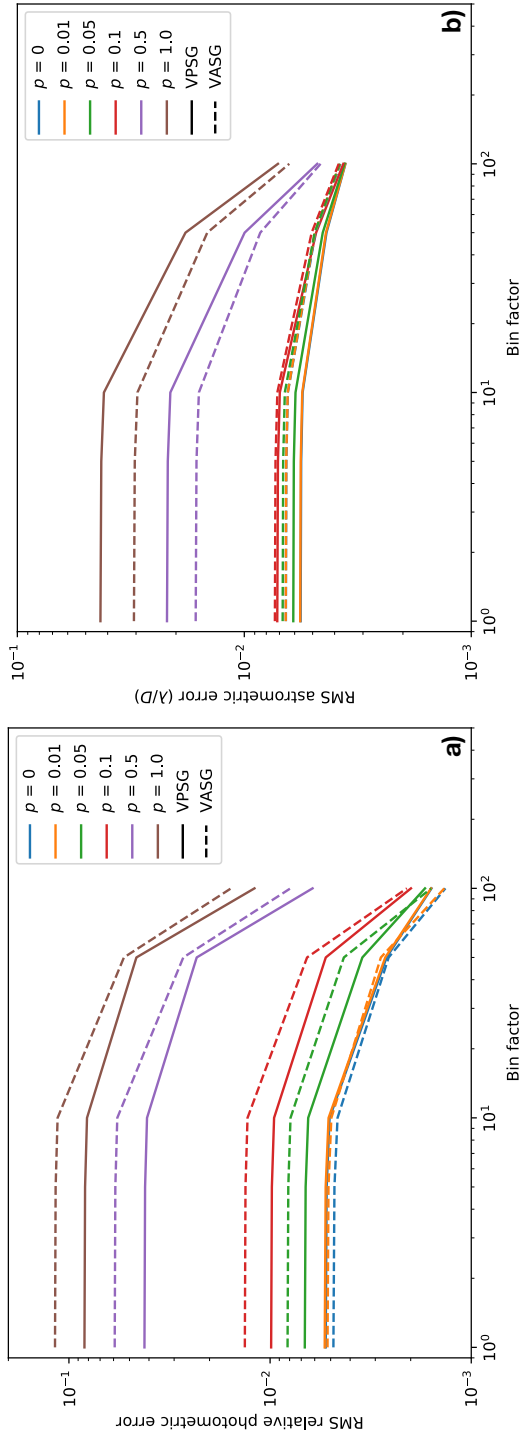


Figure 7.4: Photometric and astrometric performance of the VPSG and VASG as a function of the number of frames averaged and various degrees of polarization (p) under medium atmospheric conditions (Table 7.2). (a) The rms relative photometric error. (b) The rms astrometric error.

7.4 Implementation of vector speckle grid

Now that we have demonstrated that VSGs can drastically improve the photometric and astrometric performance, we discuss how VSGs can be implemented in a HCI system. We focus on the VPSG as we have not found a straightforward implementation of the VASG.

The most attractive solution for the implementation of the VPSG is the geometric phase (Pancharatnam 1956; Berry 1987), which applies the required phase to the opposite circular polarization states. The geometric phase is introduced when the fast-axis angle of a half-wave retarder is spatially varying. The phase that is induced is twice the fast-axis angle, and is opposite for the opposite circular polarization states. Due to its geometric origin, the geometric phase is completely achromatic. However, the efficiency with which the phase is transferred to the light depends on retardance offsets from half wave. Increasing the retardance offset decreases the amount of light that acquires the desired phase. The VPSGs simulated in section 7.3 are implemented by geometric phase.

Half-wave retarders with a spatially varying fast-axis angle can be constructed in various ways. For example, metamaterials have been used to induce geometric phase, but their efficiency is generally low (Mueller et al., 2017). The most mature and promising is liquid-crystal technology (Escuti et al., 2016). By a direct-write system, the desired fast-axis angle can be printed into a liquid-crystal photo-alignment layer that has been deposited on a substrate (Miskiewicz & Escuti, 2014). To achromatise the half-wave retarder, several layers of carefully designed, self-aligning birefringent liquid crystals can be deposited on top of the initial layer (Komanduri et al., 2013). In astronomy, there have already been several successful (broadband) implementations of this technology: in coronagraphy (Mawet et al. 2009; Snik et al. 2012), polarimetry (Tinyanont et al. 2018; Snik et al. 2019), wavefront sensing (Haffert 2016; Doelman et al. 2019), and interferometry (Doelman et al., 2018).

The major drawback of liquid-crystal technology is when there are retardance offsets from half-wave, as the efficiency with which the light accumulates the desired phase decreases. The light that does not acquire the desired phase will form an on-axis PSF, which is regularly referred to as the leakage. In coronagraphy, the leakage severely limits the coronagraphic performance of the liquid-crystal optic (Bos et al. 2018; Doelman et al. 2020). However, for the VSG the impact is much less severe, because the leakage will overlap with the stellar PSF and therefore be occulted by the coronagraph. The relative intensity of the VSG will be affected, but this effect will be relatively small as $I_s \propto (1 - L)$ (Bos et al., 2019), with L the leakage strength. The leakage strength is generally on the order of $\sim 2 \cdot 10^{-2}$ (Doelman et al., 2017) for broadband devices.

7.5 Discussion and conclusion

Here, we show that by applying opposite modulation on opposite polarization states in the pupil-plane amplitude or phase, a speckle grid in the focal plane is generated that can be used as a photometric and astrometric reference. We refer to this as the Vector Speckle Grid (VSG). In this implementation, the speckle grid will not interfere with the central stellar PSF and will therefore be effectively incoherent. This greatly decreases the photo-

metric and astrometric errors when the PSF is distorted by aberrations. Furthermore, we identified that the remaining limiting factor is the cross-talk between the speckles in the grid itself. This can be mitigated by increasing the separation between the speckles.

We performed simulations with various atmospheric conditions to quantify the performance increase with respect to regular SGs. We find that for the conditions simulated, the VSGs improve the photometric and astrometric errors by a factor of ~ 20 and ~ 5 , respectively, reaching a $\sim 0.3\text{--}0.8\%$ photometric and a $\sim 3 - 10 \cdot 10^{-3} \lambda/D$ astrometric error on short exposure images. We note that the performance increase depends on the brightness difference between the speckle and the residual speckle background. When the brightness difference increases, the performance increase is more moderate. If the speckles are dimmer, the performance increase is higher. We also investigated the effects of partially polarized light on the performance of the VSGs. The simulations showed that when the degree of polarization was below 5%, the performance was barely affected. The polarization signal introduced by the telescope and instrument is on this level or less, and therefore not relevant. We note that it is hard to predict what the on-sky performance will be as it is notoriously difficult to capture all relevant effects in simulation (Guyon et al., 2019). Therefore, these results are an indication of the performance increase that the VSGs could bring. We also note that the performance of the ASG and PSG reported in these simulations is better than what has been reported on-sky, while the duration of the simulations is much shorter than the actual observations. This is because these simulations only consider the effects of AO-corrected atmospheric wavefront errors, while observations are also affected by noise processes that generate background speckles with much longer decorrelation timescales. The VSG would also be incoherent to these background speckle noise sources.

We identified that the most attractive implementation of VSGs would be a Vector Phase Speckle Grid (VPSG) by the geometric phase. Liquid-crystal technology allows for a broadband half-wave retarder with a varying fast-axis angle that will induce the geometric phase on the light. This has the major advantage that the VPSG can be implemented as a one pupil-plane optic.

Implementing the VPSG by liquid-crystal technology has the following advantages: it achieves instantaneous incoherency, it is a static component and therefore easy to calibrate, the artificial speckles can be positioned anywhere in the focal plane, the geometric phase is achromatic and therefore the speckles have a constant brightness with wavelength. Another advantage, not discussed in this paper, is that the VPSG could be multiplexed with holograms for wavefront sensing (Wilby et al., 2017). The main disadvantage of the VPSG is that the position of the speckles is fixed, making accurate background estimates more difficult, and decreasing the flexibility of speckle grid positioning.

To conclude, the VSG has proven to be a promising method for generating speckle grids as photometric and astrometric references. We show that the VSG reaches a satisfactory performance in simulation, and the next steps will be an investigation of broadband effects, a lab demonstration, and subsequent on-sky tests. The VSG could be part of the future upgrades of SPHERE and GPI (Beuzit et al. 2018; Chilcote et al. 2018).

Bibliography

- Apai, D., Kasper, M., Skemer, A., et al. 2016, *The Astrophysical Journal*, 820, 40
- Berry, M. V. 1987, *Journal of Modern Optics*, 34, 1401
- Beuzit, J.-L., Mouillet, D., Fusco, T., et al. 2018, in *Adaptive Optics Systems VI*, Vol. 10703, International Society for Optics and Photonics, 107031P
- Beuzit, J.-L., Vigan, A., Mouillet, D., et al. 2019, arXiv preprint arXiv:1902.04080
- Bos, S. P., Doelman, D. S., de Boer, J., et al. 2018, in *Advances in Optical and Mechanical Technologies for Telescopes and Instrumentation III*, Vol. 10706, International Society for Optics and Photonics, 107065M
- Bos, S. P., Doelman, D. S., Lozi, J., et al. 2019, *Astronomy & Astrophysics*, 632, A48
- Cavarroc, C., Boccaletti, A., Baudoz, P., Fusco, T., & Rouan, D. 2006, *Astronomy & Astrophysics*, 447, 397
- Chilcote, J. K., Bailey, V. P., De Rosa, R., et al. 2018, in *Ground-based and Airborne Instrumentation for Astronomy VII*, Vol. 10702, International Society for Optics and Photonics, 1070244
- Doelman, D. S., Auer, F. F., Escuti, M. J., & Snik, F. 2019, *Optics letters*, 44, 17
- Doelman, D. S., Por, E. H., Ruane, G., Escuti, M. J., & Snik, F. 2020, *Publications of the Astronomical Society of the Pacific*, 132, 045002
- Doelman, D. S., Snik, F., Warriner, N. Z., & Escuti, M. J. 2017, in *Techniques and Instrumentation for Detection of Exoplanets VIII*, Vol. 10400, International Society for Optics and Photonics, 104000U
- Doelman, D. S., Tuthill, P., Norris, B., et al. 2018, in *Optical and Infrared Interferometry and Imaging VI*, Vol. 10701, International Society for Optics and Photonics, 107010T
- Escuti, M. J., Kim, J., & Kudenov, M. W. 2016, *Optics and Photonics News*, 27, 22
- Fitzgerald, M. P., & Graham, J. R. 2006, *The Astrophysical Journal*, 637, 541
- Guyon, O., Bottom, M., Chun, M., et al. 2019, *BAAS*, 51, 203
- Haffert, S. 2016, *Optics express*, 24, 18986
- Hinkley, S., Oppenheimer, B. R., Soummer, R., et al. 2007, *The Astrophysical Journal*, 654, 633
- Jovanovic, N., Guyon, O., Martinache, F., et al. 2015a, *The Astrophysical Journal Letters*, 813, L24
- Jovanovic, N., Martinache, F., Guyon, O., et al. 2015b, *Publications of the Astronomical Society of the Pacific*, 127, 890
- Kemp, J. C., Henson, G., Steiner, C., & Powell, E. 1987, *Nature*, 326, 270
- Komanduri, R. K., Lawler, K. F., & Escuti, M. J. 2013, *Optics Express*, 21, 404
- Kostov, V., & Apai, D. 2012, *The Astrophysical Journal*, 762, 47
- Langlois, M., Vigan, A., Moutou, C., et al. 2013, in *Proceedings of the Third AO4ELT Conference*, 63
- Macintosh, B., Poyneer, L., Sivaramakrishnan, A., & Marois, C. 2005, in *Astronomical Adaptive Optics Systems and Applications II*, Vol. 5903, International Society for Optics and Photonics, 59030J
- Macintosh, B., Graham, J. R., Ingraham, P., et al. 2014, *proceedings of the National Academy of Sciences*, 111, 12661
- Marois, C., Lafreniere, D., Macintosh, B., & Doyon, R. 2006, *The Astrophysical Journal*, 647, 612
- Martinez, P., Kasper, M., Costille, A., et al. 2013, *Astronomy & Astrophysics*, 554, A41
- Martinez, P., Loose, C., Carpentier, E. A., & Kasper, M. 2012, *Astronomy & Astrophysics*, 541, A136
- Mawet, D., Riaud, P., Absil, O., & Surdej, J. 2005, *The Astrophysical Journal*, 633, 1191
- Mawet, D., Serabyn, E., Liewer, K., et al. 2009, *Optics Express*, 17, 1902
- Milli, J., Banas, T., Mouillet, D., et al. 2016, in *Adaptive Optics Systems V*, Vol. 9909, International

- Society for Optics and Photonics, 99094Z
- Miskiewicz, M. N., & Escuti, M. J. 2014, *Optics Express*, 22, 12691
- Mueller, J. B., Rubin, N. A., Devlin, R. C., Groever, B., & Capasso, F. 2017, *Physical Review Letters*, 118, 113901
- Pancharatnam, S. 1956in , Springer, 398–417
- Por, E. H., Haffert, S. Y., Radhakrishnan, V. M., et al. 2018, in *Proc. SPIE*, Vol. 10703, Adaptive Optics Systems VI
- Roberts, L. C. J., Perrin, M. D., Marchis, F., et al. 2004, in *Advancements in Adaptive Optics*, Vol. 5490, International Society for Optics and Photonics, 504–515
- Sivaramakrishnan, A., Lloyd, J. P., Hodge, P. E., & Macintosh, B. A. 2002, *The Astrophysical Journal Letters*, 581, L59
- Sivaramakrishnan, A., & Oppenheimer, B. R. 2006, *The Astrophysical Journal*, 647, 620
- Snik, F., Otten, G., Kenworthy, M., et al. 2012, in *Modern Technologies in Space-and Ground-based Telescopes and Instrumentation II*, Vol. 8450, International Society for Optics and Photonics, 84500M
- Snik, F., Keller, C. U., Doelman, D. S., et al. 2019, in *Polarization Science and Remote Sensing IX*, Vol. 11132, International Society for Optics and Photonics, 111320A
- Soummer, R., Ferrari, A., Aime, C., & Jolissaint, L. 2007, *The Astrophysical Journal*, 669, 642
- Tinyanont, S., Millar-Blanchaer, M. A., Nilsson, R., et al. 2018, *Publications of the Astronomical Society of the Pacific*, 131, 025001
- Van Holstein, R. G., Girard, J. H., De Boer, J., et al. 2020, *Astronomy & Astrophysics*, 633, A64
- Wang, J. J., Rajan, A., Graham, J. R., et al. 2014, in *Ground-based and Airborne Instrumentation for Astronomy V*, Vol. 9147, International Society for Optics and Photonics, 914755
- Wang, J. J., Graham, J. R., Pueyo, L., et al. 2016, *The Astronomical Journal*, 152, 97
- Wilby, M. J., Keller, C. U., Snik, F., Korkiakoski, V., & Pietrow, A. G. 2017, *Astronomy & Astrophysics*, 597, A112
- Zhou, Y., Apai, D., Schneider, G. H., Marley, M. S., & Showman, A. P. 2016, *The Astrophysical Journal*, 818, 176

8 | Outlook

The current generation of HCI instruments will continue to target young giant gas planets after their upgrade programs (Beuzit et al., 2018; Chilcote et al., 2018). One of the key upgrades are focal-plane wavefront sensors to address non-common path aberrations. Several focal-plane wavefront sensors have been successfully tested on-sky (Chapter 2, 4, and 6; Bottom et al. 2017; Galicher et al. 2019; Huby et al. 2017; Martinache et al. 2016, 2014; Wilby et al. 2017). However, they have not been used during science observations, except for QACITS (Huby et al., 2017), making it difficult to assess the impact of focal-plane wavefront sensing on the post-processed contrast. Therefore, to assess the impact of focal-plane wavefront sensing on the end-to-end system performance (including post-processing), on-sky testing during science observations should be a prime test for the immediate future.

Current ground-based HCI instruments have been unsuccessful in detecting exoplanet variability due to speckle noise. The VSG concept, presented in Chapter 7, is a new concept to dramatically increase the signal-to-noise ratio of exoplanet variability measurements with HCI instruments. Combining the VSG concept with alternating the position of the artificial speckles, as presented in Sahoo et al. (2020), by rotating the optic's mount between images is a promising solution to reach the required photometric precision. When this is implemented at HCI instruments, it will open up an exciting new avenue to study the variability of already directly-imaged exoplanets.

The long term goal of high-contrast imaging is the detection and characterization of rocky exoplanets in the habitable zone of nearby stars, and look for signs of life. An important part of this future are the next generation of Giant Segmented Mirror Telescopes (GSMTs), such as the Extremely Large Telescope (ELT; Gilmozzi & Spyromilio 2007), the Thirty Meter Telescope (TMT; Nelson & Sanders 2008), and the Giant Magellan Telescope (GMT; Johns et al. 2012). These telescopes have primary mirrors with diameters between 25 and 39 meter, resulting in a tremendous increase in light-gathering power and angular resolution compared to current telescopes. Therefore it is expected that GSMTs will acquire the first spectra of rocky habitable exoplanets around M-type main sequence stars by means of direct imaging (Guyon et al., 2012).

Due to the massive support structures required to support the secondary mirrors of GSMTs, which can be the size of a current 4-meter class telescope, it is expected that the low-wind effect will play a dominant role in their wavefront error budget (Holzlöhner & Brinkmann, 2020). Furthermore, these telescopes have segmented primary mirrors, and the segments have to be carefully co-phased to reach their ultimate performance (Quirós-Pacheco et al., 2018). The island effect will limit the most common pupil-plane based wavefront sensors in dealing with these problems. Focal-plane wavefront sensors do not have this limitation as they do not sense in the pupil plane and are therefore among the prime solutions for these issues. Especially for the Fast&Furious focal-plane wavefront sensing algorithm (F&F; Chapter 6) there is a big opportunity to step in and provide the wavefront sensing solution. We have proven on sky that F&F is able to deal with the LWE, and are currently testing it on sky at the segmented Keck telescope, as shown in Figure 8.1.

GSMTs will host high-contrast imaging instruments that are expected to image and char-

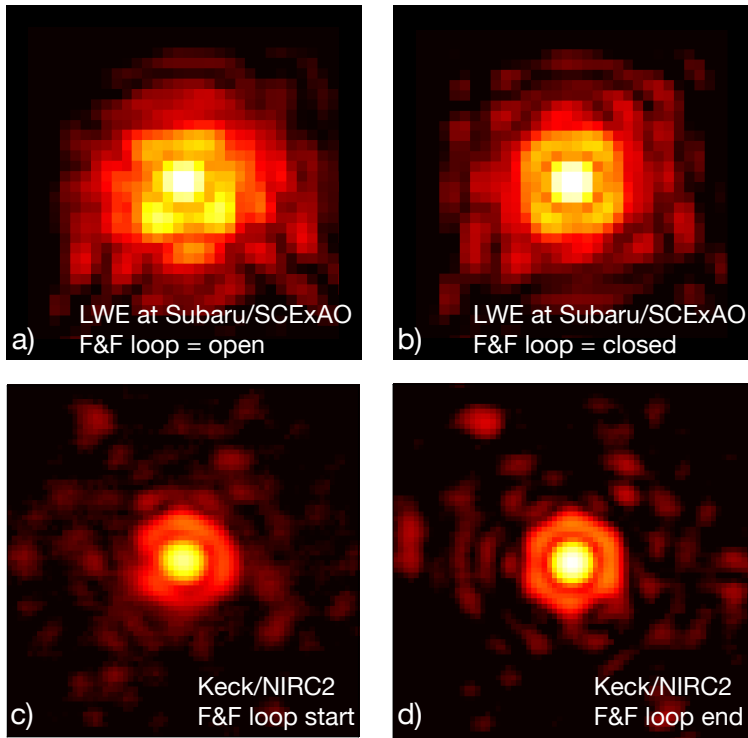


Figure 8.1: On-sky F&F tests at Subaru/SCEXAO and Keck/NIRC2. The average PSF during a LWE event at Subaru/SCEXAO when the F&F loop was a) open and b) closed. Tests at Keck/NIRC2 for low-order aberration correction with F&F, c) start and d) end of the correction loop. Collaborators of the Keck/NIRC2 tests are M. Bottom, J. Delorme, S. Ragland, S. Cetre, and L. Pueyo. The images are shown in log scale.

acterize rocky exoplanets in the habitable zone of nearby stars. Instruments under consideration are the Exo-Planet Imaging Camera and Spectrograph (EPICS; Kasper et al. 2010) for the ELT and the Planetary Systems Imager (PSI; Fitzgerald et al. 2019) for the TMT. The Mid-Infrared ELT Imager and Spectrograph instrument (METIS; Carlomagno et al. 2020) is already under construction for the ELT, and will try to image the closest exoplanet Proxima b. To reach the extreme contrasts at small angular separations required to image a rocky exoplanet, it is of the utmost importance that the entire HCI instrument is optimized as a whole, and not per individual subsystem. The work presented in this thesis provides such integrated solutions. We have shown that the vAPP coronagraph can be integrated with focal-plane wavefront sensing in Chapters 2, 3 and 4. Furthermore, it has been shown that the vAPP is suitable for broadband coronagraphic imaging (Otten et al., 2014), and can be combined with polarimetry (Bos et al., 2018; Snik et al., 2014). It is possible to combine all these functionalities, and a first design for such a vAPP is presented in Bos et al. (2020). In Chapter 5 we have presented the PESCC – a combination of focal-plane coronagraphy with focal-plane wavefront sensing. As detailed in Chapter 5, the PESCC encodes wavefront information into one of the polarization states, and therefore many of the necessary components for polarimetry are already in place. This presents a unique opportunity to combine coronagraphy, focal-plane wavefront sensing and control, coherent differential imaging and polarimetry, which will enable the direct imaging and characterization of rocky exoplanets in the habitable zone.

Bibliography

- Beuzit, J.-L., Mouillet, D., Fusco, T., et al. 2018, in *Adaptive Optics Systems VI*, Vol. 10703, International Society for Optics and Photonics, 107031P
- Bos, S. P., Doelman, D. S., de Boer, J., et al. 2018, in *Advances in Optical and Mechanical Technologies for Telescopes and Instrumentation III*, Vol. 10706, International Society for Optics and Photonics, 107065M
- Bos, S. P., Doelman, D. S., Miller, K. L., & Snik, F. 2020, in *Adaptive Optics Systems VII*, Vol. 11448, International Society for Optics and Photonics, 114483W
- Bottom, M., Wallace, J. K., Bartos, R. D., Shelton, J. C., & Serabyn, E. 2017, *Monthly Notices of the Royal Astronomical Society*, 464, 2937
- Carlomagno, B., Delacroix, C., Absil, O., et al. 2020, *Journal of Astronomical Telescopes, Instruments, and Systems*, 6, 035005
- Chilcote, J. K., Bailey, V. P., De Rosa, R., et al. 2018, in *Ground-based and Airborne Instrumentation for Astronomy VII*, Vol. 10702, International Society for Optics and Photonics, 1070244
- Fitzgerald, M., Bailey, V., Baranec, C., et al. 2019, *Bulletin of the American Astronomical Society*, 51, 251
- Galicher, R., Baudoz, P., Delorme, J.-R., et al. 2019, *Astronomy & Astrophysics*, 631, A143
- Gilmozzi, R., & Spyromilio, J. 2007, *The Messenger*, 127, 3
- Guyon, O., Martinache, F., Cady, E. J., et al. 2012, in *Adaptive Optics Systems III*, Vol. 8447, International Society for Optics and Photonics, 84471X
- Holzlöhner, R., & Brinkmann, M. 2020, in *Ground-based and Airborne Telescopes VIII*, Vol. 11445, International Society for Optics and Photonics, 114450Y
- Huby, E., Bottom, M., Femenia, B., et al. 2017, *Astronomy & Astrophysics*, 600, A46
- Johns, M., McCarthy, P., Raybould, K., et al. 2012, in *Ground-based and Airborne Telescopes IV*, Vol. 8444, International Society for Optics and Photonics, 84441H
- Kasper, M., Beuzit, J.-L., Verinaud, C., et al. 2010, in *Ground-based and Airborne Instrumentation for Astronomy III*, Vol. 7735, International Society for Optics and Photonics, 77352E
- Martinache, F., Jovanovic, N., & Guyon, O. 2016, *Astronomy & Astrophysics*, 593, A33
- Martinache, F., Guyon, O., Jovanovic, N., et al. 2014, *Publications of the Astronomical Society of the Pacific*, 126, 565
- Nelson, J., & Sanders, G. H. 2008, in *Ground-based and Airborne Telescopes II*, Vol. 7012, International Society for Optics and Photonics, 70121A
- Otten, G. P., Snik, F., Kenworthy, M. A., et al. 2014, in *Advances in Optical and Mechanical Technologies for Telescopes and Instrumentation*, Vol. 9151, International Society for Optics and Photonics, 91511R
- Quirós-Pacheco, F., Schwartz, D., Das, K., et al. 2018, in *Ground-based and Airborne Telescopes VII*, Vol. 10700, International Society for Optics and Photonics, 107000N
- Sahoo, A., Guyon, O., Lozi, J., et al. 2020, *The Astronomical Journal*, 159, 250
- Snik, F., Otten, G., Kenworthy, M., Mawet, D., & Escuti, M. 2014, in *Ground-based and Airborne Instrumentation for Astronomy V*, Vol. 9147, International Society for Optics and Photonics, 91477U
- Wilby, M. J., Keller, C. U., Snik, F., Korkiakoski, V., & Pietrow, A. G. 2017, *Astronomy & Astrophysics*, 597, A112

Nederlandstalige samenvatting

Inleiding

Het bestaan van werelden buiten ons zonnestelsel en hun bewoonbaarheid tart de fantasie van de mensheid al honderden jaren. Menig filosoof heeft gefilosofeerd over het bestaan van leven op planeten rondom andere sterren, ook wel genaamd exoplaneten. Dit intrigerende onderwerp heeft daarom velen mensen geïnspireerd om daadwerkelijk op zoek te gaan naar het bestaan van exoplaneten. Al in 1855 claimde de directeur van de sterrenwacht in Madras, William Stephen Jacob, een exoplaneet te hebben ontdekt rondom 70 Ophiuchi. Deze en vele andere claims die volgden in de 19^e en 20^e eeuw werden onderdrukt. Meestal omdat er een systematische fout over het hoofd was gezien.

Pas aan het einde van de 20^e eeuw was de technologie zover gevorderd dat de eerste exoplaneten konden worden gedetecteerd. In 1992 werden twee exoplaneten gevonden in een baan rondom een pulsar, het overblijfsel van een ster na een supernova explosie. Drie jaar later, in 1995, ontdekten Michel Mayor en Didier Queloz de eerste planeet in een baan rondom een ster vergelijkbaar met de zon. Sindsdien zijn er duizenden exoplaneten ontdekt en is onze kennis over exoplaneten enorm toegenomen. Er is echter nog veel onderzoek nodig voordat we kunnen bevestigen dat er ook daadwerkelijk exoplaneten bestaan die de benodigde ingrediënten hebben om leven te laten ontstaan en in stand te houden. Om dit te weten te komen moeten we onderzoeken wat de samenstelling van de atmosfeer is en of er vloeibaar water op het oppervlak voorkomt.

Er zijn verschillende methodes ontwikkeld om exoplaneten waar te nemen. Deze zijn te verdelen in indirecte en directe methodes. Indirecte methodes richten zich op de effecten die de exoplaneet heeft op de begeleidende ster. Bij de planeetovergangmethode wordt heel precies de helderheid van de ster gedurende de tijd gemeten. Regelmatige dipjes in de helderheid van de ster duiden dan op de aanwezigheid van een of meerdere exoplaneten. De radiële-snelheid- en astrometriemethode richten zich op regelmatige bewegingen van de ster veroorzaakt door een exoplaneet die in een baan rondom de ster beweegt. De radiële-snelheidmethode richt zich specifiek op de radiële snelheid van de ster. Deze wordt gemeten door naar dopplerverschuivingen in het spectrum van de ster te kijken. De astrometriemethode gebruikt de tangentiële beweging van de ster om exoplaneten te vinden. Deze beweging wordt gemeten door heel erg nauwkeurig de positie van de ster aan de hemel vast te leggen gedurende de tijd. De planeetovergang- en radiële-snelheidmethode hebben samen al enkele duizenden exoplaneet detecties opgeleverd. Helaas kunnen indirecte methodes niet of maar in beperkte mate het oppervlak en de atmosfeer van exoplaneten in kaart brengen. De directe waarneemmethode is in dat opzicht veelbelovender, want bij deze methode wordt licht direct afkomstig van de exoplaneet opgevangen. Dit licht kan vervolgens worden geanalyseerd in intensiteit, spectrum, polarisatie en temporale variaties en daarmee kan veel informatie over de exoplaneet worden verzameld. Dit is extreem interessant voor het bepalen van de bewoonbaarheid van de exoplaneet en het detecteren van mogelijke tekenen van buitenaards leven.

Directe waarnemingen van exoplaneten

Directe waarnemingen van exoplaneten is de meest veelbelovende techniek om de atmosfeer en het oppervlak van exoplaneten te bestuderen en op zoek te gaan naar tekenen van leven. Maar voordat we op zoek kunnen gaan naar rotsachtige exoplaneten moeten er nog vele technische uitdagingen worden overwonnen. Er zijn twee fundamentele problemen in dit vakgebied: hoekscheiding en contrast. Deze problemen worden veroorzaakt door het golfachtige karakter van licht en de eindige grootte van de spiegels van telescopen. Dit zorgt ervoor dat het beeld van een waargenomen ster niet oneindig scherp is. Het ziet er uit als een centrale kern van licht, omringd door zwakkere ringen van licht. Deze structuur van licht wordt de puntspreidingsfunctie (*point spread function*; PSF) genoemd. De PSF is veel helderder dan een exoplaneet en beperkt de minimale hoekscheiding, ook wel hoekresolutie genoemd, die een telescoop kan waarnemen.

Een telescoop met een primaire spiegel diameter van 8 meter die waarneemt op een golflengte van 1 micron heeft een minimale hoekscheiding van 30 milliboogseconden. Stel dat we deze telescoop in de ruimte zouden plaatsen op een afstand van 10 parsec vanaf het zonnestelsel. Als we dan de Aarde zouden proberen waar te nemen, dan is de hoekscheiding tussen de Aarde en de Zon ongeveer 0.1 boogseconde en de verhouding in helderheid, ook wel het contrast genoemd, een factor 10 miljard. Door dit extreme contrast wordt direct waarnemen ook wel hoog-contrast afbeelden (*high-contrast imaging*; HCI) genoemd. De meeste telescopen staan op Aarde en hebben de extra uitdaging van turbulentie in de atmosfeer. Dit zorgt ervoor dat de PSF wordt uitgesmeerd tot een wolk van sterlicht en dat de hoekresolutie verslechtert.

Om de uitdagingen van het golfachtige karakter van licht en atmosferische turbulentie het hoofd te bieden zijn HCI instrumenten complexe optische systemen. Ze bestaan uit verschillende subsystemen die ontworpen zijn om golffrontfouten in het systeem te meten en corrigeren, sterlicht te onderdrukken en het licht van de exoplaneet te analyseren. Een schematisch overzicht van een HCI instrument voor een op de grond geplaatste telescoop is weergegeven in Figuur 8.2. Licht van de ster is verstoord door de atmosfeer van de Aarde voordat het wordt opgevangen door de telescoop. Dit soort verstoringen noemen we golffrontfouten of aberraties. Het eerste subsysteem van het instrument is het adaptieve-opticasysteem dat de golffront verstoring meet met een golffrontsensor en vervolgens corrigeert met een vervormbare spiegel. Daarna komt de coronagraaf; een optisch systeem dat sterlicht onderdrukt in een gebied dat we het donkere veld noemen. In het donkere veld kan naar exoplaneten worden gezocht. Door golffrontfouten is de onderdrukking van de coronagraaf niet perfect en blijft een restant van sterlicht over. Om dit restant te scheiden van exoplaneet licht wordt dit doorgestuurd naar een of meerdere afbeeldingsystemen. Deze systemen gebruiken verscheidene waarneemstrategieën om het licht van de exoplaneet te onderscheiden van het overgebleven sterlicht. Deze waarneemstrategieën kunnen bijvoorbeeld gebruiken maken van verschillen in het spectrum, polarisatie of coherentie tussen het sterlicht en exoplaneet licht.

Naast de hierboven beschreven uitdagingen zijn nog andere factoren die directe waarne-

Een hoog contrast beeldvorming systeem

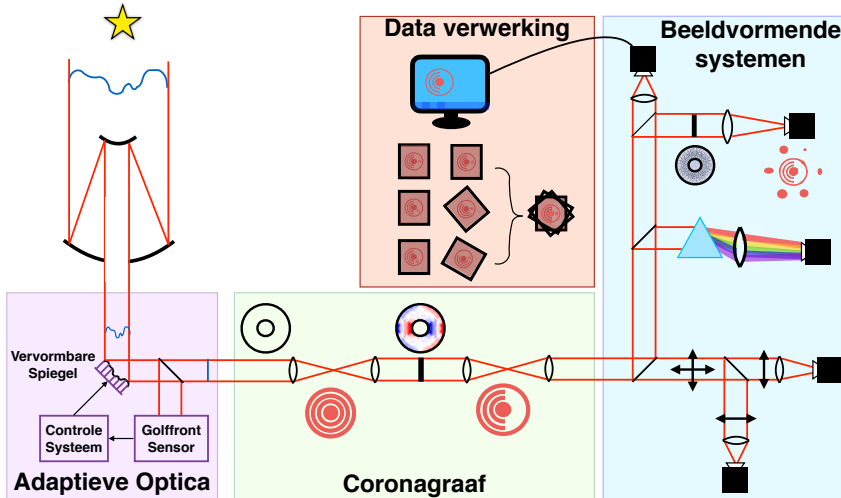


Figure 8.2: Schematisch overzicht van een hoog-contrast afbeeldingsinstrument. Het golffront van sterlicht wordt vervormd door de atmosfeer van de Aarde. De telescoop vangt het licht op en stuurt het door naar het adaptieve-opticasysteem. In dit systeem meet de golffrontsensor de golffront verstoring en geeft deze meting door aan het controlesysteem. Het controlesysteem berekent vervolgens hoe de vormbare spiegel moet worden vervormd om de golffront verstoring te corrigeren. De coronagraaf onderdrukt vervolgens het sterlicht door middel van optische manipulaties en stuurt het overgebleven sterlicht en exoplaneet licht door naar verschillende afbeeldingsystemen. Deze systemen meten de verschillende eigenschappen van het licht om het exoplaneet licht te onderscheiden van sterlicht (bijvoorbeeld spectrum en polarizatie). Tijdens de data verwerking wordt zo veel mogelijk van het overgebleven sterlicht weggehaald om de exoplaneet zichtbaar te maken. Figuur gemaakt door David Doelman.

mingen van exoplaneten lastig maken. Een van deze factoren zijn golffrontfouten die niet worden gemeten door de primaire golffrontsensor in het systeem. Niet-gemeenschappelijk-pad aberraties (*non-common path aberrations*; NCPA) zijn aberraties die voortkomen uit de optica die na de primaire golffrontsensor zijn geplaatst. NCPA worden veroorzaakt door uitlijnfouten, productiefouten en turbulentie in het optische systeem. Deze aberraties zijn dynamisch en veranderen van vorm en sterkte gedurende tijdschalen van seconden, minuten en uren. Deze veranderingen worden veroorzaakt door temperatuur en luchtvochtigheid schommelingen gedurende de waarnemingen.

Het lage-windsnelheidseffect (*low-wind effect*; LWE) is een ander soort golffrontfout dat exoplaneet waarnemingen lastig maakt. De golffrontfouten van het LWE ontstaan door de telescoopstructuur vóór de primaire golffrontsensor, maar hebben een specifieke vorm die lastig te meten zijn door de gebruikelijke golffrontsensoren. Het LWE komt voor gedurende situaties dat de windsnelheid laag is (lager dan een paar meter per seconde), dit zijn omstandigheden die normaal gesproken tot de beste waarneem omstandigheden worden gerekend. Wanneer de koepel opengaat voor waarnemingen stelt het de telescoopconstructie bloot aan de nachtelijke hemel. Dit resulteert in een snelle straling gedreven koeling van de constructie tot een temperatuur onder die van de omgevingslucht. Als lucht dan met een lage windsnelheid over de koude telescoopstructuur stroomt dan koelt de lucht snel af en verandert de brekingsindex van lucht. Dit introduceert aberraties met scherpe stappen in het golffront aan weerszijden van de telescoopconstructie die veranderen op tijdschalen van seconden.

Golffrontfouten, onder andere veroorzaakt door NCPA en het LWE, veroorzaken structuren in het beeldvlak die erg lijken op exoplaneten. Deze structuren worden spikkels genoemd en zijn de voornaamste bron van ruis die directe waarnemingen van exoplaneten verhinderen.

Beeldvlak golffrontsensoren

Een beeldvlak golffrontsensor (*focal-plane wavefront sensor*; FPWFS) is een uitermate geschikte oplossing om de hierboven beschreven aberraties te meten. Een FPWFS is een sensor die gebruik maakt van afbeeldingen van de ster om golffrontfouten te meten. Afhankelijk van de vorm en sterkte van de golffrontfout ziet de afbeelding van de ster er anders uit. Helaas geven niet alle golffrontfouten een unieke vervorming van de ster. Golffrontfouten met een even puntsymmetrie van gelijke sterkte maar met een verschil in teken (plus of minus) geven dezelfde afbeelding. Door deze ambiguïteit is het lastig om accuraat de golffrontfout te meten. Er zijn verschillende optische technieken bedacht om de ambiguïteit te breken. Zo kan bijvoorbeeld een kunstmatige puntsymmetrische aberratie worden geïntroduceerd, bijvoorbeeld door de camera uit focus te plaatsen. Belangrijk voor dit soort technieken is dat het beeldvlak van de wetenschappelijke camera wordt gebruikt, want dit zorgt er voor dat het niet-gemeenschappelijke pad wordt geëlimineerd. Het is dan wel belangrijk dat de FPWFS de capaciteit heeft om simultaan met wetenschappelijk waarnemingen de golffront metingen te doen om de waarneem efficiëntie hoog te

houden. Dit betekent dat de FPWFS geïntegreerd moet worden in de coronagraaf en de afbeeldsystemen.

Exoplaneetvariabiliteit

We verwachten dat exoplaneten, net zoals de meeste planeten in het zonnestelsel, wolken in hun atmosfeer hebben. Het detecteren en bestuderen van wolken op exoplaneten zal ons begrip van de atmosferische samenstelling en weersystemen op deze andere werelden verbeteren. Wolkenstructuren uiten zich als helderheid variaties in de tijd terwijl de exoplaneet roteert rondom zijn as.

Het waarnemen van variabiliteit bij exoplaneten is niet triviaal, want de meeste coronagrafen schermen de ster af en die is meestal de fotometrische referentie. Dit maakt het een uitdaging om de variabiliteit van exoplaneten te onderscheiden van veranderingen in de atmosfeer die gelijkaardige helderheid variaties geven. Om dit probleem te verhelpen zijn diffractieve methoden ontwikkeld die kunstmatige spikkels genereren om te dienen als fotometrische referenties. Deze spikkels zijn kopieën van de ster en ontworpen om niet te worden afgedekt door de coronagraaf en hebben een vooraf bepaalde helderheid. Ze worden gevormd door statische fase- of amplitudemodulaties toe te passen in het pupilvlak vóór het beeldvlakoptiek van de coronagraaf. De beperkende factor van deze oplossingen is echter hun coherentie met de in de tijd variërende spikkelachtergrond. Dit resulteert in interferentie die de vorm en helderheid van de kunstmatige spikkels dynamisch vervormt. Uiteindelijk beperkt dit op zijn beurt de fotometrische precisie.

Het probleem van interferentie kan worden omzeild door snelle, temporele modulatie van de vervormbare spiegel te gebruiken om de fase van de kunstmatige spikkels binnen een milliseconde te schakelen tussen 0 en π . Hierdoor wordt de interferentie uitgemiddeld en worden de kunstmatige spikkels effectief incoherent met de spikkel achtergrond. Dit verhoogt de fotometrische precisie van de kunstmatige spikkels. Bij een geavanceerdere methode wordt ook de positie van de kunstmatige spikkels afgewisseld, waardoor een nauwkeurige schatting van de achtergrond mogelijk is en de fotometrische precisie nog meer wordt verbeterd. Belangrijk bij de techniek met temporale modulate van de vervormbare spiegel is dat de primaire golffrontsensor en de vervormbare spiegel goed gekalibreerd zijn, omdat anders de kunstmatige spikkels niet de verwachte fase krijgen en daarmee hun fotometrische precisie kan afnemen.

Overzicht proefschrift

Dit proefschrift presenteert en valideert nieuwe beeldvlak golffrontsensoren in theorie, numerieke simulatie en gedurende waarnemingen. Daarnaast wordt een nieuwe optische methode geïntroduceerd om exoplaneetvariabiliteit metingen te verbeteren. Het ultieme doel is om de directe waarneming van rotsachtige exoplaneten met toekomstige extreem grote telescopen mogelijk te maken. De belangrijkste focus van dit proefschrift ligt op het

ontwikkelen van geïntegreerde oplossingen van coronagrafen en beeldvlak golffrontsensoren om niet-gemeenschappelijk-pad aberraties te meten in hoog-contrast afbeeldinstrumenten (Hoofdstukken 2 – 5). De laatste twee hoofdstukken onderzoeken een beeldvlak golffrontsensor om de aberraties van het lage-windsnelheidseffect te meten (Hoofdstuk 6) en een nieuwe optische methode om de signaal-ruisverhouding van exoplaneetvariabiliteit waarnemingen te verhogen (Hoofdstuk 7).

Hoofdstuk 1: Inleiding

In dit hoofdstuk wordt een algemeen beeld geschetst van het vakgebied en de belangrijkste problemen waarvoor dit proefschrift een oplossing poogt te bieden. Er wordt tevens een uitgebreide introductie gegeven over beeldvlak golffront detectie en de meest gebruikte beeldvlak golffront detectiemethodes in het vakgebied worden gecategoriseerd aan de hand van de optische manipulaties waarmee ze het teken ambiguïteit breken.

Hoofdstuk 2: Beeldvlak golffront detectie met de vector-apodiserende faseplaat

Dit hoofdstuk introduceert een nieuwe beeldvlak golffrontsensor door de vector-apodiserende faseplaat (*vector-Apodizing Phase Plate*; vAPP) coronagraaf te combineren met een asymmetrische-pupil golffrontsensor. Er wordt ook een niet-lineair, op een model gebaseerd algoritme voor het meten van golffronten gepresenteerd. We bestuderen de nauwkeurigheid van de vAPP en het golffront-detectiealgoritme in geïdealiseerde simulaties. Vervolgens worden deze getest op het SCE_xAO instrument met de interne bron en gedurende waarnemingen. Voor de tests gedurende waarnemingen rapporteren we een verbetering van het ruwe contrast van een factor ~ 2 tussen 2 en $4 \lambda/D$ door het meten en controleren van de dertig laagste zernikecoëfficiënten.

Hoofdstuk 3 en 4: Ruimtelijke lineaire donkerveldcontrole met de vector-apodiserende faseplaat

Deze twee hoofdstukken presenteren de succesvolle implementatie van ruimtelijke lineaire donkerveldcontrole (*Linear Dark Field Control*; LDFC) voor het SCE_xAO instrument. LDFC veronderstelt een lineair verband tussen intensiteitsveranderingen in sommige delen van het heldere veld van de coronagrafische PSFs van de vAPP en golffront aberraties. We laten zien dat, om LDFC succesvol te laten werken met de vAPP zonder defocus, een amplitude-asymmetrie moet worden geïntegreerd in het vAPP-ontwerp.

Hoofdstuk 3 beschrijft de implementatie van LDFC bij SCE_xAO, inclusief een ruis analyse van de prestaties van LDFC met de SCE_xAO vAPP. Verder worden de resultaten van de tests met de interne bron gepresenteerd die temporeel gecorreleerde, evoluerende fase-aberraties simuleren met de vervormbare spiegel. We vinden dat, wanneer LDFC als een controlesysteem met terugkoppeling opereert, er een factor van ongeveer 3 aan verbetering is in het ruwe contrast in het donkere veld tijdens de volledige duur van de test.

Hoofdstuk 4 beschrijft de resultaten van de eerste succesvolle LDFC test gedurende waarnemingen. Er worden twee soorten tests gepresenteerd: (1) correctie van kunstmatig geïntroduceerde aberraties, en (2) correctie van golffrontfouten die afkomstig zijn van de telescoop, het instrument en de atmosfeer. Bij het introduceren van aberraties met de vervormbare spiegel, vinden we dat LDFC het ruwe contrast verbetert met een factor 3–7

over het donkere veld door de resterende golffrontfout te verkleinen van ~ 90 nm naar ~ 40 nm kwadraatgemiddeld. Voor het tweede type tests laten we zien dat de huidige implementatie van LDFC in staat is om evoluerende aberraties te onderdrukken met tijdschalen $< 0.1 - 0.4$ Hz, en wordt beperkt door de huidige Python-implementatie. We vinden dat het vermogen bij 10 mHz wordt verminderd met een factor ~ 20 , 7 en 4 voor de ruimtelijke frequenties van respectievelijk 2.5, 5.5 en $8.5 \lambda/D$.

Hoofdstuk 5: De polarisatie-gecodeerde zelf-coherente camera

Dit hoofdstuk presenteert de polarisatie-gecodeerde zelf-coherente camera (*polarization-encoded self-coherent camera*; PESCC), een geïntegreerde beeldvlak golffrontsensor en coronagraaf, die een nieuwe en krachtige variant van de zelf-coherente camera (*self-coherent camera*; SCC) is. De PESCC implementeert een Lyot-stop met een referentiegat die een polarisator bevat en een stroomafwaartse polariserende bundelsplitser. We laten zien dat de PESCC de vereisten voor de grootte van de optica, de bemonstering van het beeldvlak door de detector en de spectrale resolutie versoepelt in vergelijking tot de SCC. Verder vinden we door middel van numerieke simulaties dat de PESCC effectief toegang heeft tot ~ 16 keer meer fotonen, waardoor de gevoeligheid van de golffront meting met een factor ~ 4 wordt verbeterd. We laten ook zien dat, zonder aanvullende metingen, coherente differentiële afbeelden (*coherent differential imaging*; CDI) gebruikt kan worden als contrastversterkende nabewerkingstechniek voor elke waarneming. In geïdealiseerde simulaties die representatief zijn voor instrumenten van ruimtetelescopen met een lading twee vortex coronagraaf, laten we zien dat golffront meting en -controle, gecombineerd met CDI, een 1σ ruw contrast kan bereiken van $\sim 3 \cdot 10^{-11} - 8 \cdot 10^{-11}$ tussen 1 en $18 \lambda/D$.

Hoofdstuk 6: Het lage windeffect controleren met Fast and Furious beeldvlak golffront detectie

Dit hoofdstuk presenteert de inzet van het *Fast and Furious* (F&F) beeldvlak golffront-detectiealgoritme op het SCEXAO instrument om het lage-windsnelheidseffect (*low-wind effect*; LWE) te meten en corrigeren. F&F is een sequentieel fase-diversiteitsalgoritme en een softwarematige oplossing voor het detecteren van golffronten in het beeldvlak. Tests met de interne bron laten zien dat F&F een breed scala aan LWE-achtige aberraties kan corrigeren en de PSF terug kan brengen naar een hoge Strehl-ratio ($> 90\%$) en hoge symmetrie. Verder presenteren we resultaten genomen gedurende waarnemingen die aantonen dat F&F in staat is om de PSF-kwaliteit te verbeteren onder zeer uitdagende atmosferische omstandigheden. Gelijktijdige waarnemingen van de PSF in het zichtbare golflengte bereik ($\lambda = 750$ nm, $\Delta\lambda = 50$ nm) laten zien dat we afwijkingen aan het corrigeren waren die gemeenschappelijk waren voor de optische en NIR-paden binnen SCEXAO.

Hoofdstuk 7: Zeer nauwkeurige astrometrie en fotometrie van direct in beeld gebrachte exoplaneten met het vectorspikkelraster

Dit hoofdstuk presenteert de theorie en simulaties van het vectorspikkelraster (*vector speckle grid*; VSG). Het VSG is een nieuw optisch element om kunstmatige spikkels te genereren die dienen als fotometrische en astrometrische referenties bij het bestuderen van direct in beeld gebrachte exoplaneten. We laten zien, door tegengestelde amplitude-

of fasemodulatie op te leggen aan de tegenovergestelde polarisatietoestanden in het pupilvlak, dat kunstmatige spikkels worden gegeneerd die incoherent zijn met de onderliggende spikkel achtergrond. Dit verhoogt de astrometrische en fotometrische precisie aanzienlijk. In simulatie vinden we dat, voor opnamen met een korte belichtingstijd, het VSG een prestatieverbetering levert van respectievelijk een factor ~ 20 voor fotometrie en ~ 5 voor astrometrie vergeleken met scalaire varianten. Verder schetsen we hoe VSGs kunnen worden geïmplementeerd met behulp van vloeibaar-kristaltechnologie om de geometrische fase aan de circulaire polarisatietoestanden op te leggen. Het voordeel van de VSG ten opzichte van methodes die kunstmatige, incoherente spikkels genereren met de vervormbare spiegel is dat de VSG een statische oplossing is die onafhankelijk is van de kalibratie en de beperkingen van de vervormbare spiegel en primaire golffrontsensor.

Toekomst

De huidige generatie HCI-instrumenten zal zich na hun upgradeprogramma's blijven richten op het detecteren en karakteriseren van jonge, gigantische gasplaneten. Een van de belangrijkste upgrades zijn beeldvlak golffrontsensoren om niet-gemeenschappelijk-pad aberraties aan te pakken. Verschillende beeldvlak golffrontsensoren zijn met succes tijdens waarnemingen getest. Ze zijn echter nog niet gebruikt tijdens wetenschappelijke waarnemingen, een enkele uitzondering daargelaten, waardoor het moeilijk is om de impact te beoordelen wat de impact van beeldvlak golffrontsensoren op het nabewerkte contrast op dit moment is. Daarom, om de impact van beeldvlak golffrontdetectie op de end-to-end-systeemprestatie (inclusief nabewerking) te beoordelen, zouden tests tijdens wetenschappelijke observaties de hoogste prioriteit van de nabije toekomst moeten zijn.

De huidige op de grond gebaseerde HCI-instrumenten zijn er tot nu toe nog niet in geslaagd de variabiliteit van exoplaneten te detecteren door spikkelruis. Het VSG-concept, gepresenteerd in Hoofdstuk 7, is een nieuw concept om de signaal-ruisverhouding van exoplaneet variabiliteitsmetingen met HCI-instrumenten drastisch te verhogen. Door het VSG-concept te combineren met het afwisselen van de positie van de kunstmatige spikkels, door het VSG optiek tussen metingen te draaien, is dit een veelbelovende oplossing om de vereiste fotometrisch golffrontsensorhe precisie te bereiken. Wanneer dit wordt geïmplementeerd bij HCI-instrumenten, zal het een opwindende nieuwe manier zijn om de variabiliteit van reeds direct in beeld gebrachte exoplaneten te bestuderen.

Het langetermijndoel van hoog-contrast afbeelden is de detectie en karakterisering van rotsachtige exoplaneten in de bewoonbare zone van nabije sterren, en het zoeken naar tekenen van leven. Een belangrijk onderdeel van deze toekomst zijn de volgende generatie van gigantische gesegmenteerde-spiegel telescopen (*Giant Segmented Mirror Telescopes*; GSMTs). Deze telescopen hebben primaire spiegels met een diameter tussen de 25 en 39 meter, wat resulteert in een enorme toename in lichtopbrengst en hoekresolutie in vergelijking met de huidige telescopen. Daarom wordt verwacht dat GSMTs de eerste spectra van rotsachtige bewoonbare exoplaneten rond M-type hoofdreekssterren zullen verwerven door middel van directe waarnemingen.

Vanwege de enorme ondersteuningsconstructies die nodig zijn om de secundaire spiegels van GSMTs te ondersteunen, die de grootte kunnen hebben van een huidige telescoop van 4-meter klasse, wordt verwacht dat het lage-windsnelheidseffect een dominante golffrontfout zal zijn. Bovendien hebben deze telescopen gesegmenteerde primaire spiegels die zorgvuldig moeten worden gefaseerd om hun ultieme prestatie te kunnen bereiken. Beeldvlak golffrontsensoren behoren ze tot de belangrijkste oplossingen voor deze problemen. Vooral voor het Fast & Furious beeldvlak golffront-detectiealgoritme (F&F; Hoofdstuk 6) is er een grote kans om de golffrontsensor oplossing te bieden. We hebben tijdens waarnemingen met de Subaru telescoop bewezen dat F&F in staat is om met de LWE om te beheersen en hebben de eerste succesvolle tests met de gesegmenteerde Keck-telescoop tijdens waarnemingen gedaan.

GSMT's zullen hoog-contrast afbeeldinstrumenten bevatten die naar verwachting rotsachtige exoplaneten in de bewoonbare zone van nabije sterren in beeld zullen brengen en karakteriseren. Om de extreme contrasten te bereiken bij kleine hoekafstanden die nodig zijn om een rotsachtige exoplaneet in beeld te brengen, is het van het groot belang dat het hele HCI-instrument als geheel wordt geoptimaliseerd, en niet per afzonderlijk subsysteem. Het werk dat in dit proefschrift wordt gepresenteerd, biedt dergelijke geïntegreerde oplossingen. Dit biedt een unieke kans om coronagrafie, beeldvlak golffront detectie en beheersing, coherente differentiële afbeelden en polarimetrie te combineren, die de directe waarneming en karakterisering van rotsachtige exoplaneten in de bewoonbare zone mogelijk zal maken.

Publication list

Refereed publications

1. *Imaging the water snow-line during a protostellar outburst*
L.A. Cieza, S. Cassassus, J.J. Tobin, **S.P. Bos**, J.P. Williams, S. Perez, Z. Zhu, C. Caceres, H. Canovas, M.M. Dunham, A. Hales, J.L. Prieto, D.A. Principe, M.R. Schreiber, D. Ruiz-Rodriguez, A. Zurlo
2016, *Nature*, 535(7611), 258-261
2. *The Envelope Kinematics and a Possible Disk Around the Class 0 Protostar within BHR7*
J.J. Tobin, **S.P. Bos**, M.M. Dunham, T.L. Bourke, N. Van der Marel
2018, *The Astrophysical Journal*, 856(2), 164.
3. *Spatial Linear Dark Field Control and Holographic Modal Wavefront Sensing with a vAPP Coronagraph on MagAO-X*
K.L. Miller, J.R. Males, O. Guyon, L.M. Close, D.S. Doelman, F. Snik, E.H. Por, M.J. Wilby, C.U. Keller, C. Bohlman, K. Van Gorkom, A. Rodack, J. Knight, J. Lumbres, **S.P. Bos**, N. Jovanovic
2019, *Journal of Astronomical Telescopes, Instruments, and Systems*, 5(4), 049004
4. *Focal-plane wavefront sensing with the vector-Apodizing Phase Plate*
S.P. Bos, D.S. Doelman, J. Lozi, O. Guyon, C.U. Keller, K.L. Miller, N. Jovanovic, F. Martinache, F. Snik
2019, *Astronomy & Astrophysics*, 632, A48
5. *Vector speckle grid: instantaneous incoherent speckle grid for high-precision astrometry and photometry in high-contrast imaging*
S.P. Bos
2020, *Astronomy & Astrophysics*, 638, A118
6. *On-sky verification of Fast and Furious focal-plane wavefront sensing: Moving forward toward controlling the island effect at Subaru/SCEXAO*
S.P. Bos, S. Vievard, M.J. Wilby, F. Snik, J. Lozi, O. Guyon, B.R.M. Norris, N. Jovanovic, F. Martinache, J.F. Sauvage, C.U. Keller
2020, *Astronomy & Astrophysics*, 639, A52
7. *Detection of polarization neutral points in observations of the combined corona and sky during the Aug. 21 2017 total solar eclipse*
F. Snik, **S.P. Bos**, S.A. Brackenhoff, D.S. Doelman, E.H. Por, F. Bettonvil, M. Rodenhuis, D. Vorobiev, L.M. Eshelman, J.A. Shaw
2020, *Applied Optics*, 59(21), F71-F77
8. *Laboratory Demonstration of Spatial Linear Dark Field Control For Imaging Extrasolar Planets in Reflected Light*
T. Currie, E. Pluzhnik, O. Guyon, R. Belikov, K.L. Miller, **S.P. Bos**, J.R. Males, D. Sirbu, C. Bond, R. Frazin, T. Groff, B. Kern, J. Lozi, B.A. Mazin, B. Nemati, B. Norris, H. Subedi, S. Will
2020, *Publications of the Astronomical Society of the Pacific*, 132(1016), 104502

9. *The polarization-modulated self-coherent camera*
S.P. Bos
2021, *Astronomy & Astrophysics*, 646, A177
10. *Spatial linear dark field control on Subaru/SCExAO: Maintaining high contrast with a vAPP coronagraph*
K.L. Miller, **S.P. Bos**, J. Lozi, O. Guyon, D.S. Doelman, S. Vievard, A. Sahoo, V. Deo, N. Jovanovic, F. Martinache, F. Snik, T. Currie
2021, *Astronomy & Astrophysics*, 646, A145
11. *The vector-apodizing phase plate coronagraph: design, current performance, and future development*
D.S. Doelman, F. Snik, E.H. Por, **S.P. Bos**, G.P.P.L. Otten, M. Kenworthy, S.Y. Haffert, M.J. Wilby, A.J. Bohn, B.J. Sutcliffe, K.L. Miller, M. Ouellet, J. de Boer, C.U. Keller, M.J. Escuti, S. Shi, N.Z. Warriner, K.J. Hornburg, J.L. Males, K.M. Morzinski, L.M. Close, J. Codona, J. Long, L. Schatz, J. Lumbres, A. Rodack, K. Van Gorkom, A. Hedglen, O. Guyon, J. Lozi, T. Groff, J. Chilcote, N. Jovanovic, S. Thibault, C. de Jonge, G. Allain, C. Vallée, D. Patel, O. Côté, C. Marois, P. Hinz, J. Stone, A. Skemer, Z. Briesemeister, A. Boehle, A.M. Glauser, W. Taylor, P. Baudoz, E. Huby, O. Absil, B. Carlomagno, C. Delacroix
2021, *Applied Optics*, 60(19), D52-D72
12. *First on-sky demonstration of spatial Linear Dark Field Control with the vector-Apodizing Phase Plate at Subaru/SCExAO*
S.P. Bos, K.L. Miller, J. Lozi, O. Guyon, D.S. Doelman, S. Vievard, A. Sahoo, V. Deo, N. Jovanovic, F. Martinache, T. Currie, F. Snik
Accepted for publication in *Astronomy & Astrophysics*.
13. *Circular polarimetric imaging at planetary-system scales by hacking SPHERE-IRDIS: Full-Stokes observations of the asymmetric nebula surrounding VY CMa*
K.N. Strelow, D. Abbink, R.G. van Holstein, **S.P. Bos**, Z. Wahhaj, J. de Boer, C. Ginski, J. Milli, F. Ménard, F. Snik
In preparation.
14. *Polarization-dependent beam shifts upon metallic reflection in high-contrast imagers and telescopes*
R.G. van Holstein, C.U. Keller, F. Snik, **S.P. Bos**, H.M. Schmid
In preparation.

Conference proceedings

1. *Rigorous vector wave propagation for arbitrary flat media*
S.P. Bos, S.Y. Haffert, C.U. Keller
2017, *Proc. of SPIE Vol. 10407, Polarization Science and Remote Sensing VIII*, 1040709
2. *A review of high contrast imaging modes for METIS*
M. Kenworthy, O. Absil, B. Carlomagno, F. Snik, T. Agócs, E.H. Por, B.R. Brandl,

- S.P. Bos**
2018, Proc. of SPIE Vol. 10702, Ground-based and Airborne Instrumentation for Astronomy VII, 10702A3
3. *High Contrast Imaging for Python (HCIPy): an open-source adaptive optics and coronagraph simulator*
E.H. Por, S.Y. Haffert, V.M. Radhakrishnan, D.S. Doelman, M. van Kooten, **S.P. Bos**
2018, Proc. of SPIE Vol. 10703, Adaptive Optics Systems VI, 1070342
 4. *On-sky results of the Leiden EXoplanet Instrument (LEXI)*
S.Y. Haffert, M.J. Wilby, C.U. Keller, I.A.G. Snellen, D.S. Doelman, E.H. Por, M. van Kooten, **S.P. Bos**, J. Wardenier
2018, Proc. of SPIE Vol. 10703, Adaptive Optics Systems VI, 1070323
 5. *Fully broadband vAPP coronagraphs enabling polarimetric high contrast imaging*
S.P. Bos, D.S. Doelman, J. de Boer, E.H. Por, B. Norris, M.J. Escuti, F. Snik
2018, Proc. of SPIE Vol. 10706, Advances in Optical and Mechanical Technologies for Telescopes and Instrumentation III, 107065M
 6. *New NIR spectro-polarimetric modes for the SCExAO instrument*
J. Lozi, O. Guyon, N. Jovanovic, B. Norris, T. Groff, J. Chilcote, J. Kasdin, T. Kudo, M. Tamura, J. Zhang, **S.P. Bos**, F. Snik, D.S. Doelman, S. Vievard, A. Sahoo, T. Currie, F. Martinache
2019, Proc. of AO4ELT 6
 7. *Status of the SCExAO instrument: recent technology upgrades and path to a system-level demonstrator for PSI*
J. Lozi, O. Guyon, S. Vievard, A. Sahoo, N. Jovanovic, B. Norris, B. Mazin, A. Walter, P. Tuthill, T. Kudo, H. Kawahara, T. Kotani, M. Ireland, N. Cvetojevic, E. Huby, S. Lacour, T.D. Groff, J. Chilcote, J. Kasdin, F. Martinache, R. Laugier, J. Knight, **S.P. Bos**, F. Snik, D.S. Doelman, E. Bendek, R. Belikov, T. Currie, Y. Minowa, C. Clergeon, N. Takato, M. Tamura, H. Takami, M. Hayashi
2019, Proc. of AO4ELT 6
 8. *Overview of focal plane wavefront sensors to correct for the Low Wind Effect on SUBARU/SCExAO*
S. Vievard, **S.P. Bos**, F. Cassaing, A. Ceau, O. Guyon, N. Jovanovic, C.U. Keller, J. Lozi, F. Martinache, A. Montmerle-Bonnefois, L. Mugnier, M. N'Diaye, B. Norris, A. Sahoo, J.F. Sauvage, F. Snik, M.J. Wilby, A. Wong
2019, Proc. of AO4ELT 6
 9. *New NIR spectro-polarimetric modes for the SCExAO instrument*
J. Lozi, O. Guyon, T. Kudo, J. Zhang, N. Jovanovic, B. Norris, M.A. Martinod, T.D. Groff, J. Chilcote, M. Tamura, **S.P. Bos**, F. Snik, S. Vievard, A. Sahoo, V. Deo, F. Martinache, J. Kasdin
2020, Proc. of SPIE Vol. 11448, Adaptive Optics Systems VII, 114487C

10. *Status of the SCExAO instrument: recent technology upgrades and path to a system-level demonstrator for PSI*
 J. Lozi, O. Guyon, S. Vievard, A. Sahoo, V. Deo, N. Jovanovic, B. Norris, M.A. Martinod, B. Mazin, A. Walter, N. Fruitwala, S. Steiger, K. Davis, P. Tuthill, T. Kudo, H. Kawahara, T. Kotani, M. Ireland, T. Anagnos, C. Schwab, N. Cvetojevic, E. Huby, S. Lacour, K. Barjot, T.D. Groff, J. Chilcote, J. Kasdin, F. Martinache, R. Laugier, M. N'Diaye, J. Knight, J.R. Males, **S.P. Bos**, F. Snik, D.S. Doelman, K.L. Miller, E. Bendek, R. Belikov, E. Pluzhnik, T. Currie, M. Kuzuhara, T. Uyama, J. Nishikawa, N. Murakami, J. Hashimoto, Y. Minowa, C. Clergeon, Y. Ono, N. Takato, M. Tamura, H. Takami, M. Hayashi
 2020, Proc. of SPIE Vol. 11448, Adaptive Optics Systems VII, 114480N
11. *Validating advanced wavefront control techniques on the SCExAO testbed/instrument*
 O. Guyon, J. Lozi, S. Vievard, R. Belikov, E. Bendek, **S.P. Bos**, T. Currie, V. Deo, M. Fitzgerald, D. Gratadour, T. Groff, N. Jovanovic, H. Kawahara, T. Kotani, T. Kudo, C. Lopez, H. Ltaief, J.R. Males, F. Martinache, M.A. Martinod, B.A. Mazin, K.L. Miller, B. Norris, M. N'diaye, E. Pluzhnyk, A. Sahoo, A. Sevin, N. Skaf, F. Snik, M. Tamura, A. Wong
 2020, Proc. of SPIE Vol. 11448, Adaptive Optics Systems VII, 114481Z
12. *Adaptive optics real-time control with the compute and control for adaptive optics (Cacao) software framework*
 O. Guyon, A. Sevin, F. Ferreira, H. Ltaief, J.R. Males, V. Deo, D. Gratadour, S. Centre, F. Martinache, J. Lozi, S. Vievard, N. Fruitwala, **S.P. Bos**, N. Skaf
 2020, Proc. of SPIE Vol. 11448, Adaptive Optics Systems VII, 114482N
13. *MagAO-X first light*
 J.R. Males, L.M. Close, O. Guyon, A.D. Hedglen, K. Van Gorkom, J.D. Long, M. Kautz, J. Lumbres, L. Schatz, A. Rodack, K.L. Miller, D.S. Doelman, F. Snik, **S.P. Bos**, J.M. Knight, K. Morzinski, V. Gasho, C.U. Keller, S.Y. Haffert, L. Pearce
 2020, Proc. of SPIE Vol. 11448, Adaptive Optics Systems VII, 114484L
14. *Focal plane wavefront sensing on SUBARU/SCExAO*
 S. Vievard, **S.P. Bos**, F. Cassaing, T. Currie, V. Deo, O. Guyon, N. Jovanovic, C.U. Keller, M. Lamb, C. Lopez, J. Lozi, F. Martinache, K.L. Miller, A. Montmerle-Bonnefois, L.M. Mugnier, M. N'Diaye, B. Norris, A. Sahoo, J.F. Sauvage, N. Skaf, F. Snik, M.J. Wilby, A. Wong
 2020, Proc. of SPIE Vol. 11448, Adaptive Optics Systems VII, 114486D
15. *Calibration of the instrumental polarization effects of SCExAO-CHARIS' spectropolarimetric mode*
 R.G. van Holstein, **S.P. Bos**, J. Ruigrok, J. Lozi, O. Guyon, B. Norris, F. Snik, J. Chilcote, T. Currie, T.D. Groff, N. Jovanovic, J. Kasdin, T. Kudo, F. Martinache, B. Mazin, A. Sahoo, M. Tamura, S. Vievard, A. Walter, J. Zhang
 2020, Proc. of SPIE Vol. 11447, Ground-based and Airborne Instrumentation for Astronomy VIII, 114475B

16. *New concepts in vector-Apodizing Phase Plate coronagraphy*
S.P. Bos, D.S. Doelman, K.L. Miller, F. Snik
2020, Proc. of SPIE Vol. 11448, Adaptive Optics Systems VII, 114483W
17. *“Fast” and Furious focal-plane wavefront sensing at W.M. Keck Observatory*
S.P. Bos, M. Bottom, S. Ragland, J.R. Delorme, S. Cetre, L. Pueyo
In preparation.
18. *Full characterization of the instrumental polarization effects of the spectropolarimetric mode of SCEXAO/CHARIS*
J. 't Hart, R.G. van Holstein, **S.P. Bos**, J. Ruigrok, F. Snik, J. Lozi, O. Guyon, T. Kudo, J. Zhang, N. Jovanovic, B. Norris, M.A. Martinod, T.D. Groff, J. Chilcote, T. Currie, M. Tamura, S. Vievard, A. Sahoo, V. Deo, K. Ahn, F. Martinache, J. Kasdin
In preparation.

Curriculum Vitae

I was born on May 8th, 1993 in Delft, the Netherlands, the place where I also grew up. From 2005 to 2011 I attended the Stanislascollege Westplantsoen in Delft with a specialization in the natural sciences and technology. During this period I was a member of the Stanislas Tech Team and participated with this team in the FIRST Tech Challenge, which is a robotics competition for high-school students. We became national champions of the Netherlands and qualified for the world championships in Atlanta, USA, in which we participated in 2010. My interest in astronomy developed during my high school period while reading books and internet pages on space travel, stars, galaxies and the universe.

Due this to interest I decided to start the Bachelor's program in astronomy at Leiden University in September, 2011. During this time I got more and more interested in astronomical instrumentation. This led in the summer of 2014 to a six week internship at the opto-mechatronics department of TNO in Delft studying the feasibility of a tip/tilt mirror to counteract atmospheric turbulence for the BlackGEM telescope. I finished my Bachelor's in 2015 with a research project on "Achromatic liquid crystal linear polarization modulation" supervised by Frans Snik in the group of Christoph Keller. In the following summer I attended the summer school "Introduction to Astronomical Instrumentation" in Toronto, Canada organized by the Dunlap Institute.

To deepen my knowledge on instrumentation I joined in August, 2015 the Master's program at Leiden University in the specialization "Astronomy & Instrumentation". To deepen my knowledge on optics I also followed some courses at the Technical University in Delft, which turned out to be essential for my later research projects. My minor research project was on "Determining the masses and disk sizes of the youngest protostars and proto-binary stars" supervised by John Tobin in the group of Ewine van Dishoeck. I got the opportunity to present this work during the *Nederlandse Astronomen Conferentie* in 2016. My graduation project was "Rigorous vector diffraction for arbitrary flat surfaces" supervised by Sebastiaan Haffert in the group of Christoph Keller.

In September, 2017 I started a PhD under the supervision of Frans Snik in the instrumentation group of Christoph Keller at Leiden Observatory. The original goal of the project was to integrate the vector-Apodizing Phase Plate coronagraph with polarimetry, spectroscopy and focal-plane wavefront sensing. But this slowly evolved towards the development and on-sky demonstration of new focal-plane wavefront sensors for the direct imaging of exoplanets. In the autumn of 2017 I went to Raleigh, USA for a six weeks visit to the Geometric-Phase Photonics Lab led by Michael Escuti to learn all about liquid-crystal technology. I made another trip to the USA during the last few months of 2018 when I spent two months with the SCEXAO team in Hawaii. During this time I learned to operate the SCEXAO high-contrast imaging instrument and tested my first focal-plane wavefront sensor on this instrument. I presented my work during multiple in-person and digital conferences in Europe, North America and Japan. During my PhD I have given multiple talks on the search for exoplanets for the general public and assisted in multiple outreach activities of the observatory and university. I have been a teaching assistant of the first-year Bachelor's course *planetenstelsels* for five years, and (co-)supervised six Bachelor's and four Master's students.

During my time at Leiden Observatory I have served in various committees. During my Master I was a member of the *Onderwijs Faciliteiten* committee. In my PhD I joined

the social committee and soon after became its chairman, been a member of the Institute Council and (briefly) of the Social Support committee. In 2018 I was one of the organizers of the annual workshop of the Network of Young Researchers in Instrumentation for Astronomy when it was held in Leiden. I have also been a member of the board of editors of the *Nederlands Tijdschrift van de Natuurkunde*.

I had the opportunity to observe with some of the world's largest optical telescopes during my time in astronomy. For a Bachelor's course I observed with the Isaac Newton Telescope on La Palma, Spain to look for a bridge of stars between two star clusters. I joined two observation runs with the LEXI instrument led by Sebastiaan Haffert at the William Herschel Telescope, La Palma during my Master's and PhD. Later on in my PhD I observed with the Subaru telescope and Keck telescope at Hawaii, USA during engineering nights to test new focal-plane wavefront sensors. Other highlights of my PhD were the 2017 and 2019 solar eclipses in the USA and Chile respectively, the launch of the balloon-based HiCIBaS telescope in Timmins, Canada, and looking down on the ALMA telescope while standing on the summit of Cerro Toco, Chile.

I will start working as Design Engineer at ASML in the EUV Projection group on July 1st, 2021.

Acknowledgements

It feels good to be typing the last words of this PhD thesis. It marks the end of a journey with many ups and downs. From the moment when I had no idea of what I was doing and everything seemed to simultaneously go wrong, to celebrating the successful on-sky demonstration of a new algorithm. All these moments are precious to me, because without the one you cannot truly appreciate the value of the other. I could not have completed this journey, with its ups and downs, on my own. Many people have contributed in some way and I would like to thank them here.

First of all, I would like to thank Frans for all the adventures around the world during the last few years and giving me encouragements and the freedom to pursue my own ideas. And Christoph, thank you for your help in the last months when it was most necessary.

Within Leiden Observatory there are many people that make sure that everything runs smoothly. Erik, Eric and David, thank you for your support with computer related issues. Marjan, Monica, Susanne, Hafize, Els, Alexandra and Evelijn, thank you for all your help with practical matters that come up during a PhD.

I spent the majority of my time in the instrumentation group, and have seen many of its members come and go. David, Rob and Alex thanks for all the fun times drinking beer and eating pizza, and especially for the fun night in Tokyo. I think that we have to improve our rapping skills before we can attempt another Eminem song during karaoke. Sebastiaan and Emiel, you have taught me so much about programming and optics. Your knowledge and insights have always been very valuable to me. Maaïke and Kelsey, thank you for being the co-members of the gurl squad during our trip to Quebec and introducing me to *How I met your mother*. Can't wait to try another of those vanilla soft serve cones with white chocolate dip! Mireille, I'm glad that you came to join us in Leiden after your balloon adventures, and I enjoyed our time being officemates. Rico, Willeke, Floor, Elina and Thijs, thank you for bringing new energy into the group. Your presence made the last year so much more enjoyable. And all the other members of the research group: Olivier, Patrick, Fedde, Dirk, Dora, Mike, Vikram, Jos, Christian, Schuyler, Remko, Matt, Bernard, Rudolf, Leo and Chad, thank you for the interesting discussions during the meetings, and the relaxed and friendly environment.

Leindert, Leon, Stijn, and Kirsty, sorry for all the instrumentation talk all day, every day. We sometimes tend to forget that there are more things in astronomy than exoplanets and instruments. Thank you for your friendship, the fun chats during the borrels and coffee breaks on either the 11th or the 5th floor.

Harold, Michiel, Marijn en Anthony, there was always pleasant cooperation when organizing and teaching the *Planetenstelsels* course. Jens, Vincent and all the other teaching assistants, thank you for all the laughs when grading the (sometimes endless) streams of homework. I would also like to thank the students that I have (co-)supervised: Stefanie, Pieter, David, Nicky, Daphne, Kira, Jasper, Alex, Andy and Joost. Good luck with your future studies!

Although we only briefly shared an office at the start of my PhD, Jorryt and Geert-Jan, thank you for teaching me a thing or two about transit observations of exoplanets and those galaxies really far far away.

A big thanks to the members of the SCEXAO team. During my visit to Hilo I really en-

joyed all the Hawaiian adventures that you took me on, and the weekly volleyball matches were perfect for testing the reaction time of my reptile brain. Those two months were the absolute highlight of my PhD. I can't wait to come back and eat a delicious sandwich at the Le Yellow Sub and some tasty pork ribs at Jackie Rey's. Especially Olivier, Julien, Sebastian, Nemanja and Ananya, without your hard work, help, and fruitful discussions the majority of my thesis would not be here today.

Although the results did not make it into this thesis, I would also like to thank Michael, Sam, Jacques and Sylvain for their help with the on-sky demonstration of Fast&Furious at the Keck telescope. Our sessions during my evening and your morning were always pleasant and it was very satisfying when we finally managed to crack the convergence problem.

Michael, Shuoja, Zane and all the others at the Geometric Phase Lab, thank you for the warm welcome during my visit to Raleigh and teaching me all about the wonders of liquid-crystal technology.

Tot slot is het prettig om dit proefschrift in het Nederlands te kunnen eindigen. Vincent, Fré, Sam, Falko en Sebastiaan, aan de dagen dat we tot diep in de nacht aan calculus opdrachten zaten heb ik toch merkwaardig goede herinneringen overgehouden. Bavo en Kasper, dank voor alle goede gesprekken en de gezelligheid wanneer we weer eens naar Delft afreisden om te leren hoe het nou eigenlijk precies zit met Fourier optica.

Ik wil graag de mannen bedanken uit de verscheidene waterpoloteams bij LZ 1886, ZVL 1886 en d'Elft. Niks is beter om de gedachten van werk te halen dan 1,5 uur keihard trainen en ballen op het goal te knallen.

Daarnaast zijn er nog vele vrienden die allemaal heel erg belangrijk voor mij zijn. Ik dank jullie allemaal voor jullie vriendschap, de gezelligheid en het aanhoren van al mijn eideloze verhalen over sterrenkunde.

Mijn broertje en zusje, Tom en Dorine, bedankt hoe jullie altijd klaar staan voor mij. Ik waardeer jullie hulp echt enorm en ben zo trots op wat jullie al hebben bereikt en nog gaan bereiken in de toekomst. Pap en Mam, zonder jullie was dit nooit allemaal gelukt. Erg dankbaar ben ik voor al de aandacht, het advies, de steun en stimulans om mijn eigen pad te kiezen. Ook waardeer ik de moeite die jullie steken in het begrijpen van mijn werk, want dat is lang niet altijd eenvoudig.

Als laatste wil ik mijn lieve vriendin Charlotte bedanken. Zonder jouw liefde, enthousiasme en steun door dik en dun zou het me nooit gelukt zijn om dit proefschrift te schrijven. Wij hebben het altijd zo leuk samen en zijn altijd aan het lachen. Ik kijk zo enorm uit naar al onze toekomstige avonturen, want samen gaan we de wereld veroveren!